NANOENGINEERING FOR ENHANCED TOXIC METALS ADSORPTION: FROM SYNTHESIS TO BIORECOGNITION

Allwin Mabes Raj

Doctoral Dissertation
Jožef Stefan International Postgraduate School
Ljubljana, Slovenia

Supervisor: Prof. Dr. Aleksandra Lobnik, IPS, Ljubljana, and IOS d.o.o., Maribor, Slovenia
Co-Supervisor: Assoc. Prof. Dr. Aleš Lapanje, IPS and Jožef Stefan Institute, Ljubljana, Slovenia

Evaluation Board:
Prof. Dr. Milena Horvat, Chair, IPS and Jožef Stefan Institute, Ljubljana, Slovenia
Prof. Dr. Urban Bren, Member, Faculty of Chemistry and Chemical Engineering, University of Maribor, Slovenia
Prof. Dr. Ivana Murković Steinberg, Member, Faculty of Chemical Engineering and Technology, University of Zagreb, Croatia

MEDNARODNA PODIPLOMSKA ŠOLA JOŽEFA STEFANA
JOŽEF STEFAN INTERNATIONAL POSTGRADUATE SCHOOL

Allwin Mabes Raj

NANOENGINEERING FOR ENHANCED TOXIC METALS ADSORPTION: FROM SYNTHESIS TO BIORECOGNITION

Doctoral Dissertation

NANOINŽENIRING ZA IZBOLJŠANO ADSORPCIJO STRUPENIH KOVIN: OD SINTEZE DO BIOLOŠKEGA PREPOZNAVANJA

Doktorska disertacija

Supervisor: Prof. Prof. Dr. Aleksandra Lobnik, IPS, Ljubljana, and IOS d.o.o., Maribor, Slovenia

Co-Supervisor: Assoc. Prof. Dr. Aleš Lapanje, IPS, and Jožef Stefan Institute, Ljubljana, Slovenia

Ljubljana, Slovenia, June, 2025

To

Tamilpavai Allwin Mabes Raj (my wife) and Chezhiyan Raj
Pandian Allwin Mabes Raj (my son) and my readers

Acknowledgments

First and foremost, I would like to express my heartfelt gratitude to **Dr. Aleksandra Lobnik**, **Luka Lobnik**, and **Tina Lobnik**, who have supported me in Slovenia not only as academic mentors but also as a second family. Their unwavering guidance, care, and encouragement have been fundamental to both my professional and personal journey.

A special note of thanks goes to my supervisor, **Dr. Aleš Lapanje**, whose intellectual brilliance and insightful ideas were indispensable throughout this project. It has been an honor to work with such an inspiring mentor. Without his profound input and innovative solutions, the development of the sensor would not have been possible.

I am also deeply grateful to **Prof. Milena Horvat**, coordinator of the **GMOS-Train project**, whose leadership, vision, and continued support have been instrumental in ensuring the success of this research.

I extend my sincere appreciation to my colleagues and working supervisors at the **Jožef Stefan Institute (JSI)** and **IOS, Maribor**, who contributed to my work and growth. At JSI, I would like to thank **Dr. Tomaž Rijavec**, who provided constructive leads for molecular cloning, **Dmitrii Deev**, **Farzaneh Hosseini**, **Dr. Tayebeh Sharifi**, **Raghuraj S. Chouhan**, and from the mercury group – **Dr. Igor Živković**, **Dr. Ermira Begu**, **Adna Alilović**, **Polona Klemenčič**, **Waqar Ali**, **Saeed**, and **Dr. Jan Gačnik**.

At IOS, I am especially thankful to **Dr. Aljoša Košak**, my working supervisor, for his consistent support. My appreciation also goes to **Maja Bauman** for her professional guidance, and to **Andreja Gutmaher** for her thorough support. I would also like to thank **Dr. Ajra Hadela** for conducting the FTIR analyses, **Prof. Dr. Urban Bren** and his team for his supervision of the electrochemical impedance studies and performing the HD modeling., and **Zala Štukovnik** for her insights on EIS measurements. I am also grateful to **Vid Šumak**, **Dr. Žiga Žebec**.

This project has received funding from the **European Union's Horizon 2020 research and innovation programme** under the **Marie Skłodowska-Curie grant agreement No. 860497**.

I also gratefully acknowledge support from the project titled **"Electrochemical detection of methylmercury"**, funded by **ARIS (L7-60161(C))** through slovenian national research funding ARIS.

Finally, I wish to express my deepest gratitude to my family. To my wife, **Tamilpavai Allwin Mabes Raj**, who not only applied for this Marie Skłodowska-Curie position on my behalf but has remained my steadfast guide in all aspects of life. To my beloved son, **Chezhiyan Raj Pandian**, who is my world. I acknowledge my sister-in-law **Dr. Manimozhi** for her constant prayers and heartfelt support, which have meant a great deal to me. I am also grateful to **my mother-in-law and father-in-law** for their daily encouragement and sincere interest in my work—their kindness and humility have been truly inspiring. And to my parents, whose unconditional love and support have been my foundation throughout this journey.

Lastly, with a touch of scientific humor and humility, I extend my thanks to the ever-resilient ***Escherichia coli*** and the **MerB proteins**—without which this research would quite literally not have existed.

Abstract

Environmental contamination by toxic metals—such as Pb^{2+}, Cr^{3+}, and Hg^{2+}—and organometallic species like monomethylmercury (MeHg) presents one of the most persistent global challenges due to their bioaccumulation, long-term toxicity, and resistance to degradation. This thesis addresses this critical issue through a multidisciplinary approach combining nanotechnology, environmental chemistry, biosensor engineering, and sustainable materials science.

The first part of this work investigates the synthesis and functionalization of nanostructured adsorbents for efficient toxic metal removal. Amino-functionalized SiO_2 nanoparticles and γ-Fe_2O_3@NH_2 magnetic nanoparticles were developed and evaluated for their metal ion adsorption efficiency under varying environmental conditions. These materials demonstrated excellent performance in removing Pb^{2+}, Cr^{3+}, and Hg^{2+}, with enhanced selectivity, regeneration capability, and recyclability—paving the way for practical use in decentralized water treatment systems.

Building on this, superparamagnetic spinel ferrite nanomaterials were engineered for dual-functionality: remediation of Hg^{2+} and recovery of valuable rare earth elements (REEs) such as Dy^{3+} and Tb^{3+}. Characterized by sol–gel auto-combustion synthesis, these nano-adsorbents offered high adsorption capacity, Langmuir-type isotherm behavior, and environmental safety validated through ecotoxicity testing. This supports a circular economy framework in pollutant management.

The second core of the thesis centers on the development of a highly sensitive and selective biosensor for the detection of MeHg, a compound known for its neurotoxic and teratogenic effects, even at femtogram levels. As part of the H2020-MSCA-ITN GMOS-Train project, MerB (organomercurial lyase), a bacterial enzyme evolved for MeHg detoxification, was cloned, expressed, and immobilized on gold nanoparticle-modified screen-printed electrodes using Ni^{2+}-chelating linker chemistry. The resulting biosensor demonstrated unprecedented sensitivity—capable of detecting MeHg at 3 femtograms—with high selectivity and no interference from inorganic Hg^{2+}.

Electrochemical techniques including cyclic voltammetry (CV) and electrochemical impedance spectroscopy (EIS) confirmed the redox activity and conformational changes of MerB upon MeHg binding, establishing real-time quantitative readout capabilities. The biosensor proved portable, cost-effective, and user-friendly, with successful trials in environmental and fish tissue matrices—offering a transformative alternative to labor-intensive techniques like CVAFS and ICP-MS.

Overall, this thesis delivers a unified platform of smart nanomaterials and biosensors for comprehensive toxic metals and MeHg management. It bridges molecular biology with advanced materials and electrochemical engineering, contributing significantly to sustainable development goals, public health protection, and global mercury monitoring in alignment with the Minamata Convention.

Povzetek

Okoljsko onesnaženje s strupenimi kovinami – kot so Pb^{2+}, Cr^{3+} in Hg^{2+} – ter organskokovinskimi spojinami, kot je monometilživo srebro (MeHg), predstavlja enega najbolj trdovratnih globalnih izzivov zaradi njihove bioakumulacije, dolgotrajne toksičnosti in odpornosti proti razgradnji. Ta disertacija obravnava to ključno problematiko z multidisciplinarnim pristopom, ki združuje nanotehnologijo, okoljsko kemijo, inženiring biosenzorjev ter znanost o trajnostnih materialih.

V prvem delu raziskave je predstavljena sinteza in funkcionalizacija nanostrukturiranih adsorbentov za učinkovito odstranjevanje strupenih kovin. Razviti in ovrednoteni so bili amino-funkcionalizirani SiO_2 nanodelci in magnetni nanodelci γ-Fe_2O_3@NH_2, katerih sposobnost adsorpcije kovinskih ionov je bila testirana v različnih okoljskih pogojih. Ti materiali so izkazali izjemno učinkovitost pri odstranjevanju Pb^{2+}, Cr^{3+} in Hg^{2+}, z izboljšano selektivnostjo, možnostjo regeneracije in večkratne uporabe – kar odpira možnosti za njihovo praktično uporabo v decentraliziranih sistemih za čiščenje vode.

Nadalje so bili razviti superparamagnetni spinele feritni nanomateriali z dvojno funkcionalnostjo: za odstranjevanje Hg^{2+} in hkrati za pridobivanje dragocenih elementov redkih zemelj (REE), kot sta Dy^{3+} in Tb^{3+}. Ti nano-adsorbenti, pripravljeni s sol–gel samovžigovno sintezo, so pokazali visoko adsorpcijsko kapaciteto, Langmuirjevo izotermno obnašanje in okoljsko varnost, potrjeno z ekotoksikološkimi testi – kar podpira okvir krožnega gospodarstva pri obvladovanju onesnaževal.

Drugo jedro disertacije se osredotoča na razvoj visoko občutljivega in selektivnega biosenzorja za zaznavanje MeHg, spojine, znane po svojih nevrotoksičnih in teratogenih učinkih že pri femtogramskih koncentracijah. V okviru projekta H2020-MSCA-ITN GMOS-Train je bila bakterijska encimska beljakovina MerB (organomerkurialna liaza), ki sodeluje pri razstrupljanju MeHg, klonirana, izražena in imobilizirana na z zlatimi nanodelci modificiranih elektrodah s pomočjo Ni^{2+}-kelatne vezave. Nastali biosenzor je pokazal izjemno občutljivost – sposoben zaznave MeHg pri 3 femtogramih – z visoko selektivnostjo in brez motenj zaradi anorganskega Hg^{2+}.

Elektrokemijske tehnike, kot sta ciklična voltametrija (CV) in elektrokemijska impedančna spektroskopija (EIS), so potrdile redoks aktivnost in konformacijske spremembe MerB ob vezavi MeHg, kar omogoča kvantitativno sprotno zaznavanje. Biosenzor je mobilen, cenovno ugoden in uporabniku prijazen, uspešno pa je bil preizkušen v okoljskih vzorcih in tkivih rib – kar ponuja prebojno alternativo zahtevnim tehnikam, kot sta CVAFS in ICP-MS.

Skupno ta disertacija predstavlja celostno platformo pametnih nanomaterialov in biosenzorjev za učinkovito upravljanje s strupenimi kovinami in MeHg. Združuje molekularno biologijo z naprednimi materiali in elektrokemijskim inženiringom, s čimer pomembno prispeva k ciljem trajnostnega razvoja, varovanju javnega zdravja in globalnemu spremljanju živega srebra v skladu z Minamatsko konvencijo.

Contents

List of Figures

List of Tables

Abbreviations

AAS	...	Atomic Absorption Spectroscopy
AFS	...	Atomic Fluorescence Spectroscopy
IPS	...	International Postgraduate School
AI	...	Artificial Intelligence
AL	...	Aluminium
AS	...	Arsenic
Au	...	Gold
AuNPs	...	Gold Nanoparticles
BET	...	Brunauer Emmett Teller
CNTs	...	Carbon Nanotubes
CO_2	...	Carbon Dioxide
Cr	...	Chromium
CV	...	Cyclic Voltammetry
CVAFS	...	Cold Vapor Atomic Fluorescence Spectrometry
CVD	...	Chemical Vapor Deposition
Dy	...	Dysprosium
EDX	...	Energy Dispersive X-ray Spectroscopy
EIS	...	Electrochemical Impedance Spectroscopy
FTIR	...	Fourier Transform Infrared Spectroscopy
GO	...	Graphene Oxide
Hg	...	Mercury
HCl	...	Hydrochloric Acid
H_2O	...	Water
ICP-MS	...	Inductively Coupled Plasma Mass Spectrometry
IPS	...	International Postgraduate School
JSI	...	Jožef Stefan Institute
LOQ	...	Limit of Quantification
LOD	...	Limit of Detection
MeHg	...	Monomethylmercury
ML	...	Machine Learning
MNPs	...	Magnetic Nanoparticles
MOFs	...	Metal Organic Frameworks
MWCNT	...	Multi-Walled Carbon Nanotube
NaOH	...	Sodium Hydroxide
O_2	...	Oxygen
Pb	...	Lead

pH	...	Potential of Hydrogen (acidity/alkalinity)
QDs	...	Quantum Dots
REEs	...	Rare Earth Elements
SEM	...	Scanning Electron Microscopy
SMP	...	Small Molecule Probe
SWCNT	...	Single-Walled Carbon Nanotube
TEM	...	Transmission Electron Microscopy
WCB	...	Whole-Cell Biosensor
XPS	...	X-ray Photoelectron Spectroscopy
XRD	...	X-ray Diffraction

Symbols

L	...	Liter
M	...	Molarity (mol/L)
≤	...	Less than or equal to
≥	...	Greater than or equal to
≈	...	Approximately equal to
≠ –	...	Not equal to
Δ –	...	Change in (Delta)
∑ –	...	Summation
∫ –	...	Integral
→	...	Reaction direction or implies
←	...	Reverse reaction or implies
±	...	Plus-minus (uncertainty range)
°C	...	Degrees Celsius
°	...	Degrees (angle or temperature)
µ / μ	...	Micro (10^{-6} prefix)
×	...	Multiplication or “times”
=	...	Equals
+	...	Plus
-	...	Minus
/	...	Division
^	...	Exponentiation
%	...	Percent
(	...	Opening bracket
)	...	Closing bracket
M	...	Molar concentration (mol/L)
n	...	Number of moles (sample size)
µg	...	Microgram
mg	...	Miligram
g	...	Gram
kg	...	Kilogram
mm	...	Millimeter

Glossary

Term	Definition
MeHg (Monomethylmercury)	An organometallic form of mercury known for its high toxicity and bioaccumulation in food chains.
Hg^{2+}	Inorganic divalent mercury ion, less toxic than MeHg but still hazardous.
Pb^{2+}, Cr^{3+}	Lead and Chromium ions, common environmental pollutants with chronic health risks.
Nanoparticles	Engineered particles with dimensions <100 nm, used here for adsorption and sensing applications.
γ-Fe_2O_3@NH_2	Amino-functionalized maghemite nanoparticles, used for metal ion adsorption.
MerB (Organomercurial Lyase)	Enzyme that cleaves the C–Hg bond in MeHg, enabling detoxification and detection.
Screen-Printed Electrode (SPE)	A disposable electrode platform used for biosensing, modified with nanomaterials.
Ni^{2+}-NTA Linker	Nickel-chelating chemistry used to immobilize His-tagged proteins like MerB on surfaces.
CV (Cyclic Voltammetry)	Electrochemical technique to study redox properties of analytes.
EIS (Electrochemical Impedance Spectroscopy)	Technique that measures impedance to detect binding events on electrodes.
Langmuir Isotherm	A model describing adsorption behavior on surfaces, assuming monolayer coverage.
REE (Rare Earth Elements)	Valuable elements like Dy^{3+} and Tb^{3+} recovered during nanoparticle-based remediation.
Circular Economy	A sustainability concept emphasizing resource reuse and recycling.
Minamata Convention	A global treaty to reduce mercury pollution and protect human health and the environment.
CVAFS	Cold Vapor Atomic Fluorescence Spectroscopy, a standard but complex method for mercury analysis.
ICP-MS	Inductively Coupled Plasma Mass Spectrometry, a powerful but costly technique for metal detection.

Chapter 1

Introduction

1.1 The Silent Poison: How Toxic Metals Have Shaped Civilizations and Still Threaten Our Future

Throughout history, humans have been both beneficiaries and victims of the metals that surround us. Metals like lead, mercury, cadmium, and arsenic have played crucial roles in technological advancement, economic power, and cultural development. Yet, hidden beneath their utility lies a darker legacy: toxicity that can quietly but devastatingly impact human health and the environment. These toxic metals, often imperceptible to the naked eye, continue to infiltrate water, food, and air, turning our progress into potential peril. These narrative traces the journey of toxic metals from their early uses in ancient civilizations to their insidious presence in today's ecosystems.

1.1.1 Ancient Civilizations and the Rise of Metal Use

Metals like lead and mercury were among the first to be manipulated by ancient societies. The Romans, for instance, extensively used lead for plumbing, hence the term "plumbing" from the Latin plumbum. Lead-lined aqueducts and pipes were engineering marvels of their time, but modern analysis suggests chronic lead poisoning may have contributed to the decline of Roman society (Gilfillan S.C, 1965). Lead was also added to cosmetics, wine, and cooking utensils, further increasing the exposure levels among both elites and commoners.

Similarly, mercury was used in ancient China and India for medicinal purposes, often seen as a magical or spiritual substance. Alchemists believed it could grant immortality, a tragic irony given its neurotoxic effects. In medieval Europe, mercury was also used to treat syphilis, a practice that often resulted in poisoning rather than a cure. These early applications reflect humanity's long-standing fascination with metals, often coupled with a profound misunderstanding of their biological consequences.

The Minamata disaster in 20th-century Japan, where industrial mercury discharge caused widespread neurological disease, echoes these early misuses and misbeliefs (Harada, 1995). Victims exhibited symptoms of severe brain damage, including loss of motor control, hearing and speech impairments, and in extreme cases, death. The event remains a stark reminder of the dangers of unregulated metal use.

1.1.2 Industrial Revolution and Environmental Consequences

The Industrial Revolution exponentially increased the extraction and use of metals. Coal combustion released arsenic, mercury, and cadmium into the atmosphere. Industrial runoff and mining wastes contaminated rivers and soils, and the establishment of smelting industries accelerated the spread of these contaminants.

These metals do not degrade over time; instead, they bioaccumulate in plants, animals, and humans, entering the food chain with devastating results. For instance, methylmercury, a highly toxic form of mercury, biomagnifies through aquatic food webs. By the time it reaches top predators, including humans, its concentration may be millions of times higher than in the surrounding water (Mabes Raj et al., 2025).

Lead gasoline, introduced in the 1920s, marked another dark chapter. It improved engine performance but at the cost of public health. Children exposed to leaded gasoline showed reduced IQs and cognitive function well into adulthood(Needleman et al., 1990). Though leaded gasoline has now been phased out globally, its legacy lingers in urban dust and soils. In many developing cities, dust and paint from old buildings still contribute to chronic low-level lead exposure.

1.1.3 Sources of Toxic Metals in the Environment

Toxic metals enter the environment through both natural and anthropogenic sources. Natural processes, such as volcanic eruptions, forest fires, and the weathering of rocks, release metals like mercury and arsenic into the environment. However, human activities have significantly amplified the presence of these metals in various ecosystems.

Industrial Activities: Mining, smelting, and the manufacturing of products like batteries and electronics are major contributors to metal pollution. For instance, lead and mercury are often released from industrial plants and can be found in the surrounding soils and waterways (Moghimi Dehkordi et al., 2024).

Urbanization and Waste Disposal: Industrial waste, improper disposal of electronic waste, and lead-based paints in old buildings contribute to metal pollution in urban areas. Contaminated landfills, as well as the burning of fossil fuels, release toxic metals into the atmosphere and surrounding environments (Caravanos et al., 2011).

Toxic metals enter the environment through both natural and anthropogenic sources. Natural processes, such as volcanic eruptions, forest fires, and the weathering of rocks, release metals like mercury and arsenic into the environment. However, human activities have significantly amplified the presence of these metals in various ecosystems.

Agricultural Practices: The use of pesticides, fertilizers, and herbicides that contain toxic metals, such as cadmium, further exacerbates contamination. These metals accumulate in soils and enter food chains through agricultural products (Kabata-Pendias, 2010).

1.1.4 Modern-Day Exposure and Health Impacts

Today, toxic metal exposure is more insidious than ever. Mercury from artisanal gold mining and coal combustion still contaminates water bodies. Arsenic in groundwater affects millions across South Asia, particularly in Bangladesh, where natural arsenic leaches into shallow tube wells. Chronic arsenic poisoning, known as arsenicosis, leads to skin lesions, organ damage, and cancer.

Cadmium, often found in batteries and phosphate fertilizers, accumulates in crops such as rice. In Japan, cadmium poisoning caused Itai-Itai disease, a painful condition marked by brittle bones and kidney dysfunction. These examples illustrate how metals, once released into the environment, become almost impossible to eliminate.

Currently active mining operations remain significant sources of toxic metal contamination globally. Regions with intensive mining activities—such as the Peruvian Andes (gold and silver mining), the Democratic Republic of Congo (cobalt and copper), China (rare earths and lead), India (bauxite and chromium), and South Africa (gold and platinum group metals)—frequently report elevated levels of metals like mercury, lead,

cadmium, arsenic, and chromium in surrounding ecosystems (Chirinos-Peinado et al., 2025; Hou et al., 2023).

These metals interfere with cellular metabolism, disrupt enzyme functions, and damage DNA. Chronic exposure, even at low levels, is linked to cancers, cardiovascular diseases, kidney damage, and neurodegenerative disorders (L Järup et al., 1998).The most vulnerable are children and pregnant women, who suffer lifelong consequences from early exposure. Even prenatal exposure to metals like mercury and lead has been linked to developmental delays, attention disorders, and learning disabilities.

Table 1: Toxic metals and human health risks.

TOXIC METAL	**PRIMARY EXPOSURE SOURCES**	**HUMAN HEALTH RISKS**	**KEY REFERENCES**
Mercury (Hg)	Contaminated fish, industrial emissions, artisanal gold mining	Neurotoxicity, developmental delays, kidney damage	(Mabes Raj et al., 2025)
Lead (Pb)	Lead-based paints, contaminated soil and water, battery manufacturing	Neurodevelopmental disorders in children, hypertension, kidney damage	(Lanphear et al., 2005)
Cadmium (Cd)	Industrial discharge, phosphate fertilizers, cigarette smoke	Kidney damage, bone demineralization, respiratory issues	(L Järup et al., 1998)
Arsenic (As)	Contaminated groundwater, mining, pesticides	Skin lesions, cancer (lung, bladder, skin), cardiovascular disease	(Quansah et al., 2015)
CHROMIUM (CR^{6+})	**INDUSTRIAL PROCESSES, ELECTROPLATING, TANNERIES**	**LUNG CANCER, NASAL AND SKIN IRRITATION, KIDNEY AND LIVER DAMAGE**	**(HOSSINI ET AL. 2022)**

Beyond individual health, toxic metal contamination threatens food security, biodiversity, and clean water access. Contaminated irrigation water can impair crop yield and introduce toxins into the food supply, while aquatic organisms suffer from reduced reproduction and altered growth rates is depicted in Figure 1.

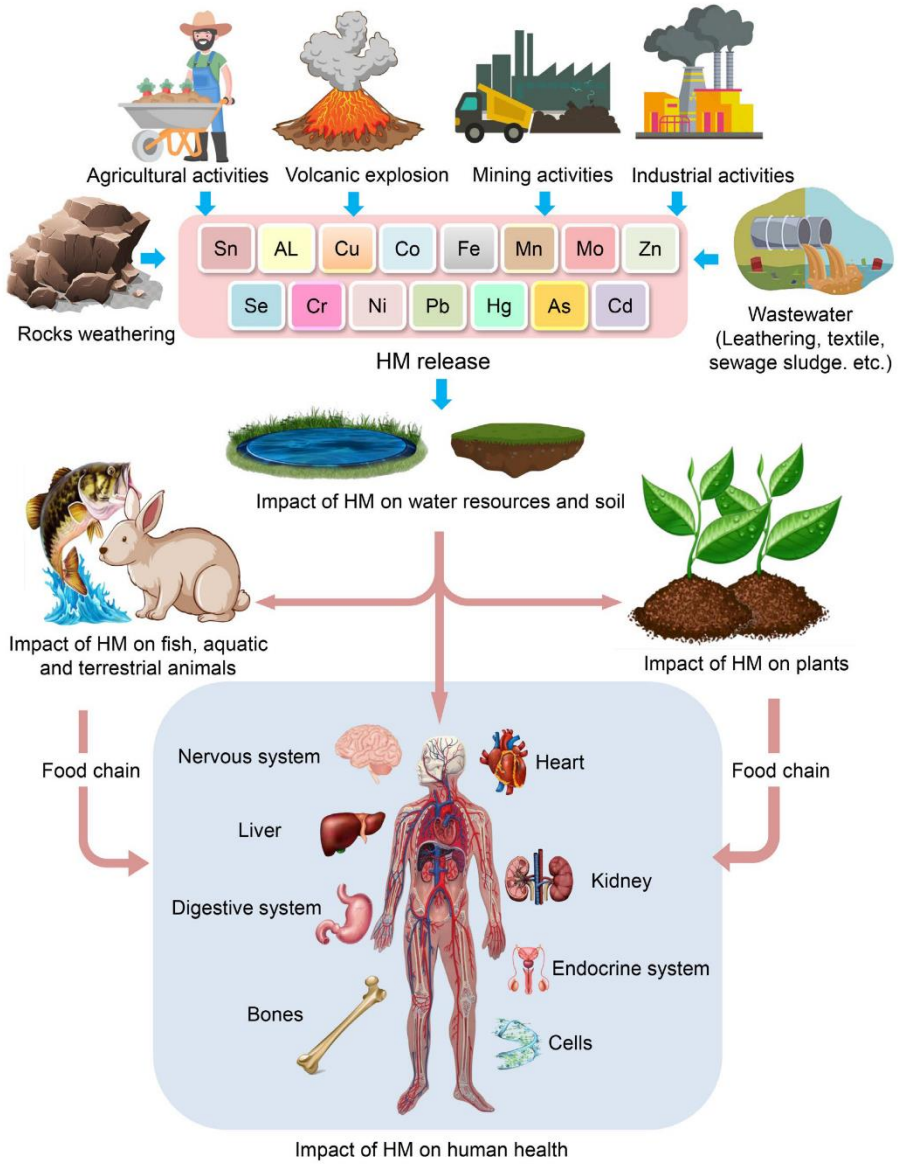

Figure 1: Impact of toxic metals on human health.

Reproduced from (Abd Elnabi et al., 2023), with permission from MDPI, under the terms of the Creative Commons Attribution License, CC BY 4.0.

1.1.5 The Global Response and Remaining Challenges

Global treaties like the Minamata Convention on Mercury aim to curb mercury emissions. Signed by over 120 countries, the treaty mandates a phase-out of mercury-containing products, stricter emission controls, and public health strategies. Efforts to replace toxic metals in consumer products and industrial processes are underway.

Yet enforcement is uneven, and monitoring is still insufficient in many regions. In parts of Africa, Latin America, and Southeast Asia, informal e-waste recycling, battery smelting, and illegal gold mining continue to release toxic metals into the environment. Often, these practices are driven by poverty and lack of education, making regulation difficult.

Furthermore, the lack of real-time detection technologies and rapid-response systems hampers mitigation. Often, contamination is only detected after significant exposure has already occurred.

1.1.6 The Future: Innovations and Hope

Emerging technologies offer a glimmer of hope. Nanoengineered adsorbents and biosensors are being developed to detect and remove trace metals from water with high specificity and sensitivity. Nanomaterials such as metal-organic frameworks (MOFs), carbon nanotubes, and functionalized magnetic nanoparticles have shown promise in removing arsenic, lead, and mercury.

Phytoremediation, using plants to extract metals from soil, and mycoremediation, utilizing fungi, are cost-effective and environmentally friendly methods gaining traction. Researchers are also working on synthetic biology approaches to engineer microbes capable of selectively binding or transforming toxic metals.

Public awareness, combined with rigorous policy and innovation, can drive meaningful change. Community-level initiatives in India and Bangladesh have introduced arsenic filters and promoted deeper tube wells, dramatically reducing exposure. In the EU and North America, regulatory frameworks have driven industries to innovate and reduce metal emissions.

Efforts to combat toxic metal contamination include both technological solutions and policy initiatives. The development of cleaner industrial technologies, the enforcement of environmental regulations, and the promotion of sustainable agricultural practices are essential to reducing metal pollution.

1.2 When Old Tools Fail: Why Traditional Methods Can't Keep Up with the Modern Metal Menace

For centuries, humankind has faced the challenge of purifying water and soil from natural and anthropogenic contaminants. Among these, toxic metals such as lead (Pb), cadmium (Cd), arsenic (As), and mercury (Hg) have posed persistent threats to human health and ecosystems. While conventional adsorption techniques have long been employed to mitigate this threat, given traditional methods are inadequate in coping with today's complex contamination scenarios.

1.2.1 Historical Background and Development of Adsorption Techniques

Adsorption as a water purification method has deep historical roots. Ancient Egyptian and Indian civilizations used sand, charcoal, and gravel to purify water—a practice mentioned in early Sanskrit texts and Egyptian papyri (Smith, 2017). During the 18th and 19th centuries, the understanding of physical adsorption improved significantly with the study of gases on charcoal, eventually giving rise to activated carbon filtration systems. By the mid-20th century, activated carbon, alumina, and zeolites became the cornerstones of metal ion removal in industrial and municipal wastewater treatment systems (Y. Huang et al., 2019).

Despite their longevity, these traditional materials primarily rely on non-specific physical adsorption, which lacks selectivity for particular ions and exhibits poor regeneration capacity under complex environmental conditions.

1.2.2 Limitations of Conventional Adsorbents

Several limitations challenge the efficacy of traditional adsorbents in handling modern contamination profiles:

Low Selectivity: Activated carbon and similar porous materials are non-specific and bind multiple species without discrimination. This results in competitive adsorption, reducing the uptake of target toxic metals when other ions are present (Liu et al., 2019).

Limited Adsorption Capacity: Traditional materials often reach saturation quickly, especially in high-metal-load scenarios such as mine tailings, electroplating wastewater, or electronic waste leachate. Regeneration is often incomplete, further reducing efficiency over time (Gkika et al., 2025).

Incompatibility with Low Concentration and Complex Matrices: Many modern contaminants are present at trace levels in complex matrices containing organic matter and multiple interfering species. Conventional adsorbents struggle to capture metals at parts-per-billion (ppb) levels without pre-treatment steps (Y. Huang et al., 2024).

Environmental and Economic Costs: The large volume of waste generated during regeneration and the energy-intensive processes required for material recovery further complicate the sustainability of conventional adsorbents.

1.2.3 The Turning Point: Demand for High-Efficiency Adsorbents

By the late 20th and early 21st centuries, the proliferation of toxic metal pollution—especially from electronics, battery disposal, and artisanal gold mining—revealed the insufficiencies of conventional methods. A demand emerged for "smart" materials capable

of targeting metals with high specificity, operating under environmentally relevant conditions, and regenerating efficiently.

This demand, coupled with advances in material science, led to the exploration of functionalized adsorbents, particularly nanoengineered materials, which offered higher surface area, enhanced reactivity, and tunable surface chemistry.

1.2.4 Toward the Future: Innovations in Adsorption Technology

Nanoengineered Adsorbents: Nanomaterials such as metal–organic frameworks (MOFs), carbon nanotubes (CNTs), graphene oxide (GO), and magnetic nanoparticles have revolutionized adsorption. Their high surface area-to-volume ratio and modifiable surfaces enable selective adsorption of metal ions (Sheoran et al., 2022).

Functionalization with Chelating Groups: Advanced adsorbents are now functionalized with thiol (-SH), amine (-NH_2), or carboxyl (-COOH) groups to mimic natural metal-binding sites, significantly improving metal specificity. These modifications allow selective uptake even in multicomponent systems (Liu et al., 2021).

Hybrid Adsorbents: Composites integrating natural materials (e.g., biochar, clays) with nanomaterials provide a balance between affordability and performance. These hybrid systems improve mechanical strength, adsorption kinetics, and regeneration efficiency (L. Wang et al., 2022)

Biopolymer-Based Adsorbents: Chitosan, alginate, and cellulose-based materials functionalized with nanoparticles are gaining interest for their biodegradability and efficiency in binding metal ions. Their biocompatibility makes them attractive for water purification applications in low-resource settings (Doyo et al., 2023). Various Materials used in Adsorption Technology and different adsorption mechanisms are depicted in Figure 2

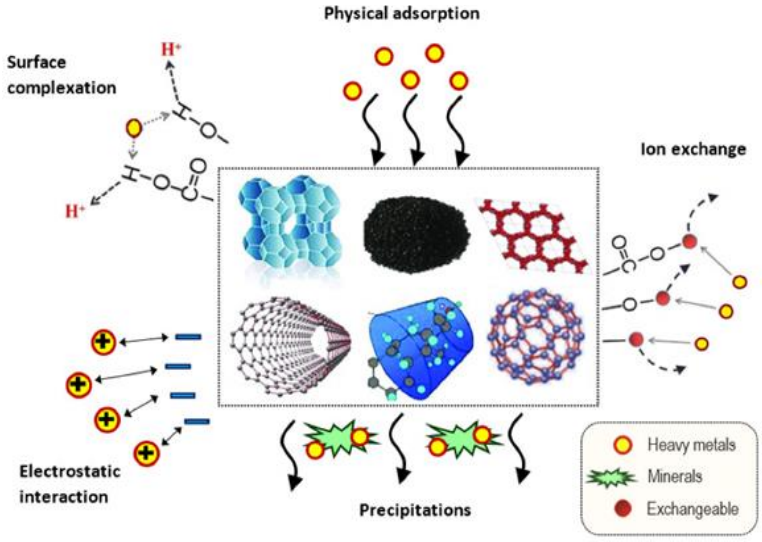

Figure 2: Schematic of different adsorption mechanisms.

Reproduced from (Rezania et al., 2024), with permission from MDPI, under the terms of the Creative Commons Attribution License (CC BY 4.0).

1.2.5 Challenges in Adsorbent Regeneration

One of the main limitations of conventional adsorption techniques is the difficulty in regenerating adsorbents for repeated use. Activated carbon, while highly effective, suffers from a limited adsorption capacity, especially when dealing with large volumes of contaminants. Once saturated, the adsorbent needs to be regenerated to restore its functionality.

Regeneration Process: The regeneration of adsorbents typically involves thermal treatment, chemical desorption, or solvent washing. However, these processes are not always efficient. Thermal regeneration can be energy-intensive, leading to increased operational costs, while chemical regeneration might result in secondary waste and environmental concerns (Mourão et al., 2008). Furthermore, the regeneration process may not always fully restore the adsorbent's original capacity, leading to the need for more frequent replacement.

Limitations in Regeneration: Many adsorbents, especially activated carbon, lose their effectiveness after multiple regeneration cycles. This results in the need for continuous replenishment of adsorbent materials, contributing to increased operational costs and waste generation (Lan et al., 2023). In addition, the high energy demand for thermal regeneration exacerbates the sustainability challenges of this process.

Limited Adsorption Capacity: Another key challenge of conventional adsorption techniques is the limited adsorption capacity of the adsorbents. While materials like activated carbon have high surface areas, their capacity to adsorb pollutants is finite and is often reached quickly, especially when dealing with complex mixtures or high concentrations of contaminants.

Saturation of Adsorbents: Adsorbent saturation occurs when all available active sites on the adsorbent surface are occupied by the pollutant molecules. This leads to a decrease in the efficiency of the adsorption process. For instance, in the case of activated carbon, the adsorption capacity can be influenced by factors such as temperature, pH, and the nature of the pollutants (Santos et al., 2022).

Competitive Adsorption: In many real-world applications, adsorbents are exposed to complex mixtures of pollutants. This can result in competitive adsorption, where the presence of multiple pollutants reduces the overall adsorption efficiency. For example, when removing toxic metals from water, different metals may compete for the same adsorption sites, limiting the efficiency of the process (Fouda-Mbanga et al., 2024).

High Operational Costs: Conventional adsorption techniques can be costly due to several factors, including the purchase and regeneration of adsorbents, the energy required for regeneration processes, and the disposal of spent adsorbents. The high operational costs often limit the widespread application of adsorption in large-scale industrial processes.

Cost of Adsorbents: Activated carbon is expensive to produce and purchase, and its high cost is one of the primary obstacles to its large-scale application. While alternatives such as natural adsorbents (e.g., clay or biosorbents) are being explored, they often come with limitations in terms of adsorption capacity and efficiency (Dabioch et al., 2013).

Energy Consumption: The regeneration of adsorbents, particularly through thermal methods, requires significant energy inputs. This not only increases the operational costs but also raises environmental concerns due to the increased carbon footprint associated with high-energy processes.

Disposal Costs: After the adsorbent is saturated with pollutants, it must be disposed of or treated. The disposal of spent adsorbents, particularly those that contain hazardous materials, adds an additional layer of cost and environmental impact (Fouda-Mbanga et al., 2024).

Environmental Concerns: Although adsorption techniques are often considered environmentally friendly, they are not without their own environmental concerns. The

disposal of spent adsorbents and the use of chemicals during the regeneration process can lead to pollution if not managed properly.

Secondary Pollution: In some cases, the regeneration process generates secondary pollutants. For example, thermal regeneration of activated carbon can release harmful gases, and chemical regeneration may leave behind toxic residues that need to be treated.

Waste Generation: The use of conventional adsorbents can also generate large amounts of waste, particularly if the adsorbent cannot be effectively regenerated. This waste must be managed carefully to avoid contributing to environmental contamination.

1.2.6 Emerging Solutions and Alternatives

Several strategies are being explored to address the challenges of conventional adsorption techniques. These include the development of more efficient adsorbent materials, innovations in the regeneration process, and the use of alternative adsorption methods.

Emerging Adsorbents: New materials such as nanomaterials, graphene-based adsorbents, and bioadsorbents are being investigated for their superior adsorption capacities and lower environmental impact (Y. Huang et al., 2024). These materials have shown promise in terms of higher adsorption efficiency and the ability to target specific pollutants.

Advanced Regeneration Methods: Research is ongoing into more energy-efficient and environmentally friendly regeneration techniques. For example, microwave-assisted regeneration has been shown to reduce energy consumption and regeneration time compared to conventional thermal methods (Jang et al., 2023).

Integration with Other Treatment Methods: Combining adsorption with other techniques, such as filtration or photocatalysis, can improve overall treatment efficiency. Hybrid systems may help overcome the limitations of adsorption alone by providing more comprehensive pollution removal (X. Zhang et al., 2022).

1.3 Nanoengineering for Metal Adsorption

Nanoparticles: The last ten years have been an era for the use of various nanomaterials/ NPs / nanotechnology for the fabrication of NPs based absorbents. Selectivity, specificity, detection time and lower assay costs are rapidly enhanced by the employment of NPs (Sapountzi et al., 2017). Nanostructures of varied sizes (1 to 100 nm) can be used for the betterment of absorbents, which brings in portability, stability and analytical technologies. NPs can be used for catalytic characteristics, amplification of the electrochemical signal and surface area improvisation.

1.3.1 Gold Nanoparticles (AuNPs)

Gold nanoparticles (AuNPs) are predominantly used NPs in MeHg adsorbtion/sensing and various other environmental toxins due to their stability against oxidation and non-toxicity effects(Vigneshvar et al., 2016). AuNPs have unique features such as simple one-pot synthesis, easy functionalization, electronic and optical ownership, special interaction with biological compounds and excellent conductivity. AuNPs develop different colors based on their shape, size and aggregation state in the colloidal solution. When employing techniques such as SPR, the incident of a light beam with a wavelength larger than the AuNPs but the oscillating electrons cannot move through the surface of the particles; additionally, the electrons cloud will be accumulated at one side of the AuNPs, opposite direction of the incident light beam. The above-mentioned strategy was demonstrated by Mie's theory (Mulvaney, 1996) and it governs dimension, morphology and the surrounding dielectric constant. Consequently, this set-up is favorable for the sensing analyte depending on interaction with the AuNPs that will cause changes in the electron's oscillation followed by color change used NPs. Several AuNPs integrated biosensors have been developed with SPR sensing properties (Yuan et al., 2018; Zeng et al., 2013). AuNPs can offer an excellent matrix for the transfer of electrons from biological molecules towards electrodes for some redox reaction between host molecule and guest analyte. When employing bulk materials in electrochemical sensors, there is a huge loss of redox species when transferring to the surface of the electrode; employing AuNPs can accelerate the transfer of electrons which increases the electrochemical sensing by several orders of magnitude.

1.3.2 Quantum Dots (QDs)

Quantum dots (QDs) are semiconducting nanocrystal that has remarkable luminous properties in nanoscale dimension. QDs nanocrystal narrow band gap is associated with the emission spectral from binary electron-hole relaxation. In the last decade, various optical sensing advancements have been using QDs after finding the potential in various spectral emissions from its varied size, which makes it an incredible matrix. Recently facile immobilization of various biological molecules has been achieved in QDs, which does not interfere with the emission properties; this also reduces the toxicity of the QDs to a great extent.

1.3.3 Magnetic Nanoparticles (MNPs)

There are many magnetic NPs (MNPs) used for absorbtion, but particularly ferromagnetic materials such as Iron-oxide and cobalt ferrite have been predominantly used. The main advantage of using MNPs is the ability to manipulate the MNPs using an external magnet in various solutions; for example, the aggregation of MNPs can be done

in the first step after functionalization of the biomolecules such as DNA, protein or any other functionalization.

1.3.4 Carbon Nanotubes (CNTs)

Carbon nanotubes (CNTs) can be attributed to various recent electronic and electrochemical transducer-based biosensing platforms and absorbents platform due to their excellent thermal, mechanical and electronic properties (Holzinger et al., 2014; Le Goff et al., 2011), nanowire morphology, unique bio-species interaction and large electron transition properties. The above properties of CNT can be used to wire the output from immobilized functional group onto the bulk material of the electrode. The surface area porous network facilitated by the CNTs can be used for absorbing various analyte host interactions with high specificity.

1.3.5 Nanofibers (NFs)

Nanofibers (NFs) is a polymeric material that is fabricated using the electrospinning technique (applied on a solution using high electric difference) with a fibre-like structure with a submicron dimension. NFs are economical, easy operational, and contain high porosity and high surface area, which enables its utilization in energy storage and conversion (Sun et al., 2016), electronics, tissue engineering and targeted drug delivery (Luzio et al., 2014), protein purification (Quirós et al., 2016) and development of various sensors (Amaly et al., 2018; El-Moghazy et al., 2016).

The NFs can be secondary collected on plate rotating disc, rotating drum electrode for various bio-sensing applications. The most useful application of NFs is its grafting into MNPs (Zhu et al., 2013) , CNTs (Manesh et al., 2008), AuNPs (Abd-Elhamid et al., 2019) or construction of another layer of conducting polymer (Çetin M.Z., 2018).

1.3.6 Carbon-Based Nanomaterials

Carbon-based nanomaterials have been extensively studied for their high adsorption efficiency and surface modifiability. Among them, graphene oxide (GO), carbon nanotubes (CNTs), and activated carbon are widely researched due to their large surface area, structural robustness, and surface functionalities.

Graphene sheet (GS): 2D carbon lattice with Sp2 hybridization C-atoms makes a Graphene sheet (GS). Various graphene architectures of adsorption applications are depicted below, among which GS forms a hexagonal pattern of the honeycomb structure. GS as a 2-D material serves as a good interacting matrix enabled by carbon atoms in different positions. Electronic properties such as easy electron-donating or electron-accepting of GS makes it the best skeletal structure for adsorbtion (Atta, 2015).

Graphene oxide is known for its oxygen-containing groups such as hydroxyl, epoxy, and carboxyl, which facilitate the adsorption of metal ions through electrostatic interactions and complexation. The two-dimensional structure of GO allows for enhanced exposure of functional sites and thus improved adsorption capacities. In parallel, CNTs—especially multi-walled and single-walled varieties—demonstrate excellent potential in metal adsorption. Their π-conjugated systems and ability to undergo surface modifications further boost their effectiveness in binding with metals such as Pb^{2+} and Cd^{2+} (Cao et al., 2019). For instance, functionalizing CNTs with carboxyl or amine groups enhances their metal-binding selectivity and capacity.

Sustainable sources of carbon materials, such as those derived from agricultural waste, have also shown promise in recent studies. These bio-inspired carbon nanomaterials not only reduce production costs but also offer eco-friendly alternatives to conventional adsorbents (X. Zhao et al., 2018).

1.3.7 Metal Oxide Nanoparticles

Metal oxides such as iron oxides (Fe_3O_4 and Fe_2O_3), titanium dioxide (TiO_2), and zinc oxide (ZnO) are widely recognized for their adsorption performance due to their surface charge characteristics, high reactivity, and redox behavior. Iron oxide nanoparticles, in particular, are efficient adsorbents for arsenic and chromium due to their strong affinity for oxyanion species.

A notable advantage of Fe_3O_4 nanoparticles is their magnetic property, which allows for easy separation from treated water using external magnets, enhancing reusability and minimizing environmental risks. Titanium dioxide nanoparticles not only adsorb metal ions but also demonstrate photocatalytic activity under UV light, enabling degradation of certain organic-metal complexes. The development of composite materials, such as TiO_2-GO hybrids, has further improved the dual capability of metal adsorption and photocatalysis.

Zinc oxide nanoparticles are amphoteric, meaning they function effectively in both acidic and alkaline environments, which broadens their applicability for diverse water systems. Their relatively simple synthesis and cost-effectiveness make ZnO a viable option for large-scale water treatment (K. Li et al. 2020).

1.3.8 Polymeric and Composite Nanomaterials

Polymeric nanomaterials offer great versatility and stability for metal adsorption applications. Chitosan-based nanocomposites, are particularly attractive due to their biodegradability, non-toxicity, and abundance of functional groups capable of chelating metal ions. When functionalized with thiol or amine groups, chitosan-based materials show enhanced selectivity toward specific toxic metals (Hsu et al. 2024).

Recent studies have introduced polymer-metal oxide hybrids, which merge the sorption power of metal oxides with the mechanical flexibility of polymers. For instance, chitosan-Fe_3O_4 nanocomposites not only offer high sorption efficiency but also enable magnetic recovery. Other materials like polyaniline and polyacrylamide have also shown strong binding affinities for various metal cations due to their polar groups and porous structures.

Hybrid nanocomposites: The combination of different nanomaterials—such as carbon with metal oxides—has created synergies that improve adsorption kinetics and extend material lifespans.

Magnetic nanomaterials: These materials allow for simplified post-treatment recovery processes, reducing the cost and complexity of water purification systems.

Green synthesis: Biosynthetic routes using plant extracts, bacteria, fungi, or agricultural waste offer eco-friendly alternatives to chemical synthesis. These approaches minimize toxic by-products and promote sustainability (Díez-Pascual, 2022).

Furthermore, artificial intelligence (AI) and machine learning (ML) tools are now being integrated into material design. These technologies assist in predicting adsorption behavior, optimizing synthesis routes, and modeling adsorption processes in real time. Such interdisciplinary approaches are expected to accelerate the transition of lab-scale innovations to full-scale applications

1.4 Synthesis and Characterization of Nanoengineered Adsorbents

The synthesis of nanoengineered adsorbents involves the creation of nanomaterials with engineered structures, chemical compositions, and functional groups that are optimized for specific adsorption processes. These materials can be synthesized using various methods, such as sol-gel processes, hydrothermal synthesis, electrospinning, and chemical vapor deposition, to create nanomaterials with high surface-to-volume ratios, porosity, and functional group density. Moreover, the size, shape, and surface chemistry of nanomaterials can be precisely controlled during the synthesis process to enhance their adsorption capacity and selectivity for specific pollutants, such as toxic metals, organic compounds, and dyes (Thekkudan et al., 2017). The Schematic representation on Synthesis of Magnetic Nanoparticles (MNPs) is depicted in Figure 3.

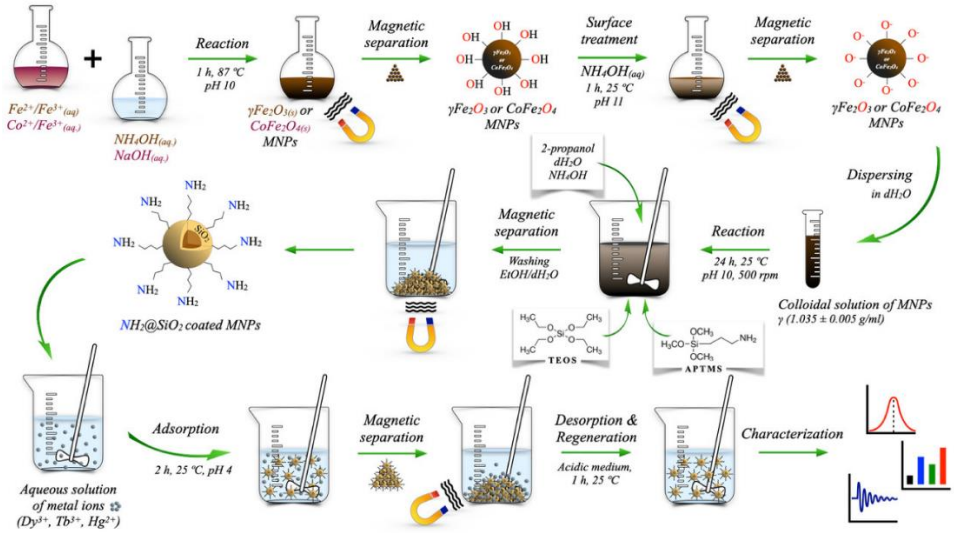

Figure 3: Schematic representation of the experimental procedure.

Synthesis of Magnetic Nanoparticles (MNPs). Reproduced from (Allwin Mabes Raj et al., 2023), with permission from MDPI, under the terms of the Creative Commons Attribution License (CC BY 4.0).

1.4.1 Methods of Synthesis of Nanoengineered Adsorbents

The synthesis of nanoengineered adsorbents involves the creation of nanomaterials with properties that maximize their adsorption efficiency. Various methods are employed to synthesize these nanomaterials, each providing different advantages depending on the desired properties of the final product. The most commonly used synthesis methods include sol-gel processes, hydrothermal synthesis, electrospinning, and chemical vapor deposition (CVD).

Sol-Gel Process: The sol-gel method is a widely used technique for the synthesis of nanoengineered adsorbents, particularly for the creation of porous nanomaterials such as silica, titanium oxide (TiO2), and alumina-based adsorbents. This process involves the formation of a colloidal solution (sol) followed by the gelation of the sol into a solid material. The sol-gel process allows for the control of particle size, porosity, and surface chemistry, making it ideal for producing adsorbents with high surface areas and tunable

properties. The sol-gel method has been used to synthesize materials for toxic metal adsorption, dye removal, and water purification (Sakka, 2013).

Hydrothermal Synthesis: Hydrothermal synthesis is another common method used to create nanoengineered adsorbents. This technique involves the use of high-pressure and high-temperature conditions to promote the crystallization of nanomaterials from aqueous solutions. Hydrothermal synthesis is often used to produce nanostructured materials such as metal oxide nanoparticles, carbon-based materials, and metal-organic frameworks (MOFs), which are then used for adsorption applications (Byrappa & Adschiri, 2007). The ability to precisely control the size and morphology of nanoparticles makes hydrothermal synthesis ideal for producing adsorbents with optimized adsorption properties.

Electrospinning: Electrospinning is a method used to produce nanofibers, which are then utilized as adsorbents in various environmental applications. In electrospinning, a polymer solution is subjected to a high-voltage electric field, causing the formation of fine fibers that can be collected on a substrate. Electrospun nanofibers exhibit high surface area and porosity, which make them ideal for applications such as toxic metal adsorption, air filtration, and water purification. Additionally, the surface of electrospun nanofibers can be functionalized with various chemical groups to enhance their adsorption capacity for specific contaminants.

Chemical Vapor Deposition (CVD): CVD is a process that involves the deposition of thin films or nanostructures onto a substrate through chemical reactions occurring in the vapor phase. This method is often used for the synthesis of carbon nanotubes (CNTs) and graphene, which are known for their high surface area and conductivity. CVD allows for the creation of nanoengineered adsorbents with excellent adsorption properties for the removal of metals, organic pollutants, and gases (Manawi et al., 2018).

1.4.2 Surface Modification of Nanoengineered Adsorbents

Surface modification is a critical step in the synthesis of nanoengineered adsorbents, as it enhances their ability to interact with specific contaminants. By introducing functional groups on the surface of nanoparticles, the adsorption capacity and selectivity of these materials can be improved. Common surface modification techniques include chemical functionalization, polymer grafting, and biomolecular immobilization.

Chemical Functionalization: Chemical functionalization involves the introduction of specific chemical groups on the surface of nanomaterials to enhance their adsorption properties. For example, thiol groups (-SH) are often introduced on the surface of nanoparticles to create strong coordination bonds with metal ions, such as mercury, lead, and cadmium. Similarly, carboxyl (-COOH) and amino (-NH2) groups are commonly introduced to enhance the adsorption of organic pollutants and toxic metals.

Polymer Grafting: Polymer grafting is a technique in which polymer chains are attached to the surface of nanoparticles, providing functional groups for adsorption. This method is often used to create composite adsorbents that combine the properties of both the polymer and the nanoparticle. The polymer matrix can be designed to interact with specific contaminants, such as dyes or metals, while the nanoparticles provide structural support and enhance the overall adsorption capacity (Wieszczycka et al., 2021).

Biomolecular Immobilization: Biomolecular immobilization involves attaching biological molecules, such as enzymes, antibodies, or aptamers, to the surface of nanomaterials. This technique enhances the selectivity of the adsorbent for specific pollutants. For example, the use of aptamers, which are short, single-stranded DNA or RNA molecules that bind specifically to target analytes, has shown promise in the development of adsorbents for toxic metal removal (Shukla et al., 2020).

1.4.3 Adsorption Mechanisms of Nanoengineered Adsorbents

The adsorption mechanisms of nanoengineered adsorbents are influenced by their surface properties, size, and morphology. These mechanisms can include physical adsorption, chemical adsorption, ion exchange, and complexation (Khan et al., 2023). Adsorption and desorption of Toxic metal ions is depicted in Figure 4.

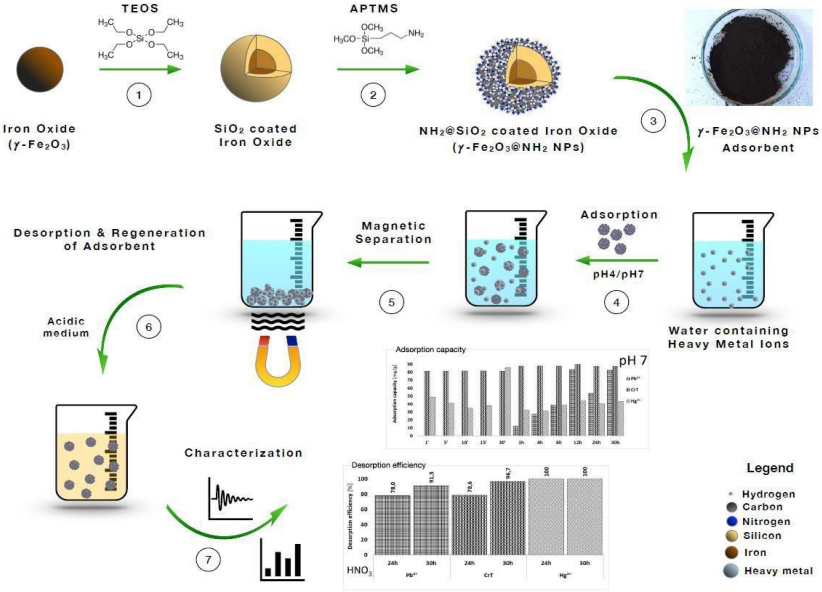

Figure 4: Adsorption and desorption of toxic metal ions.

from aqueous solutions. Reproduced from (Allwin Mabes Raj et al., 2022), with permission from MDPI, under the terms of the Creative Commons Attribution License (CC BY 4.0).

1.4.4 Characterization of Adsorbents

The efficiency of adsorbents in removing these contaminants is largely dependent on their structural, chemical, and physical properties. Characterizing the adsorbents thoroughly is, therefore, essential to optimize their performance and design more effective materials for environmental remediation applications.

The adsorption capacity, selectivity, stability, and reusability of adsorbents are some of the most critical aspects that must be assessed. These characteristics depend on the surface area, morphology, pore structure, and functional groups on the adsorbent. Understanding these properties allows researchers to design adsorbents that are not only efficient but also cost-effective and sustainable for long-term use. For instance, adsorbents with high surface areas and a large number of active sites can interact more efficiently with contaminants, improving the overall adsorption capacity (Alkhaldi et al., 2024).

The characterization of adsorbents involves the use of various analytical techniques, which can be broadly categorized into physical techniques and chemical techniques. Physical characterization methods provide information about the structural and morphological features of adsorbents, such as surface area, pore size distribution, and particle size. Common techniques in this category include Brunauer-Emmett-Teller (BET) surface area analysis, scanning electron microscopy (SEM), transmission electron microscopy (TEM), and X-ray diffraction (XRD). These techniques help in understanding the structural integrity of adsorbents, as well as the arrangement of their atoms and the size and distribution of their pores (Pellenz et al., 2023).

On the other hand, chemical characterization methods focus on identifying the chemical composition and functional groups present on the adsorbent's surface. Techniques such as Fourier-transform infrared spectroscopy (FTIR) and X-ray photoelectron spectroscopy (XPS) provide detailed information on the chemical bonds, surface functional groups, and elemental composition of adsorbents, which are critical in understanding how adsorbents interact with contaminants. FTIR helps to identify the specific functional groups, such as carboxyl, amine, or hydroxyl groups, which play a crucial role in the adsorption process by forming strong bonds with metal ions (Hu et al., 2022).

1.4.5 Physical Characterization of Adsorbents

The physical characterization of adsorbents is essential for understanding their structure and properties, which directly affect their performance in adsorbing contaminants. Several physical techniques are commonly used to analyze adsorbents, including BET surface area analysis, SEM, TEM, and XRD.

Brunauer-Emmett-Teller (BET) Surface Area Analysis: The BET method is widely used to determine the specific surface area of adsorbents. This technique involves the adsorption of nitrogen gas onto the surface of the adsorbent, and the amount of nitrogen adsorbed is measured at different pressures. The surface area is calculated based on the adsorption isotherms. A higher surface area typically corresponds to a greater number of adsorption sites, which enhances the material's efficiency in pollutant removal. The BET surface area is especially crucial for adsorbents like activated carbon, carbon nanotubes (CNTs), and graphene-based materials, which exhibit large surface areas and are widely used for the adsorption of toxic metals and organic pollutants (Sinha et al., 2019).

Scanning Electron Microscopy (SEM): SEM is a widely used technique to study the surface morphology and topography of adsorbents at high magnification. SEM provides detailed images of the adsorbent surface, showing the distribution of pores, particle size, and surface roughness. These structural features play a significant role in the adsorbent's interaction with pollutants. For example, adsorbents with a rough surface or high porosity often have more accessible active sites for metal ion adsorption (Abegunde et al., 2020). SEM has been extensively used to investigate the surface morphology of adsorbents like silica, activated carbon, and nanoengineered materials.

Transmission Electron Microscopy (TEM): TEM offers even higher magnification than SEM and is used to analyze the internal structure and particle size of adsorbents at the nanoscale. TEM is particularly useful for examining the structural integrity of nanoengineered adsorbents, such as metal-organic frameworks (MOFs), carbon-based nanomaterials, and other nanocomposites. The size and shape of nanoparticles significantly influence their adsorption capacity, with smaller particles typically exhibiting a higher surface area and enhanced adsorption properties (Zheng et al., 2023).

X-ray Diffraction (XRD): XRD is a technique used to determine the crystallinity and phase composition of adsorbents. By analyzing the diffraction pattern produced when X-rays are scattered by the adsorbent material, researchers can identify the crystal structure and assess the degree of crystallinity. XRD is particularly useful for materials like metal oxides and MOFs, where the crystallinity can influence the material's adsorption behavior. Crystalline materials often exhibit more stable and predictable adsorption properties compared to amorphous materials.

1.4.6 Chemical Characterization of Adsorbents

Chemical characterization techniques are crucial for understanding the chemical composition, surface functional groups, and bonding interactions of adsorbents, which directly impact their adsorption capacity and selectivity.

Fourier-transform Infrared Spectroscopy (FTIR): FTIR is a widely used technique for identifying the functional groups present on the surface of adsorbents. By measuring the absorption of infrared light at specific wavelengths, FTIR provides information on the molecular vibrations of functional groups such as hydroxyl (-OH), carboxyl (-COOH), and amine (-NH2) groups. These functional groups play a critical role in the adsorption process by interacting with metal ions through coordination, electrostatic attraction, or hydrogen bonding. FTIR is particularly useful for characterizing bioadsorbents like chitosan and other polysaccharides, as well as synthetic adsorbents like metal oxide nanoparticles and activated carbon.

X-ray Photoelectron Spectroscopy (XPS): XPS is a surface-sensitive technique used to analyze the elemental composition and chemical state of the elements present on the adsorbent's surface. XPS provides valuable information about the oxidation state of metal ions, the functionalization of nanomaterials, and the bonding interactions between adsorbents and pollutants. This technique has been widely used to study the surface chemistry of adsorbents such as graphene oxide, carbon nanotubes, and metal-organic frameworks (MOFs), which often exhibit complex surface chemistry that influences their interaction with contaminants.

Energy-dispersive X-ray Spectroscopy (EDX): EDX is often used in conjunction with SEM or TEM to provide elemental analysis of the adsorbent surface. EDX detects the characteristic X-rays emitted by elements when they are bombarded with electrons, allowing for the identification and quantification of elements on the adsorbent. This technique is particularly useful for understanding the adsorption of metal ions onto adsorbents and confirming the removal of target contaminants from aqueous solutions (Ahsan et al., 2019).

1.4.7 Adsorption Capacity and Selectivity

The effectiveness of an adsorbent in removing pollutants depends on several factors, including its surface area, pore size distribution, and chemical composition. The adsorption capacity refers to the amount of contaminant that can be removed per unit mass of adsorbent, while selectivity refers to the adsorbent's ability to preferentially bind specific pollutants in the presence of other contaminants.

Surface Area and Pore Size Distribution: A high surface area provides more adsorption sites, which can increase the adsorbent's capacity for pollutant removal. Additionally, the pore size distribution plays a critical role in determining the adsorbent's selectivity, as materials with smaller pores may selectively adsorb smaller molecules, while larger pores may accommodate larger molecules or metal ions.

Surface Functionalization: Surface functionalization is often used to enhance the selectivity of adsorbents for specific contaminants. Functional groups such as amines, thiols, and carboxyls can be introduced to the surface of adsorbents to selectively interact with metal ions or organic pollutants. The presence of these functional groups can significantly enhance the adsorption capacity and selectivity for specific contaminants, such as mercury, lead, or dyes (Xie et al., 2017).

1.4.8 Applications of Characterized Adsorbents

Characterized adsorbents have been widely applied in environmental remediation, particularly in the removal of toxic metals and organic pollutants from wastewater. The characterization of adsorbents ensures that the materials can be optimized for specific application

1.5 Adsorption Mechanisms and Kinetics

Adsorption is a surface-based phenomenon in which molecules or ions from a liquid or gas phase adhere to the surface of an adsorbent. It is a critical process in environmental remediation, particularly for removing toxic substances such as toxic metals, dyes, and organic pollutants from water, air, and soil. The efficiency of adsorption depends on various factors, including the adsorbent's surface area, functional groups, and the chemical properties of the adsorbate (Raji et al., 2023). Understanding the mechanisms and kinetics of adsorption is essential to optimize materials for specific applications and to improve the performance of adsorption-based systems for environmental cleanup.

Adsorption mechanisms can be classified into physical adsorption (physisorption) and chemical adsorption (chemisorption). Physisorption occurs due to weak van der Waals forces or electrostatic interactions between the adsorbent and adsorbate, whereas chemisorption involves the formation of stronger covalent or ionic bonds between the adsorbent and the adsorbate. The nature of the adsorption mechanism plays a crucial role in determining the adsorption capacity, selectivity, and reversibility of the process. Furthermore, the efficiency of adsorption is influenced by the properties of the adsorbent, such as surface area, pore structure, and functional groups, as well as external conditions like temperature, pH, and the concentration of the adsorbate.

Understanding the kinetics of adsorption is equally important for predicting the time required for an adsorbent to reach equilibrium and for evaluating the efficiency of different adsorbents under varying operational conditions. The adsorption process is typically governed by several kinetic models that describe the rate at which adsorbate molecules are bound to the adsorbent surface. Common models include the pseudo-first-order and pseudo-second-order kinetic models, which provide insight into the dynamics of the adsorption process. Additionally, the Langmuir and Freundlich isotherms describe the relationship between the concentration of adsorbate and the amount adsorbed at equilibrium, helping to assess the capacity and nature of adsorption (Hamidi et al., 2024).

The study of adsorption kinetics and mechanisms is fundamental to developing more efficient adsorbents for various applications, including wastewater treatment, air purification, and the recovery of valuable metals from industrial effluents. In the context of environmental remediation, optimizing adsorption systems involves not only selecting the right adsorbent material but also understanding how the adsorbate interacts with the adsorbent under different conditions. Moreover, understanding adsorption kinetics can also help design continuous flow adsorption systems and predict breakthrough times in dynamic adsorption columns. The mechanisms, kinetics, and applications of various adsorbents for the removal of toxic metals from an effluent are depicted in Figure 5.

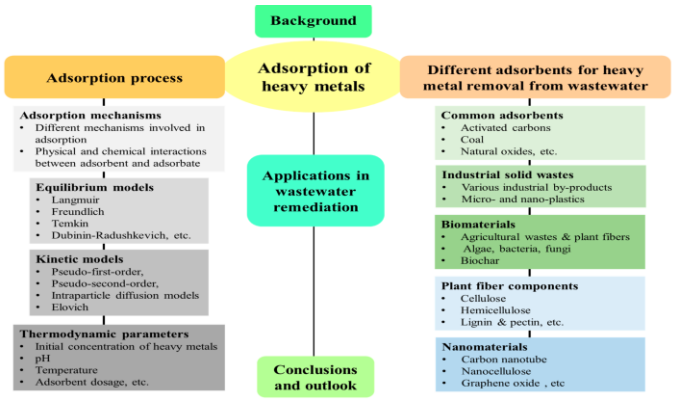

Figure 5: The mechanisms, kinetics, and applications of various adsorbents.

for the removal of toxic metals from an effluent. Reproduced from (Raji et al., 2023), with permission from MDPI, under the terms of the Creative Commons Attribution License (CC BY 4.0).

1.5.1 Adsorption Mechanisms

The mechanisms of adsorption can be broadly classified into physical adsorption (physisorption) and chemical adsorption (chemisorption). The type of interaction between the adsorbent and the adsorbate determines the nature of the adsorption process.

Physisorption: Physisorption is characterized by weak interactions, such as van der Waals forces, between the adsorbate molecules and the adsorbent surface. This type of adsorption typically occurs at low temperatures and high pressures, where the adsorbate molecules are weakly bound to the adsorbent. Physisorption is usually reversible, and the amount of adsorbate adsorbed is proportional to the surface area of the adsorbent. Adsorbents like activated carbon, silica, and polymeric materials often exhibit physisorption, making them suitable for the removal of non-polar molecules like hydrocarbons, gases, and volatile organic compounds.

Chemisorption: Chemisorption, on the other hand, involves the formation of stronger chemical bonds, such as covalent or ionic bonds, between the adsorbate and the adsorbent surface. This type of adsorption is typically more selective and occurs at higher temperatures compared to physisorption. Chemisorption often leads to irreversible adsorption and results in a higher adsorption capacity. Adsorbents like metal oxides, functionalized carbon materials, and bioadsorbents often exhibit chemisorption, making them effective for removing toxic metals, dyes, and other polar contaminants (Hamidi et al., 2024). The presence of functional groups such as hydroxyl, carboxyl, and amino groups on the adsorbent surface plays a significant role in chemisorption by facilitating the formation of strong bonds with metal ions or organic molecules.

Ion Exchange: In addition to physisorption and chemisorption, ion exchange is another important mechanism of adsorption, especially for the removal of metal ions. Ion exchange occurs when ions from the adsorbent surface are replaced by ions from the adsorbate, typically in aqueous solutions. This process is commonly observed in materials like zeolites, chitosan, and resins, which contain exchangeable ions that can adsorb metal ions like lead, cadmium, and mercury (Y.-K. Yang et al., 2009) (X. Yang et al., 2019).

1.5.2 Adsorption Kinetics

The study of adsorption kinetics is crucial for understanding the dynamics of the adsorption process, including how quickly the adsorbate molecules are adsorbed onto the adsorbent surface and how long it takes to reach equilibrium. The rate of adsorption

depends on several factors, such as the adsorbent surface area, the concentration of adsorbate, temperature, and the nature of the adsorbent and adsorbate.

$$d[ln(qe - qt)] / dt = k1 \quad (1)$$

Pseudo-First-Order Kinetic Model: The pseudo-first-order kinetic model is one of the most commonly used models to describe the adsorption rate. It is based on the assumption that the rate of adsorption is proportional to the difference between the equilibrium concentration and the concentration of the adsorbate at any given time. The equation for the pseudo-first-order model is expressed in (1).

where qe is the equilibrium adsorption capacity, qt is the adsorption capacity at time t, and k1 is the rate constant. This model is often applied to adsorption processes where the adsorption rate decreases as the adsorption sites are occupied.

$$d(q_e - q_t)/dt = k_2(q_e - q_t)^2 \quad (2)$$

Pseudo-Second-Order Kinetic Model: The pseudo-second-order kinetic model assumes that the rate of adsorption is proportional to the square of the difference between the equilibrium adsorption capacity and the current adsorption capacity. This model is often more suitable for systems where the adsorption rate is not dependent on the concentration of adsorbate at higher concentrations and when chemisorption is the dominant mechanism. The equation for the pseudo-second-order model is presented in Eq. (2), where k2 is the rate constant. The pseudo-second-order model is often used to describe the adsorption of metal ions onto adsorbents like chitosan, activated carbon, and metal oxide nanoparticles.

Intraparticle Diffusion Model: The intraparticle diffusion model is used to describe the diffusion of adsorbate molecules within the pores of the adsorbent. According to this model, the rate of adsorption is controlled by the diffusion of the adsorbate molecules into the adsorbent particles.

$$qt = k_p \, t^{(1/2)} \quad (3)$$

where kp is the intraparticle diffusion rate constant, and t is the time. Eq.(3) presented the equation for intraparticle diffusion. This model is used to evaluate whether the adsorption process is controlled by particle diffusion or by surface interaction (J. Wang & Guo, 2022)

1.5.3 Adsorption Isotherms

Adsorption isotherms describe the relationship between the amount of adsorbate and its concentration in the solution at equilibrium. Several models are used to describe adsorption isotherms, including the Langmuir, Freundlich, and Temkin models.

Langmuir Isotherm: The Langmuir isotherm model assumes that adsorption occurs on a surface with a finite number of identical sites, each capable of adsorbing one molecule. The model describes a monolayer adsorption process with no interaction between adsorbed molecules.

$$1/\mathrm{q_e} = 1/(q_\mathrm{m}K_\mathrm{l}) + (1/q_\mathrm{m}) \cdot (1/C_\mathrm{e}) \tag{4}$$

where qe is the equilibrium adsorption capacity, qm is the maximum adsorption capacity, KL is the Langmuir constant, and Ce is the equilibrium concentration of adsorbate in solution. The equation for the Langmuir isotherm in Eq.(4)

Freundlich Isotherm: The Freundlich isotherm model is an empirical model that describes adsorption on heterogeneous surfaces with different adsorption energies. It is suitable for systems where adsorption sites are not identical (Babatunde et al., 2022).

$$\mathrm{qe} = \mathrm{K_f\,C_e\text{^}\{1/n\}} \tag{5}$$

where Kf is the Freundlich constant and n is the heterogeneity factor. This model is often used for systems exhibiting non-ideal adsorption behavior. The equation for the Freundlich isotherm in Eq.(5)

1.5.4 Applications of Adsorption Mechanisms and Kinetics

Understanding adsorption mechanisms and kinetics is critical for optimizing the design and operation of adsorption systems used in environmental remediation, such as water treatment and air purification. Adsorbents are widely used to remove pollutants such as toxic metals, organic dyes, pesticides, and pharmaceuticals from wastewater. By tailoring the adsorbent's properties based on the adsorption mechanisms and kinetics, it is possible to enhance the efficiency of the adsorption process and achieve better removal of pollutants at lower costs.

1.6 Biorecognition Strategies in Metal Adsorption

1.6.1 Biorecognition Mechanisms in Metal Adsorption

Biorecognition involves the specific interaction between biological entities and target molecules. In the case of metal ion removal, the biological materials—such as microorganisms, proteins, or peptides—use their functional groups (thiols, amines, carboxyls, etc.) to bind metal ions selectively. The mechanisms of biorecognition can be broadly classified into coordination bonding, complexation, electrostatic interactions, and ionic exchange (Fu et al., 2024).

Coordination Bonding: One of the primary mechanisms for metal ion removal is the formation of coordination bonds between metal ions and the functional groups on biological surfaces. Metallothioneins, for example, are small, cysteine-rich proteins that can form stable complexes with toxic metals such as mercury, cadmium, and copper. These proteins contain thiol groups (-SH) that bind strongly to metal ions, providing a selective and effective method for their removal from aqueous solutions. Similarly, other metal-binding proteins like ferritin and phytochelatins can interact with metal ions through similar coordination bonds, enhancing the adsorption process.

Electrostatic Interactions: Many microorganisms and biomolecules involved in metal adsorption rely on electrostatic interactions to bind metal ions. The cell walls of bacteria and algae, for example, are negatively charged, allowing them to attract and adsorb positively charged metal ions. The electrostatic attraction between the adsorbent and metal ions is a critical factor in the adsorption process, especially when dealing with metals such as lead (Pb), copper (Cu), and zinc (Zn) (Chugh et al., 2022).

Complexation: In addition to coordination bonding and electrostatic interactions, complexation is a significant mechanism in biorecognition-based metal adsorption. Complexation occurs when metal ions form stable chemical complexes with the functional groups on the biological material. This mechanism is commonly observed in adsorbents like chitosan, which contains amino and hydroxyl groups that can bind with metal ions through complexation.

1.6.2 Biorecognition Agents: Microorganisms and Biomolecules

Microorganisms, such as bacteria, fungi, and algae, have been identified as effective agents for biorecognition in metal adsorption due to their ability to adapt to various environmental conditions and their natural affinity for metal ions. Different target biomarkers, bioreceptor molecules, and transducing nanomaterials integrated platform is depicted in Figure 6.

Bacteria: Bacteria, particularly those in the genus Pseudomonas and Escherichia, have shown a remarkable ability to adsorb metal ions from water through surface interactions. These microorganisms possess functional groups, including carboxyl and phosphate groups, that can interact with metal ions, facilitating their uptake and removal from solution. Bacteria such as Pseudomonas fluorescens and Bacillus subtilis have been shown to effectively remove metals like cadmium (Cd), copper (Cu), and arsenic (As). The ability of these bacteria to regenerate and adapt to various metal concentrations makes them ideal candidates for large-scale remediation (Yan et al., 2024).

Fungi: Fungal species such as Aspergillus and Penicillium have also been identified as effective biorecognition agents for metal adsorption. Fungi possess complex cell wall structures rich in polysaccharides and proteins that can bind metal ions through complexation and electrostatic interactions. Aspergillus niger, in particular, has been shown

to efficiently remove metals like lead, cadmium, and copper from contaminated water, offering a promising bioremediation strategy.

Algae: Algae, including species like Chlorella vulgaris and Spirulina platensis, have been extensively studied for their ability to remove toxic metals from aqueous solutions. The cell walls of algae contain polysaccharides, proteins, and lipids that can adsorb metal ions through electrostatic interactions and complexation. Algae offer an advantage in biorecognition due to their rapid growth rates and ability to survive in diverse environmental conditions, making them an attractive option for large-scale environmental remediation.

Biomolecules: In addition to microorganisms, biomolecules such as proteins, enzymes, and aptamers are highly effective for metal adsorption due to their specific binding sites and high selectivity. Aptamers, which are short single-stranded DNA or RNA molecules, can be engineered to selectively bind metal ions with high affinity Metallothioneins and phytochelatins, naturally occurring proteins in plants, are particularly useful for removing toxic metals like cadmium and mercury through their metal-binding capacities (Xu et al., 2023).

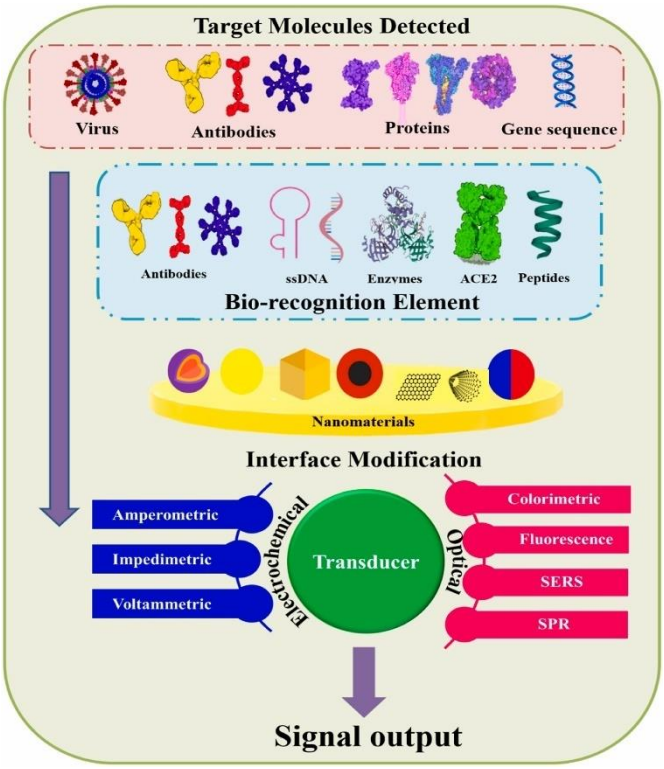

Figure 6: Schematic representation of different target biomarkers.

bioreceptor molecules, and transducing nanomaterials integrated platform. Reproduced from (Karuppaiah et al., 2023), ScienceDirect (Elsevier), Open Access, Licensed under CC BY-NC-ND 4.0.

1.6.3 Integration of Biorecognition with Nanotechnology

The integration of biorecognition strategies with nanotechnology has provided significant improvements in the removal of toxic metals from contaminated water. Nanomaterials such as carbon nanotubes (CNTs), graphene, and metal-organic frameworks (MOFs) have large surface areas and can be functionalized with biomolecules to enhance their adsorption capabilities. Nanobiosorbents that combine biological recognition elements

with nanoparticles have shown enhanced selectivity and efficiency for metal ion removal (Zuo et al., 2024).

Figure 7 shows the main components of Biosensor with analyte, biorecognition element and transducer which produces a detectable signal. The integration of biorecognition with nanotechnology has further enhanced the efficiency and selectivity of these strategies. Nanoparticles, with their large surface areas and high reactivity, can be functionalized with biological recognition elements, such as enzymes, antibodies, or peptides, to create nanobiosorbents. These hybrid materials combine the selectivity of biological systems with the high surface area and tunable properties of nanomaterials, thereby improving the adsorption capacity and selectivity for metal ions. The combination of nanotechnology and biorecognition offers a powerful tool for the efficient and targeted removal of toxic metals from contaminated water (X. Wang et al., 2024).

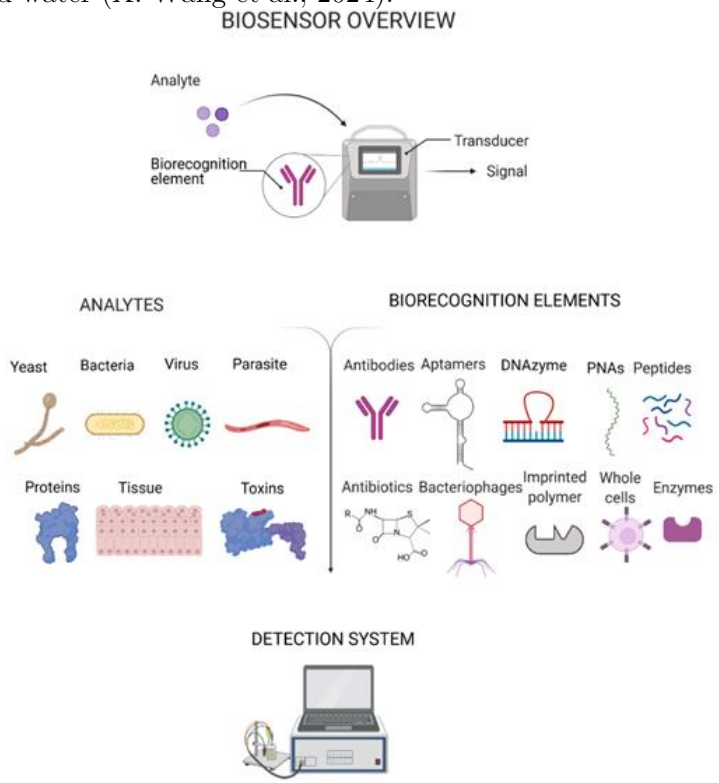

Figure 7: Main components of biosensor.

Reproduced from (Sande et al., 2021), with permission from MDPI, under the terms of the Creative Commons Attribution License, CC BY 4.0.

Despite the numerous advantages of biorecognition strategies, several challenges still remain in their practical application. The efficiency of biorecognition processes can be influenced by factors such as pH, temperature, and the concentration of competing ions in solution. The long-term stability and regeneration of biological adsorbents are also key concerns that need to be addressed for large-scale applications. Additionally, scaling up laboratory-scale biorecognition processes to industrial levels requires overcoming both technical and economic challenges. These challenges are significant but not insurmountable, and ongoing research is focused on improving the efficiency, scalability, and sustainability of biorecognition-based metal removal strategies.

1.7 Functionalization with Biomolecules

1.7.1 Proteins and Peptides in Functionalization

Proteins, particularly those with metal-binding domains, are widely used for functionalizing materials due to their ability to form stable complexes with metal ions. Metallothioneins (MTs), a class of small, cysteine-rich proteins, have been extensively studied for their high affinity for metal ions such as zinc (Zn), copper (Cu), and cadmium (Cd). MTs are known to coordinate with metal ions through the sulfur atoms of cysteine residues, forming stable metal-protein complexes. Due to their high selectivity for certain metals, MTs have been employed to functionalize adsorbents like carbon nanotubes and nanoparticles for the removal of toxic metals from water (Peris-Díaz et al., 2021).

Peptides, which are shorter chains of amino acids, also show promise in metal ion adsorption. Certain peptides with metal-binding motifs, such as cysteine-rich peptides or histidine-rich peptides, have been synthesized for toxic metal removal. These peptides can be tailored to exhibit high specificity and affinity for particular metals, making them ideal candidates for functionalizing adsorbents for targeted metal removal. For instance, peptides containing thiol groups have been shown to effectively remove metals like mercury (Hg) and lead (Pb) from contaminated water through complexation (Luo et al., 2024).

1.7.2 Enzymes and Other Bioactive Molecules

In addition to proteins and peptides, enzymes have also been explored for functionalization due to their ability to interact with metal ions through specific binding sites. Different bioreceptors as key components for biosensing and Single electron transfer-based peptide/protein bioconjugations driven by biocompatible energy input-Recent bioconjugation strategies is depicted in Figure 8 & Figure 9 respectively. Enzymes such as laccases and peroxidases, which are involved in sulfur and nitrogen metabolic pathways, have been used to functionalize materials for the selective removal of metal ions. These enzymes can form stable complexes with metals like copper (Cu), zinc (Zn), and chromium (Cr), enhancing the efficiency of metal removal from aqueous solutions (Akbarian et al., 2022).

Other bioactive molecules, including nucleic acids and polysaccharides, have also been investigated for their ability to adsorb metals. Nucleic acids, particularly aptamers, are single-stranded DNA or RNA molecules that can be engineered to bind with high specificity to metal ions. These molecules are useful for functionalizing materials to selectively remove metal ions from complex mixtures. Polysaccharides like chitosan, which contain amino and hydroxyl groups, have been widely used for the functionalization of adsorbents due to their ability to bind metal ions like lead (Pb), cadmium (Cd), and copper (Cu) (C. Zhao et al., 2023).

1.7.3 Polysaccharides in Functionalization

Polysaccharides are natural biopolymers that have gained popularity for use in metal ion removal due to their biodegradability, non-toxicity, and ability to interact with metal ions. Chitosan, derived from chitin, is one of the most widely studied polysaccharides for metal adsorption. The amino groups present on chitosan allow it to form chelates with metal ions, such as copper, cadmium, and lead, making it an efficient adsorbent for metal removal. Functionalizing chitosan with metal-binding biomolecules, such as peptides or proteins, can further enhance its adsorption capacity and selectivity for specific metals.

Chitosan-based adsorbents functionalized with biomolecules have been shown to exhibit high adsorption efficiency for various metals, including toxic metals like arsenic (As), mercury (Hg), and chromium (Cr). These functionalized adsorbents offer the advantage of high selectivity, enabling the removal of specific metals from contaminated water or soil, even in the presence of other contaminants (D. Huang et al., 2020).

1.7.4 Mechanisms of Metal-Biomolecule Interactions

The interaction between metal ions and biomolecules on functionalized adsorbents is primarily governed by several mechanisms, including ion exchange, electrostatic interactions, complexation, and coordination bonding. These mechanisms allow biomolecule-functionalized adsorbents to selectively bind and remove metal ions from contaminated solutions (Zhu et al., 2023).

1.7.5 Applications of Biomolecule-Functionalized Adsorbents in Metal Removal

Recovery of Valuable Metals: In addition to removing toxic metals, biomolecule-functionalized adsorbents have been used for the recovery of valuable metals, such as gold, silver, and platinum, from electronic waste and industrial effluents. These adsorbents provide a selective and efficient means of recovering metals from complex mixtures (González Fernández et al., 2025).

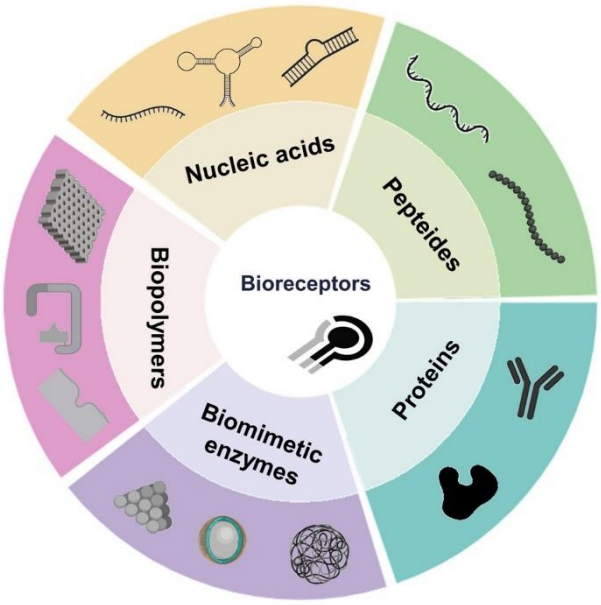

Figure 8: Bioreceptors as the key components.

Adapted from (X. Wang et al., 2024), Cell Rep. Phys. Sci. (2024), Licensed under CC BY 4.0.

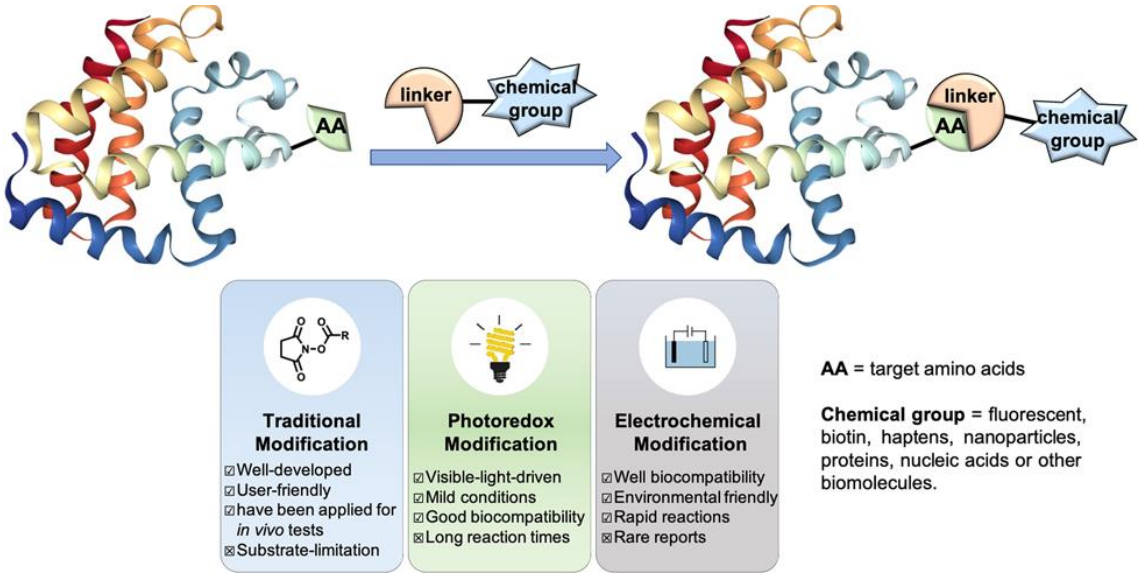

Figure 9: Single electron transfer-based peptide/protein bioconjugations.

driven by biocompatible energy input-Recent bioconjugation strategies. Reproduced from (Weng et al., 2020).

1.8 Bioinspired and Biomimetic Adsorbents

1.8.1 Bioinspired Adsorbents: Design and Mechanisms

Bioinspired adsorbents are materials designed by mimicking the structures, surfaces, and mechanisms of biological organisms that efficiently capture or filter pollutants from their environment. Nature has evolved highly specialized systems for contaminant removal, which can be applied to environmental remediation through bioinspired materials. One of the most famous examples is the lotus leaf, which exhibits superhydrophobic properties due to its unique micro- and nano-structured surface, allowing it to repel water and dirt effectively. The design of bioinspired adsorbents involves incorporating similar structures or features that enhance their interaction with contaminants, particularly pollutants like toxic metals (X. Zhang et al., 2022).

The fundamental principle behind bioinspired adsorption is to replicate natural affinity for contaminants, such as metals and organic pollutants. For instance, bacterial cell walls contain a variety of functional groups that can adsorb metals like cadmium (Cd), lead (Pb), and copper (Cu). Chitosan, a natural polymer derived from the shells of crustaceans, has also been studied as a bioinspired material due to its amine groups, which readily bind with metal ions. The inherent biological interactions, such as chelation, complexation, and electrostatic interactions, are key mechanisms that drive the adsorption of metals onto bioinspired adsorbents.

Bioinspired materials can also involve mimicking specific biological features that enhance the binding of contaminants. Algae, for example, can adsorb a wide range of metals through the secretion of extracellular polymeric substances (EPS), which contain functional groups that form strong complexes with metal ions. By mimicking the EPS-producing mechanism of algae, synthetic adsorbents can be designed with specific functional groups to enhance metal ion binding. These materials also provide additional benefits such as high biodegradability and sustainability, which are important features for long-term environmental remediation strategies (Alkhaldi et al., 2024).

1.8.2 Biomimetic Adsorbents: Integration of Biological and Synthetic Components

Biomimetic adsorbents extend the concept of bioinspired materials by integrating synthetic elements with biological components to improve the overall performance of the adsorbent. These materials often combine the high surface area and tunability of nanomaterials with the selective functionality of biomolecules. By designing adsorbents that mimic biological processes while incorporating the advantages of synthetic chemistry, biomimetic adsorbents can be fine-tuned for specific applications, such as selective metal ion removal or organic pollutant degradation (Gu et al., 2024)

Another approach to biomimetic adsorption involves the integration of biomolecules with synthetic adsorbents to mimic the specific interactions between biological entities and pollutants. Aptamers, which are short, single-stranded DNA or RNA molecules, can be engineered to bind with high affinity and specificity to target metal ions, such as arsenic (As) and lead (Pb) (Z. Chen et al., 2018). These biomolecules, when incorporated into synthetic adsorbent systems, create highly selective adsorbents that outperform conventional materials by selectively targeting specific contaminants while leaving other substances unaffected.

1.8.3 Functionalization of Nanomaterials for Enhanced Adsorption

The functionalization of nanomaterials is a critical strategy for improving the performance of bioinspired and biomimetic adsorbents. Nanoparticles possess several advantages over bulk materials, including increased surface area, enhanced reactivity, and tunable surface properties. Functionalizing nanomaterials with specific biological molecules or chemical groups enhances their adsorption capacity and selectivity for toxic metals, organic contaminants, or dyes (Tian et al., 2025).

1.9 Nanobiosensors for MeHg Detection

1.9.1 Bio Inspired Nanobiosensors for MeHg Detection

Mercury exists in various chemical forms including Elemental Mercury (Hg^0), Mercuric Ion (Hg^{2+}), Methylmercury (MeHg), Dimethylmercury (CH_3HgCH_3), Mercury Sulfide (HgS) and Ethylmercury ($C_2H_5Hg^+$). Among these, MeHg is the most toxic, posing a significant risk to both the environment and human health, even at concentrations as low as nanomolar (nM) levels. This concentration threshold is remarkably minuscule, diverging by two orders of magnitude from any other mercury species. Despite its minute presence, MeHg has the tendency for biomagnification within the food chain, thereby accumulating in organisms and resulting in neurological disorders, exemplified by Minamata disease (L. Chen, Li, and Chen 2014). Wild piscivorous fish, mammals, and birds, animals at the highest trophic level, are at risk for elevated dietary methylmercury intake and toxicity due to biomagnification through the food chain. Its neurotoxic effects are especially harmful to developing fetuses and young children, making precise quantification in food samples critical for public health. Monitoring MeHg levels in fish is essential for assessing exposure risks and ensuring food safety standards. Regulatory agencies rely on accurate MeHg detection to guide consumption advisories and protect vulnerable populations. Consequently, the demand for meticulous, sensitive methodologies to detect MeHg with precision has surged, especially in the context of evaluating water pollution dynamics. Biosensors for detecting methylmercury (MeHg) in food samples offer several advantages, including rapid detection and high sensitivity, making them effective at trace-level detection. These devices enable real-time monitoring, providing immediate feedback on MeHg levels, essential for ensuring food safety in vulnerable populations like pregnant women and fetuses. Their cost-effectiveness and potential for on-site application, especially in industries such as aquaculture and agriculture, make them suitable for widespread use. Additionally, integration with smartphone technology allows for automation and ease of use, improving overall food safety protocols (Anchidin-Norocel et al., 2024; Mandal et al., 2024; Scheuhammer et al., 2007).

Current conventional methods for MeHg detection employ techniques such as atomic fluorescence spectrometry (AFS) with gold traps and automated systems based on cold vapour atomic fluorescence spectrometry (CVAFS). The CVAFS mechanism involves the conversion of MeHg into volatile ethylmercury through the use of sodium tetraethyl borate. After this conversion, alkyl forms of mercury are purged using nitrogen gas and captured on Tenax columns. After desorption at an elevated temperature, gas chromatography is employed to identify alkyl mercury compounds post-pyrolysis (Leermakers et al., 2005; Leopold et al., 2009; Segade & Tyson, 2007). This method currently stands as the most sensitive for MeHg, with an impressively low limit of detection (LOD) at 0.004 ng/L. However, it necessitates the laborious task of sample collection from sites and transport to laboratories, which can be time-consuming and resource-intensive. In addition to sample collection challenges, laboratory-based MeHg measurement entails the extraction of MeHg from complex matrices, including organisms and cells. Specific sample preparation steps are crucial, and tailored to the physicochemical properties of each matrix. Even seemingly simple samples like water require meticulous processing, involving pH adjustment to 4.5 before the addition of sodium tetraethyl borate and overnight derivatization into volatile ethylmercury.

Although the necessary steps to obtain MeHg from biota or naturally occurring complexes cannot be omitted, the specific preparation of samples in laboratories might be

simplified, resulting in rapid usage, fewer experts and decreased costs, if sensors can be used instead of using expensive laboratory equipment. Therefore, sensors that can enable measurement of MeHg in the environment are of high priority to increase the amount of data that will precisely map the routes of MeHg for thwarting toxicity reaching the global nutrient cycle and to enable us to determine contaminated food. This will yield biologically relevant information about the biomagnification and bioaccumulation of MeHg under real environmental conditions. Since the processes of methylation and demethylation are continuous, the onsite measurement will give us dense time points, resulting in time and spatially dependant distribution when followed by the precise sampling locations, since laboratory measurements can give results only for a limited number of samples.

Among the several developed platforms, biosensors for detecting methylmercury (MeHg) in food samples offer several advantages, including rapid detection and high sensitivity, making them effective at trace-level detection. These devices enable real-time monitoring, providing immediate feedback on MeHg levels, essential for ensuring food safety in vulnerable populations like pregnant women and fetuses. Their cost-effectiveness and potential for on-site application, especially in industries such as aquaculture and agriculture, make them suitable for widespread use. Additionally, integration with smartphone technology allows for automation and ease of use, improving overall food safety protocols. Microfluidic devices offer high sensitivity and accuracy but may require technical expertise. Lateral flow assays and paper-based assays provide moderate to high sensitivity with ease of use but less accuracy in quantification. Smartphone-based sensors, electrochemical sensors, and optical biosensors achieve high sensitivity and accuracy, with the latter two being highly precise and user-friendly for real-time monitoring.

Although sensors for measuring inorganic mercury (Hg^{2+}) or Total Mercury (THg) have been developed, most MeHg sensors remain at the proof-of-concept stage (L. Chen, Li, and Chen 2014). To advance the development of MeHg sensors we categorized existing sensors into six major types: Whole-cell biosensors (WCB), Immunostrip sensors, small molecule probe-based (SMP) sensors, Metal-Organic Framework (MOF) sensors, Nanoparticle (NPs)-based sensors, and Nanoarchitectonics sensors. This comprehensive overview provides insights and strategies for advancing MeHg sensors by integrating biological, chemical, and nanotechnological approaches. A critical bottleneck in the development of MeHg sensors is the need for a well-integrated system that includes a receptor with high specificity for MeHg, efficient signal transduction, low noise amplifier, and reporters capable of showing realtime high quality data. Addressing these challenges is essential for creating effective and reliable MeHg sensing solutions.

Electrochemical transducers, for example, enable precise quantification of MeHg concentrations across diverse environmental matrices (T. Zhang T., Zhou, Y., &. Han, 2021). In enzymatic sensors, electrochemical transduction is commonly employed, capitalizing on the enzymatic conversion of MeHg into electroactive species (Y. Chen et al. , 2019). Immunosensors, on the other hand, utilize antibodies or aptamers as receptors and often integrate surface plasmon resonance (SPR) transducers to enable real-time detection (Rantala et al., 2011).

For efficient MeHg sensors, prioritise the development of advanced materials and biorecognition elements with high specificity for MeHg, such as novel nanomaterials and selective aptamers/ antibodies. Optimize signal processing using advanced technologies to improve accuracy and interpret complex data effectively. Implement real-time calibration and adaptive systems to maintain sensor performance under varying environmental conditions. Focus on increasing sensitivity to detect lower concentrations of MeHg and reducing response times for rapid, reliable measurements. Ensure the sensor's usability, cost-effectiveness, and scalability, and validate its performance through extensive field testing and adherence to regulatory standards.

From a biological point of view, MeHg detection is particularly challenging: Even at extremely low concentrations, MeHg can cause biological amplification due to time-dependent or chronic exposure. This makes even current gold-standard laboratory methods not sensitive enough, as MeHg concentrations are often below the limit of detection (LOD). In contrast to the Hg^{2+} where biological responses tend to show concentration-dependent effects in living cells, the biological impact of MeHg is usually only evident in multicellular organisms at higher trophic levels, which is then separating the concentration levels in environmental matrices from the concentrations in organisms, for example ocean waters and fish, respectively, by more than five orders of magnitude.

Future developments will focus on refining these sensors to improve their integration into real-world monitoring systems, further enhancing public health safety and environmental protection efforts against mercury contamination Figure 10.

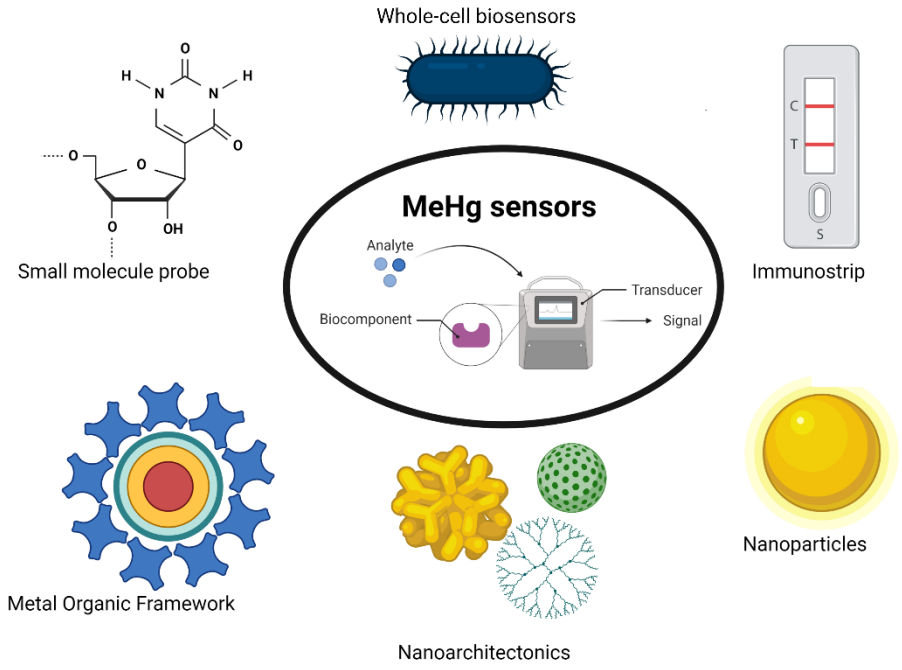

Figure 10: Illustrates a range of detection techniques employed in MeHg sensors.

including small molecule probes, whole-cell biosensors (WCB), immunostrip assays, metal-organic frameworks (MOFs), and nanoarchitectonics-based sensors. The central diagram highlights the core components of currently known MeHg sensors, emphasizing the interaction between the analyte and the recognition element, followed by signal transduction. These diverse approaches showcase the integration of biological components with advanced materials, significantly enhancing the performance of MeHg detection technologies. Adapted from Adapted from (Mabes Raj et al., 2025)

1.9.2 Whole-cell Biosensors (WCB)

This type of sensor is especially important in determining the ecologically relevant bioavailable fraction of mercury. However, the bioavailable fraction is dependent on the type of the cell and environmental conditions and therefore it is hard to clearly differentiate real bioavailable fraction from the low sensitivity. Based on the current synthetic biology tools the repertoire of the hosts for introducing genetically engineered genes is expanded

and should be the concept of bioavailability tackled by combining and comparing (i) chemical laboratory based tools with (ii) the outcome in the environment, e.g. bioaccumulation and (iii) results of using a battery of different WCB environmentally relevant hosts, similar as it was shown by using native marine and freshwater WCB hosts, but it should be utilized many different hosts relevant for particular either geochemical cycle or foodchain transformations.

Moreover, the WCB can determine the level of MeHg in the environment in contrast to the standardized approaches therefore minimal disturbance of the environment can be much easier achieved Figure 11, but still in most cases the samples are tested in laboratory conditions since there are not many attempts to use WCB directly in the field. Therefore, it should be further developed as self-sustainable WCB platform bearing alive cells and should be biologically safe not deploying genetically modified strains in the environment. The miniaturisation and portable platforms are set to make on-site analysis more desirable but this is facing many challenges such as preserving low fluxes of nutrients and samples such as in microreactors since small designs are prone to clogging, preserving suspended or immobilized cells for monthly operations as well as appropriate calibration. Perhaps advances in cell encapsulation, microfluidics and multi-cell systems are expected to enhance, on one hand the stability and reproducibility and on the other hand the extension of the environmentally relevant information. In this regards the key organisms in the environment must be first identified using state-of-the-art metagenomic approaches, then utilizing advanced culturomics to be able to obtain strains that can be then at the end available for introducing genetic components by using genetic engineering tools and transforming them into WCB.

The WCB often might have lower genetic stability which hampers the performance over time and calls for either approach to replenish the cells using lyophilized cultures or monitoring sensitivities by appropriate on-site calibration.

Although various factors such as complexation with cysteine would increase the uptake of MeHg and the addition of humic acid can reduce the MeHg uptake within the cells, we do not know the precise mechanisms that are aiding in MeHg uptake and WCB can serve us not only as a sensor platform but also to determine key environmentally relevant aspects of MeHg bioavailability. Therefore, further advances need to be carried out in research that clarifies the meaning and applicability of the use of WCB in ecological and human health risk assessment. WCB are best in conditions similar to their natural environment and the temperature, incubation time, medium type, pH, and reagents can all have effects on the performance of the biosensors that can only be understood with further research and testing. Employing advanced cell encapsulation techniques to enhance stability, and optimizing growth conditions to ensure cell functionality will prolong the WCB performance.

Since WCB are also prone to the high background noise that is affecting LOD it would be very important to incorporate the currently developed advanced AI tools or autocorrelative mathematical models to better distinguish signal from the cellular, genetic or environmentally introduced noises resulting in updated sensing platform. By addressing these factors, WCBs can become more reliable, sensitive, and effective for accurate MeHg

detection, standing out as the only type of sensor capable of providing environmentally relevant data.

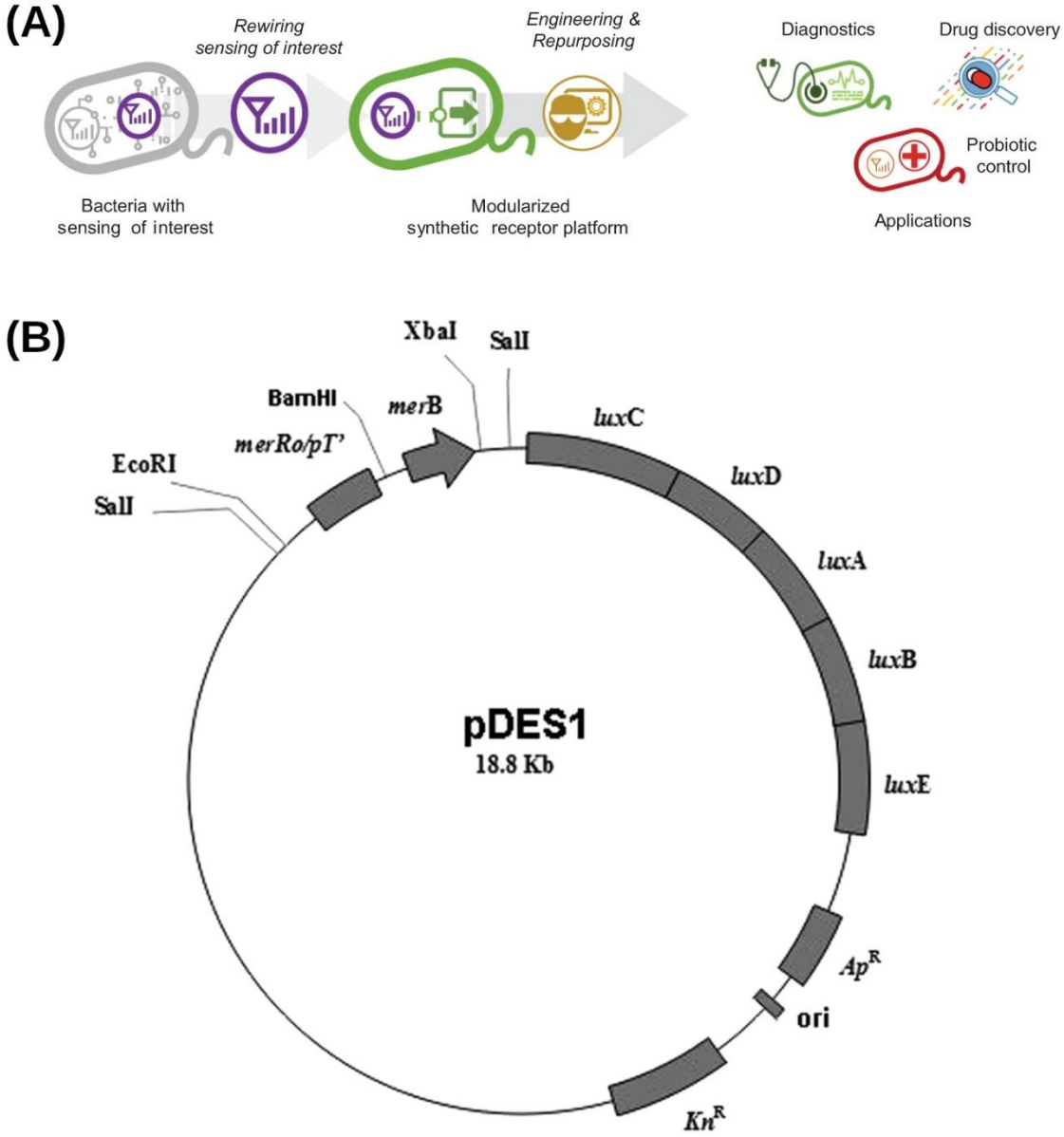

Figure 11: a) Illustration for genetically engineering bacterial sensing modules.

into surrogate hosts for the development of a synthetic receptor platform that can be used for multiple application. b) Diagram of the modification of Prb28 by inserting the merB gene.

1.9.3 Immunostrip Based MeHg Detection

Immunostrips colourimetric detection platforms for MeHg often suffer sensitive limitations, especially for trace levels. They also encounter non-specific bindings or cross-reactivity with other metal ions that can affect the accuracy. The strips can degrade over time, affecting the stability of immobilized biomolecules (antibodies, aptamers, and enzymes). Though the platforms bring advantages such as simplicity, speed and cost-effectiveness, making them suitable for on-field detection platforms, they often encounter

lower sensitivity compared with other methods are susceptible to matrix interference and limited ability to distinguish from other mercury species. Principle illustration of the immunochromatographic strip assay for MeHg detection is depicted in Figure 12.

Employing MeHg-specific antibodies in conjunction with an improved reporter system could provide enhanced solutions for future MeHg sensors. Integrating antibodies against MeHg with mesoporous materials or AuNPs could significantly improve sensitivity. Additionally, leveraging advanced techniques such as Surface Plasmon Resonance (SPR) or Surface-Enhanced Raman Spectroscopy (SERS) could enable sensors with detection limits several orders of magnitude lower.

The sensitivity of immunostrips can be enhanced by incorporating nanomaterials into the conjugate pads and selecting biomolecules with high affinity for MeHg. A further approach to improve platform sensitivity involves integrating a reflectometer to enhance pixel detection of gold nanoparticle test lines, facilitating more precise intra-sample comparison. Since this platform is useful in semi-quantitative analysis and can be used for rapid onsite "yes" and "No" type detection of MeHg.

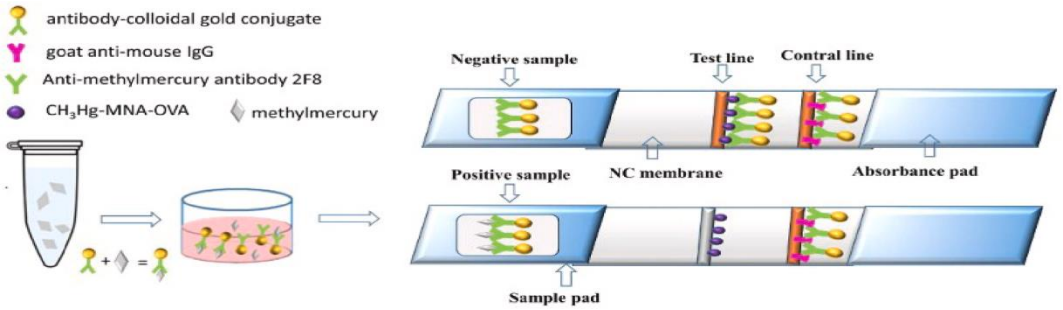

Figure 12: Illustration of the immunochromatographic strip assay for MeHg detection.

Adapted from (Mabes Raj et al., 2025).

1.9.4 Small Molecule Probe (SMP) Detection Platforms

SMP are extensively utilized in various sensing platforms due to their ability to selectively interact with the specific analyte through chemical and physical changes. Most of the SMP utilize fluorescence probes which exhibit lower detection limits compared to more sophisticated platforms like immunoassay or nanoparticle-based systems. The platforms also have limited stability with probes, potential interference from other Hg species and metal ions, and difficulty in achieving real-time detection in complex matrices. Though the SMP is designed for selective analysis, cross-reactivity with structurally similar molecules or ions can occur. The probes often degrade over time, particularly under harsh environmental conditions (eg. UV light, and temperature extremes). SMPs are usually tailored for single analyte detection, making them less suitable for multiplex detection of target analytes. SMPs often require precise environmental control or additional instrumentation for effective detection, such as fluorescence readers or spectrophotometers. Some SMPs may involve the use of organic solvents or chemicals that are less environmentally friendly. A chemodosimeter was developed and demonstrated potential for mercury detection; however, it is limited to single-use applications due to its reliance on an irreversible reaction mechanism.

Among the fluorescent SMP, near-infrared (NIR, 650–900 nm) probes have several advantages over other probes, such as reducing photo-bleaching due to the lower energy of excitation required. As described by Denk et al., 1990, the use of two-photon (TP) excitation has been predominantly used in NIR fluorescent probes. Over the last few decades, there have been tremendous improvements in the SMP in the realm of biological

sensing and bio-imaging. As described in Chapter 4 and Table 2, most of the SMPs utilize turn-on probe strategy for dual mode detection of mercury species and the major advantage was a shorter detection time (1–5 min), compared with available analytical methods. No SMP can measure MeHg in the seawater matrix and using FRET, ICT, PeT, ESIPT, AIE, and probes combining these modalities can be developed in the future for MeHg onsite detection in seawater. Combinatorial fluorescence techniques have to be used to overcome the issue of interference and sensitivity for MeHg detection. Several boundaries have to be dismantled to push forward the development of enhanced SMP for MeHg detection in seawater or other environmental matrices beyond the current state-of-the-art.General scheme for recent advances in SMP is shown in Figure 13.

Future direction in the line of SMPs functionalizing with nanomaterials and integrating into a hybrid platform combined with biological elements (eg aptamers and antibodies) would be an option to increase the sensitivity and stability. Development of SMPs with improved environmental stability and reduced cross-reactivity through advanced chemical synthesis techniques. Enhancing the chemical specificity of the probes and integrating advanced signal processing methods can also improve accuracy and reliability, making SMPs biosensors more effective for MeHg detection in diverse applications.

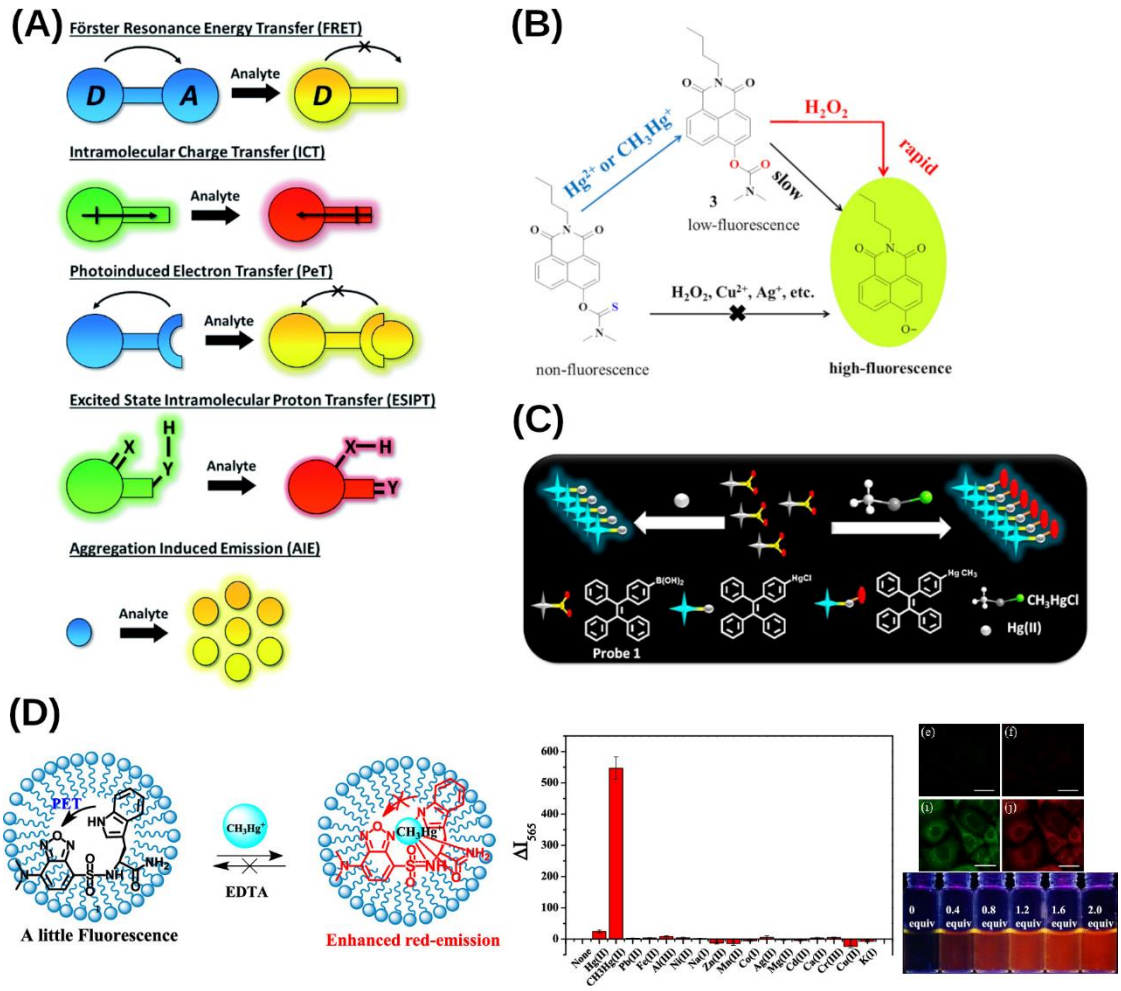

Figure 13: General scheme for recent advances in SMP.

b) Reaction mechanism of probe 1 for mercury species with the help of H2O2. c) A schematic representation of the sensing process of probe 1 towards Hg2+ and CH3Hg+ by turn-on type AIE. d) Flurescent molecular probe Adapted from (Mabes Raj et al., 2025).

1.9.5 Metal Organic Framework (MOF)

MOFs can suffer from non-specific adsorption, leading to interference from other metal ions and compounds which restricts its limited selectivity. This is because of the porous structure which allows non-target analytes to occupy binding sites, reducing specificity for MeHg detection. Moreover, they encounter challenges including potential instability and degradation under varying environmental conditions, complex and costly synthesis and functionalization processes, and susceptibility to interference from complex sample matrices. The lack of sensitivity is a general barrier when using MOFs for the detection of MeHg as well as other analytes. MOFs often degrade under harsh conditions because of their metal-ligand bonds which are prone to hydrolysis or photodegradation. A complex and time-consuming synthesis process might hinder scalability and widespread use because controlled pore size, structure and functionality is required for selective MeHg sensing. Scheme for the preparation of a MOF is depicted in Figure 14.

Most of the MOFs developed in the past are made for gas sensing applications because of their excellent adsorption capacities. Very limited structures of MOFs have been explored to date such as MOF-5,1 HKUST-1,2 MIL-101,3 and classical ZIF-8. As detailed in Chapted 5, MOFs have been used in different layers as selective applications. Although the MOFs offers sensitivity for the detection of MeHg (1 aM), then complicated and sophisticated nanoparticle thin films often limit its scalability and practicality for commercialization. The research should focus on developing more stable MOF materials with improved chemical and mechanical durability, refining synthesis and functionalization protocols to ensure reproducibility and efficiency, and integrating sample pre-treatment techniques to reduce matrix effects. MOFs can be engineered with specific ligands, functional groups, or structural modifications to enhance selectivity for MeHg. Combining MOFs with advanced nanomaterials such as graphene, fullerenes, carbon nitrides, and MXene along with signal amplification strategies, enables the use of different transducers and facilitates optical and electrochemical detection methods, thereby enhancing performance through improved sensitivity and selectivity. MOFs can be engineered with specific ligands, functional groups and should aim at creating portable, cost-effective sensors with improved stability and versatility for diverse environmental and industrial applications, thus expanding their practical use in precise MeHg detection.

Functionalized MOFs with specific sensing molecules might be the most suitable to target MeHg and would help reach lower sensitivity for MeHg detection. To the best of our knowledge there are no reports on using analyte-specific aptamers that can be used to link MOFs to build architectures that can specifically coordinate with MeHg. This approach and integration of MOF hybrid aptamer on microfluidic devices allow the high-performance biosensing and the controlled synthesis of MOFs. Develop robust MOFs using hydrophobic linkers, metal clusters, or post-synthetic modifications to withstand harsh environmental conditions. Integrate MOFs with nanomaterials (e.g., gold nanoparticles, carbon dots) or employ advanced detection techniques like SERS or SPR to amplify detection signals. Focus on cost-effective, scalable synthesis methods, such as microwave-assisted or mechanochemical approaches, to promote widespread use. Combine MOFs with other materials, such as polymers or biodegradable membranes, to create hybrid systems that improve selectivity, durability, and detection range in future MeHg based detection platforms.

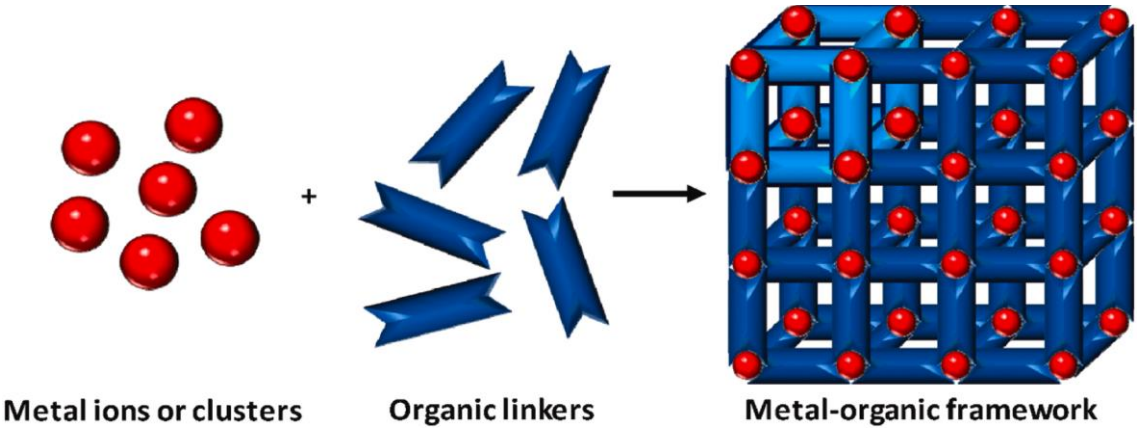

Figure 14: Scheme for the preparation of a MOF.

Different metal ions or clusters are mixed together with organic linkers using a convenient solvent. Over the past few decades, over 100,000 structures have been reported in the ‘‘MOF subset’’ Adapted from (Mabes Raj et al., 2025).

1.9.6 Nanoparticles (NPs)

Nanoparticles such as AuNPs, carbon dots, silver nanoparticles, QDs, Magnetic Nanoparticles (MNPs), Carbon Nanotubes (CNTs), graphene, and nanofibres have been put forth for miniaturizing biosensing platforms to the nanoscale to improve the understanding of various properties like optical, electronic, and magnetic characteristics, which would pave the way for their use in bio-sensing systems (Mabes Raj et al., 2025). However, some drawbacks such as cross-reactivity with non-targeted metal ions or compounds, reducing their specificity towards MeHg detection should be the main future focus since these are the main factors limiting their selectivity. These drawbacks are probably the result of unspecific binding to functional groups or surface ligands which interact with a range of analytes leading to false positive results. NPs are being used in various research fields and their potential release into the environment can pose ecological harm and health risks, especially metal-based ones, which are not biodegradable and can accumulate in organisms. NPs possess low stability and often tend to aggregate or degrade in complex matrices like biological fluids or wastewater affecting their performance. This is mainly because of changes in pH, ionic strength or the presence of organic matter. Cost and scalability are the biggest challenges for the synthesis and functionalization of NPs which can be expensive in maintaining the precise size, shape and surface chemistry for effective detection.

NPs integrated with fluorescence, colorimetry, SERS, SPR, and electrochemistry improve the sensitivity of MeHg detection. NPs (AuNPs and AgNP) functionalized with DDTC, Lysozyme, thymine, HEPPSO and DAOC display enhanced selectivity and sensitivity towards MeHg. This is mainly because of the selection of functional groups which interact with MeHg to form a special complex. However, though the methods are promising and can able to detect MeHg at a trace level, they often lack challenges such as large-scale synthesis, complex functionalization process and stability in relevant natural conditions. Attention has been made towards the development of aptamers-based conjugated NPs sensing platforms for the selective detection of MeHg. This type of approach is time-consuming and laborious in the production of aptamer specific towards MeHg is depicted in Figure 15. Adapted from (Mabes Raj et al., 2025).

To the best of our knowledge, bioconjugated NPs with highly specific biomolecules such as aptamers, antibodies or molecularly imprinted polymers (MIPs) very well minimise cross reactivity, but should be further evaluated in real samples or determining applicability.

More research in the direction of the stability of NPs by modifying their surfaces with polymers such as PEG or hydrophobic coating to prevent aggregation and degradation in complex matric are required to be developed in future engineering approaches. Biodegradable NPs with less toxic formulations will mitigate the environmental and health risks. Research directions in the field of QDs, nanofibers and CNTs would remarkably increase the transduction sensitivity and detection capabilities. Cost-effective synthesis based on a greener approach (plant based or biomimetric routes) will reduce the production costs of the NPs for the detection of MeHg. Signal amplification might be better achieved by the integrating NPs with SERS platforms. Combining NPs with MOFs and 2D materials will enhance the performance of the sensors and add multifunctionality and specificity due to the filtration effects of MOFs or higher surface area for attaching sensing part that introduce more higher signal-to-noise ratio (Mabes Raj et al., 2025).

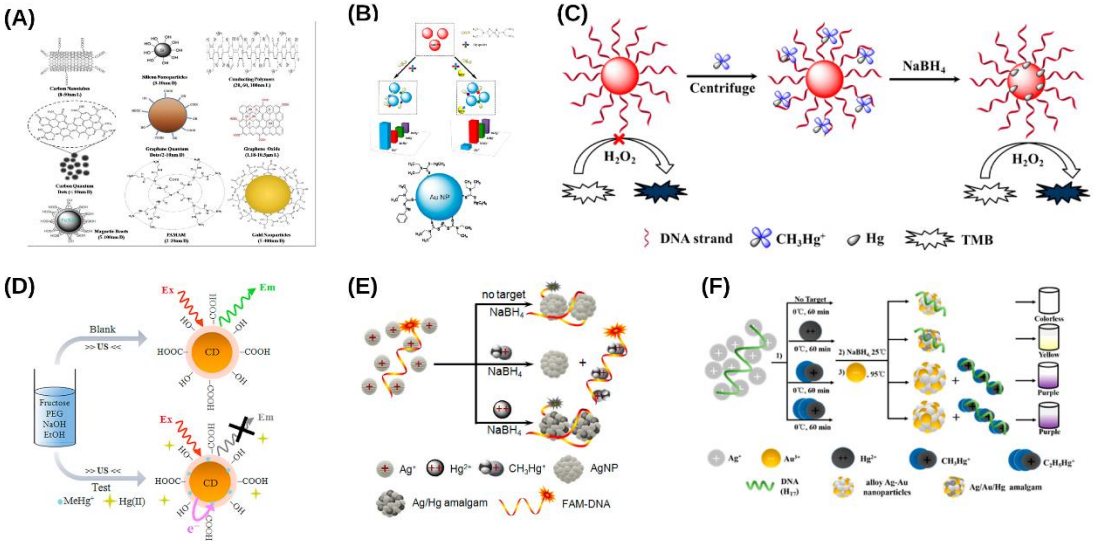

Figure 15: Commonly used nanomaterials in various kinds of sensors.

fabrication with their sizes. L: length; D: Diameter. b) Illustrations of AuNP-Based colorimetric sensing strategy for Hg Species and Hg– DDTC complex attached to the surface of AuNPsc) MeHg sensing mechanism. c) MeHg sensing mechanisim. d) Schematic representation of the mechanism involved in the fluorescence quenching caused by the presence of MeHg. e) Schematic illustration for fluorescent detection of MeHg based upon a dye-labeled T-rich DNA (FAM-DNA). Formation of AgNPs or Ag/Hg amalgams on FAM-DNA template quenches the FAM fluorescence emission; the presence of MeHg suppresses formation of the metal nanostructures, revealing fluorescence enhancement. f) Schematic illustration of the experimental principle for the colorimetric detection of MeHg and C2H5Hg. Adapted from (Mabes Raj et al., 2025)

1.9.7 Nanoarchitectonics

Nanoarchitectonics involves designing, fabrication and assembling nanoscale structures in a controlled and purposeful manner to achieve special function and properties. Nanoarchitectonic structures enhance the sensitivity and selectivity of biosensors and chemical sensors. For MeHg detection, nanoarchitectonics helps create hybrid structures, such as combining metal nanoparticles with porous frameworks or functionalized surfaces. These tailored architectures enhance sensitivity, selectivity, and stability, providing effective platforms. The complex and intricate design can be time-consuming and expensive, due to nanoscale interactions and self-assembly processes, requiring advanced

techniques and resources. Very few studies have been reported on the detection of mercury ions with high sensitivity using thymine interactions and ligands-striped monolayers. These sensors failed to distinguish between inorganic and organic mercury which limited its applicability and reduced selectivity of the sensors when exposed to mixtures of cations. Basic concept, and detection methods of nanoarchitectonics are depicted in Figure 16.

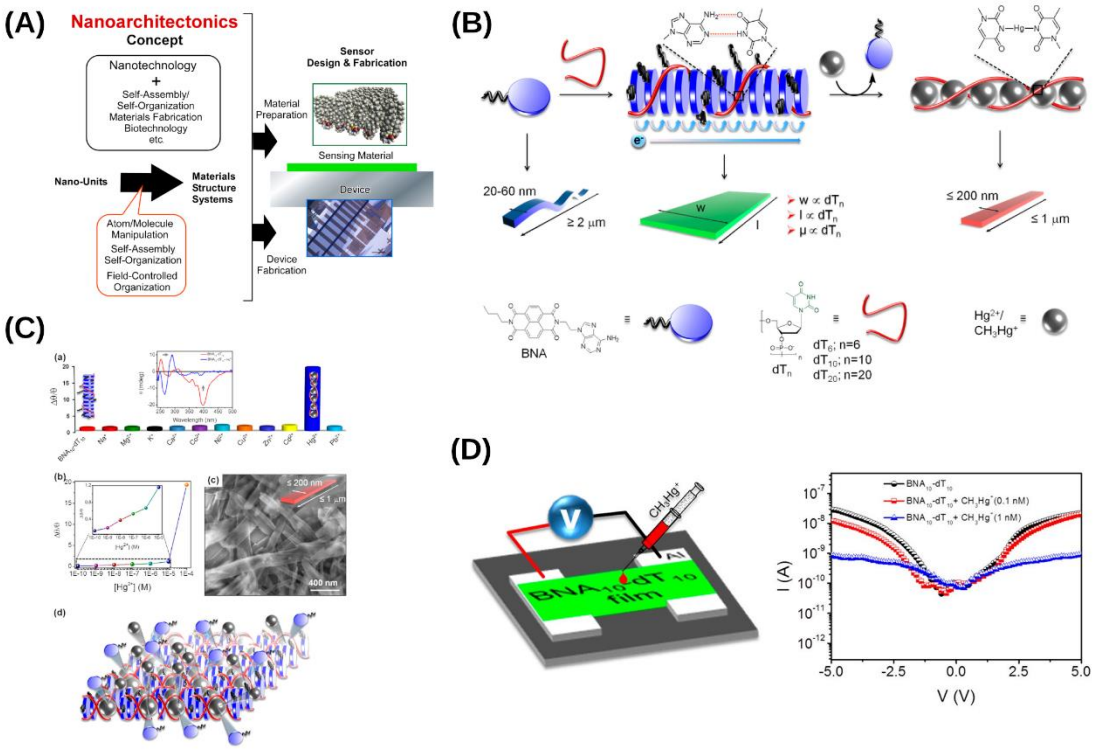

Figure 16: Basic concept of nanoarchitectonics.

Copyright (2019) Beilstein Journal of Nanotechnology. b) Schematic illustration of the nanoarchitectonics of BNA and dTn coassembly as well as the corresponding molecular structures. c) Chiroptical sensing of Hg^{2+}. Schematic representation of Hg^{2+} induced displacement of BNA from the BNAn-dTn 2D assembly via formation of a metallo-DNA duplex [dT-Hg-dT] n and self-assembled BNA 1D tapes. d) Conductometric sensing of MeHg. Schematic representation of MeHg detection device structure. BNA10-dT10 device response before and after the addition of different MeHg concentrations (0.1 nM and 0.5 mM). Adapted from (Mabes Raj et al., 2025).

The large-scale production of nanoarchitectonic-based sensors with consistent quality remains challenging. This is mainly because small deviations in synthesis or assembly processes can lead to significant variations in performance. Simplified fabrication methods will scale up the production such as microwave assistant synthesis or templating to streamline the sensor production. One of the main disadvantages of nanoarchitectonics is the structural stability, which can be enhanced by modifying using graphene derivatives, MOFs and polymer coating. Plasmonic signals of MOFs can be enhanced by integrating plasmonic nanostructures (e.g., gold or silver) to amplify localized electromagnetic fields, boosting optical detection sensitivity. Their porous structure supports high-density functionalization with selective agents like aptamers or thiols, minimizing cross-reactivity. MOF pre-concentration of analytes and reduced interference improve signal clarity, while their scaffolding enables multi-step signal amplification for superior detection performance.

For efficient MeHg sensors, prioritise the development of advanced materials and biorecognition elements with high specificity for MeHg, such as novel nanomaterials and selective aptamers/antibodies. Optimize signal processing using advanced technologies to improve accuracy and interpret complex data effectively. Implement real-time calibration and adaptive systems to maintain sensor performance under varying environmental conditions. Focus on increasing sensitivity to detect lower concentrations of MeHg and reducing response times for rapid, reliable measurements. Ensure the sensor's usability, cost-effectiveness, and scalability, and validate its performance through extensive field testing and adherence to regulatory standards.

Based on literature-gained knowledge and on our experiences, we have identified five key steps that should be specifically followed when developing an effective MeHg sensor.

Interdisciplinarity: Developing a sensor requires collaboration between analytical chemists, material scientists, physicists, and experts in biology (e.g., biochemists, molecular biologists). A bottom-up approach is needed, beginning with an understanding of interactions of the MeHg with the selected sensing component at the molecular level.

Matrix Consideration: The sensor development must begin by selecting the matrix (e.g., fish tissue, ocean water), as this determines the required sample pre-treatment, potential interferences (e.g., co-contaminants, extraction chemicals), expected concentration ranges, and physicochemical conditions such as ionic strength, pH, and temperature.

Relevance: Sensor relevance must be evaluated not just by concentration levels but also by the intended application –whether ecological (e.g., bioavailability), health-related, research-orientated, or commercial. The sensor's design should reflect its intended use.

Detection Modalities: The sensor should be able to measure concentration (quantitatively or semi-quantitatively), temporal changes, accumulation, or microspatial information (e.g., intracellular accumulation). The specific modality should align with the sensor's intended purpose.

Coupling Sensing Element with Transducer: The choice of transducer (electromagnetic, electrical, etc.) must be considered along with noise-to-signal ratio, signal range, and signal linearity. These factors impact signal amplification, filtration, correlation, and other signal-processing steps.

The recent surge in artificial intelligence (AI) has led to substantial advancement across various research domains. To date, most of the currently known MeHg sensing parts are designed based either on the known properties of selected sensing components or materials that preferentially interact with various Hg species, or by trial-and-error experiments. Currently, artificial intelligence tools offer new approaches in material design, discovery, and manufacturing, which can accelerate the development of sensors with improved sensitivity and especially increased selectivity towards MeHg. Furthermore, based on our experiences working on WCBs and detecting very low levels of analytes, this process is often prone to a high noise-to-signal ratio. However, adopting machine learning approaches could help refine detection, possibly not for quantitative measurements, but more appropriately for qualitative information. This could be crucial for filtering out contaminated samples, ensuring reliable detection even in complex samples affected by matrix effects.

In conclusion, given the complexities discussed above, creating a universal sensor that functions across all matrices while providing relevant data would be extremely challenging. Therefore, work focused on matrix-specific sensors is necessary to achieve accurate and meaningful MeHg detection.

Chapter 2

Aim and Hypothesis

2.1 Aim

This research aspires to contribute not only to fundamental scientific understanding but also to real-world applications in environmental monitoring, public health, and regulatory policy. The outcomes support the transition toward a circular and sustainable future by enabling closed-loop metal recovery and safer environmental diagnostics.

Specific aims:

1. To synthesize and characterize a library of functional nanomaterials (SiO_2, $NH_2@SiO_2$, γ-$Fe_2O_3@NH_2$, γ-$Fe_2O_3@SiO_2–NH_2$, and $CoFe_2O_4@SiO_2–NH_2$) tailored for selective adsorption of toxic and strategic metals.
2. To evaluate the adsorption capacity and selectivity of these nanomaterials for various metal ions, including Hg^{2+}, Pb^{2+}, Cr^{3+}, Dy^{3+}, and Tb^{3+}, under environmentally relevant conditions.
3. To optimize the desorption process for efficient recovery and reusability of the nanomaterials and adsorbed metals, ensuring long-term performance and cost-effectiveness.
4. To assess the cytotoxicity and nanotoxicity of the developed materials using in vitro cell-based assays (human and murine lines) and in vivo zebrafish embryo tests.
5. To engineer a biosensor system integrating MerB enzyme and gold nanoparticles for the specific and ultra-sensitive electrochemical detection of MeHg in food and environmental samples.
6. To enhance the biosensor's performance through optimized immobilization strategies (MPA, NTA, His-tag linkers) and to evaluate detection limits, selectivity, and stability.

2.2 Hypothesis

In natural systems, toxic metals are often sequestered via coordination with electron-rich amino and thiol groups. Metalloproteins (e.g., metallothioneins), enzymes (e.g., carbonic anhydrase), and low-molecular-weight ligands (e.g., glutathione, phytochelatins) utilize nitrogen and sulfur donor atoms to regulate and detoxify metal ions. Similarly, microbial cell walls rich in amino-containing polymers act as biosorbents for toxic metals. Inspired by these evolved biological mechanisms, this research hypothesizes that nanoparticles functionalized with amino groups can act as synthetic analogs of natural metal-binding systems, exhibiting high selectivity and affinity for soft and borderline metal ions.

The increasing burden of toxic metal pollution, driven by industrialization and urbanization, calls for advanced remediation technologies that are both efficient and environmentally safe. This dissertation hypothesizes that amino-functionalized nanomaterials, particularly those based on silica and iron oxide, can mimic biological detoxification strategies to selectively and efficiently adsorb toxic metal ions—such as Hg^{2+}, Pb^{2+}, Cr^{3+}, Dy^{3+}, and Tb^{3+}—from aqueous solutions.

This affinity can be explained by Lewis's acid–base theory and the Hard and Soft Acids and Bases (HSAB) theory, where soft metal ions (e.g., Hg^{2+}, Pb^{2+}) act as Lewis's acids and preferentially bind to soft Lewis bases like $–NH_2$ or –SH groups. Functionalized nanoparticles such as $NH_2@SiO_2$ and γ-$Fe_2O_3@NH_2$ are expected to form stable coordination complexes through chelation, enabled by the nucleophilicity of amino groups and the high surface reactivity and porosity of the nanomaterial scaffold.

Additionally, nanotoxicity and environmental safety are central to this hypothesis. While functionalization is expected to improve selectivity and reduce toxicity, certain uncoated or reactive nanomaterials may still induce cytotoxicity by disrupting membranes or generating toxic ions. Therefore, a dual approach will be taken: (i) assessment of metal-binding efficacy, and (ii) toxicological profiling in vitro (human-derived and murine cells) and in vivo (zebrafish embryos), to determine biocompatibility and safe operational limits.

Finally, the use of magnetically separable nanomaterials will be explored to enhance recovery and reuse, aligning the remediation approach with circular economy principles. Through bioinspired functionalization, controlled nanostructuring, and thorough toxicity evaluation, this study hypothesizes that amino-functionalized nanoparticles can offer a sustainable, selective, and reusable platform for removing toxic metals from contaminated waters.

In a parallel approach, this research extends its hypothesis to the development of an enzyme-based biorecognition system targeting MeHg, a particularly hazardous form of mercury due to its strong neurotoxicity and biomagnification in aquatic food chains. Despite its low concentrations in environmental matrices, MeHg poses disproportionate risks, especially to pregnant women and young children. Conventional detection methods like CVAFS and GC-AFS, while highly sensitive, are time-consuming, resource-intensive, and unsuitable for on-site monitoring. There is an urgent need for portable, cost-effective sensors capable of rapid and selective MeHg detection.

This dissertation posits that MerB, an organomercurial lyase evolved in mercury-resistant bacteria, can serve as a highly specific biorecognition element for MeHg. MerB binds MeHg via conserved cysteine residues (Cys-96 and Cys-159), cleaving the carbon–mercury bond and forming a reactive mercuric ion complex. The cleaved Hg^{2+} is subsequently transferred to MerA for reduction, demonstrating a natural detoxification mechanism that can be mimicked in a biosensing platform. The hypothesis suggests that immobilizing MerB on gold screen-printed electrodes—using linkers like nitrilotriacetic acid (NTA) or 3-mercaptopropionic acid—will allow the development of a biosensor with

femtogram-level detection limits, high specificity for MeHg over Hg^{2+}, and potential for reuse through magnetic nanoparticle incorporation.

Furthermore, it is hypothesized that such a bioengineered sensor system will outperform conventional methods in terms of portability, speed, and field applicability. Integration with electrochemical transducers and smartphone-based interfaces is anticipated to facilitate real-time environmental monitoring, particularly in regions where laboratory infrastructure is lacking. Ultimately, this research hypothesizes that the combined application of functionalized nanomaterials and enzyme-based recognition systems will lead to advanced tools for both remediation and detection of toxic metals, particularly MeHg. These innovations are expected to significantly enhance environmental monitoring, reduce health risks, and provide a foundation for sustainable pollution control technology.

Chapter 3

Publications and Patent

3.1 Publications 1

Summary of Publication 1: With the continued rise of industrialization, contamination of water resources by toxic metals such as lead (Pb^{2+}), chromium (Cr^{3+}), and mercury (Hg^{2+}) has become a pressing global concern. These metals, due to their toxicity, non-biodegradability, and tendency to accumulate in living organisms, pose serious risks to both ecosystems and human health. Developing affordable, scalable, and environmentally friendly adsorbent materials for the selective removal of these toxic ions is therefore a top priority in the field of water treatment. This article presents a focused study on the design, synthesis, and application of SiO_2 (silica) particles and amino-functionalized SiO_2 particles for the removal of Pb^{2+}, Cr^{3+}, and Hg^{2+} ions from aqueous solutions.

At the core of the research is the use of the sol–gel method, a well-established technique for fabricating silica-based materials with controlled porosity, morphology, and surface chemistry. The authors successfully synthesize both bare SiO_2 particles and Amino-SiO_2 particles, the latter being surface-modified with aminopropyltriethoxysilane (APTES) to introduce functional $–NH_2$ groups. This modification is designed to improve the binding affinity toward metal ions through enhanced electrostatic interactions, hydrogen bonding, and potential chelation mechanisms.

Comprehensive material characterization is carried out using techniques such as Fourier Transform Infrared Spectroscopy (FTIR) to confirm surface functionalization, Scanning Electron Microscopy (SEM) to analyze particle morphology, Brunauer–Emmett–Teller (BET) analysis for surface area determination, and Zeta potential measurements to evaluate colloidal stability and surface charge behavior. These analyses confirm that the amino-functionalization increases both the surface reactivity and the potential for metal ion capture.

The article's strength lies in its comparative adsorption studies. Batch experiments are conducted to assess the adsorption performance of both unmodified and modified silica particles under varying conditions of pH, contact time, initial metal ion concentration, and temperature. The results show that the Amino-SiO_2 particles significantly outperform bare SiO_2, particularly in removing Pb^{2+} and Hg^{2+}, which show stronger interactions with the amine groups. Optimal adsorption occurs at slightly acidic to neutral pH ranges, aligning with the chemistry of the metal-ligand interactions.

Kinetic modeling reveals that the adsorption process follows a pseudo-second-order model, suggesting chemisorption as the dominant mechanism. Isotherm studies demonstrate that the adsorption behavior aligns best with the Langmuir isotherm, indicating monolayer adsorption on a homogeneous surface. Thermodynamic analyses further support the spontaneity and feasibility of the adsorption process, with negative Gibbs free energy values observed across the board.

Importantly, the study addresses regeneration and reusability, showing that the Amino-SiO_2 particles maintain a high percentage of their adsorption capacity over several cycles of desorption and re-adsorption, which is critical for sustainable and cost-effective application.

From an application standpoint, this work makes a compelling case for the use of functionalized silica nanoparticles in environmental remediation, offering a practical, efficient, and scalable approach to remove harmful metal ions from contaminated waters. The ease of synthesis, tunable surface chemistry, and strong performance metrics make Amino-SiO_2 particles attractive candidates for real-world wastewater treatment systems.

In conclusion, this article adds meaningful insight into the field of nanostructured adsorbents by demonstrating how surface modification of silica can significantly enhance metal ion uptake. It bridges material science with environmental engineering, offering a powerful platform for mitigating toxic metal pollution through smart, selective, and recyclable sorbent materials.

Journal of Sol-Gel Science and Technology (2022) 103:290–308
https://doi.org/10.1007/s10971-022-05830-z

ORIGINAL PAPER: SOL-GEL AND HYBRID MATERIALS WITH SURFACE MODIFICATION FOR APPLICATIONS

Removal of Pb^{2+}, Cr^{3+} and Hg^{2+} ions from aqueous solutions using SiO_2 and amino-functionalized SiO_2 particles

A. F. P. Allwin Mabes Raj[1,2] · Sara Krajnc[1] · Maja Bauman[1] · Marijana Lakić[1] · Andreja Gutmaher[1] · Aleksandra Lobnik[1,3] · Aljoša Košak[1,3]

Received: 30 November 2021 / Accepted: 26 April 2022 / Published online: 21 May 2022

Abstract

Herein we present silica (SiO_2) and amino-functionalized SiO_2 particles (NH_2@SiO_2) based on the Stöber method involving the reaction of hydrolysis and condensation of alkoxide precursors tetraethoxysilane (TEOS), 3- (trimethoxysilylpropyl) diethylenetriamine (DETA) and (3-aminopropyl) trimethoxysilane (APTMS) for specific and selective removal of heavy metal ions such as Lead (Pb^{2+}), Chromium (Cr^{3+}) and Mercury (Hg^{2+}). The prepared SiO_2 and NH_2@SiO_2 particles were characterized by Fourier Infrared Spectroscopy (FTIR) spectroscopy, thermogravimetric analysis (TGA), specific surface area (BET), transmission electron microscopy (TEM), zeta potential (ζ) measurements and potential titration measurements. We studied the adsorption efficiency toward heavy metal ions (Pb^{2+}, Cr^{3+} and Hg^{2+}) in model salt solutions. The adsorption process was evaluated in terms of adsorption efficiency, adsorption capacity, adsorption isotherms, kinetics and thermodynamic parameters and desorption efficiency based on the result of the atomic absorption spectroscopy (AAS) measurements for Pb^{2+} and Cr^{3+} ions and inductively coupled plasma optical emission spectrometer (ICP-OES) measurements for Hg^{2+}. The results showed the highest adsorption efficiency and capacity for heavy metal ions (Pb^{2+}, Cr^{3+} and Hg^{2+}) by NH_2@SiO_2 using APTMS. Furthermore, the adsorption efficiency was 99.3 % for Pb^{2+}, 98.4 % in the case of Cr^{3+} ions and 88% for Hg^{2+}. The adsorption process for Pb^{2+}, Cr^{3+} and Hg^{2+} ions using non-functionalized SiO_2 and NH_2@SiO_2 particles follows pseudo-second-order kinetics and is best described by the Langmuir adsorption model. The desorption results showed potential for reusing NH_2@SiO_2 particles with more than 91.8 % desorbed Pb^{2+} ions using 0.1 M HCl and 100% desorbed Hg^{2+} ions using 1.5 M $C_6H_8O_7$.

Graphical abstract

Three alkoxide precursors (tetraethoxysilane (TEOS), 3-(trimethoxysilylpropyl), diethylenetriamine (DETA) and (3-aminopropyl) trimethoxysilane (APTMS)) were used in the one-pot synthesis of silica (SiO_2) and amino-functionalized SiO_2 (NH_2@SiO_2) particles. The prepared adsorbent materials were characterized and used for adsorption tests and desorption toward heavy metals ions (Pb^{2+}, Cr^{3+} and Hg^{2+}). Adsorption efficiency, adsorption capacity, adsorption isotherms, kinetics and thermodynamic parameters were determined. Desorption efficiency was tested using 0.1 M HCl or 1.5 M $C_6H_8O_7$.

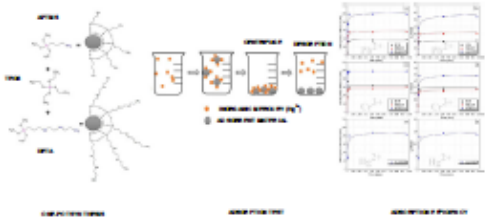

✉ Aljoša Košak
aljosa.kosak@um.si

[1] IOS, Institute of Environmental Protection and Sensors, Ltd., Beloruska 7, SI-2000 Maribor, Slovenia

[2] Jožef Stefan International Postgraduate School, Jamova cesta 39, Ljubljana, Slovenia

[3] University of Maribor, Faculty of Mechanical Engineering, Centre of Sensor Technology, Smetanova 17, SI-2000 Maribor, Slovenia

Journal of Sol-Gel Science and Technology (2022) 103:290–308 291

Keywords Amino functionalized SiO_2 particles · Adsorption efficiency · Chromium · Lead · Mercury · Desorption

Highlights

- Silica (SiO_2) particles and amino-functionalized SiO_2 (NH_2@SiO_2) particles were synthesized and characterized.
- APTMS precursor showed maximal adsorption efficiency.
- Adsorption efficiency for Pb^{2+}, Cr^{3+} and Hg^{2+} were 99.3%, 98.4%, and 88%, respectively.
- Langmuir's adsorption model describes the kinetics of pseudo-second-order for the adsorption process.
- Desorption of 91.8% and 100% were achieved for Pb^{2+} and Hg^{2+} ions, respectively.

1 Introduction

One of the greatest challenges worldwide, as described in the European Union (EU) Water Framework Directive (Directive 2000/60/EC) [1], is to ensure suitable water/wastewater quality due to its major impact on all aspects of human life, including health, food, energy and economy [2, 3]. The EU Water Framework Directive (Directive 2000/60/EC) aims to draw the assessment of ecological status for surface waters, defines water quality standards and specific pollutants, including heavy metals, such as mercury (Hg^{2+}), cadmium (Cd), lead (Pb^{2+}), arsenic (As) and chromium (Cr^{3+}), to improve water/wastewater quality [4, 5]. Although the implementation of the Directive varies from country to country, the national legislations are usually stricter [6]. According to the Slovenian legislation (Directive 2013/39/EU)—amending Directives 2000/60/EC and 2008/105/EC as regards priority substances in the field of water policy [7, 8], limit values for Pb^{2+} varies from 10 µg/L in Rules on drinking water [9] and 0.5 mg/L in Decree on the discharge and treatment of urban wastewater [10], while for Cr^{3+} from 50 µg/L in Rules on drinking water [9] and 0.5 mg/L in Decree on the discharge and treatment of urban wastewater [10]. The limit for Hg^{2+} and its compounds is 0.07 µg/L in Rules on drinking water [11].

Due to their toxicities, inability to biodegrade and tendency to bioaccumulate, heavy metals must be detected and efficiently removed from wastewater [12, 13]. Different techniques, such as liquid-liquid extraction [14], crystallization [15], ion exchange [16], membrane processes [17] and adsorption [18], are used for the removal of heavy metal ions from aqueous medium. Most of these techniques are limited by the solubility of metals, high-pressure operation, expensive analytical instruments and requirements for qualified personnel [19]. Among these methods, adsorption prevails by using different adsorbents, such as activated carbon, chitosan [20], zeolites [21], polymeric materials, clays and synthesized particles [22].

In order to improve different adsorption materials for environmental applications [23], new materials, such as functionalized SiO_2 particles [24] or magnetic particles [25] with increased affinity, capacity and selectivity for removal of specific pollutants were being developed [26]. Among those, SiO_2 (nano) particles have drawn attention due to their high specific surface area, non-toxicity and possibility of surface modification [27]. In the last decade, the means of improving physical-chemical properties and size, shape and porosity of SiO_2 particles were intensively studied [28–30].

Different ways have been adopted to develop SiO_2 particles, such as reverse microemulsion [31], flame synthesis [32] and sol-gel method [33]. Synthesis via sol-gel is predominantly used because of its simplicity, flexibility, low costs, energy efficiency and ability to control the synthesis conditions [34]. By varying reaction conditions, Stöber synthesis can lead to the formation of a three-dimensional gel network, or, in most cases, to monodisperse functional SiO_2 particles with the potential to bind heavy metal ions [35]. By using alkoxyde precursors, which differ in the number of alkoxyde groups, the length of the aliphatic chain and the types of functional groups (phenol, carbonyl, hydroxyl, amine, and ether), efficient functionalization is possible [36]. Precursors with the long aliphatic hydrophobic chains with amino (-NH_2) functional groups at the end have proven to be an efficient material for heavy metal ions binding [37–39].

We performed a thorough literature review on various adsorbent materials for comparing removal efficiency and adsorption capacity. Košak et al. performed adsorption using mercaptopropyl functionalized silica (SiO_2) nanoparticles towards different heavy metal ions (Zn^{2+}, Pb^{2+}, Hg^{2+}, Cd^{2+}) [35]. Interestingly, they were many natural adsorbents such as eggshells [40] and *Moringa oleifera*, *opis juliflora* and peanut shell [41] for Pb^{2+}, Peanut shell [42] and iron (III)-impregnated sorbent prepared from sugarcane bagasse for Cr^{3+} ions [43]. Su et al. used activated carbon modified with micro-sized goethite to study the adsorption in Cr^{3+} ions [44]. Also, a variety of adsorbents were tested for their removal efficiency towards Hg^{2+} palm shell [45], Gold nanoparticle-coated silica [46] and activated carbon [47]. Surprisingly there are not many existing works of literature on desorption studies.

So far, to our knowledge, no research using DETA and APTMS precursor for functionalization of SiO_2 particles for

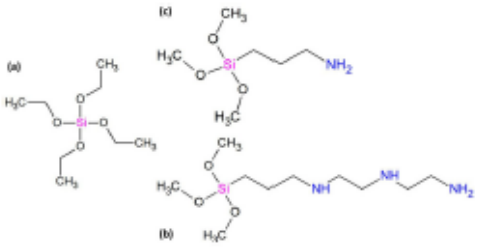

Fig. 1 Structural formula of precursor tetraethoxysilane (TEOS) (a), 3-(trimethoxysilylpropyl) diethylenetriamine (DETA) (b) and (3-aminopropyl) trimethoxysilane (APTMS) (c)

the specific removal of Pb^{2+}, Cr^{3+} and Hg^{2+} ions from aqueous solutions have been reported. The DETA precursor contains two additional secondary amino (-NH) groups and the primary amino group (-NH_2) at the end of the aliphatic chain compared to the APTMS precursor, which contains only -NH_2 (Fig. 1).

This research focused on synthesising SiO_2 and NH_2@SiO_2 adsorbent material using TEOS, DETA and APTMS precursors. Prepared particles were characterized using transmission electron microscopy (TEM), Fourier Infrared Spectroscopy (FTIR), thermogravimetric analysis (TGA), Specific Surface Area Analysis (BET) and zeta potential (ζ) measurements in order to determine their surface and morphological properties. Additionally, interactions of the prepared particles with Pb^{2+}, Cr^{3+} and Hg^{2+} heavy metal ions were evaluated using Langmuir and Freundlich adsorption isotherm models. Adsorption kinetics using pseudo-first and pseudo-second kinetic models were studied, and thermodynamic parameters of the adsorption were determined. Finally, the desorption efficiency was investigated in order to evaluate the adsorbent reusability.

2 Materials and methods

For the preparation of the sol-gel particles, tetraethoxysilane (98%, TEOS, Sigma-Aldrich), 3-(trimethoxysilylpropyl) diethylenetriamine (97%, DETA, Sigma-Aldrich) and (3-aminopropyl) trimethoxysilane (97%, APTMS, Sigma-Aldrich) as alkoxyde precursors were used. Iso-propanol (99.8%, Sigma-Aldrich) and ethanol (99.8%, Sigma-Aldrich) served as alcoholic medium and ammonium hydroxide solution (25% NH4OH, Sigma-Aldrich) as an alkaline catalyst. The adsorption of heavy metal ions was tested using aqueous solutions of lead (II) nitrate (99%, Pb $(NO_3)_2$, Sigma-Aldrich) and chromium (III) nitrate nonahydrate (99%, $Cr(NO_3)_3 \cdot 9H2O$, Sigma-Aldrich), Mercury(II) nitrate (99%), $Hg(NO_3)_2$ (Sigma-Aldrich). The desorption efficiency of the bound ions was tested using hydrochloric acid (37%, HCl, Sigma-Aldrich) and citric acid (99%, $C_6H_8O_7$, Sigma-Aldrich). The solutions were prepared with ultrapure water. All the chemicals reagents were used as received.

2.1 Synthesis and surface functionalization of SiO_2 particles

The amorphous silica (SiO_2) particles were prepared according to the Stöber method [36], based on the hydrolysis and condensation of a TEOS precursor in the presence of ammonia within an alcoholic solution. Synthesis of SiO_2 particles (non-functionalized and functionalized) was carried out under the conditions presented in Table 1. In the synthesis, 2-propanol distilled water and 25% aqueous ammonia solution as a catalyst was mixed in the reaction vessel up to the pH value of 10. After that, an appropriate amount of tetraethoxysilane (TEOS) and (3-aminopropyl) trimethoxysilane (APTMS) precursors were simultaneously admixed to the reaction mixture in order to obtain a constant water-to-TEOS molar ratio (R) 525, and variable TEOS-to-APTMS molar ratios (P) (Fig. 2A). The reaction was kept stirring for 3 h at room temperature (RT) and 50 °C, respectively. Afterwards, the white colloidal suspension was repeatedly centrifuged at 7500 rpm for 5 min, washed with distilled water and ethanol and finally dried at 120 °C. In the case of SiO_2 particles synthesis using 3-(trimethoxysilylpropyl) diethylenetriamine (DETA) precursor pH value was lowered from pH 10 to pH 7 with 3 M HCl after adding TEOS precursor (Fig. 2B) in order to prevent the formation of gel as discovered in previous research [37].

2.2 Characterization techniques

The formation of dried SiO_2 particles was confirmed with Fourier infrared spectroscopy (FTIR; Perkin Elmer). The thermal stability of the dried SiO_2 particles was analysed using thermogravimetric analysis (PerkinElmer, Thermogravimetric Analyzer TGA 4000); the specific surface area of the dried samples was measured by BET (Tristar 3020, Micromeritics). The Zeta potential (ζ) of the prepared particles in colloidal solution was determined with Laser-Doppler Zetasizer (Nano ZS Analyzer, Malvern). A double-burette automatic titrator (T70, Mettler Toledo) combined with a glass electrode (InLab Routine-L, Mettler Toledo) was used for the dynamic addition of the titrants/reagents for potentiometric titration measurements. The morphology of obtained material redispersed in ethanol was investigated with the transmission electron microscope (TEM, JEM-2100, JEOL).

2.3 Adsorption of heavy metal ions

The adsorption capacity of SiO_2 and functionalized (NH_2@SiO_2) particles was tested using lead (II), chromium

Table 1 Reaction conditions for the synthesis and surface functionalization of SiO_2 particles

Precursor	Sample*	Molar ratio R [H_2O]/[TEOS]	Molar ratio P [TEOS]/[precursor**]	T [°C]	pH	t [h]
TEOS	T/25	525	∞	25	10	3
	T/50			50		
TEOS: DETA	TD1/25	525	1	25	7	24
	TD1/50			50		
	TD2/25		2	25		
	TD2/50			50		
	TD4/25		4	25		
	TD4/50			50		
TEOS: APTMS	TA1/25	525	1	25	10	3
	TA1/50			50		
	TA0.5/25		0.5	25		
	TA0.5/50			50		
	TA2/25		2	25		
	TA2/50			50		
	TA0.25/25		0.25	25		
	TA0.25/50			50		
	TA4/25		4	25		
	TA4/50			50		

*T = TEOS; TD = TEOS: DETA; TA = TEOS: APTMS

**precursor DETA or APTMS

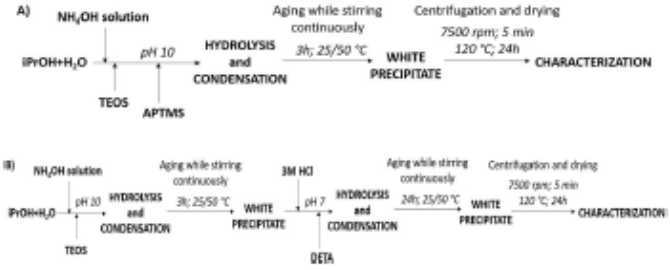

Fig. 2 Schematic presentation of SiO_2 surface-modified particles using precursors TEOS/APTMS (**A**) and TEOS/DETA (**B**)

(III) and mercury (II) nitrate aqueous salt solutions. Adsorption solutions were prepared by dissolving 100 mg of Pb $(NO_3)_2$, Cr $(NO_3)_3 \cdot 9H_2O$, Hg $(NO_3)_2$ salt in a 1-litre flask with distilled water. The solution's pH were adjusted to pH four by adding 0.1 M HCl. In the next step, 45 mg of the dried adsorbent material was added to the 20 mL of Pb (II), Cr (III) and Hg (II) salt solutions. After specific adsorption time, the obtained suspensions were centrifuged at 7500 rpm for 5 min in order to separate the particles from the supernatant. The concentration of heavy metal ions in the supernatant was determined by Atomic Absorption Spectroscopy (AAS, Perkin Elmer) for Pb (II), Cr (III) and inductively coupled plasma optical emission spectrometer (ICP-OES, SPECTRO Analytical Instruments) measurements for Hg (II) measurements. Adsorption efficiency (%) was calculated using below equation:

$$\text{adsorption efficiency}\,(\%) = \frac{C_0 - C_t}{C_0} * 100 \quad (1)$$

where C_0 (mg/L) and C_t (mg/L) are the initial and residual concentrations of metal ions at different times, while adsorption capacity (qt) was calculated using below equation:

$$q_t = \frac{(C_0 - C_t) * V}{m} \quad (2)$$

where C_0 (mg/L) and C_t (mg/L) are the initial and residual concentrations of metal ions at different times, V (L) is the volume of the adsorption solutions, and m (g) is the mass of adsorbent material used.

To determine the interactions between the adsorbent material and heavy metal ions, the obtained results were modeled using isothermal adsorption models. Linear forms of adsorption models, Langmuir (Eq. (3)) and Freundlich (Eq. (4)), were used to obtain the isothermal curves and to determine adsorption parameters that are characteristic for each model [48, 49]

$$\frac{C_e}{q_e} = \frac{1}{q_t K_L} + \frac{C_e}{q_t} \tag{3}$$

$$\log q_e = \log K_F + \frac{1}{n} \log C_e \tag{4}$$

where C_e (mg/L) is the equilibrium concentration of metal ions, q_e (mg/g) is adsorption capacity at equilibrium, qt (mg/g) is adsorption capacity at the time, KL (L/mg) is Langmuir equilibrium adsorption constant related to the affinity of binding sites, KF (l/mg) is Freundlich constant related to the adsorption capacity of the adsorbent and n is the constant related to the adsorption intensity of the adsorbent.

Linear forms of kinetic models of the pseudo-first (Eq. (5)) and pseudo-second (Eq. (6)) order were used to determine the adsorption dynamic behavior [50]

$$\ln(q_e - q_t) = \ln q_e - k_1 t \tag{5}$$

$$\frac{t}{q_t} = \frac{1}{k_2 q_e^2} + \frac{1}{q_e} t \tag{6}$$

where q_e (mg/g) is adsorption capacity at equilibrium, q_t (mg/g) is adsorption capacity at time, k_1 (L/min) is constant of pseudo-first-order and k_2 (g/mg·min) is the rate constant of pseudo-second-order.

Thermodynamic parameters that gave additional information on energy changes associated with the adsorption process were determined. The most common equations that connect thermodynamic parameters were used: Gibbs free energy (ΔG^0), enthalpy (ΔH^0) and entropy (ΔS^0). The spontaneity of the adsorption process was determined based on the sign of Gibbs free energy (Eq. (7)) and the change in enthalpy (ΔH^0), and change in entropy (ΔS^0) (Eq. (8)) [51]

$$\Delta G^0 = -RT \ln K \tag{7}$$

$$\Delta G^0 = \Delta H^0 - T\Delta S^0 \tag{8}$$

where R is the universal gas constant (8.3143 J/molK), T (K) is temperature, and K is the equilibrium constant for adsorption and desorption.

2.4 Desorption of heavy metal ions

In this study, two different desorption solutions, i.e., 0.1 M HCl and 1.5 M $C_6H_8O_7$, were tested for the desorption of Pb^{2+}, Cr^{3+} and Hg^{2+} ions from the functionalized (NH_2@SiO_2) particles with APTMS precursor. After completing the adsorption process, 20 mL of desorption solutions were added to dried adsorbent material and stirred at room temperature for one hour. The obtained suspensions were centrifuged at 7500 rpm for 5 min to separate the particles from the supernatant.

3 Results and discussion

The characterization of adsorption materials, SiO_2 particles in comparison to functionalized (NH_2@SiO_2) particles and its adsorption and desorption efficiency for Pb^{2+}, Cr^{3+} and Hg^{2+} ions are presented and discussed.

3.1 Characterization of adsorption materials

3.1.1 Morphological properties

Morphological characteristics of the prepared samples were determined using TEM. Among all the prepared samples (Table 1), T/25; T/50; TD1/25, TD4/25, TA0.5/25, and TA4/25 have been selected for TEM analysis.

In the case of the nonfunctionalized particles, where only TEOS precursor was used (sample T/25) and the synthesis temperature was 25 °C, relatively spherical SiO_2 particles with an average particle size of 100 nm were formed (Fig. 3A). With the increase of synthesis temperature to 50 °C (sample T/50), the SiO_2 particles size decreased to 60 nm (Fig. 3B). The particles had a relatively spherical shape and a higher level of agglomeration compared to the particles synthesized at 25 °C. Figure 3C, E show amino-functionalized particles using DETA precursor, prepared at 25 °C for TEOS-to-DETA molar ratio (P) 1 and 4, respectively. Babalou et al. [52] attributed this effect to the increased nucleation rate due to the rising reaction temperature. The second offered explanation is decreased saturation concentration of ammonia catalyst at higher temperatures, resulting in the lower dissolution of TEOS precursor. Reduction and hydrolysis reaction rates are also lower, and ultimately the particles size decreases.

Figure 3C, E shows amino-functionalized silica particles using DETA precursor. It is evident that the SiO_2 particles functionalized at 25 °C (TD1/25) consist of two phases. Larger SiO_2 particles of approximately 140 nm in size were coated with smaller, 10–20 nm-sized DETA particles. The occurrence of smaller particles can be attributed to the homocondensation of the DETA precursor. DETA functionalized SiO_2 particles (TD1/25) reached the average particle size of about 150–160 nm, as shown in Fig. 3C. Despite the fact that the reaction temperature generally affects the particle sizes, we did not observe significant

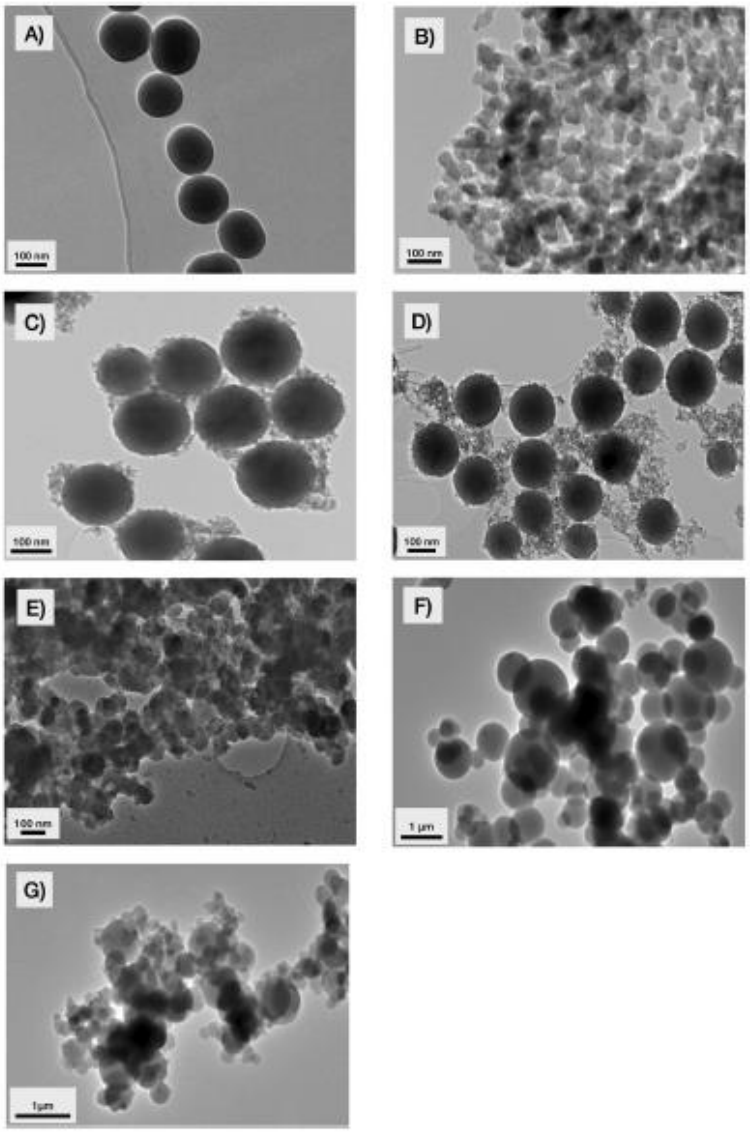

Fig. 3 TEM images of SiO_2 samples: **A** T/25 and (**B**) T/50; DETA functionalized SiO_2 samples: **C** TD1/25 and (**D**) TD1/50, **E** TD4/25; APTMS functionalized SiO_2 samples: **F** TA4/25 and (**g**) TA0.5/25

deviations in particle sizes, and morphologies with any increases in the reaction temperature from 25 to 50 °C for DETA functionalized SiO_2 samples (Fig. 3D). At a higher synthesis temperature (50 °C), the TEM image confirms the existence of large SiO_2 particles that are closely surrounded by a large number of tiny DETA particles that appeared to be taking part in a strong aggregation process, as shown in Fig. 3D. The average size of larger SiO_2 particles for the sample TD1/50 did not exceed 150 nm while the small ones of DETA retained a particle size of about 10–20 nm.

At higher molar ratios, TEOS-to-DETA (P = 4), for the sample TD4/25 one could expect the formation of larger particles with increasing TEOS concentrations, but the average particle size was found to remain about

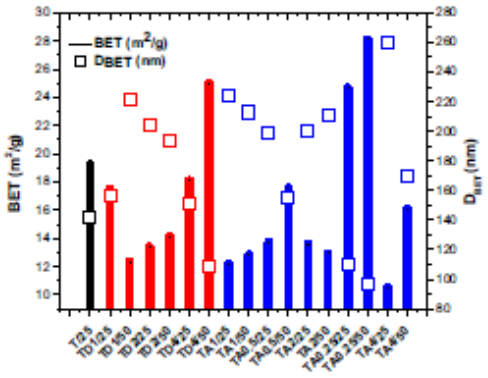

Fig. 4 BET specific surface area and particle size (D_{BET}) for the prepared samples

120–130 nm (Fig. 3E) with uniformity in terms of their morphology. Although many authors reported on increasing the particle size with increasing TEOS, concentration we did not notice any effect of TEOS concentration on the final particle size in this step of the research [53]. From Fig. 3F, it is evident that the APTMS functionalized SiO_2 particles (sample TA4/25) were formed with broad size distribution and an average size of about 500 nm. As the molar ratio P decreases (sample TA0.5/25), the wide particle size distribution becomes even more pronounced, and a high degree of particle agglomeration is observed (Fig. 3G). Such mechanism of particle formation is based on LaMer's and Dinegar's [54, 55] assumption that particle uniformity results from a short nucleation period followed by particle growth with controlled diffusion of molecules from the solution to the nucleus surface. Nowadays, it is well known that the nucleation period often continues into the particle growth period leading to the emergence of a wide distribution of particle sizes [56].

3.1.2 Specific surface area (BET) analysis

The specific surface area was measured for all the prepared samples (Table 1). As seen on TEM micrographs (Fig. 3), the particles were spherical in shape; thus, the average particle size (D_{BET}) was calculated using (Eq. (9)) [57, 58]:

$$D_{BET} = \frac{6}{\rho \times BET} \quad (9)$$

where ρ (2.2 g/cm^3) is the theoretical density of SiO_2 particles [59], and BET (m^2/g) is measured for specific surface area. In Fig. 4. the results indicated increasing specific surface area (BET) with the rise of the reaction temperature from 25 to 50 °C for all prepared samples,

Table 2 Specific surface area BET (m^2/g) and particle size D_{BET} (nm) for the prepared samples

Sample	Temperature [°C]	Molar ratio, P ([TEOS]/[precursor*])	Specific surface area, BET [m^2/g]	Particle size, D_{BET} [nm]
T25	25	–	20 ± 2	138 ± 14
TD1/25	25	1	18 ± 2	153 ± 17
TD1/50	50		13 ± 1	211 ± 16
TD2/25	25	2	14 ± 1	196 ± 14
TD2/50	50		14 ± 1	196 ± 14
TD4/25	25	4	19 ± 2	145 ± 15
TD4/50	50		25 ± 2	110 ± 9
TA0.25/25	25	0.25	25 ± 2	109 ± 8
TA0.25/50	50		28 ± 2	97 ± 6
TA0.5/25	25	0.5	14 ± 2	195 ± 24
TA0.5/50	50		18 ± 2	152 ± 15
TA1/25	25	1	12 ± 2	227 ± 32
TA1/50	50		13 ± 2	210 ± 28
TA2/25	25	2	14 ± 3	195 ± 34
TA2/50	50		13 ± 3	210 ± 39
TA4/25	25	4	11 ± 1	248 ± 21
TA4/50	50		17 ± 2	160 ± 17

except for sample TD1/25 due to the thickness of the surface layer. The maximum specific surface area value was obtained with the samples synthesized at a molar ratio P = 4:1 or when the addition of TEOS precursor was the highest. The same effect can be noticed when using precursor APTMS (Fig. 4). Calculated D_{BET} values corresponded to the TEM micrographs. The obtained values decreased with increased reaction temperature, and the exceptions were in the case of the samples TD1 and TA2.

Specific surface area values (BET) measured for the prepared samples and their particle size (D_{BET}) calculated according to Eq. (9) are presented in Fig. 4 and Table 2. As can be seen, the specific surface area of non-functionalized silica particles prepared at room temperature (T25) was about 20 m^2/g and the calculated average particle size (D_{BET}) was about 138 nm. Results revealed that the specific surface area of amino-functionalized silica particles (TA and TD) prepared at different temperatures (25 °C and 50 °C) and molar ratios P (0.25, 0.5, 1, 2, 4) reduced on average and the particle size increased, compared to non-functionalized silica particles.

As can be seen from Table 2, the reaction temperature is an important parameter that significantly affects changing the specific surface area. The results showed that the specific surface area of the silica samples amino-functionalized with DETA precursor at constant TEOS-to-DETA molar ratios (P), increased with increasing reaction temperature from 25 to 50 °C, which was reflected in decreasing their particle size. Specific surface area for the samples prepared

at molar ratio P = 2 and the reaction temperatures 25 °C (TD2/25) and 50 °C (TD2/50) remained constant at about 14 m^2/g with the average particle size of 196 nm. For the samples TD4/25 and TD4/50, the specific surface area increased from about 19 m^2/g to 25 m^2/g and their average particle size decreased from 145 nm to 110 nm, respectively. An exception is the TD1/25 sample in which the specific surface area decreased from about 18 m^2/g to 13 m^2/g with increasing temperature from 25 to 50 °C and its average particle size increased from 153 to 211 nm, respectively. This can be most probably attributed to the increased agglomeration of the prepared particles. The formation of smaller agglomerated particles was also confirmed by TEM images of the morphology of particles prepared at 50 °C (Fig. 3).

Similar findings could be obtained in the case of amino-functionalized silica samples prepared at different temperatures (25 °C and 50 °C) and molar ratios P (0.25, 0.5, 1, 2, 4). The results, in that case, also confirmed that the specific surface area of the silica samples amino-functionalized with APTMS precursor at constant TEOS-to-APTMS molar ratios (P), increased on average with increasing reaction temperature from 25 to 50 °C, which was consequently reflected in decreasing their particle size, as shown in Table 2. It was also found that the specific surface area of silica samples amino-functionalized with APTMS precursor, prepared at a constant reaction temperature of 25 °C decreased in general from 25 to 11 m^2/g with increasing molar ratio P from 0.25 to 4, while it was decreased from 28 to 17 m^2/g with increasing molar ratio P from 0.25 to 4 for the samples prepared at a constant reaction temperature of 50 °C. We assume that the reason for such behavior can be found in the increasing concentration of TEOS precursor relative to APTMS precursor in the reaction system and thus poor coverage of the surface of the silica particles with the APTMS molecules, along with increasing the molar ratio P, which reflects in decreasing the specific surface area and increasing the particle size. In contrast, the pronounced saturation of the silica surface with the APTMS silane molecules at P = 0.25 due to the lower TEOS concentration relative to the increasing APTMS concentration in the reaction system reflects in higher specific surface area and thus smaller particle size [60].

On the contrary, this does not seem to be the case for silica samples amino-functionalized with DETA where the values of specific surfaces are not as arranged as in the case of silica samples amino-functionalized with APTMS. In that case, we are dealing with long-chain silane molecules that include amine groups in their structure (Fig. 1). We hypothesize that such long chains of molecules can attach to the silica surface in a variety of (and more likely) ways, such as loops, trains, and tails, and thus hinder surface interactions between amino-silane molecules and silica surface [61]. In addition, there can exist certain interactions between the adjacent amine groups in the amino-silane chains (via hydrogen bond). All of this can significantly affect the change in specific surface area and consequently the particle size [62].

3.1.3 FTIR analysis

FTIR spectra of all prepared and dried SiO_2 and NH_2@SiO_2 particles, as listed in Table 1, were compared to FTIR spectra of pure TEOS, DETA and APTMS chemicals. Particles prepared at different molar ratios P and synthesis temperature showed similar results; therefore, only samples prepared at molar ratio P = 1 and temperature 25 °C (T/25, TD1/25 and TA1/25 samples) are presented (Fig. 5). The peak at 2975 cm^{-1} was present at all precursor spectra as a result of stretching vibrations in ester (-$SiOC_2H_5$) groups, while the peak at 957 cm^{-1} was ascribed to the bending deformation of the ester groups [24]. In the case of pure precursors, the peaks were clearly visible, whereas in the synthesized nonfunctionalized and functionalized SiO_2 particles peak at 2975 cm^{-1} completely disappeared and was slightly reduced at 958 cm^{-1}. This difference indicates the complete hydrolysis of the precursors or the change in ester silanolzeta groups [37]. The intense peak at 1070 cm^{-1} in all precursors and prepared samples corresponded to the Si-O-Si bond due to long Si-O-Si chains in the silane [39]. The structure of SiO_2 particles with Si-O-Si bindings occurs due to the complete hydrolysis of the silanes with a high number of SiOH groups available for binding. The characteristic amino (N-H) groups in the precursors DETA and APTMS were at about 3363 cm^{-1} and 1610 cm^{-1} [51, 59, 63].

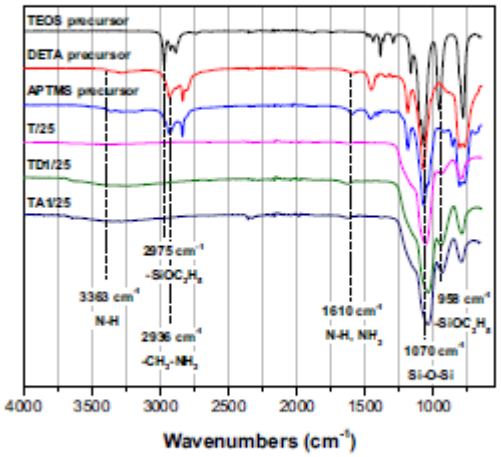

Fig. 5 FTIR spectra of TEOS, DETA and APTMS precursors and T/25, TD1/25 and TA1/25 samples

The same peaks can be observed at the spectra of all prepared amino-functionalized samples, which confirmed the successful functionalization of particles.

3.1.4 Thermal stability

The thermal stability of the SiO_2 and $NH_2@SiO_2$ particles has been established by thermogravimetric analysis (TGA). Figure 6 shows the TGA analysis of unmodified silica (T25) and amino-coated silica samples (TD2/25 and TA0.5/25). TGA curves clearly showed that the organic amino-silane coating completely degraded within 900 °C. As can be seen, the decomposition profile for the amino-coated silica (TD2/25 and TA0.5/25) samples is very similar, showing two main degradation steps. The first step, with a gradual weight loss of 5 wt% on the heating from room temperature up to 150 °C, could be mainly attributed to the loss of physically adsorbed water within the silica particles and evaporation of ethanol residue, as a consequence of a previous condensation of the alkoxysilane groups [64]. The second degradation step at temperatures between 250 and 900 °C with a gradual weight loss of 10 wt% for TD2/25 and 20 wt% for TA0.5/25, is associated with the loss of the surface amino-functional layers, presumably due to the oxidation of the CH_2 and NH_2 units in the structure of APTMS and DETA molecules [65, 66], resulting in the formation of CO_2, NO_x and H_2O and cleavage of individual parts of surface-anchored APTMS and DETA molecules, while Si-O-Si bonds among silicon atoms in the structure of silicon dioxide remain stable. The samples left a residue of about 65 wt% for TA0.5/25 and 85 wt% for TD2/25, respectively. That increase in weight loss for TA0.5/25 can be attributed to the higher APTMS concentration in the sample, in contrast to the TD0.5/25 sample at which the DETA concentration was lower. Comparing these results with the thermogravimetric behavior of the pure silica sample (T25), it is clear that the weight loss of the second step is related to the degradation of the organic amino-silane coating segments. The thermal stability of the prepared samples analyzed is also in accordance with previous results shown in the literature for other functionalized silica nanomaterials [67–70].

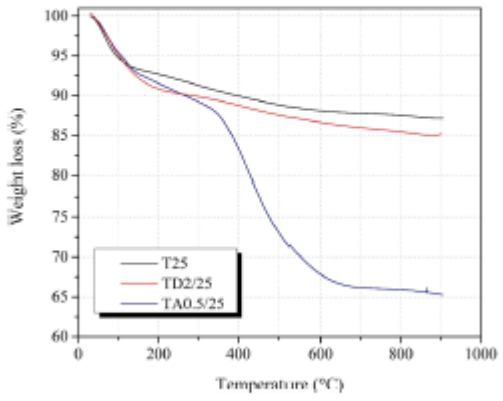

Fig. 6 TGA curves for T25, TD2/25 and TA 0.5/25 samples

3.1.5 Electrokinetic potential

In order to obtain surface charge/isoelectric point, the samples T/25, TD1/25 and TA1/25 were re-dispersed in distilled water. In the case of SiO_2 particles (T/25 sample), the isoelectric point at a pH value of 2.5 was determined. The measured zeta potential (ζ) indicated the formation of SiO_2 particles with positively charged $-OH^{2+}$ groups and negatively charged -O- groups in the SiO_2 surface layer at the pH values below 2.5 and above 2.5, respectively. For the $NH_2@SiO_2$ particles (TD1/25 and TA1/25 samples), the isoelectric point moved from the acidic pH 2.5 to the slightly basic pH at 7.5 in the case of TD1/25 sample and the pH 9.5 in the case of TA1/25 sample, as a consequence of the deprotonation of amino groups in the surface layer of SiO_2 particles. The positive zeta potential (ζ) was the result of the protonation of the amino groups in the acidic medium (pH < 6) [17, 37].

$$-NH_3^+ \Leftrightarrow -NH_2^0 \Leftrightarrow -NH^-$$

acidic medium neutral medium basic medium

The pH-potentiometric titrations were used for the total charge determination of samples T/25, TD2/25 and TA0.5/25 (Fig. 7). They were carried out in the forward (with potassium hydroxide) and backward direction (with hydrochloric acid) within the pH region 2.5 < pH < 11.0. A detailed description for calculating the pH-titration isotherms can be found elsewhere [56, 71].

The titration curve of the T/25 sample showed that dissociation/protonation of the functional groups occurred in the pH range between 8 < pH < 11. The transition in the titration curve is the result of the decomposition of SiO_2 particles in water. In the case of TD2/25 and TA0.5/25 samples, two separate steps of protonation were observed. The first occurred in the pH range of 4.5 < pH < 6.5 and the second in the same area as in the case of the T/25 sample (8 < pH < 11). The obtained separate protonation steps were in accordance with the theory where the primary amines (-NH_2) protonate at the pH~9 and the secondary amines (-NH-) at the pH~4.5 [72]. The quantity of charge or functional groups were calculated from the curve plateaus. The quantities of functional groups were similar in the case of T/25 and TD2/25 samples (0.95 mmol/g and 0.97 mmol/g, respectively), while the highest value was determined in the case of the TA0.5/25 sample (6.04 mmol/g).

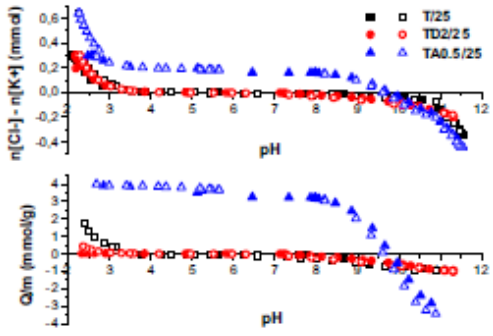

Fig. 7 Potentiometric titration results for the SiO_2 particles (T/25 sample) and NH_2@SiO_2 particles (TD2/25 and TA0.5/25 samples)

3.2 Adsorption studies

Adsorption efficiency tests were performed for all prepared samples (Table 1) using the Pb^{2+}, Cr^{3+} and Hg^{2+} model salt solutions. SiO_2 (T/25 sample) and functionalized SiO_2 particles (TD2/25 and TA0.5/25 samples) indicated the highest affinity towards each heavy metal ion (Pb^{2+}, Cr^{3+} and Hg^{2+}) and were further tested to determine optimal adsorption parameters. By calculating the adsorption efficiency (Eq. (1)) and adsorption capacity (Eq. (2)), the fastest ions binding time onto the surface of the synthesized sample was determined (Fig. 8).

Table 3 depicts the comparison of removal efficiency and desorption efficiency with other adsorbent materials in the existing literature. Different heavy metal ions (Zn^{2+}, Pb^{2+}, Hg^{2+}, Cd^{2+}) were adsorbed using mercaptopropyl functionalized silica (SiO_2) nanoparticles prepared by Košak et al. The maximum removal efficiency for Pb^{2+} was found to be 55.9% and adsorption capacity is 10.42 mg/g [35]. When studying the removal of Pb^{2+} ions from aqueous solution using various adsorbent materials, surprisingly, there are not many desorption experiments done in other works. Pandey et al. demonstrated removal efficiency of 80% and 4.33 mg/g of adsorption capacity towards Pb^{2+} using eggshells in an aqueous phase [40]. Removal of Pb^{2+} using natural adsorbents such as *Moringa oleifera*, *opis juliflora* and peanut shell by Gautam et al. in textile wastewater displayed 86% adsorption efficiency and 5.6 mg/g of adsorption capacity [41]. To facilitate better adsorption of Cr^{3+} ions from the aqueous phase, Liyas et al. used Peanut shell, which yielded 61.5–80% removal efficiency with 4.32 mg/g of adsorption capacity [42]. Zhu et al. analyzed the influence of iron (III)-impregnated sorbent prepared from sugarcane bagasse on the adsorption of Cr^{3+} from aqueous solutions and demonstrated 93% of removal efficiency and 13.37 mg/g of adsorption capacity [43]. Activated carbon modified with micro-sized goethite was used by Su et al. to demonstrate 85.4% removal efficiency of Cr^{3+}, but unfortunately, a very low desorption efficiency of 16.9% was obtained [44]. The maximum removal efficiency for Hg^{2+} was 29.39%, and adsorption capacity was 7.13 mg/g by Kushwaha et al., using palm shell[45]. Solis et al. used Gold nanoparticle-coated silica to demonstrate 96% removal efficiency and 0.1 mg/g of adsorption capacity of Hg^{2+} ions in an aqueous medium [46]. According to Faulconer et al., using activated carbon yielded a removal efficiency of 84%, but they did not perform any desorption experiments [47].

Adsorption efficiency (%) and adsorption capacity q_t (mg/g) of Pb^{2+}, Cr^{3+} and Hg^{2+} ions as a function of contact time (Fig. 8) were studied using SiO_2 particles (T/25 sample) and NH_2@SiO_2 particles (TD2/25 and TA0.5/25 samples). Obtained results have shown that the adsorption efficiency and adsorption capacity increased exponentially by prolonging the adsorption time from 2 min up to 16 h. The equilibrium adsorption time was found to be less than one hour for all tested samples. The adsorption efficiency and adsorption capacity for heavy metal ions (Pb^{2+}, Cr^{3+} and Hg^{2+}) removal were the highest using functionalized SiO_2 particles with APTMS precursor. Adsorption efficiency of 99.3% of Pb^{2+} ions, 98.4% of Cr^{3+} ions and 88% of Hg^{2+} ions removed from aqueous solution when using NH_2@SiO_2 particles with APTMS precursor.

Validating our results, the adsorption capacity using TA0.5/25 sample was 54.13 mg/g in the case of Pb^{2+} ions and 29.16 mg/g in the case of Cr^{3+} ions and 14.4 mg/g in the case of Hg^{2+}. Contrary to predictions, SiO_2 (T/25 sample) and functionalized SiO_2 particles (TD2/25) displayed no adsorption on Hg^{2+}. Based on the results of potential titration measurements, which showed the highest quantity of functional groups in the case of the TA0.5/25 sample (6.04 mmol/g), the obtained results of adsorption capacity were expected. The number of functional groups was similar in the case of T/25 and TD2/25 samples (0.95 mmol/g and 0.97 mmol/g, respectively); Therefore, similar adsorption capacities were observed. Comparison of adsorption capacity of NH_2@SiO_2 particles with other similar adsorbents for removal of Pb^{2+}, Cr^{3+} and Hg^{2+} ion showed similar results (Table 3).

3.2.1 Adsorption Isotherms

The obtained results were modeled using Langmuir (Eq. (3)) and Freundlich (Eq. (4)) adsorption models to determine the adsorbent and adsorbate interactions and the adsorbent surface properties. The characteristic parameters of adsorption isotherms of Pb^{2+} and Cr^{3+} ions for T/25, TD2/25 and TA0.5/25 samples and adsorption isotherms of Hg^{2+} ions for TA0.5/25 samples were determined.

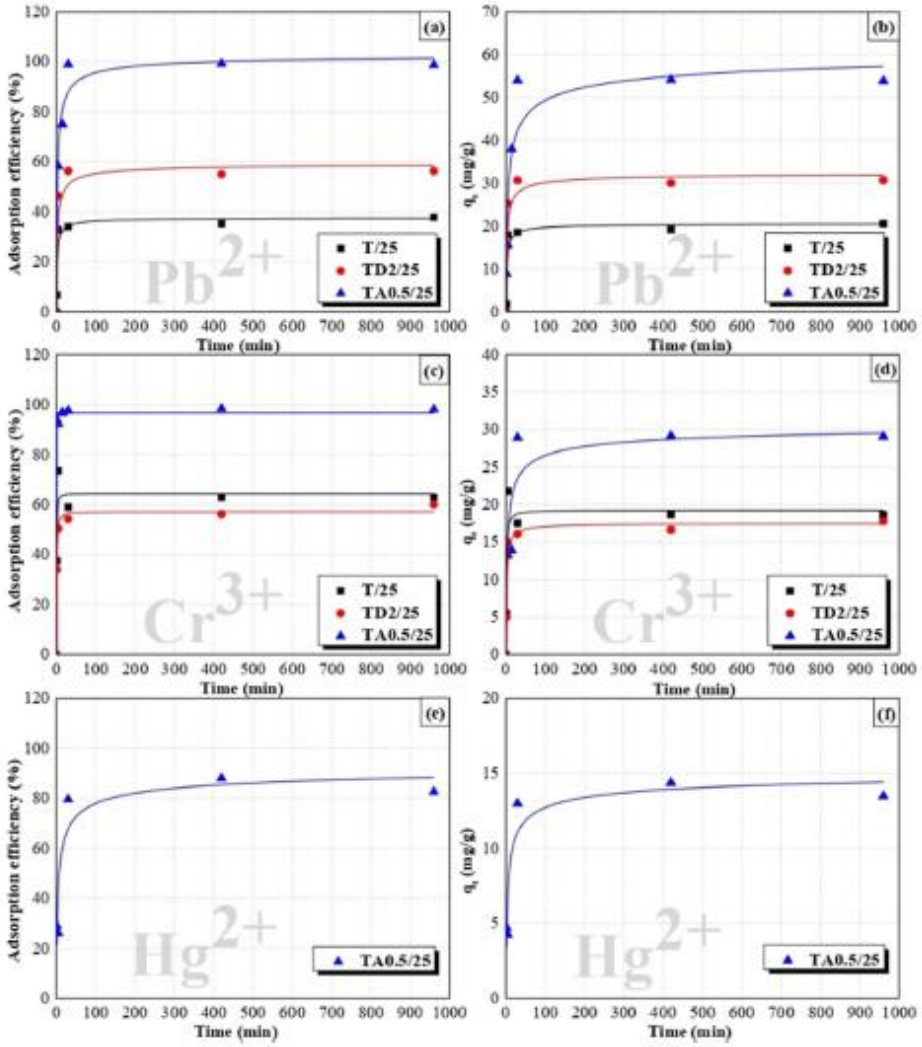

Fig. 8 Adsorption efficiency and capacity of Pb^{2+} ions (**a**, **b**); Adsorption efficiency and capacity of Cr^{3+} ions (**c**, **d**) ions as a function of contact time for the T/25, TD2/25 and TA0.5/25 samples; Adsorption efficiency and capacity of Hg^{2+} ions (**e**, **f**) as a function of contact time for TA0.5/25 samples

The Langmuir isotherm is used to describe the balance between adsorbate and adsorbent, assuming that adsorption is monomolecular, all surface sites are energetically equivalent, and the surface itself is homogeneous, whereas Freundlich isotherm considers heterogeneous surfaces by multilayer adsorption [73, 74] All the values for the parameters and the correlation coefficients (R^2) of the Langmuir and Freundlich models are listed in Table 4. The comparison of correlation coefficients (R^2) showed that the Langmuir isotherm fitted well within the experimental data for Pb^{2+}, Cr^{3+}, and Hg^{2+}. As shown, all the values of R^2 for Langmuir were ranged much higher (R^2 in the range 0.90–0.98) than those estimated from the Freundlich model, which was in the range R^2 0.51–0.95. This indicates the adequacy of the Langmuir isotherm model for describing the adsorption processes and confirming monolayer adsorption.

All the isotherms in Fig. 8 showed characteristic Type I isotherm shape according to IUPAC classification [75] with

Table 3 Comparison of adsorption efficiency (%), adsorption capacity (mg/g) and desorption (%) of SiO_2 and NH_2@SiO_2 particles with other adsorbents for removal of Pb^{2+}, Cr^{3+} and Hg^{2+}

Heavy metal ions	Adsorbent	Removal efficiency %	Adsorption capacity (mg/g)	Desorption efficiency %	Reference
Pb^{2+}	Mercapto-modified silica particles	55.9	10.42	–	[35]
	Egg Shells	80	4.33	–	[40]
	Natural adsorbents	86	5.6	–	[41]
	SiO_2 particles	37.8	20.5	–	Present work
	NH_2@SiO_2 particles (DETA)	56.3	30.7	–	Present work
	NH_2@SiO_2 particles (APTMS)	99.3	54	91.8 (0.1 M HCl)	Present work
Cr^{3+}	Natural adsorbent	61.5–80	4.32	–	[42]
	Iron (III)-impregnated sorbent	93	13.37	–	[43]
	Activated carbon modified with micro-sized goethite	85.4	4.5	16.9	[44]
	NH_2@SiO_2 particles (DETA)	60	21.1	–	Present work
	SiO_2 particles	73.5	17.7	–	Present work
	NH_2@SiO_2 particles (APTMS)	98.4	29.1	>2 (0.1 M HCl)	Present work
Hg^{2+}	Palm shell	29.39	7.13	–	[45]
	Gold nanoparticle-coated silica	96	0.1	–	[46]
	Activated carbon	84	Not given	–	[47]
	NH_2@SiO_2 particles (APTMS)	88	14.4	100 (1.5 M $C_6H_8O_7$)	Present work

*(–) Desorption were not performed in literature for such labeling

Table 4 Adsorption isotherms (Langmuir and Freundlich) parameters of Pb^{2+} and Cr^{3+} ions for T/25, TD2/25 and TA0.5/25 samples and adsorption isotherms (Langmuir and Freundlich) parameters of Hg^{2+} ions for TA0.5/25

Heavy metal ions	Sample	Langmuir				Freundlich		
		Q_{max} [mg/g]	K_L [l/mg]	R_L	R^2	K_F	n	R^2
Pb^{2+}	T/25	18.29	1.12	0.008	0.9702	3.36E–24	0.25	0.8941
	TD2/25	253.81	0.06	0.182	0.9539	2.12E–04	0.58	0.6088
	TA0.5/25	9.89	0.51	0.023	0.9084	7143.32	2.61	0.7667
Cr^{3+}	T/25	17.37	0.92	0.018	0.9739	36081.95	1.95	0.9856
	TD2/25	25.10	0.10	0.131	0.7045	8.88E–03	0.73	0.5127
	TA0.5/25	277.01	0.11	0.163	0.6871	1203.37	1.75	0.5573
Hg^{2+}	TA0.5/25	3.75	0.23	0.1063	0.9888	47.58	−1.40	0.9583

a sharp initial slope for the Pb^{2+}, Hg^{2+} and Cr^{3+} metal species, that indicates high adsorbent efficiency at low metal concentrations, with a typical equilibrium plateau when the metal concentration increases.

The adsorption of the Pb^{2+} and Cr^{3+} by the amino-coated silica adsorbents (TA0.5/25) was noticeably enhanced with respect to the Hg^{2+} at whom the lowest adsorption capacity (3.75 mg/g) was obtained. This can could be interpreted using Pearson's Theory of hard and soft acids and bases (HSAB). Based on the Lewis definition of acids as electron acceptors and bases as electron donors, this concept states that a soft acid prefers to coordinate and form stronger bonds and more stable complexes with soft bases, and vice versa, a hard acid prefers to coordinate and form stronger bonds and more stable complexes with hard bases. Relatively smaller metal ions of low polarizabilities and high electronegativity, such as Cr^{3+}, are classified as hard acids, and amino groups ($–NH_2$) are a hard base. Thus Cr^{3+} has a much higher affinity for amino groups than Hg^{2+}, which is soft acid, whereas borderline acids such as Pb^{2+} exhibit slightly lower preferences for amino ligands [35].

As can be seen, the affinity of surface nonfunctional silica adsorbent (T25) to Pb^{2+} and Cr^{3+} does not differ significantly, 18.29 mg/g for Pb^{2+} and 17.37 mg/g for Cr^{3+}. This can be clarified as the increased activity of surface -OH groups for Pb^{2+} and Cr^{3+} adsorption [76]. Hydroxyl (-OH) groups on the particle surface generally act as adsorption sites for binding heavy metal ions. According to the HSAB concept, -OH groups are classified as hard bases and

therefore prefer stronger bonds with hard or borderline acids, like Cr^{3+} and Pb^{2+}, respectively.

On the other hand, the results for TA0.5/25 adsorbent revealed that the Pb^{2+} (9.89 mg/g) was not removed as efficiently as the Cr^{3+} (277.01 mg/g), most probably because of its weaker binding strength to the amino groups ($–NH_2$). This can be explained by the use of an absolute hardness parameter. Parr et al. [77] stated that the absolute hardness parameter of the amino groups ($–NH_2$) as a hard base is 5.3, while the parameters of Pb^{2+} and Cr^{3+} are 8.5 and 3.05, respectively. Although Pb^{2+} is classified as a borderline acid, the value of its absolute softness, which is defined as the reciprocal value of hardness (a value of zero denotes maximum softness), indicated the slightly softer nature of Pb^{2+} as compared with the Cr^{3+} [35]. Therefore, a higher affinity of the amino groups ($–NH_2$) for the harder Cr^{3+} and a lower affinity for the softer Pb^{2+} is expected. This is in good agreement with the obtained results. In contrast, the results for TD2/25 adsorbent showed much higher adsorption capacity for the Pb^{2+} (253.81 mg/g) in comparison to Cr^{3+} (25.10 mg/g).

Such differences in the adsorption of Pb^{2+}, Cr^{3+} and Hg^{2+} ions by amino-functionalized silica particles (TA0.5/25, TD2/50) can be attributed to the uneven reactivity of different types of amine groups on the silica surface due to the many different ways that the primary amines can interact with its environment [78]. Particularly, the weakly basic amino groups ($-NH_2$) can interact with the weakly acidic silanol groups (Si-OH) at the silica surface, the amine sites can also interact with adjacent amine groups via a hydrogen bond, or they can be mutually non-interacting if the amino groups are isolated from each other [62]. All of that distinctly hinder the chemical interactions of heavy metal ions with the active amino groups and affects the adsorption efficiency and capacity. We can also conclude that the adsorption of heavy metal ions on the amino ($-NH_2$) functionalized silica surface depends so on the concentration of the amino-functional groups at the surface of the adsorbent and the number of N-donor groups in the ligand structure; however, many studies state that adsorption capacity is not always proportional to the number of amino ($-NH_2$) functional groups of the adsorbent [62, 78–83].

Graphically, this can be illustrated by an equilibrium plateau, where no adsorption is possible once a molecule takes place [84].

The R_L value, characteristic for the Langmuir adsorption model, shows that the adsorption process is favorable if $R_L > 1$, is linear if $R_L = 1$ and is irreversible if $R_L = 0$ [85].

As shown in Table 4, the R_L values for the adsorption of Pb^{2+}, Cr^{3+} and Hg^{2+} were found to be in the range $0 < R_L < 1$, which is consistent with the requirement for a favorable adsorption process under the conditions used during this study Fig. 9.

3.2.2 Adsorption kinetics

Figure 10 shows the pseudo-second-order kinetics for adsorption of Pb^{2+}, Cr^{3+} and Hg^{2+} ions from model salt solutions with SiO_2 (T/25 sample) and $NH_2@SiO_2$ particles (TD2/25 and TA0.5/25 samples). From the slope and segment on the ordinate axis, the value of the reaction rate constants (k_1 and k_2) and equilibrium adsorption capacities (q_e) were determined [50]. Calculated values of kinetic parameters and coefficients of linear regression correlations (R^2) are summarized in Table 5. Comparison of the correlation coefficients (R^2) for each sample and heavy metal ion showed the adsorption process of Pb^{2+}, and Cr^{3+} ions on samples T/25, TD2/25 and TA0.5/25 and the adsorption process of Hg^{2+} ions on samples TA0.5/25 follows a pseudo-second-order. The adsorption mechanism of Pb^{2+}, Cr^{3+} and Hg^{2+} ions include the activation and chemisorption processes of strong chelation between Pb^{2+}, Cr^{3+} and Hg^{2+} ions and OH- groups and free-electron pairs present on the surface of the adsorbent material. Moreover, the adsorption process will likely occur by moving the metal ions from the aqueous phase to the adsorbent surface [86–88].

3.2.3 Thermodynamics

For insight into the adsorption process, it is necessary to consider the thermodynamic activation parameters. These adsorption process parameters are activation enthalpy (ΔH), activation entropy (ΔS) and free energy of activation (ΔG) [89]. Taking into account the value of the equilibrium constant (K), the value of Gibb's free energy (ΔG) at a specific temperature (298.15; 323.15 and 348.15 K) was calculated. Based on the calculated values, the value of enthalpy (ΔH) and entropy (ΔS) were graphically determined [90]. The values of the individual thermodynamic parameters for the adsorption of Pb^{2+} and Cr^{3+} ions from model salt solutions onto the T/25, TD2/25 and TA0.5/25 samples and Hg^{2+} ions from model salt solutions onto the TA0.5/25 samples are listed in Table 6.

For significant adsorption to occur, Gibbs free energy change must be negative [91, 92]. As shown in Table 6, Gibb's free energy change (ΔG) values were found to be negative at 298.15 K for adsorption of Hg^{2+} ions with TA0.5/25 sample and Cr^{3+} ions with T/25 sample, at 323.15 and 323.15 K with TD2/25 sample and at all temperature with TA0.5/25 sample, which shows the feasibility and spontaneity of the adsorption process. In other cases, the ΔG values were positive, which indicates that the energy for the activation of the adsorption process should be conveyed from the surroundings [91].

As is evident from Table 6, in the case of the adsorption of Pb^{2+} and Cr^{3+} ions with the T/25 sample and Pb^{2+} ions adsorption with the TD2/25 sample, Hg^{2+} ions with the

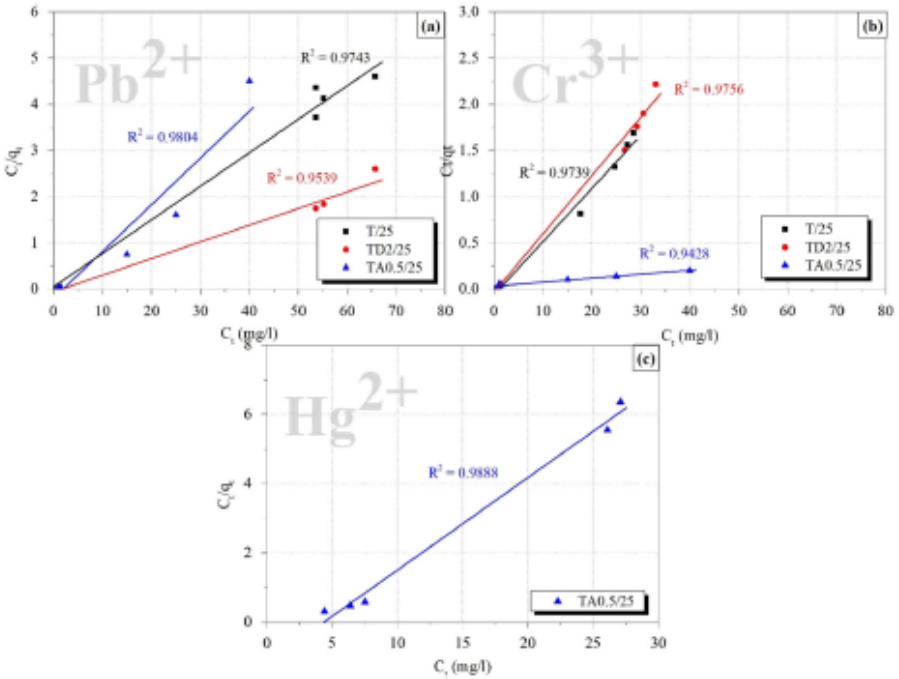

Fig. 9 Langmuir adsorption model of (**a**) Pb^{2+} and (**b**) Cr^{3+} with T/25, TD2/25 and TA0.5/25 samples and Langmuir adsorption model of (**c**) Hg^{2+} with TA0.5/25 samples

TA0.5/25 samples, the value of ΔG significantly increased with the increasing temperature, which implies that lower temperature makes the adsorption easier. On the contrary, a decrease of the ΔG value with an increase in temperature in the case of adsorption of Pb^{2+} ions with the TA0.5/25 sample and Cr^{3+} ions with the TD2/25 sample indicates that the adsorption process is more favorable at higher temperatures. This could be explained by the increased mobility of Pb^{2+} and Cr^{3+} ions in the solution with increasing temperature.

The enthalpy change (ΔH) was negative in cases of adsorption of Hg^{2+} ions with the TA0.5/25 samples, Pb^{2+} ions on T/25, and TD2/25 samples and in cases of binding Cr^{3+} ions on T/25 and TA0.5/25 samples, which implies that the adsorption phenomenon is exothermic [93]. In an exothermic process, the total energy absorbed in bond breaking is lower than the total energy released in the bond making between Pb^{2+}, Cr^{3+} and Hg^{2+} ions and samples' surface, resulting in the release of extra thermal energy. In the case of adsorption Pb^{2+} ions on TA0.5/25 sample and Cr^{3+} ions on TD2/25 sample, a positive ΔH value implies that the adsorption process is endothermic [94]. The adsorption process of the heavy metal ions on the solid surface (solid-liquid system) is a combination of two processes: (a) the desorption of the solvent (water) molecules previously adsorbed, and (b) the adsorption of the heavy metal ions. In an endothermic process, the heavy metal ions have to displace more than one water molecule for their adsorption, resulting in the endothermicity of the adsorption process. The magnitude of ΔH may also give an idea about the type of sorption. The heat that develops during the physical adsorption is of the same extent as the heat formed during the condensation and has the value of 2.1–20.9 kJ mol^{-1}. The heat generated during the chemisorption process is generally in a range of 80–200 kJ mol^{-1} [92]. Therefore, in given conditions, the adsorption of Pb^{2+} and Cr^{3+} ions from salt solutions with T/25, TD2/25 and TA0.5/25 samples and the adsorption of Hg^{2+} ions from salt solutions with TA0.5/25 samples can be attributed to a physicochemical adsorption process (Table 6).

A positive value of ΔS of the T/25, TD2/25 and TA0.5/25 samples reflects the affinity of the functional groups towards the Pb^{2+} and Cr^{3+} ions. In addition, the positive value of ΔS suggests increased randomness at the solid/solution interface with some structural changes in the sample and the Pb^{2+} and Cr^{3+} ions [92]. The value of ΔS was negative in the case of adsorption of Cr^{3+} and Hg^{2+} ions

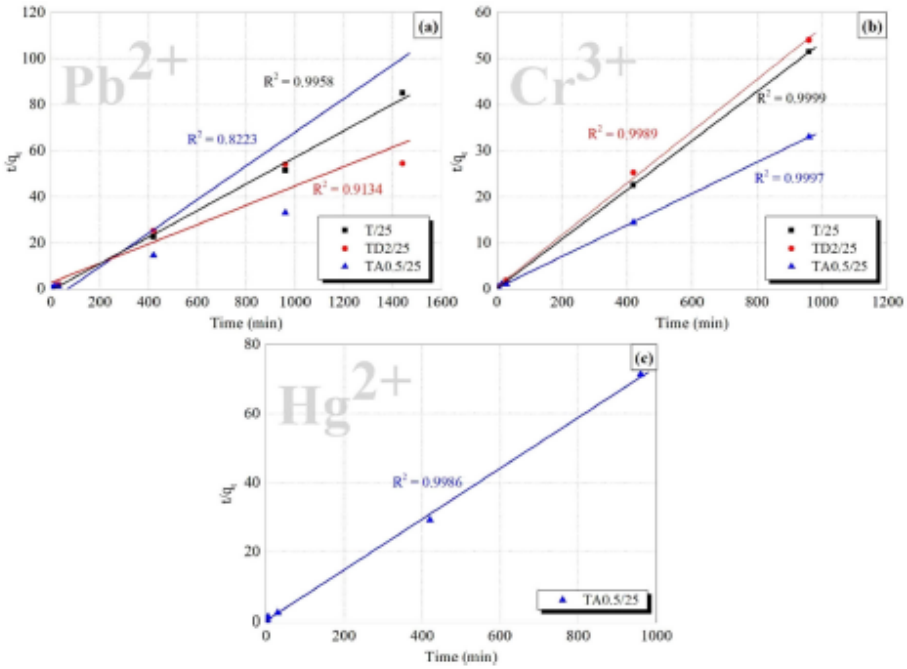

Fig. 10 Kinetic model of the pseudo-second-order for Pb^{2+} (**a**) and Cr^{3+} **b** ions for the T/25, TD2/25 and TA0.5/25 samples and kinetic model of the pseudo-second-order of Hg^{2+} ions (**c**) for TA0.5/25 samples

Table 5 Kinetics parameters of Pb^{2+} and Cr^{3+} ions for T/25, TD2/25 and TA0.5/25 samples and kinetics parameters of Hg^{2+} ions for TA0.5/25 samples

Heavy metal ions	Sample	Pseudo-first order			Pseudo-second order		
		q_e [mg/g]	k_1 [l/min]	R^2	q_e [mg/g]	k_2 [g/[mg·min]]	R^2
Pb^{2+}	T/25	6.96	0.0077	0.8351	20.67	0.0040	0.9986
	TD2/25	2.80	0.0036	0.1191	30.69	0.0132	0.9999
	TA0.5/25	9.29	0.0027	0.1140	54.67	0.0016	0.9993
Cr^{3+}	T/25	9.37	0.0008	0.1309	18.71	0.0281	0.9999
	TD2/25	15.96	0.0007	0.2263	17.74	0.0080	0.9969
	TA0.5/25	9.81	0.0030	0.3663	29.29	0.0059	0.9997
Hg^{2+}	TA0.5/25	1.75	0.0011	0.8744	13.62	0.8755	0.9986

with TD2/25 sample and TA0.5/25 samples, respectively, suggesting that the adsorption process is enthalpy driven. A negative value of entropy change (ΔS) also indicates a reduced disorder at the solid/liquid interface throughout the adsorption process resulting in the escape of Cr^{3+} ions from the solid phase to the liquid phase [50].

3.3 Desorption studies

In order to synthesis an ideal adsorbent material, two key parameters must be evaluated, adsorption and desorption efficiency. Adsorbent materials that show higher adsorption efficiency and possesses better desorption property can considerably reduce the cost of the recycling process. In this study, the desorption of Pb^{2+}, Cr^{3+} and Hg^{2+} ions from $NH_2@SiO_2$ particles (TA0.5/25 sample) was tested using two different acids (0.1 M HCl and 1.5 M $C_6H_8O_7$). It was thought that if metal ions were adsorbed on the adsorbent material by electrostatic interactions, then acid solutions, such as HCl and $C_6H_8O_7$, would regenerate the metal-adsorbed materials due to increased concentration of H^+, giving place to ion exchange with the adsorbed

Table 6 Thermodynamic parameters of Pb^{2+} and Cr^{3+} ions for T/25, TD2/25 and TA0.5/25 samples and thermodynamic parameters of Hg^{2+} ions for TA0.5/25 samples

Heavy metal ions	Sample	T (K)	ΔG (kJ/mol)	ΔH (kJ/mol)	ΔS (kJ/mol)
Pb^{2+}	T/25	298.15	1.98	−3.27	0.019
		323.15	3.72		
		348.15	2.93		
	TD2/25	298.15	1.00	−10.21	0.038
		323.15	2.72		
		348.15	2.93		
	TA0.5/25	298.15	9.74	26.13	0.056
		323.15	7.47		
		348.15	6.94		
Cr^{3+}	T/25	298.15	−0.70	−21.82	0.071
		323.15	0.99		
		348.15	2.84		
	TD2/25	298.15	0.14	6.93	−0.024
		323.15	−1.38		
		348.15	−1.05		
	TA0.5/25	298.15	−11.06	−10.86	0.001
		323.15	−9.86		
		348.15	−11.02		
Hg^{2+}	TA0.5/25	298.15	−1.17	−22.04	−0.070
		323.15	0.58		
		348.15	2.83		

metals. The results showed that 0.1 M HCl and 1.5 M $C_6H_8O_7$ was suitable for very high recovery (91.8% and 59.4%, respectively) of Pb^{2+} from the TA0.5/25 sample. 1.5 M $C_6H_8O_7$ and 0.1 M HCl showed 100% and 16% recovery, respectively, for Hg^{2+} from the TA0.5/25 sample. However, low recovery (>2%) of Cr^{3+} from the TA0.5/25 sample suggested that Cr^{3+} ions form more stable chemical bonds (i.e., coordinated covalent bonds) with a synthesized adsorbent material. The irreversibility of the Cr^{3+} adsorption process onto different adsorption materials using various acid solutions was also reported by Flores-Cano et al. [95], Tytłak et al. [96] and Bernardo et al. [97].

4 Conclusions

In this study, silica (SiO_2) and amino-functionalized SiO_2 particles ($NH_2@SiO_2$) were synthesized according to the Stöber method and used as the adsorbent material for heavy metal ions removal (Pb^{2+}, Cr^{3+} and Hg^{2+}) from aqueous solutions. Adsorbent materials were prepared using precursors tetraethoxysilane (TEOS), 3-(trimethoxysilylpropyl) diethylenetriamine (DETA) and (3-aminopropyl) trimethoxysilane (APTMS) with different molar ratios (P) at room and elevated temperature at various pH values. The formation and functionalization of relatively spherical SiO_2 particles were confirmed by Fourier Infrared (FTIR) Spectroscopy, Thermogravimetric analysis (TGA) and Transmission Electron Microscopy (TEM). The isoelectric point obtained by zeta potential (ζ) measurements were in the pH range > 2.5 for SiO_2 particles, while the functionalized $NH_2@SiO_2$ particles was around pH 7.

The results showed that the adsorption efficiency and adsorption capacity for studied heavy metal ions (Pb^{2+}, Cr^{3+} and Hg^{2+}) removal were the highest when using APTMS precursor to functionalize SiO_2 particles. Furthermore, adsorption capacity using $NH_2@SiO_2$ particles with APTMS precursor was 54.13 mg/g in the case of Pb^{2+}, 29.16 mg/g in the case of Cr^{3+} ions and 14.4 mg/g for Hg^{2+}. The adsorption efficiency was 99.3%, 98.4% and 88% of Pb^{2+}, $Cr^{3+}$and Hg^{2+} ions respectively removed from aqueous solution.

The comparison of correlation coefficients (R_2) of Langmuir and Freundlich isotherms showed that the adsorption of Pb^{2+}, Cr^{3+} and Hg^{2+} with all tested samples best describes the Langmuir adsorption model. Comparison of correlation coefficients for each adsorbent and adsorbate showed that the adsorption process targeted heavy metal ions followed pseudo-second-order kinetics. The results suggested that 0.1 M hydrochloric acid (HCl) was suitable for very high recovery (91.8%) of Pb^{2+} and 1.5 M citric acid ($C_6H_8O_7$) was ideal for 100% recovery of Hg^{2+} from adsorption material. However, further investigation will be focused on the desorption studies of Cr^{3+} from adsorption materials and regeneration of as-prepared particles for reuse purposes. The binding efficiency of other heavy metal ions such as cadmium, zinc, etc., will also be studied.

Acknowledgements The result presented is performed with financial support from the GMOS-Train Program European Union Horizon 2020 research and innovation programme under the Marie Sklodowska-Curie grant agreement no. 860497. The work is co-funded by the project HMRecycle from the Eurostars-2 joint programme. We express our gratitude to the national funding organisation Slovenian Ministry of Education, Science and Sport (www.mizs.gov.si/en) for additional co-financing of this work. The results were created within the Research program Design of new properties of (nano) materials & applications, No. P2-0424 and authors acknowledge the financial support from the Slovenian Research Agency.

Compliance with ethical standards

Conflict of interest The authors declare no competing interests.

Publisher's note Springer Nature remains neutral with regard to jurisdictional claims in published maps and institutional affiliations.

References

1. European Community (2000) Directive 2000/60/EC of the European Parliament and of the Council of 23 October 2000 establishing a framework for Community action in the field of water policy. Official Journal of the European Parliament vol. L327, no. September 1996. pp. 1–82. https://doi.org/10.1039/ap9842100196
2. Gupta A, Singh MR (2017) Water Pollution-Sources,Effects and Control [Online]. Available: https://www.researchgate.net/publication/321289637
3. Enderlein U, Enderlein RE, Williams W (1997) Water Quality Requirements, Water Pollution Control - A Guide to the Use of Water Quality Management Principles. p. 29. https://doi.org/10.4324/9780203477540
4. Verma R, Dwivedi P (2013) Heavy metal water pollution- A case study, Recent Res. Sci. TechnoL, vol. 5, no. 5, pp. 98–99, [Online]. Available: http://recent-science.com/
5. Gorito AM, Ribeiro AR, Almeida CMR, Silva AMT (2017) A review on the application of constructed wetlands for the removal of priority substances and contaminants of emerging concern listed in recently launched EU legislation. Environ Pollut 227:428–443. https://doi.org/10.1016/j.envpol.2017.04.060
6. Escribano Francés G, Quevauviller P, San Martín González E, Vargas Amelin E (2017) Climate change policy and water resources in the EU and Spain. A closer look into the Water Framework Directive. Environ Sci Policy 69:1–12. https://doi.org/10.1016/j.envsci.2016.12.006
7. The European Parlament and the Council of the European Union, (2013) Directives of 12 August 2013 amending Directives 2000/60/EC and 2008/105/EC as regards priority substances in the field of water policy. Official Journal of the European Union. pp. 1–17, 2013, eur-lex.europa.eu/legal-content/EN/TXT/?uri=celex:32013L0039
8. Kos Durjava M, Kolar B, Balk F, Peijnenburg W (2013) Water framework directive and specific pollutants in surface waters in Slovenia. Acta Hydrotechnica 45:61–69
9. Ministry of the Environment and Spatial Planning, "Rules on drinking water," Slovenia, 2017. [Online]. Available: http://www.pisrs.si/Pis.web/pregledPredpisa?id=PRAV3713
10. Ministry of the Environment and Spatial Planning (2017) Decree on the discharge and treatment of urban wastewater. Slovenia. pp. 1–34
11. Official Journal of the European Union (2013) (Legislative acts) Directives, 2013/39/EU OF THE European Parliament and Of the Council of 12 August 2013 amending Directives 2000/60/EC and 2008/105/EC as regards priority substances in the field of water policy. https://eur-lex.europa.eu/LexUriServ/LexUriServ.do?uri=OJ:L:2013:226:0001:0017:EN:PDF
12. Arunakumara KKIU, Zhang X (2007) Heavy metal bioaccumulation and toxicity with special reference to microalgae J Ocean Univ China 7(no. 1):60–64. https://doi.org/10.1007/s11802-008-0060-y
13. Diaz S, MartinGonzalez A, Gutierrez JC (2006) Evaluation of heavy metal acute toxicity and bioaccumulation in soil ciliated protozoa. Environ Int 32(no. 6):711–717. https://doi.org/10.1016/j.envint.2006.03.004
14. Mohamed K, Morad L, Al-blewi Fawzia F, Nadjet R, Reda AM, Messali M, Rachid T (2016) Liquid-liquid extraction of metal ions, DFT and TD-DFT analysis of some 1,2,4-triazole Schiff Bases with high selectivity for Pb(II) and Fe(II). J Mol Struct 1113:99–107. https://doi.org/10.1016/j.molstruc.2016.02.046
15. de Luna MDG, Bellotindos LM, Asiao RN, Lu MC (2015) Removal and recovery of lead in a fluidized-bed reactor by crystallization process. Hydrometallurgy 155:6–12. https://doi.org/10.1016/j.hydromet.2015.03.009
16. Bolto BA, Pawĉpwski L (1987) Waste Water Treatment by Ion Exchange. New York: Chapman and Hall
17. Bauman M, Košak A, Lobnik A, Petrinić I, Luxbacher T (2013) Nanofiltration membranes modified with alkoxysilanes: Surface characterization using zeta-potential. Colloids Surfaces A Physicochem Eng Asp 422:110–117. https://doi.org/10.1016/j.colsurfa.2013.01.005
18. Da'na E (2017) Adsorption of heavy metals on functionalized-mesoporous silica: A review. Microporous Mesoporous Mater. 247:145–157. https://doi.org/10.1016/j.micromeso.2017.03.050
19. Qu X, Alvarez PJJ, Li Q (2013) Applications of nanotechnology in water and wastewater treatment. Water Res. 47(no. 12):3931–3946. https://doi.org/10.1016/j.watres.2012.09.058
20. Mende M, Schwarz D, Steinbach C, Boldt R, Schwarz S (2016) Simultaneous adsorption of heavy metal ions and anions from aqueous solutions on chitosan—Investigated by spectrophotometry and SEM-EDX analysis Colloids Surfaces A Physicochem. Eng Asp 510:275–282. https://doi.org/10.1016/j.colsurfa.2016.08.033
21. Salem Attia TM, Hu XL, Yin DQ (2013) Synthesized magnetic nanoparticles coated zeolite for the adsorption of pharmaceutical compounds from aqueous solution using batch and column studies. Chemosphere 93(no. 9):2076–2085. https://doi.org/10.1016/j.chemosphere.2013.07.046
22. Burakova AE, Galunina EV, Burakovaa IV, Kucherovaa AE, Agarwalb S, Tkacheva AG, Gupta VK (2018) Adsorption of heavy metals on conventional and nanostructured materials for wastewater treatment purposes: A review. Ecotoxicol Environ Saf 148:702–712. https://doi.org/10.1016/j.ecoenv.2017.11.034
23. Smith L, Ibn-Mohammed T, Koh SCL, Reaney IM (2018) Life cycle assessment and environmental profile evaluations of high volumetric efficiency capacitors. Appl Energy 220:496–513. https://doi.org/10.1016/j.apenergy.2018.03.067
24. Yong WYD, Zhang Z, Cristobal G, Chin WS (2014) One-pot synthesis of surface functionalized spherical silica particles. Iloids Surfaces A Physicochem Eng Asp 460:151–157. https://doi.org/10.1016/j.colsurfa.2014.03.039
25. Viltužnik B, Lobnik A, Košak A (2015) The removal of Hg(II) ions from aqueous solutions by using thiol-functionalized cobalt ferrite magnetic nanoparticles. J Sol-Gel Sci Technol, 74(1):199–207. https://doi.org/10.1007/s10971-014-3596-x
26. Amin MT, Alazba AA, Manzoor U (2014) A review of removal of pollutants from water/wastewater using different types of nanomaterials. vol. 2014. https://doi.org/10.1155/2014/825910
27. Bogush GH, Tracy MA, Zukoski CF (1988) Preparation of monodisperse silica particles: Control of size and mass fraction. J Non Cryst Solids 104(no. 1):95–106. https://doi.org/10.1016/0022-3093(88)90187-1
28. Singh LP, Bhattacharyya SK, Ahalawat S, Kumar R, Mishra G, Sharma U, Sing G (2014) Sol-Gel processing of silica nanoparticles and their applications. Adv. Colloid Interface Sci. 214:17–37. https://doi.org/10.1016/j.cis.2014.10.007
29. Kango S, Kalia S, Celli A, Njuguna J, Habibi Y, Kumar R (2013) Surface modification of inorganic nanoparticles for development of organic-inorganic nanocomposites - A review. Prog. Polym. Sci. 38(no. 8):1232–1261. https://doi.org/10.1016/j.progpolymsci.2013.02.003
30. Milea CA, Bogatu C (2011) The influence of parameters in silica sol-gel process. Bull Transilv Univ Brasov Eng Sci 4(no. 1):59–66
31. Liu S, Han MY (2010) Silica-coated metal nanoparticles. Chem - An Asian J 5(no. 1):36–45. https://doi.org/10.1002/asia.200900228
32. Vansant EF, Van Der Voort P, Vrancken KC (1995) Characterization and chemical modification of the silica surface. Vol. 93 Elsevier, Amsterdam. ISBN 0444819282

33. Brinker C, Scherer GW (1990) Sol-gel science: the physics and chemistry of sol-gel processing. 1st Edition. Academic Press. London. ISBN 9780080571034
34. Branda F (2011) The sol-gel route to nanocomposites. Adv Nanocomposites- Synth Characterisation Ind. Appl. 14:323–340. https://doi.org/10.5772/15454
35. Košak A, Lobnik A, Bauman M (2015) Adsorption of mercury(II), lead(II), cadmium(II) and zinc(II) from aqueous solutions using mercapto-modified silica particles. Int J Appl Ceram Technol 12(no. 2):461–472. https://doi.org/10.1111/ijac.12180
36. Witucki GL (1993) A silane primer: chemistry and applications of alkoxy silanes. J. Coatings Technol. 65(no. 822):57–60. https://doi.org/10.1124/dmd.109.028449
37. Bauman M, Košak A, Lobnik A, Petrinić I, Luxbacher T (2013) Nanofiltration membranes modified with alkoxysilanes: Surface characterization using zeta-potential. Colloids and Surfaces A: Physicochemical and Engineering Aspects, 422:110–117. https://doi.org/10.1016/j.colsurfa.2013.01.005
38. Li X, Shi B, Wang Y, Li M, Liu Y, Gao LI, Mao L (2015) Preparation of monodispersed mesoporous silica particles and their applications in adsorption of Au^{3+} and Hg^{2+} after mercapto-functionalized treatment. Microporous Mesoporous Mater 214:15–22. https://doi.org/10.1016/j.micromeso.2015.04.033
39. Heidari A, Younesi H, Mehraban Z (2009) Removal of Ni(II), Cd(II), and Pb(II) from a ternary aqueous solution by amino functionalized mesoporous and nano mesoporous silica. Chem Eng J 153(no. 1–3):70–79. https://doi.org/10.1016/j.cej.2009.06.016
40. Pandey S, Singh N, Shukla S, Tiwari M (2017) Removal of Lead and Copper from Textile Wastewater Using Egg Shells. Iranian (Iranica) J Energy Environ 8(3):202–209. https://doi.org/10.5829/ijee.2017.08.03.04
41. Gautam K, Markandeya Singh NB, Shukla SP, Mohan D (2020) Lead removal efficiency of various natural adsorbents (Moringa oleifera, Prosopis juliflora, peanut shell) from textile wastewater. Springer Nature Switzerland AG 2:288. https://doi.org/10.1007/s42452-020-2065-0
42. Ilyas M, Ahmad A, Saeed M (2013) Removal of Cr (VI) from aqueous solutions using peanut shell as adsorbent. J. Chem. Soc. Pak. 35(3):760–768
43. Zhu Y, Zhang H, Zeng H, Liang M, Lu R (2012) Adsorption of chromium (VI) from aqueous solution by the iron (III)-impregnated sorbent prepared from sugarcane bagasse. Int J Environ Sci Technol 9:463–472. https://doi.org/10.1007/s13762-012-0043-9
44. Su M, Fang Y, Li B, Yin W, Gu J, Liang H, Li P, Wu J (2019) Enhanced hexavalent chromium removal by activated carbon modified with micro-sized goethite using a facile impregnation method. Sci. Environ. 647:47–56. https://doi.org/10.1016/j.scitotenv.2018.07.372
45. Kushwaha S, Sodaye S, Padmaja P (2008) Equilibrium, kinetics and termodynamic studies for adsorption of Hg (II) on palm shell powder. World Acad Sci Eng Technol 19:597–603
46. Solis KL, Nam Go-Un, Hong Y (2016) Effectiveness of gold nanoparticle-coated 199silica in the removal of inorganic mercury in aqueous systems: equilibrium and kinetic studies. Environ Eng Res 21(no. 1):99–107. Crossref. https://doi.org/10.4491/eer.2015.126. †Korean Society of Environmental Engineering,
47. Faulconer EK, von Reitzenstein NVH, Mazyck DW (2012) Optimization of magnetic powdered activated carbon for aqueous Hg (II) removal and magnetic recovery. J. Hazard. Mater. 199–200:9–14
48. Yusmaniar A, Purwanto EA, Putri, Rosyidah D (2017) Adsorption of Pb(II) using silica gel composite from rice husk ash modified 3-aminopropyltriethoxysilane (APTES)-activated carbon from coconut shell. AIP Conf. Proc. 1823:no. Ii. https://doi.org/10.1063/1.4978107
49. Sertsing S, Chukeaw T, Pengpanich S, Pornchuti B (2018) Adsorption of Nickel and Chromium Ions by Amine-Functionalized Silica Aerogel. MATEC Web Conf. 156:4–7. https://doi.org/10.1051/matecconf/201815603014
50. Soltani RDC, Khorramabadi GS, Khataee AR, Jorfi S (2014) Silica nanopowders/alginate composite for adsorption of lead (II) ions in aqueous solutions. J Taiwan Inst Chem Eng 45(no. 3):973–980. https://doi.org/10.1016/j.jtice.2013.09.014
51. Zhao J, Niu Y, Ren B, Chen H, Zhang S, Jin J, Zhang Y (2018) Synthesis of Schiff base functionalized superparamagnetic Fe3O4composites for effective removal of Pb(II) and Cd(II) from aqueous solution Chem Eng J 347:574–584. https://doi.org/10.1016/j.cej.2018.04.151. no. March
52. Lai X, Sun D, Hou Y, Zuo Y, Li Y, Zhang L (2018) Amino-Functionalized Multilayer Core–Shell Mesoporous Organosilica Nanospheres for Cr(VI) Removal. Adv. Mater. Interfaces, vol. 5, no. 18. https://doi.org/10.1002/admi.201800630
53. Bogush GH, Et-zukoski CF (1991) Studies of the kinetics of the precipitation of uniform silica particles through the hydrolysis and condensation of silicon alkoxides. J Colloid Interface Sci. 142:1
54. La Mer VK (1952) Nucleation in phase transitions. Ind Eng Chem 44:1270–1277. https://doi.org/10.1021/ie50510a027
55. Look JL, Bogush GH, Zukoski CF (1990) Colloidal interactions during the precipitation of uniform submicrometre particles. Faraday Discuss. Chem. Soc. 40:345
56. Tabatabaei S, Shukohfar A, Aghababazadeh R, Mirhabibi A (2006) Experimental study of the synthesis and characterisation of silica nanoparticles via the sol-gel method. J Phys Conference Series 26 (no. 1):371–374. https://doi.org/10.1088/1742-6596/26/1/090
57. Huang H, Wang Y, Zhang Y, Niu Z, Li X (2020) Amino-functionalized graphene oxide for Cr(VI), Cu(II), Pb(II) and Cd (II) removal from industrial wastewater. Open Chem. 18(no. 1):97–107. https://doi.org/10.1515/chem-2020-0009
58. Dąbrowski A (2001) Adsorption — from theory to practice. Adv Colloid Interface Sci. 93(no. 1):135–224. https://doi.org/10.1016/S0001-8686(00)00082-8
59. Dabbaghian MA, Babalou AA, Hadi P, Jannatdoust E (2010) A Parametric Study of the Synthesis of Silica Nanoparticles via Sol-Gel Precipitation Method. International Journal of Nanoscience and Nanotechnology 6(no. 2):104–113
60. Hadela A (2020) Novel reusable functionalized magnetic cobalt ferrite nanoparticles as oil adsorbent. Adsor Sci Technol 0 (0):1–23. https://doi.org/10.1177/0263617420922014
61. Drew Myers, (1999) "Surfaces, Interfaces, and Colloids: Principles and Applications", Second Edition. John Wiley & Sons, Inc., ISBNs: 0-471-33060-4
62. Michael W, McKittrick (2003) Toward single-site functional materials preparation of amine-functionalized surfaces exhibiting site-isolated behavior. Chem Mater 15:1132–1139
63. Manyangadze M, Chikuruwo NMH, Narsaiah TB, Chakra CS, Charis G, Danha G, Mamvura TA (2020) Adsorption of lead ions from wastewater using nano silica spheres synthesized on calcium carbonate templates Heliyon 6(no. 11):e05309. https://doi.org/10.1016/j.heliyon.2020.e05309
64. Rekondo A, Irusta L, Fernández-Berridi M (2010) Characterization of silanized poly(ether-urethane) hybrid systems using thermogravimetric analysis (TG). J Therm Anal Calorim 101:331–337. https://doi.org/10.1007/s10973-010-0674-3
65. Kulkarni SA, Ogale SB, Vijayamohanan KP (2008) Tuning the hydrophobic properties of silica particles by surface silanization using mixed self-assembled monolayers. Colloid Interface Sci 318:372
66. Chan CCP, Choudhury NR, Majewski P (2011) Fabrication and characterisation of self-assembled monolayers of N-[3-(trimethoxysilyl)propyl]diethylenetriamine on silica particles. Colloids Surf: Physicochem Eng Aspects 377:20–27

67. Pérez-Quintanilla D, del Hierro I, Fajardo M, Sierra I (2006) Mesoporous silica functionalized with 2-mercaptopyridine: synthesis, characterization and employment for Hg (II) adsorption. Microporous Mesoporous Mater 89:58–68. https://doi.org/10.1016/j.micromeso.2005.10.012
68. Pérez-Quintanilla D, del Hierro I, Fajardo M, Sierra I (2006) 2-Mercaptothiazoline modified mesoporous silica for mercury removal from aqueous media. J Hazard Mater 134(30. P.):245–256. https://doi.org/10.1016/j.jhazmat.2005.11.004
69. Pérez-Quintanilla D, del Hierro I, Fajardo M, Sierra I (2006) Preparation of 2-mercaptobenzothiazole-derivatized mesoporous silica and removal of Hg (II) from aqueous solution. J Environ Monit 8:214–222. https://doi.org/10.1039/B507983G
70. Liang R, Zou H (2020) Removal of aqueous Hg (II) by thiol-functionalized nonporous silica microspheres prepared by one-step sol–gel method. RSC Adv 10(31):18534–18542. https://doi.org/10.1039/d0ra02759f
71. IUPAC (1982) Reporting physisorption data for gas/solid systems. Pure Appl Chem 54(no. 11):1–18. https://doi.org/10.1351/pac198557040603
72. ZemljičL F, Čakara D, Michaelis N, Heinze T, Kleinschek KS (2011) Protonation behavior of 6-deoxy-6-(2-aminoethyl)amino cellulose: a potentiometric titration study. Cellulose 18(no. 1):33–43. https://doi.org/10.1007/s10570-010-9467-x
73. Erdem E, Karapinar N, Donat R (2004) The removal of heavy metal cations by natural zeolites. J. Colloid Interface Sci. 280 (2):309–314. https://doi.org/10.1016/j.jcis.2004.08.028.15533402
74. Jiang Y, Pang H, Liao B (2009) Removal of copper (II) ions from aqueous solution by modified bagasse. J Hazard Mater 164 (1):1–9. https://doi.org/10.1016/j.jhazmat.2008.07.107.18790566
75. Sing KSW (1985) Reporting physisorption data for gas/solid systems with special reference to the determination of surface area and porosity (Recommendations 1984). Pure Appl. Chem 57:603–619
76. Yong Jae Suh (2015) Role of chemical hardness in the adsorption of hexavalent chromium species onto metal oxide nanoparticles. Chem Eng J 273:401–405
77. Parr RG, Pearson RG (1983) Absolute hardness: companion parameter to absolute electronegativity. J. Am. Chem. Soc. 105:7512
78. Yokoi T, Yoshitake H, Tatsumi T (2004) Synthesis of amino-functionalized MCM-41 via direct co-condensation and post-synthesis grafting methods using mono-, di- and tri-amino-organoalkoxysilanes. J Mater Chem 14:951–957
79. Manu V, Haresh MM, Bajaj HC, Jasra RV (2009) Adsorption of Cu^{2+} on amino functionalized silica gel with different loading. Ind Eng Chem Res 48:8954–8960
80. Lee J, Kim JH, Choi K, Kim HG, Park JA, Cho SH, Hong SW, Lee JH, Lee JH, Lee S, Lee SY, Choi JW (2018) Investigation of the mechanism of chromium removal in (3-aminopropyl)trimethoxysilane functionalized mesoporous silica. Sci Rep 8:12078. https://doi.org/10.1038/s41598-018-29679-x
81. Gascón V, Arencibia A, Arsuaga JM (2019) Aqueous heavy metals removal by removal on amine-functionalized mesoporous silica". Desalination Water Treatment 146:210–226
82. Zhang L, Yu C, Zhao W, Hua Z, Chen H, Li L, Shi J (2007) Preparation of multi-amine-grafted mesoporous silicas and their application to heavy metal ions adsorption. J Non-Cryst Solids 353:4055–4061
83. Dindar MH, Yaftian MR, Rostamnia S (2015) Potential of functionalized SBA-15 mesoporous materials for decontamination of water solutions from Cr(VI), As(V) and Hg(II) ions. J Environ Chem Eng 3:986–995
84. Foo KY, Hameed BH (2010) Insights into the modeling of adsorption isotherm systems. Chem Eng J 156(no. 1):2–10. https://doi.org/10.1016/j.cej.2009.09.013
85. Langmuir Freundlich Temkin AOD, Dubinin–Radushkevich (2012) Isotherms Studies of Equilibrium Sorption of Zn 2+ Unto Phosphoric Acid Modified Rice Husk. IOSR J Appl Chem 3(no. 1):38–45. https://doi.org/10.9790/5736-0313845
86. Gogoi S, Chakraborty S, Saikia MD (2018) Surface modified pineapple crown leaf for adsorption of Cr(VI) and Cr(III) ions from aqueous solution. J Environ Chem Eng 6(no. 2):2492–2501. https://doi.org/10.1016/j.jece.2018.03.040
87. Kothalawala N, Blitz JP, Gun'ko VM, Jaroniec M, Grahicka B, Semeniuc RF (2013) Post-synthesis surface-modified silicas as adsorbents for heavy metal ion contaminants Cd(II), Cu(II), Cr (III), and Sr(II) in aqueous solutions. J Colloid Interface Sci 392 (no. 1):57–64. https://doi.org/10.1016/j.jcis.2012.10.037
88. Zhuravlev LT (2000) The surface chemistry of amorphous silica. Zhuravlev model. Colloids Surf A Physicochem Eng Aspects 173 (no. 1–3):1–38. https://doi.org/10.1016/S0927-7757(00)00556-2
89. Lue L (2009) Chemical thermodynamics. Ventus Publishing Aps. ISBN 978-87-7681-497-7
90. Saha P, Chowdhury S (2011) Insight into adsorption thermodynamics. Thermodynamics https://doi.org/10.5772/13474
91. Ali Khan AS (2012) Evaluation of thermodynamic parameters of cadmium adsorption on sand from Temkin adsorption isotherm. Turkish J. Chem. 36(no. 3):437–443. https://doi.org/10.3906/kim-1108-34
92. Idris SAM (2015) Adsorption, kinetic and thermodynamic studies for manganese extraction from aqueous medium using mesoporous silica. Journal of Colloid and Interface Science 440:84–90. https://doi.org/10.1016/j.jcis.2014.10.022
93. Kushwaha AK, Gupta N, Chattopadhyaya MC (2017) Adsorption behavior of lead onto a new class of functionalized silica gel. Arabian Journal of Chemistry 10:S81–S89. https://doi.org/10.1016/j.arabjc.2012.06.010
94. Hayati B, Maleki A, Najafi F, Daraei H, Gharibi F, McKay G (2017) Adsorption of Pb^{2+}, Ni^{2+}, Cu^{2+}, Co^{2+} metal ions from aqueous solution by PPI/SiO2 as new high performance adsorbent: Preparation, characterization, isotherm, kinetic, thermodynamic studies
95. Flores-Cano JV, Leyva-Ramos R, Carrasco-Marín F, Aragón-Piña A, Salazar-Rabago JJ, Leyva-Ramos S (2016) Adsorption mechanism of Chromium(III) from water solution on bone char: effect of operating conditions. Adsorption 22(no. 3):297–308. https://doi.org/10.1007/s10450-016-9771-3
96. Tytłak A, Oleszczuk P, Dobrowolski R (2015) Sorption and desorption of Cr(VI) ions from water by biochars in different environmental conditions. Environ. Sci. Pollut. Res. 22(no. 8):5985–5994. https://doi.org/10.1007/s11356-014-3752-4
97. Bernardo Garcia-ReyesRefugio, Rene Rangel-MendezJose, Catalina Alfaro-DelaTorreMa (2009) Chromium (III) uptake by agro-waste biosorbents: Chemical characterization, sorption-desorption studies, and mechanism. J Hazard Mater 170(no. 2–3):845–854. https://doi.org/10.1016/j.jhazmat.2009.05.046

3.2 Publications 2

Summary of Publication 2: As global concerns over water pollution intensify, the demand for innovative, sustainable technologies to remediate toxic toxic metals (HMs) from aquatic environments has become more pressing than ever. Lead (Pb^{2+}), trivalent chromium (CrT), and mercury (Hg^{2+}) are among the most hazardous toxic metal pollutants due to their bioaccumulation potential, long-term environmental persistence, and severe health impacts. This article addresses this challenge through a circular economy approach, focusing on the use of amino-functionalized magnetic nanoparticles (γ-Fe_2O_3@NH_2 NPs) for the efficient removal of Pb^{2+}, CrT, and Hg^{2+} from aqueous solutions. By integrating functional surface chemistry with magnetic separation capabilities, the study contributes to the development of sustainable nanomaterials for water treatment applications.

At the core of this work is the design and synthesis of superparamagnetic iron oxide nanoparticles, chemically stabilized and functionalized with amino groups. These surface modifications enhance the adsorption performance by introducing active sites for metal ion binding while maintaining magnetic responsiveness for facile recovery. The nanoparticles are synthesized via a controlled co-precipitation process, yielding stable nanomaterials with tunable surface chemistry optimized for environmental remediation.

To evaluate their performance, the study conducts a comprehensive set of batch adsorption experiments under two pH conditions (pH 4 and 7), simulating acidic and neutral aqueous environments. The nanoparticles show markedly enhanced adsorption capacities at pH 7, attributable to the deprotonation of surface amino groups that favor electrostatic interactions with metal cations. Among the three metal ions tested, CrT exhibits the highest adsorption efficiency, followed by Hg^{2+} and Pb^{2+}, suggesting a strong affinity of the functionalized surface toward chromium species. This ion-specific performance underscores the importance of surface chemistry tuning in adsorption-based separation technologies.

The study employs a suite of physicochemical characterization techniques—Fourier-transform infrared spectroscopy (FTIR), zeta potential analysis, and atomic absorption spectroscopy (AAS)—to investigate surface functionality, nanoparticle charge behavior, and adsorption capacity. The findings confirm the successful functionalization of the γ-Fe_2O_3 surface with amino groups and highlight the role of nanoparticle charge in mediating adsorption under different pH conditions. The materials maintain good dispersion in water and exhibit sufficient stability, which are critical traits for real-world implementation.

A notable strength of this research lies in its focus on reusability and environmental compatibility. Post-adsorption, the magnetic nanoparticles are easily recovered from solution using external magnets, washed, and reused for multiple cycles. The regeneration studies reveal minimal loss in adsorption efficiency over repeated uses, highlighting the recyclability and cost-effectiveness of the material. Moreover, the use of a green synthesis method and mild processing conditions aligns the work with sustainable chemistry principles.

From an application standpoint, the dual functionality of these nanomaterials—in removing highly toxic metals and allowing magnetic separation—offers significant promise for decentralized water treatment systems and industrial effluent management. The low toxicity of the nanoparticles and their potential for regeneration bolster their candidacy for integration into circular water purification frameworks. Importantly, the study demonstrates that smart surface engineering combined with magnetic properties can lead to selective and effective metal ion removal technologies.

International Journal of *Molecular Sciences*

MDPI

Article

Removal of Pb^{2+}, CrT, and Hg^{2+} Ions from Aqueous Solutions Using Amino-Functionalized Magnetic Nanoparticles

A. F. P. Allwin Mabes Raj [1,2,3], Maja Bauman [1], Marijana Lakić [1], Nena Dimitrušev [1], Aleksandra Lobnik [1,4] and Aljoša Košak [1,4,*]

1 IOS, Institute of Environmental Protection and Sensors, Ltd., Beloruska 7, SI-2000 Maribor, Slovenia
2 Jožef Stefan International Postgraduate School, Jamova 39, 1000 Ljubljana, Slovenia
3 Department of Environmental Science, Jožef Stefan Institute, Jamova 39, 1000 Ljubljana, Slovenia
4 Faculty of Mechanical Engineering, Centre of Sensor Technology, University of Maribor, Smetanova 17, 2000 Maribor, Slovenia
* Correspondence: aljosa.kosak@um.si; Tel.: +386-5142-7567

Abstract: In this paper, a circular economy approach with the adsorption and desorption of heavy metal (HM) ions—i.e., lead (Pb^{2+}), chromium (CrT), and mercury (Hg^{2+})—from aqueous solutions was studied. Specific and selective binding of HM ions was performed on stabilized and amino-functionalized iron oxide magnetic nanoparticles (γ-Fe_2O_3@NH_2 NPs) from an aqueous solution at pH 4 and 7. For this purpose, γ-Fe_2O_3@NH_2 NPs were characterized by thermogravimetric analysis (TGA), Fourier-transform infrared spectroscopy (FTIR), specific surface area (BET), transmission electron microscopy (TEM), EDXS, and zeta potential measurements (ζ). The effects of different adsorbent amounts (m_{ads} = 20/45/90 mg) and the type of anions (NO_3^-, Cl^-, SO_4^{2-}) on adsorption efficiency were also tested. The desorption was performed with 0.1 M HNO_3. The results showed improvement of adsorption efficiency for CrT, Pb^{2+}, and Hg^{2+} ions at pH 7 by 45 mg of g-Fe_2O_3@NH_2 NPs, and the sequence was as follows: CrT > Hg^{2+} > Pb^{2+}, with adsorption capacities of 90.4 mg/g, 85.6 mg/g, and 83.6 mg/g, respectively. The desorption results showed the possibility for the reuse of γ-Fe_2O_3@NH_2 NPs with HNO_3, as the desorption efficiency was 100% for Hg^{2+} ions, 96.7% for CrT, and 91.3% for Pb^{2+}.

Keywords: superparamagnetic nanoparticles; iron-oxide; maghemite; functionalization; aminopropyltrimethoxysilane; adsorption; desorption; lead; chromium; mercury; circular economy

check for updates

Citation: Allwin Mabes Raj, A.F.P.; Bauman, M.; Lakić, M.; Dimitrušev, N.; Lobnik, A.; Košak, A. Removal of Pb^{2+}, CrT, and Hg^{2+} Ions from Aqueous Solutions Using Amino-Functionalized Magnetic Nanoparticles. *Int. J. Mol. Sci.* **2022**, *23*, 16186. https://doi.org/10.3390/ijms232416186

Academic Editor: Andreas Taubert

Received: 17 October 2022
Accepted: 30 November 2022
Published: 19 December 2022

Publisher's Note: MDPI stays neutral with regard to jurisdictional claims in published maps and institutional affiliations.

1. Introduction

Today, Europe is facing limited stocks of raw materials (RMs), such as heavy metal ions (HM ions) and rare-earth elements (REEs) [1–4], Even more obviously, in the context of the COVID-19 pandemic, Europe's economy is facing an even larger lack of RMs and HM ions. Moreover, the European Union (EU)'s industry is dependent on imports of large amounts of RMs from the Asian market [1–3]. Therefore, the EU Commission was forced to prepare a list of critical raw materials (CRMs) [2,3,5,6], with sustainable strategies to foresee a circular economy based on recycling and reuse of critical REEs [2].

Lead (Pb^{2+}), chromium (total chromium (CrT)), and mercury (Hg^{2+}) ions are listed among the top 20 most hazardous substances [7,8] (accessed on 30 August 2022), since large amounts of HM ions are released into the environment due to agriculture and specific industries, such as the automotive, textile, mining, dye, and electroplating industries, among others [5,9–11]. HM ions dissolved in water are already toxic in small quantities and non-biodegradable, and some are carcinogenic and bioaccumulative, so they need to be treated as priority pollutants and efficiently cleaned [10–12].

Among these HMs, mercury has taken the spotlight because it is a global pollutant [13–16]. Mercury exists in various forms in the natural environment, such as mercurous (Hg_2^{+2}), and mercuric (Hg^{2+}), along with organic mercury-containing methyl and

ethyl groups. It is pertinent that the highly notorious form of methylmercury is caused by the methylation of inorganic [15] and elemental mercury [17] that is present in the aquatic environment by sulfate-reducing bacteria such as *Desulfovibrio desulfuricans*. Methylmercury can bioaccumulate and biomagnify in the oceanic food chain to reach 10^6 times the concentrations that have caused several tragedies in the past, such as the Minamata tragedy in Japan [15] Negative toxic effects of versatile and highly mobile stable forms of chromium (Cr^{3+} and Cr^{6+}) are a constant threat to humans and the environment. Depending on the pH, they can be present in acidic media (pH 0–4) in the form of soluble complexes (Cr^{3+}, $[Cr(H_2O)_6^{3+}]$), while near neutral (pH 6–9) inert precipitates ($Cr(OH_3)$ (s)) can easily be adsorbed on solid media [18].

HM ions are present in different concentrations (trace and shock concentrations) and forms [19,20], in combined industrial and municipal wastewater streams. Disposal of treated wastewater into the environment necessitates adjusting its pH to neutral. Especially for recycling of HM ions and water reuse [19,21], this means raising costs and increases the complexity of the pretreatment process, as well as increasing the addition of excessive amounts of chemicals [19,21].

Therefore, it is necessary to act sustainably and environmentally consciously by removing HMs from the highly polluted wastewaters using technology/methods that allow the removal/recycling of HM ions [4].

Currently, different conventional methods are used to remove HM ions from water/industrial wastewater [5,11], such as precipitation [22], electrochemical removal [23], ion exchange [24], membrane filtration [25,26], coagulation [27], flocculation [28], and sorption on natural materials [29]. Although these methods are efficient in removing HM ions, they do not allow the recycling and reuse of HM ions. Some already well-established methods for the removal of HM ions produce toxic coproducts and large amounts of waste sludge [30], e.g., membrane filtration and coagulation/flocculation [31]. Moreover, these methods are often costly and energy-inefficient [30].

On the other hand, the adsorption method is well known, efficient, and used for the removal of HM ions due to its low adsorbent and operational costs and simple principle [5,11,12]. Adsorption can be performed with various natural materials [29] and other hybrid materials based on silica and iron oxide NPs (γ-Fe_2O_3, Fe_3O_4), as well as their functionalized forms [32–36]. The most commonly used adsorbent of HM ions from industrial and leachate wastewaters is activated carbon [31]. Activated carbon is efficient in the removal of HM ions from wastewaters, due to its high specific surface area, micropore volume, and pore volume [31,33,37–41]. At the same time, limitations of its use include non-selectivity and high material price. Furthermore, activated carbon does not enable the recycling and regeneration of HM ions and the adsorbent itself, and for now it does not enable the circular economy approach [31,33].

Due to the increased need for recycling of municipal and industrial wastewaters [42] research in nanotechnology is investing in the preparation and testing of functionalized (nano)materials that can improve the recycling of specific HM ions [34,36,43,44].

Maghemite (γ-Fe_2O_3) is a member of the family of iron oxides. It has a cubic spinel ferrite structure, and it is ferrimagnetic. When reduced to particle dimensions smaller than a certain domain—i.e., becoming a single domain—ferrimagnetic materials exhibit superparamagnetic behavior, which means that when an external magnetic field is applied, they magnetize, but when the magnetic field is removed, they no longer exhibit either residual magnetism or coercivity.

Such superparamagnetic nanoparticles, if they are surface-functionalized, provide promising applications in the adsorption of heavy metals from aqueous media, as they enable more efficient separation and recovery of heavy metals from the contaminated aqueous medium using an external magnetic field [45]. On the other hand, surface modification of superparamagnetic γ-Fe_2O_3 nanoparticles with TEOS and APTMS precursors improves their stability, prevents them from agglomerating, and increases their surface functionality by increasing the number of adsorption sites (-NH_2), facilitating and accelerating diffusion

pathways for heavy metal pollutants [46,47]. Despite all of the advantages of superparamagnetic γ-Fe_2O_3 nanocomposites for use in environmental technologies, the policy debate on their safety should not be ignored. Their toxicity is still an open question, even though much research has recently been carried out on this topic [48,49].

Surface functionalization of γFe_2O_3 nanoparticles was performed via a sol–gel method involving base-catalyzed hydrolysis and co-condensation of tetra-coordinated alkoxysilanes in an alcohol medium. Tetra-coordinated silanes can be described by the general chemical formula $R'_xSi(OR)_{(4-x)}$, $0 < x < 3$, where OR is the hydrolyzable part (e.g., methoxy, ethoxy, etc.) and R′ is the non-hydrolyzable part of the structure with functional substituents (e.g., amino, mercapto, carboxy, etc.).

Ideally, it would be expected that the 3-aminopropyltrimethoxysilane (APTMS, $(CH_3O)_3$-Si-$(CH_2)_3$-NH_2)) molecules on the surface of the γFe_2O_3 particles would polymerize into a highly homogeneous crosslinked SiO_2 coating with functional amino (-NH_2) groups present. However, the presence of a non-hydrolyzable fraction in the AMPTS structure (($CH_3O)_3$-Si-$(CH_2)_3$-NH_2)) causes steric hindrance, and the electron density on the silicon (Si) atom increases due to the inductive (+I) effect, which decreases the rate of hydrolysis and condensation of the APTMS and increases its tendency for homocondensation. The chemical reactivity is thus slowed down, leading to an undesired heterogeneous distribution of functional amino (-NH_2) groups with an insufficient surface coverage of the γFe_2O_3 nanoparticles [50–52].

In contrast to APTMS, under base-catalyzed conditions, the reactivity of tetraethoxysilane (TEOS, $Si(OCH_2CH_3)_4$) is enhanced due to the number and nature of the alkoxide (i.e., ethoxy) groups, which have a key influence on the crosslinking rate. This higher reactivity of TEOS can be attributed to the inductive stabilization of positively charged intermediates and transition states in the hydrolysis and condensation reactions by the ethoxy groups [53]. Therefore, TEOS was used as a crosslinker and APTMS (($CH_3O)_3$-Si-$(CH_2)_3$-NH_2)) was used as a supplier of the -NH_2 functional groups.

In this way, it was possible to create uniform spherical γFe_2O_3@SiO_2-NH_2 core–shell structures with the presence of amino (-NH_2) functional groups on the surface of the nanoparticles, which are required for the subsequent binding of heavy metal ions from water [54].

The adsorption process of heavy metal ions for an adsorbent is highly dependent on the initial pH of the solution, owing to its remarkable effect on the speciation of metal ions [5].

If we take a closer look at the speciation of Cr, Pb, and Hg, we can find that at an acidic pH value, the predominant Cr(VI) species consist of $H_2CrO_4^0$, $HCrO_4^-$, CrO_4^{2-}, and $Cr_2O_7^{2-}$ [5,55] while Cr(III) remains relatively stable in acidic media and is more likely to be oxidized to chromate in alkaline media [56]. For Pb(II) in the pH range from 2 to 6, the dominant form is positively charged Pb^{2+} species, while when the pH values increase above 7, other Pb(II) species—including $Pb(OH)^+$, $Pb(OH)^2$, and PbO—are usually present [57].

Mercury has two common cations in aqueous solutions: a di-ion, Hg_2^{2+}, composed of two singly charged ions; and a doubly charged Hg^{2+}. Diagrams of Eh-pH indicate that Hg(I) is stable only within a narrow band of Eh values in acidic solutions, while Hg(II) is the dominant form of the Hg species in most aqueous solutions [58]. The hydrolysis reactions of Hg(II) are significant at pH > 1, and different hydrolyzed forms can be formed depending on the aqueous mercury concentration [59] At low aqueous mercury concentrations, the dominant hydrolysis species formed are $HgOH^+$ and $Hg(OH)_{2(aq)}$, while at higher mercury concentrations the formation of $Hg_2(OH)_2^{2+}$ and $Hg(OH)^{3-}$ at pH > 13 has been reported [60].

Insoluble metal species will usually not form at pH < 7.2 as long as their concentration is below the solubility limit [61–63]. Therefore, at acidic pH values, the removal of positive heavy metal ions is mainly accomplished by adsorption. In contrast, at higher solution pH values, the precipitation of metal hydroxides or even oxides (e.g., $Pb(OH)_2$, PbO, CrO_4^{2-},

etc.) can occur as a consequence of the low solubility of metal ions [57]. Therefore, at higher pH values, precipitation of insoluble species may take place at the same time alongside adsorption in the process of heavy metal removal, negatively affecting the adsorption efficiency [64].

Many studies have shown that metal ions start to precipitate as hydroxides or oxides when the solution pH is above 7.2. To avoid precipitation of the metal ions, all adsorption experiments should be conducted at a pH below 7.2 [56,61–63].

Moreover, the adsorption capacity of heavy metal ions decreases with increasing pH values. Specifically, it was shown that the maximum adsorption capacity of Cr(VI) is observed at a pH of 2 [5]. Moreover, the optimal pH for adsorbing Pb(II) was shown to be around 5.5 [65], whereas it was about 6 for Fe_3O_4@SiO_2-NH_2 magnetic nanoparticles [54,61].

Furthermore, it is generally known that iron oxides (γFe_2O_3, Fe_3O_4, etc.) suffer from a tendency to aggregate and decompose in acid-regenerated solutions; thus, to avoid the risk of potential dissolution of iron oxide cores at low pH, in this study, we instead used them in adsorption processes at pH > 3, despite silica shell protection (γFe_2O_3@SiO_2-NH_2) [61].

Iron oxide nanoparticles—i.e., goethite (α-FeOOH), hematite (α-Fe_2O_3), magnetite (Fe_3O_4), maghemite (γ-Fe_2O_3) [66–70], —show moderate affinity towards HM ions on their surface. They appear more applicable if the surface is stabilized [71–73], and enlarged by coating with silica NPs (-SiO_2), whereby agglomeration is prevented [74]. Additionally, by using different functional groups [71–73]—e.g., amino (-NH_2) [34,66–68,75,76], mercapto (-SH) [77,78], carboxy (-COOH) [79]—the adsorption efficiency and adsorption capacity of HM ions can be improved [33,34,71].

Adsorption studies of HM ions from model water by various magnetic nanoparticles (MNPs) and functionalized magnetic nanoparticles (F-MNPs) show that the maximum adsorption capacity of specific HM ions—i.e., for lead [44,61], mercury [80], and chromium [5,81]—can be obtained in less acidic pH.

In Tables 1–3, the adsorption capacity and desorption efficiency are compared for the tested MNPs and amino-functionalized MNPs at the optimal model solution pH values for adsorbing individual HM ions (e.g., Pb^{2+}, Cr^{3+}/Cr^{3+}/Cr^{6+}, and Hg^{2+}).

Table 1 shows comparison of the adsorption capacities and desorption efficiency for Pb^{2+} ions by non-functionalized and functionalized MNPs. It can be seen that the adsorption of Pb^{2+} ions was tested mostly at acidic pH, and that the adsorption capacity is higher for the cases of functionalized magnetic nanomaterials. Ahmadi et al. (2014) [35] prepared γ-Fe_2O_3 NPs via the wet chemical method and tested adsorption at pH 7.5, while Nicola et al. (2020) [82] synthesized Fe_3O_4@SiO_2 NPs and found that the adsorption capacity on non-functionalized MNPs was relatively low at pH 6.0 (10.55 mg/g) but a shade higher (14.9 mg/g) for SiO_2-stabilized magnetic nanomaterials [82]. Nicola et al. (2020) [82] also tested the desorption efficiency of Pb^{2+} ions with 5% HCl, and the final desorption efficiency was evaluated as 95.7% [82]. Qian et al. (2019) [36] stated that the adsorption capacity of materials functionalized with chitosan and with an amino group (NH_2-functionalized Fe_2O_3/chitosan NPs) at pH 5.0 was not significantly better compared to NH_2-functionalized Fe_2O_3 materials. Higher adsorption capacity with Fe_3O_4 NPs coated with activated carbon was achieved at pH 6.0 [83], while Huang et al. (2020) [5] reached 53.9 mg/g with amino-functionalized graphene oxide at pH 5.0. Wang et al. (2010) [43] and Tang et al. (2013) [34] stated that even higher adsorption capacity at pH 6.2 (76.66 mg/g) can be achieved by pre-stabilization with SiO_2 and amino-functionalization of magnetic materials (Fe_3O_4@SiO_2–NH_2 NPs). Tang et al. (2013) [34] achieved 82.29 mg/g with amino-functionalized Fe_3O_4@mesoporous SiO_2 core–shell composite microspheres at pH 5.5. In polyethylenimine (PEI)-functionalized Fe_3O_4 magnetic nanoparticles (MNPs) (pH 5.0), adsorption capacity of 60.98 mg/g for Pb^{2+} ions was reported [84]. A maximum adsorption capacity of 60 mg/g at pH 5.0 was achieved using composite beads of *Zea mays* rachis (ZMR) and sodium alginate (AL) as adsorbents [85]. Luo et al. (2021) [86] reported the adsorption of 28.7 mg/g by carbon-doped TiO_2 (C-TiO_2) at pH 6.5 for the adsorption of Pb^{2+}. The comparison of adsorption capacities showed that the adsorption capacity of Pb^{2+}

ions depends on the pH of the medium, stabilization, and, to a large extent, the presence of -NH_2 groups.

Table 1. Comparison of adsorption capacity and desorption efficiency for tested MNPs and amino-functionalized MNPs at the optimal model solution pH for adsorbing Pb^{2+} ions.

Adsorbent	HM Ions	Tested pH	Adsorption Capacity	Desorption Efficiency	Reference
γ-Fe_2O_3 NPs	Pb^{2+}	7.5	10.55 mg/g	-	[35]
Fe_3O_4@SiO_2 NPs		6.0	14.9 mg/g	95.7%	[82]
NH_2-functionalized Fe_2O_3/chitosan NPs		5.0	32.46 mg/g	-	[36]
NH_2-functionalized Fe_2O_3 NPs		5.0	39.30 mg/g	-	[36]
Magnetic composite of activated carbon and superparamagnetic Fe_3O_4 NPs (Fe_3O_4@C magnetic composite)		6.0	41.7 mg/g	>77%	[83]
NH_2-functionalized γ-Fe_2O_3 NPs (γ-Fe_2O_3@NH_2 NPs)		**4.0**	**53.5 mg/g**	**90.7%**	**This work**
Amino-functionalized graphene oxide (GO-NH_2)		5.0	53.9 mg/g	-	[4]
Fe_3O_4@SiO_2–NH_2 NPs		6.2	0.37 mmol/g 76.66 mg/g*	-	[43]
Amino-functionalized Fe_3O_4@mesoporous SiO_2 core–shell composite microspheres		5.5	82.29 mg/g	-	[35]
NH_2-functionalized γ-Fe_2O_3 NPs (γ-Fe_2O_3@NH_2 NPs)		**7.0**	**83.6 mg/g**	**91.3%**	**This work**
Polyethylenimine (PEI)-functionalized Fe3O4 magnetic nanoparticles (MNPs)		pH 5.0	60.98 mg/g		[84]
Composite beads of *Zea mays* rachis (ZMR) and sodium alginate (AL)		pH 5.0	60 mg/g		[85]
Carbon-doped TiO_2 (C-TiO_2)		pH 6.5	28.7 mg/g		[86]

* calculated.

From the literature, it can be observed that higher adsorption of Cr^{3+}/Cr^{6+}/CrT ions was achieved using amino (-NH_2)-functionalized MNPs (Table 2). The highest adsorption of Cr^{3+} ions by bare MNPs was reported in the literature [72,87,88]. Zhang et al. (2020) [11] used bare magnetic magnetite NPs (Fe_3O_4) for the adsorption of Cr^{3+} ions at pH 4.0 and achieved an adsorption capacity of 8.67 mg/g. Additionally, in acidic media (pH 2.5), Gallo-Cordova et al. (2019) [72] performed adsorption of Cr^{3+} ions using bare iron oxide magnetic NPs and reported an adsorption capacity of 15.0 mg/g, while Hu et al. (2005) [17] achieved a very low adsorption capacity of 19.2 mg/g using maghemite NPs (γ-Fe_2O_3). Zhang et al. (2020) [11], Gallo-Cordova et al. (2019) [72], and Hu et al. (2005) [17] also performed desorption with NaOH, achieving desorption efficiency of >75%, ≅100%, and 87.7%, respectively. Other studies used amino-functionalized MNPs and achieved higher adsorption capacity in acidic media (pH 2.0 to 3.0). Adsorption of Cr^{3+} ions at pH 3.0 was performed using amino-functionalized magnetite NPs (NH_2-Fe_3O_4) [89]. Baghani et al. (2016) [89] achieved an adsorption capacity of 24.25 mg/g and desorption efficiency of 98.02%. Even better adsorption (i.e., 35.0 mg/g) was reported by Gallo-Cordova et al. (2019) [72] using APTES@TEOS@MNP at pH 2.5, and the desorption efficiency was also high (≅100%). Zhao et al. (2010) [44] prepared NH_2-functionalized nanomagnetic polymer adsorbents. Functionalization was performed with different precursors (i.e., EDA-, DETA-, TETA-, TEPA-). A maximum adsorption capacity of 38.5 mg/g at pH 2.5 was achieved using TETA-functionalized nanomagnetic polymer adsorbents. In another study, 40.0 mg/g of Cr^{3+} ions was adsorbed at pH 2.0 by TEPA-functionalized nanomagnetic polymer adsorbents [64]. Huang et al. (2020) [5] reported the adsorption properties of functionalized non-magnetic materials at pH 2.0. Using amino-functionalized graphene oxide (GO-NH_2), Huang et al. (2020) [5] achieved 90.4 mg/g, which is the same adsorption capacity that we achieved with NH_2-functionalized γ-Fe_2O_3 NPs (γ-Fe_2O_3@NH_2 NPs), but at alkaline pH (7.0). The maximum adsorption capacity for chromium(VI) ions was 76.92 mg/g at pH 3.0 when adsorbent carbon-encapsulated hematite nanocubes (αFe_2O_3@C) were

used [90]. Puszkarewicz and Kaleta (2019) [91] used activated carbon as an adsorbent, and the maximum adsorption capacity for chromium(VI) ions was 4.35 mg/g at pH 2 [91].

Table 2. Comparison of adsorption capacity and desorption efficiency for tested MNPs and amino-functionalized MNPs at optimal model solution pH for adsorbing $CrT/Cr^{3+}/Cr^{6+}/Cr(VI)$ ions.

Adsorbent	HM Ions	Tested pH	Adsorption Capacity	Desorption Efficiency	Reference
Magnetic magnetite NPs (Fe_3O_4)	$CrT/Cr^{3+}/Cr^{6+}/Cr(VI)$	4.0	8.67 mg/g	>75%	[87]
Iron oxide magnetic NPs (MNPs)		2.5	15.0 mg/g	≅100%	[72]
Maghemite NPs (γ-Fe_2O_3)		2.5	19.2 mg/g	87.7%	[88]
NH_2-functionalized γ-Fe_2O_3 NPs (γ-Fe_2O_3@NH_2 NPs)		**4.0**	**24.0 mg/g**	-	**This work**
Amino-functionalized magnetite NPs (NH_2-Fe_3O_4)		3.0	24.25 mg/g	98.02%	[89]
APTES@TEOS@MNP		2.5	35.0 mg/g	≈100%	[72]
NH_2-functionalized nanomagnetic polymer adsorbents (EDA-NMPs)		2.5	37.6 mg/g	-	[44]
NH_2-functionalized nanomagnetic polymer adsorbents (DETA-NMPs)		2.5	37.9 mg/g	-	[44]
NH_2-functionalized nanomagnetic polymer adsorbents (TETA-NMPs)		2.5	38.5 mg/g	-	[44]
NH_2-functionalized nanomagnetic polymer adsorbents (TEPA-NMPs)		2.0	40.0 mg/g	-	[44]
Amino-functionalized graphene oxide (GO-NH_2)		2.0	90.4 mg/g	-	[4]
NH_2-functionalized γ-Fe_2O_3 NPs (γ-Fe_2O_3@NH_2 NPs)		**7.0**	**90.4 mg/g**	**96.7%**	**This work**
Carbon-encapsulated hematite nanocubes (αFe2O3@C)		pH 3	76.92 mg/g		[90]
Activated carbons		pH 2	4.35 mg/g		[91]

The maximum adsorption capacity for Hg^{2+} (Table 3) was 32.88 mg/g at pH 5.0 using carboxyl-terminated hyperbranched poly(amidoamine) dendrimers grafted onto superparamagnetic NPs (CT-HPMNPs) as adsorbents, and the maximum desorption efficiency was ≅85% (using HNO_3 acid) [92]. Wang et al. (2013) [93] used rhodamine-hydrazide-modified Fe_3O_4 as an adsorbent, and the maximum adsorption capacity for Hg^{2+} was 37.4 mg/g at pH 7.5 [93]. Bolivar et al. (2018) [80] performed a study of Hg^{2+} ion adsorption, in which Fe_3O_4 nanoparticles coated with amino organic ligands and yam peel biomass displayed a maximum Hg^{2+} adsorption capacity of 60 mg/g at pH 7.0 [94]. The maximum adsorption capacity for Hg^{2+} was 50 mg/g at pH 7.0 when an adsorbent nanocomposite based on Fe_3O_4 nanoparticles, chitosan nanoparticles, and polythiophene was used [95]. Dun Chen et al. (2016) [96] studied the adsorption of Hg^{2+} using magnetic adsorbents (Fe_3O_4@SiO_2-NH-HCGs; HCG = py (2-pyridinyl); pyd (3-pyridazinyl)) formed by grafting of different heterocyclic groups onto amino groups via substitution reaction. The maximum adsorption capacity for Fe_3O_4@SiO_2-NH-HCG- (pyd) and Fe_3O_4@SiO_2-NH-HCG- (py) was 77 mg/g and 56 mg/g at pH 7.0 [96], respectively. For both adsorption materials, HCl was used as the desorption eluent, and the stated desorption efficiency was 95% [96]. Hao et al. (2021) [97] performed a study of Hg^{2+} ion adsorption with Armeniaca sibirica shell activated carbon (ASSAC) magnetized by nanoparticles (Fe_3O_4/ASSAC), showing a maximum adsorption capacity of 97.1 mg/g at pH 2. At pH 5.5, Zhang et al. (2016) [98] studied the adsorption of Hg^{2+} ions with activated carbon (XLAC) derived from *Xanthoceras sorbifolia* Bunge hull as an adsorbent, showing a maximum adsorption capacity of 235.6 mg·g^{-1}. A maximum adsorption capacity of 162 mg g^{-1} for Hg^{2+} ions at pH 5.0 was achieved using cadmium sulfide nanoparticles doped in a nanoadsorbent fabricated from polycaprolactam (nylon 6) nanofibers (CdS/N6) [99].

Table 3. Comparison of adsorption capacity and desorption efficiency for tested MNPs and amino-functionalized MNPs at optimal model solution pH for adsorbing Hg^{2+} ions.

Adsorbent	HM Ions	Tested pH	Adsorption Capacity	Desorption Efficiency	Reference
NH_2-functionalized γ-Fe_2O_3 NPs (γ-Fe_2O_3@NH_2 NPs)	Hg^{2+}	**4.0**	**16.2 mg/g**	**100%**	**This work**
CT-HPMNPs		5.0	32.88 mg/g	≃85%	[92]
Rhodamine-hydrazide-modified Fe_3O_4		7.5	37.4 mg/g	-	[93]
Nanocomposite based on Fe_3O_4 nanoparticles, chitosan nanoparticles, and polythiophene		7.0	50 mg/g	-	[95]
Fe_3O_4@SiO_2-NH-HCG- (py)		7.0	56 mg/g	95%	[96]
Fe_3O_4 nanoparticle coated with amino organic ligands and yam peel biomass		7.0	60 mg/g	-	[94]
Fe_3O_4@SiO_2-NH-HCG- (pyd)		7.0	77 mg/g	95%	[96]
NH_2-functionalized γ-Fe_2O_3 NPs (γ-Fe_2O_3@NH_2 NPs)		**7.0**	**85.6 mg/g**	**100%**	**This work**
Armeniaca sibirica shell activated carbon (ASSAC) magnetized by nanoparticles (Fe_3O_4/ASSAC)		pH 2	97.1 mg/g		[97]
Activated carbon (XLAC) derived from *Xanthoceras sorbifolia* Bunge hull		pH 5.5	235.6 mg·g		[98]
Cadmium sulfide nanoparticles doped in a nanoadsorbent fabricated from polycaprolactam (nylon 6) nanofibers (CdS/N6)		pH 5	162 mg g		[99]

Adsorption has predominantly been investigated using -NH_2 [36], -SiO_2 [82], and -SH [94]-functionalized Fe_3O_4 or γ-Fe_2O_3 NPs [67] prepared by different approaches, in model water media of various pH values [34,66], from pH 2.0 to 8.0.

There are not many previous studies [32,66] on testing adsorption by γ-Fe_2O_3 NPs functionalized with an amino (-NH_2) group—specifically, by (3-aminopropyl)trimethoxysilane (APTMS) precursors—and to the best of our knowledge, far less research has been conducted on desorption approaches to date.

Although iron oxide and hybrid iron oxide NPs can be removed from aqueous solutions with an outer magnet, their recycling and regeneration possibilities after adsorption have not been sufficiently explored to fill gaps in the circular economy [32,47,87].

Due to these facts, our challenge was to synthesize and investigate the potential of amino-functionalized γ-Fe_2O_3 MNPs (γ-Fe_2O_3@NH_2 NPs), which would allow efficient adsorption and recycling of HM ions at the shock load concentrations present in the model water, preferably at neutral pH, without pretreatment. To compare adsorption efficiencies and capacities, we tested significant concentrations of Pb^{2+}, Cr^{3}, and Hg^{2+} ions using different amounts (m_{ads} = 20/45/90 mg) of the γ-Fe_2O_3@NH_2 adsorbent NPs at two different pH values of the initial aqueous solution, i.e., at pH = 7.0, as well as at pH = 4.0. Furthermore, before the performance of adsorption tests, -NH_2-functionalized γ-Fe_2O_3 MNPs were characterized with different methods, such as FTIR, BET, TEM, and TGA. Zeta potential changes in γ-Fe_2O_3@NH_2 NPs were analyzed to understand the mechanisms taking place during the adsorption and desorption process of Pb^{2+} ions. Moreover, to evaluate the adsorbent regeneration, desorption with 0.1 M HNO_3 was tested, which is of great importance for the reuse of adsorption materials and recycling of heavy metals. The prepared γ-Fe_2O_3 and functionalized γ-Fe_2O_3@NH_2 MNPs were also characterized by X-ray powder diffractometry (XRD).

2. Results and Discussion

2.1. Properties of the Prepared γ-Fe_2O_3@NH_2 NPs

This section explains the characterization of the synthesized, stabilized, and functionalized MNPs (γ-Fe_2O_3@NH_2 NPs). In addition, the adsorption mechanisms and the results of batch adsorption and desorption experiments are also discussed.

2.1.1. Crystallographic Properties

The prepared γ-Fe_2O_3 and functionalized γ-Fe_2O_3@NH_2 MNPs were characterized by X-ray powder diffractometry (XRD) (Figure 1). In the X-ray powder diffraction pattern in Figure 1, the presence of diffraction peaks at 2θ of 30.2°, 35.5°, 43.2°, 53.6°, 57.2°, and 62.9°—which correspond to the cubic crystal planes of (220), (311), (400), (422), (511), and (440), respectively—are characteristic of the spinel crystal structure (JPCD Card 39-1346). The spinel crystal structure is evident for both samples—γ-Fe_2O_3 and functionalized γ-Fe_2O_3@NH_2 MNPs—while the presence of a broad amorphous diffraction peak for the functionalized γ-Fe_2O_3@NH_2 MNPs, which appears at a low diffraction angle 2θ of 20°, is due to the presence of the amorphous SiO_2 surface layer, indicating that the crystalline cubic spinel γ-Fe_2O_3 magnetic cores were surface-modified [78]. The average size of the γ-Fe_2O_3 crystalline magnetic cores was estimated to be 13 nm, using the Debye–Scherrer equation [100,101].

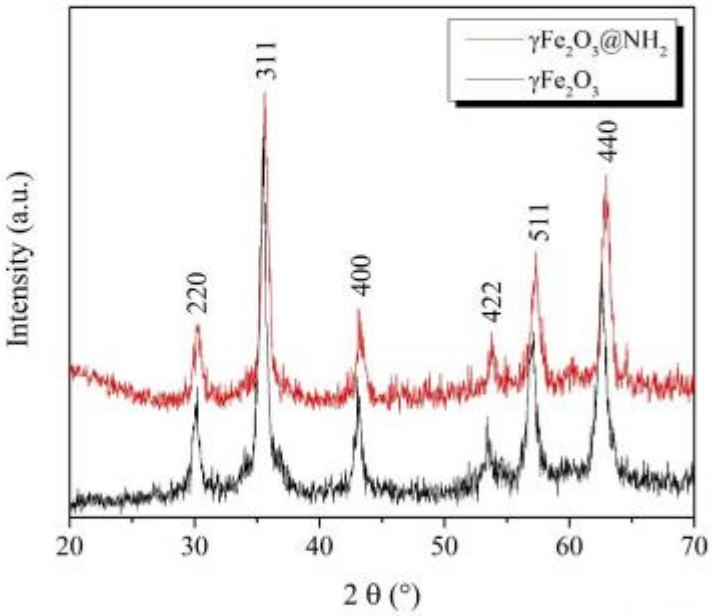

Figure 1. X-ray diffraction patterns (XRD) for the samples γ-Fe_2O_3 and γ-Fe_2O_3@NH_2.

2.1.2. Thermogravimetric Properties

The thermal stability of γ-Fe_2O_3@NH_2 NPs was determined via thermogravimetric analysis (TGA). The results of mass loss during the TGA analysis indicate the possible presence of -NH_2 functional groups on the surface of the F-MNPs. Upon heating up to 180 °C, the measured mass loss corresponds to the evaporation of absorbed moisture and NH_4OH residue. Further weight loss at heating up to 700 °C is due to the removal of aminopropyl ($NH_2(CH_2)_3$-) groups from the nanoparticles' surfaces and the consequence of cracking of the remaining siloxane groups (Si-O-Si) [75]. The TGA curve (Figure 2) shows that the synthesized, stabilized, and functionalized MNPs have good thermal stability. The weight loss during the TGA analysis was 10.3%.

The thermal stability of the particle samples analyzed was in accordance with previous results in the literature for other functionalized NPs [102–105].

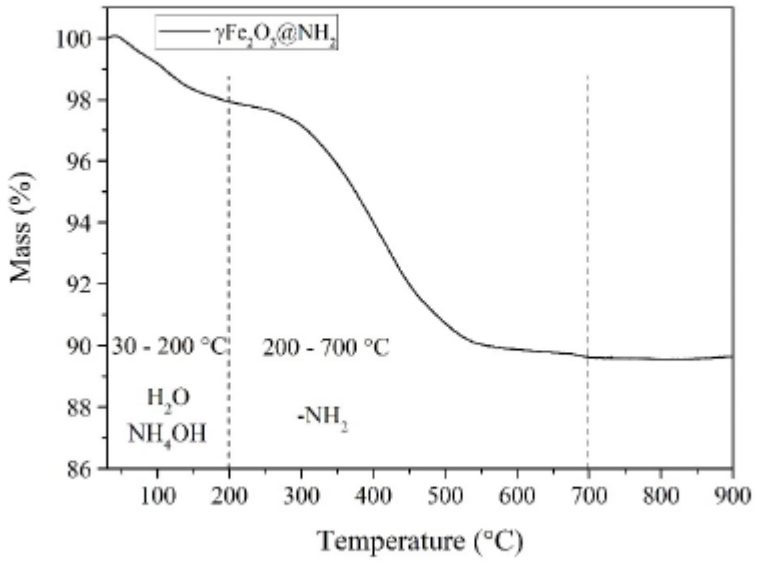

Figure 2. TGA analysis for γ-Fe_2O_3@NH_2 NPs.

2.1.3. FTIR Spectroscopy

An FTIR analysis of γ-Fe_2O_3 and γ-Fe_2O_3@NH_2 NPs was performed comparatively to identify the presence of characteristic functional groups related to the amino-silane coating of the γ-Fe_2O_3 surfaces. The FTIR spectra of γ-Fe_2O_3 and γ-Fe_2O_3@NH_2 NPs, as well as those of pure TEOS and APTMS precursors, are shown in Figure 3a.

The functional amino-silane-coated γ-Fe_2O_3 nanoparticles were derived during the sol–gel process from the mixture of TEOS and APTMS precursors according to the experimental details described in Section 2.4. In contrast to the TEOS precursor ($Si(OCH_2CH_3)_4$), the APTMS precursor ($(CH_3O)_3Si(CH_2)_3NH_2$) included a short aliphatic chain (-$(CH_2)_3$-) and a terminal amino (-NH_2) group in its structure. Thus, the main difference in the FTIR spectra of the TEOS and APTMS precursors is the presence of primary amino (N-H) vibrations in the range of 3400–3300 cm^{-1} of the APTMS spectra, while both spectra are identical to the occurrence of C-H vibrations in the range of 3000–2800 cm^{-1} and Si-O-Si vibrations in the range of 1100–1000 cm^{-1}, which are common characteristics of alkoxysilanes.

As shown in Figure 3a, the formation of the γ-Fe_2O_3 structure is closely related to the occurrence of Fe-O bending and stretching vibrations in the range of 650–550 cm^{-1}. The broad band at 3406 cm^{-1} observed for the γ-Fe_2O_3 NPs in the wavenumber region 3550–3200 cm^{-1} can be assigned to intermolecular O-H stretching (Figure 3a).

As opposed to γ-Fe_2O_3 NPs, asymmetric stretching vibrations of Si-O-Si bonds at 1050 cm^{-1} indicate the formation of a silica (SiO_2) shell in the γ-Fe_2O_3@NH_2 samples. Moreover, two weak bands can be observed for the γ-Fe_2O_3@NH_2 samples in Figure 3a, characteristic of primary amines, due to the asymmetric and symmetric N-H vibrations in the range of 3400–3300 cm^{-1}—more precisely, at 3356 cm^{-1} and 3281 cm^{-1}, respectively. These primary amino peaks in the source spectra of γ-Fe_2O_3@NH_2 NPs were not sufficiently visible, but enlarged individual peak areas confirmed their presence (Figure 3b). Specifically, the primary amine (NH_2) vibrations occurred in the same wavenumber region as the intermolecular O-H stretching [106]. Because the polarity of the N-H bonds in amines is weaker than that of the O-H bonds, the absorption band of N-H is not as intense as that of O-H, which usually shows stronger and broader absorption bands that are much easier to

identify. Primary amines have also a medium-to-strong absorption band in the wavenumber region 1650–1580 cm^{-1}, which was identified at 1598 cm^{-1} for the γ-Fe_2O_3@NH_2 NPs [107].

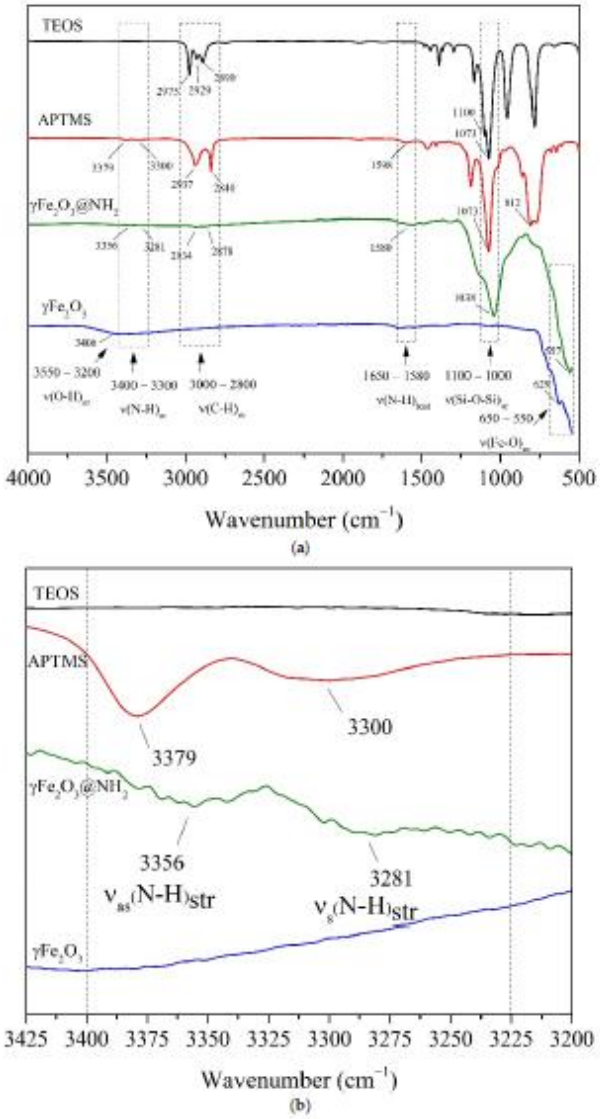

Figure 3. (**a**) FTIR spectra of γ-Fe_2O_3 NPs, γ-Fe_2O_3@NH_2 NPs, pure AMPTS precursor, and pure TEOS precursor, and (**b**) enlarged area corresponding to vibrations of amino (-NH_2) groups.

2.1.4. Specific Surface Area

The specific surface area of the prepared γ-Fe_2O_3 and γ-Fe_2O_3@NH_2 MNPs was measured by the Brunauer–Emmett–Teller (BET) method. The obtained BET curves are shown in Figure 4.

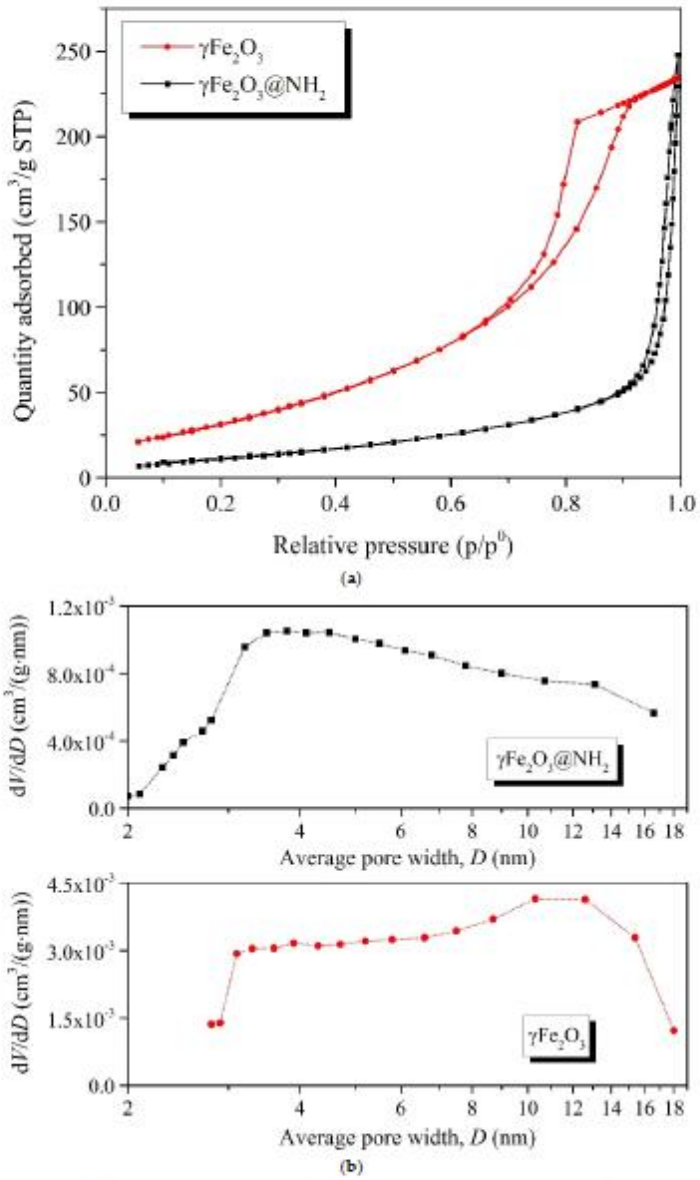

Figure 4. (**a**) BET isotherms and (**b**) pore size distribution for γ-Fe_2O_3 and γ-Fe_2O_3@NH_2 NPs.

The BET analysis showed a specific surface area of 99.9 m^2/g for γ-Fe_2O_3 and 41.3 m^2/g for γ-Fe_2O_3@NH_2. According to the Barrett–Joyner–Halenda (BJH) adsorption method, the average pore size was found to be 6.4 nm for the γ-Fe_2O_3 NPs, with a total pore volume of 0.378037 cm^3/g, while for the BJH desorption the average pore size for the γ-Fe_2O_3 NPs increased to 6.7 nm, with a total pore volume of 0.407662 cm^3/g, suggesting a mesoporous structure of the γ-Fe_2O_3 sample, with a typical type IV experimental N_2 gas

isotherm according to the IUPAC classification [108], as shown in Figure 4. In contrast to γ-Fe_2O_3, the γ-Fe_2O_3@NH_2 sample showed a BET isotherm with a narrower hysteresis, indicating a decrease in the porosity of the as-prepared γ-Fe_2O_3 sample, most likely due to the presence of the homogeneous silicate coating. For BJH adsorption, the average pore size was found to be 5.8 nm for the γ-Fe_2O_3@NH_2 NPs, with a total pore volume of 0.090762 cm^3/g, while for the BJH desorption the average pore size for the γ-Fe_2O_3@NH_2 NPs increased to 6.0 nm, with a total pore volume of 0.090311 cm^3/g.

According to the specific surface area (BET) at a relative pressure (p/p^0) of 0.3, the calculated average particle size was 11.6 nm for γ-Fe_2O_3 and 27.9 nm for γ-Fe_2O_3@NH_2 NPs [109,110]

2.1.5. Morphological Properties

The results of the TEM analysis (Figure 5a) represent the relatively spherical morphology of the γ-Fe_2O_3 MNPs, with a particle size distribution of 13 ± 1 nm, while the particle size distribution of the functionalized γ-Fe_2O_3@NH_2 MNPs was 17 ± 1 nm (magnetic core 13 ± 1 nm and surface coating 4 ± 1 nm). The electron diffraction pattern of the γ-Fe_2O_3 MNPs inset in Figure 5b indicates the crystalline nature of the as-prepared powders, with concentric diffraction rings characteristic of a cubic spinel crystal structure.

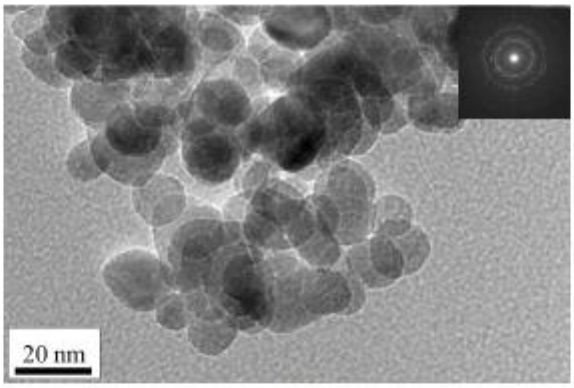

(a)

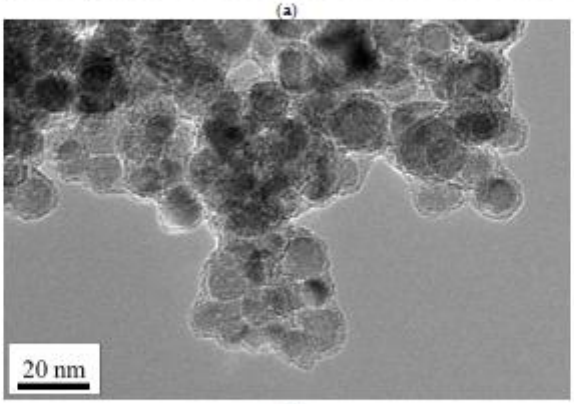

(b)

Figure 5. Transmission electron micrographs (TEM) of (**a**) γ-Fe_2O_3 NPs with inset diffraction pattern and (**b**) γ-Fe_2O_3@NH_2 NPs.

The EDXS spectra of the γ-Fe_2O_3 and γ-Fe_2O_3@NH_2 MNPs are shown in Figure 6a,b, respectively. Strong peaks for iron (Fe) and oxygen (O) can be seen in the EDXS spectrum in Figure 6a, indicating the formation of the γ-Fe_2O_3 MNPs. In contrast, the EDXS spectrum of the γ-Fe_2O_3@NH_2 MNPs shows that they contain significant amounts of silicon (Si), alongside iron (Fe) and oxygen (O), suggesting the success of the surface functionalization of γ-Fe_2O_3 MNPs with APTMS precursor molecules and, thus, the formation of the γ-Fe_2O_3@NH_2 MNPs. The lack of a nitrogen (N) peak is expected, due to its low Z-number and overlapping with the K-alpha C and O peaks. The larger peaks towards the right in both EDXS spectra are the copper (Cu) signals sourced from the TEM copper-grid-supported transparent carbon foil.

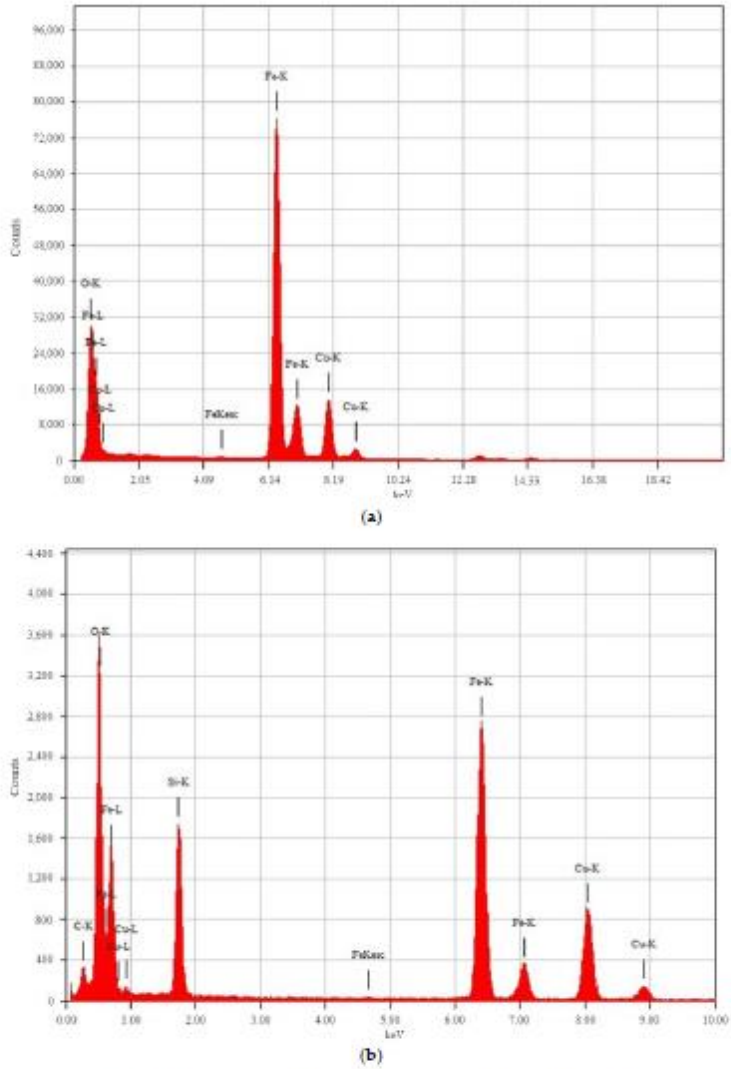

Figure 6. EDXS spectra of (**a**) γ-Fe_2O_3 NPs and (**b**) γ-Fe_2O_3@NH_2 NPs.

2.1.6. Zeta Potential

The zeta potential was measured for bare MNPs (γ-Fe_2O_3) and amino-functionalized MNPs (γ-Fe_2O_3@NH_2), as depicted in Figure 7. For bare, stabilized MNPs, the zeta potential is positive at low pH due to the presence of OH_2^+. As the pH of the solution increases, the potential decreases and approaches negative potential at high pH, due to the presence of O^-. The measured isoelectric point of the bare MNPs was 8.76 (measured potential −0.743 mV). At this value, the concentration of protonated and deprotonated amino groups is the same. Meanwhile, the measured isoelectric point for functionalized MNPs was at pH 12.1 (measured potential +0.161 mV) =, indicating successful MNP functionalization. This difference in the isoelectric point is due to the presence of amino groups on MNPs, resulting in a functionalized magnetic nanomaterial with a negative charge above pH = 12.1.

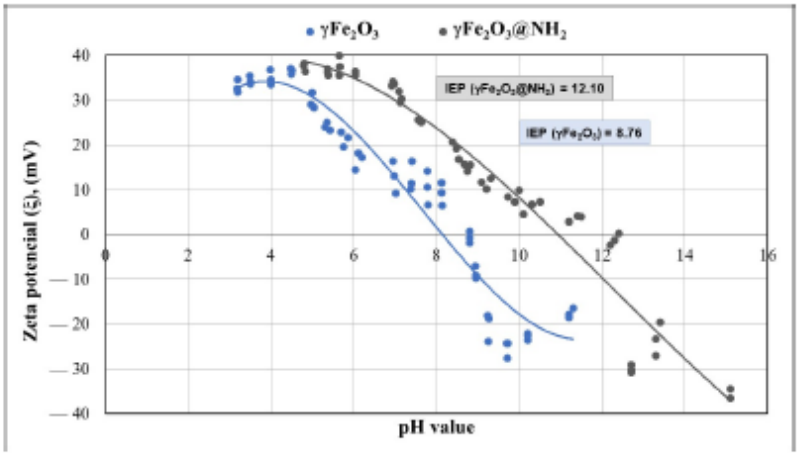

Figure 7. The zeta potential of bare γ-Fe_2O_3 and γ-Fe_2O_3@NH_2 NPs.

2.2. Adsorption Mechanisms

The solution pH is a key parameter of the effectiveness of HM ions' adsorption. HM ions have specific forms at different pH values; moreover, the adsorbent surface charge and protonation degree of the adsorbent surface coating (i.e., amino groups) are dependent on the pH [111,112]. In general, HM ions' adsorption on γ-Fe_2O_3@NH_2 NPs includes three sorption mechanisms, i.e., ion exchange, surface complexation, and electrostatic attraction [5]; the specific adsorption mechanism predominantly depends on the solution's pH value [5].

We tested the adsorption of Pb^{2+}, Cr^{3}, and Hg^{2+} ions at different pH values, i.e., pH 4 and 7. At different pH values, adsorption takes place by a different mechanism for each metal ion [5].

The adsorption of Pb^{2+} ions is entirely dependent on the pH value [70]. The adsorbent surface is negatively charged at alkaline pH, which indicates the deprotonated form of -NH_2 functional groups. The behavior of -NH_2 groups on the adsorbent material according to the pH is shown by Equations (1) and (2) [111]:

$$-NH_2 + H_3O^+ \rightarrow -NH_3^+ + H_2O \quad (1)$$

$$-NH_2 + OH^- \rightarrow -NH^- + H_2O \quad (2)$$

At pH 7, -NH_2 groups are deprotonated, causing a negatively charged adsorbent surface, while lead ions are mostly in Pb $(OH)^+$ form, which causes high electrostatic attraction

between Pb^{2+} ions and the negatively charged material surface and, consequently, high adsorption efficiency [82,111]. On the other hand, acidic conditions cause the transformation of -NH_2 groups into -NH_3^+ form, resulting in fewer available active sites for Pb^{2+} ions. Because of that, the adsorption efficiency of Pb^{2+} ions drops under acidic conditions (pH < 7) [5,111].

The solution pH value is also a key factor in the adsorption efficiency of Cr(VI) ions. Adsorption efficiency generally decreases with increasing pH values [5]. In acidic conditions, Cr(VI) ions are mainly present as $H_2CrO_4^0$, $HCrO_4^-$, and $Cr_2O_7^-$ species [68,72,81,113], while -NH_2 is present in protonated form, i.e., -NH_3^+ form (Equation (3)). Consequently, the γ-Fe_2O_3@NH_2 NPs' surfaces are positively charged [5,81,114]. Strong electrostatic attraction occurs in such cases, and chromium species can be easily captured on the amino-functionalized adsorbent surface [72,81].

$$R - NH_2 + H^+ \rightarrow R - NH_3^+ \quad (3)$$

$$-NH_3^+ + HCrO_4^- \rightarrow -NH_3^+ - HCrO_4^- \quad (4)$$

$$-NH_3^+ + Cr_2O_7^{2-} \rightarrow -NH_3^+ - Cr_2O_7^{2-} \quad (5)$$

On the other hand, at alkaline pH, negatively charged chromate ions (CrO_4^{2-}) are the predominant form [81,87,113]. At pH > 7, γ-Fe_2O_3@NH_2 NPs' surfaces are also negatively charged [5] due to the deprotonated form of the amino functional groups. A double-negative charge of the adsorbent surface and chromate decreases the adsorption efficiency [72].

In our study, zeta potential played an important role in the adsorption mechanism. The zeta potential of our γ-Fe_2O_3@NH_2 NPs was 8.76; at lower pH, amino groups on the material's surface were mainly present in protonated form (-NH_3^+).

We tested the adsorption of Cr(VI) ions at pH 4 and 7. At pH 4, the functional groups were mainly in -NH_3^+ form, while at pH 7 the amino groups were still in protonated form. Consequently, many active sites were present on the surface of the γ-Fe_2O_3@NH_2 NPs, so their adsorption capacity was very high. The adsorption efficiency at pH 4 was low due to the instability of γ-Fe_2O_3@NH_2 NPs in acidic conditions—the adsorbent material is soluble in acidic media, i.e., at pH < 4.

Hg^{2+} readily reacts with OH^- to form $Hg_2(OH)_2$ precipitates under alkaline conditions. The adsorption of Hg^{2+} ions is predominantly influenced by the concentration of hydronium ions in aqueous solutions. The change in adsorption at varying pH levels is because the concentration of surface charges governs the adsorbent particles and the degree of ionization of the ions to be removed [111,115,116]. There is a variety of literature suggesting that the adsorption of Hg^{2+} ions favors neutral and basic pH. The rationale for more adsorption of Hg^{2+} ions using amino groups at neutral and basic pH is that the amino group obtains a net positive charge at acidic pH and the Hg^{2+} ions are also positive; hence, the adsorption is made unfavorable by the repulsive force. The above rationale for mercury species in aqueous solution was theoretically determined as a function of pH by modeling chemical equilibrium using MINEQL+ software (Environmental Research Software, Hallowell, ME, USA) [80,117].

2.3. *Effects of pH*

Batch adsorption experiments of Pb^{2+}, Cr(VI), and Hg^{2+} ions for different adsorption times were performed at two pH values, i.e., pH 4 and 7 (Figures 8–11). The results show that the adsorption of Pb^{2+} and Hg^{2+} ions is more efficient at pH 7. Such results were expected, due to the opposite charges of the Pb^{2+} ions and the surface of the adsorption material. The opposite surface charges caused strong electrostatic interactions and high material uptake.

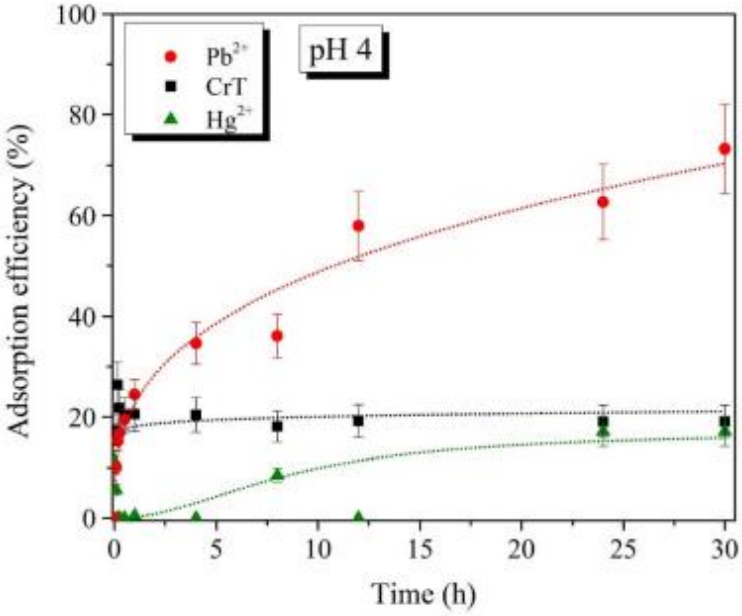

Figure 8. Adsorption efficiency (%) of Pb^{2+}, CrT, and Hg^{2+} ions at pH = 4.

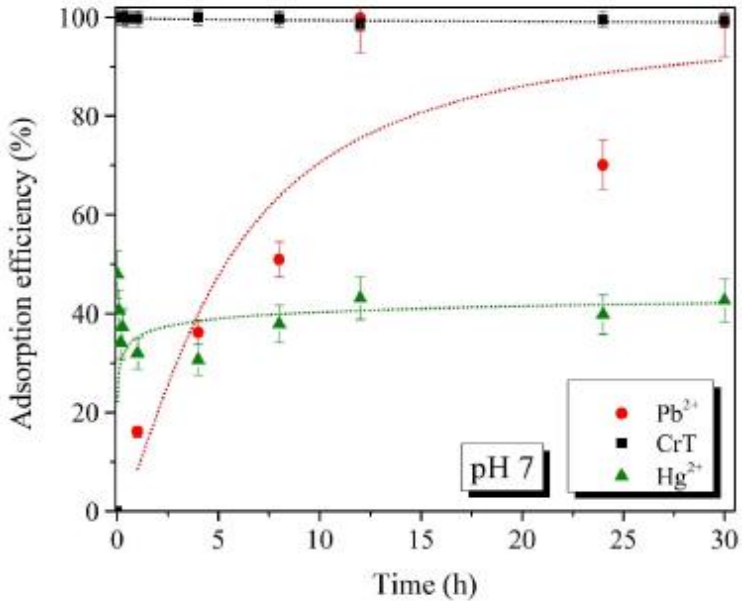

Figure 9. Adsorption efficiency (%) of Pb^{2+}, CrT, and Hg^{2+} ions at pH = 7.

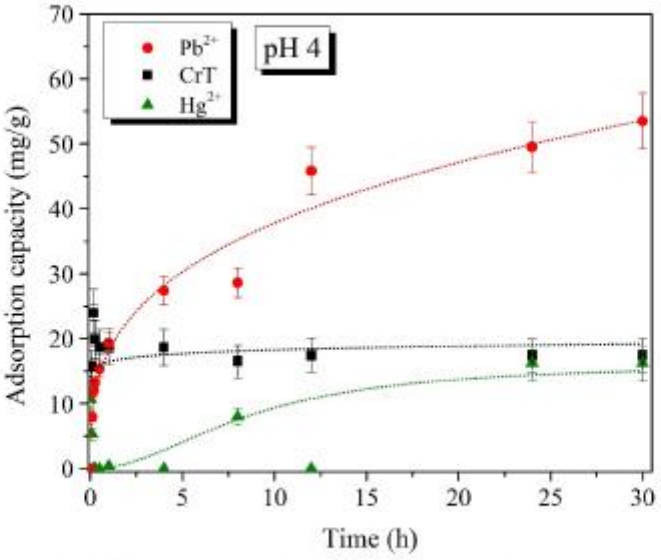

Figure 10. Adsorption capacity (mg/g) of Pb^{2+}, CrT, and Hg^{2+} ions at pH = 4.

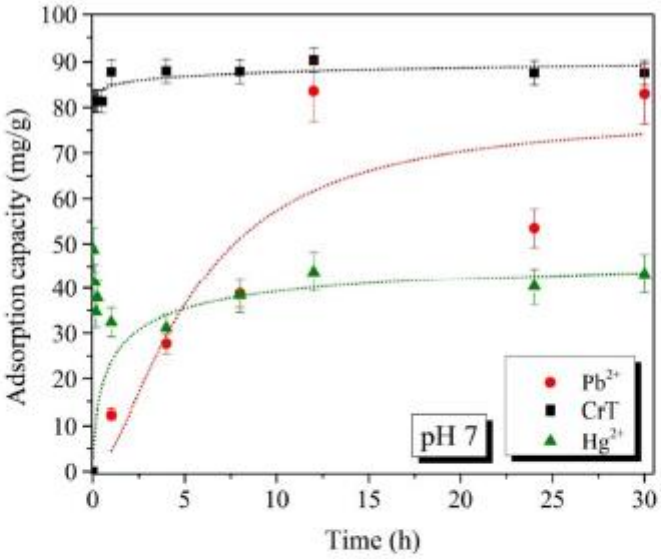

Figure 11. Adsorption capacity (mg/g) of Pb^{2+}, CrT, and Hg^{2+} ions at pH = 7.

The adsorption capacity at pH 4 and 7 slowly increased with longer specific adsorption times. At pH 4, the maximal adsorption capacity of Pb^{2+} ions was 53.5 mg/g, which was detected after 30 h. At pH 7, the maximal adsorption capacity of 83.6 mg/g was achieved already after 12 h. At both tested pH values, the adsorption of Pb^{2+} ions slowly increased with a longer adsorption time. This indicates that the adsorption of Pb^{2+} ions is a slow process but, more importantly, the process is efficient—especially at pH 7.

Adsorption of Cr^{VI} ions was much faster and very efficient at the same time. At pH 4, the adsorption efficiency was lower than 30%, and the maximal adsorption capacity was 24.0 mg/g. γ-Fe_2O_3@NH_2 NPs were less stable in acidic conditions, which was the main reason for the lower material uptake. At pH 7, we achieved 99.9% adsorption efficiency already after 1 min. When the adsorption time was extended, the efficiency stayed high, and the maximal adsorption capacity (90.4 mg/g) was achieved after 12 h.

For Hg^{2+} ions, the maximal adsorption efficiency of 84.3% displayed a corresponding adsorption capacity of 85.6 mg/g, which was reached after 30 min of adsorption time. At pH 4, Hg^{2+} ions showed a low adsorption efficiency of 17%, with a corresponding adsorption capacity of 16.2 mg/g at 30 h. As demonstrated in various studies [80,111,115–117], the increase in pH from 4 to 7 also facilitated the maximal adsorption efficiency.

2.4. Effect of Adsorbent Mass

The adsorption of Cr^{VI} ions on 45 mg of γ-Fe_2O_3@NH_2 NPs showed excellent results (q_t after 1 min was 81.4 mg/g). To determine the optimal adsorbent mass, we tested different amounts of γ-Fe_2O_3@NH_2 NPs. In adsorption experiments, 20, 45, and 90 mg of γ-Fe_2O_3@NH_2 NPs were investigated under optimal adsorption conditions (pH = 7, c = 200 mg Cr^{VI}/L and RT). Adsorption tests were performed only for 1, 4, 8, 24, and 30 h, as we expected that longer specific adsorption times would be required with smaller amounts of γ-Fe_2O_3@NH_2 NPs.

The results of Cr^{VI} ions' adsorption showed excellent adsorption efficiency (>99.2%) for all tested amounts of γ-Fe_2O_3@NH_2 NPs at all tested specific adsorption times (Figure 12). The only exception was the test using 20 mg of γ-Fe_2O_3@NH_2 NPs after 1 h. The adsorption efficiency on 20 mg of γ-Fe_2O_3@NH_2 NPs was only 35.3%, indicating insufficient adsorbent mass. Nevertheless, the adsorption efficiency reached 99.9% after 24 h, showing that the adsorption of Cr^{VI} ions with a smaller amount of γ-Fe_2O_3@NH_2 NPs required a longer adsorption time. Meanwhile, the adsorption of Cr^{VI} ions on 45 and 90 mg was equal; thus, based on the results of adsorption on 20/45/90 mg of γ-Fe_2O_3@NH_2 NPs, we concluded that 45 mg was the optimal mass of adsorbent.

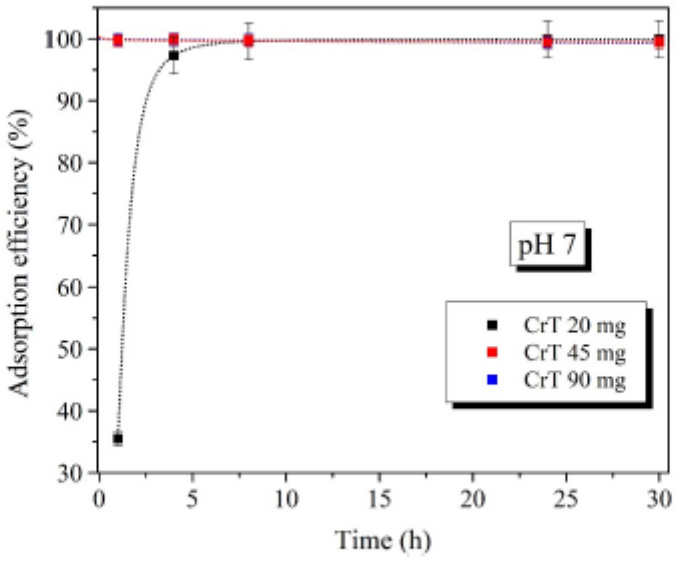

Figure 12. Adsorption efficiency of (%) Cr^{VI} ions on m_{ads} = 20/45/90 mg pH = 7.

2.5. Effects of Anions (NO_3^-, Cl^-, SO_4^{2-})

The adsorption of CrT ions showed high adsorption efficiency (99.9%) after 1 min. For these reasons, we also tested the impacts of different anions (i.e., NO_3^-, Cl^-, and SO_4^{2-}) on the adsorption efficiency of CrT ions. Experiments were performed under further optimal determined conditions (pH = 7, m_{ads} = 45 mg, c = 200 mg CrT/L), and only for 1, 5, 10, 15, 30, 45, and 60 min at RT.

The results showed no effects of different anions; furthermore, the adsorption of CrT ions remained quick, and after 1 min the adsorption efficiency rate was 99.9% for all tested anions (Figure 13).

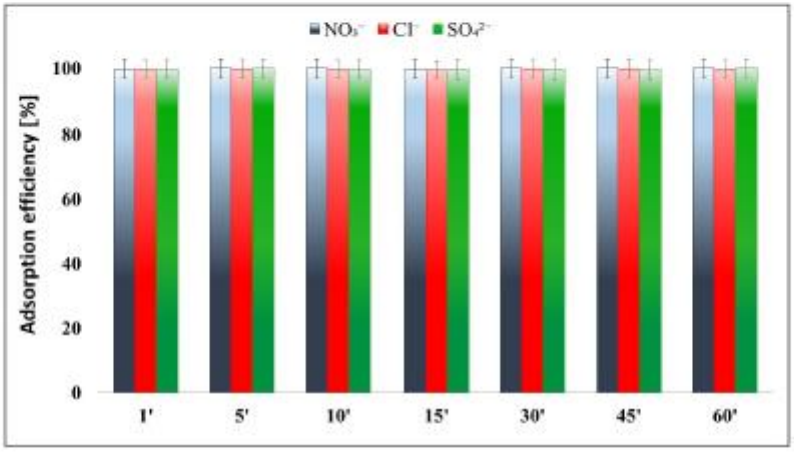

Figure 13. Effects of anions (NO_3^-, Cl^-, and SO_4^{2-}) on the adsorption efficiency (%) of CrT ions pH = 7.

2.6. Desorption

To verify the possibility of recycling HM ions and reusing adsorption materials, desorption of Pb^{2+}, CrT, and Hg^{2+} ions was performed. Due to the higher adsorption capacity of metal ions at 1140 and 1800 min, adsorption was tested for longer specific adsorption times. Desorption was performed in one cycle because of material loss during the desorption process. The results of desorption showed that the γ-Fe_2O_3@NH_2 NPs enabled high desorption efficiency for the samples on the surface of which the HM ions' adsorption was performed at pH 7. This result indicates the electrostatic binding of HM ions on the adsorption material's surface. Electrostatic binding of HM ions is weaker than covalent interactions, which probably appear at lower pH, i.e., pH 4. For this reason, only desorption results of samples after adsorption was performed at pH 7 are reported in this work (Figure 14).

The first desorption cycle performed with 0.1 M HNO_3 was more efficient for Hg^{2+}, CrT, and Pb^{2+} ions. For Pb^{2+} ions, the desorption efficiency was 91.3%; for CrT ions it was 96.7%; and for Hg^{2+} ions it was 100%. From the obtained results, it was possible to determine that higher desorption efficiency was achieved for all tested HM ions with a longer specific adsorption time (i.e., 30 h).

The desorption efficiency of Hg^{2+} ions showed that the γ-Fe_2O_3@NH_2 NPs enabled high desorption efficiency (100%) for all samples, with the adsorption process being carried out at pH 4 and 7.

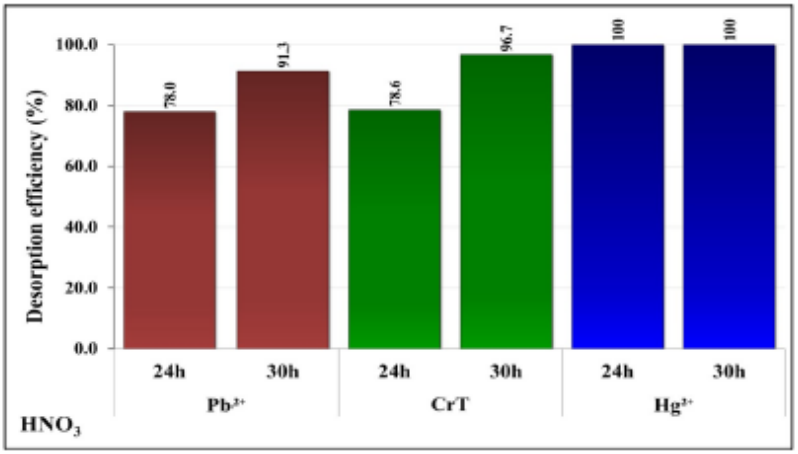

Figure 14. Desorption efficiency of Pb^{2+}, CrT, and Hg^{2+} ions (after specific adsorption times at pH = 7). Desorption was performed with 0.1 M HNO_3 for 60 min.

3. Methods and Materials

3.1. Materials

For the lab-scale synthesis, stabilization, and functionalization of γ-Fe_2O_3 MNPs, iron(II) sulfate heptahydrate ($FeSO_4$ $7H_2O$, 99.5%, 278.01 g/mol, CAS 7782-63-0, Honeywell International Inc., Charlotte, NC, USA), iron(III) sulfate hydrate ($Fe_2(SO_4)_3$ xH_2O, 97%, 399.88 g/mol, CAS 15244-10-7, Honeywell International Inc., Charlotte, NC, USA), tetraethyl orthosilicate TEOS ($C_6H_{20}O_4Si$, 99%, 208.33 g/mol, CAS 78-10-4, Sigma-Aldrich, Merck Group KGaA, Darmstadt, Germany), (3-aminopropyl)trimethoxysilane APTMS ($C_6H_{17}NO_3Si$, 97%, 179.29 g/mol, CAS 13822-56-5, Sigma-Aldrich, Merck Group KGaA, Darmstadt, Germany), ammonium hydroxide (NH_4OH, 25%, 35.05 g/mol, CAS 1336-21-6, GramMol, Zagreb, Croatia), ethanol (C_2H_5OH, 96%, 46.07 g/mol, CAS 64-17-5, GramMol, Zagreb, Croatia), and 2-propanol (C_3H_7OH, 99.9%, 60.10 g/mol, CAS 67-63-0, GramMol, Zagreb, Croatia) were used. For the batch adsorption experiments, aqueous solutions were prepared from lead(II) nitrate ($Pb(NO_3)_2$, 99.9%, 331.21 g/mol, CAS 10099-74-8, Sigma-Aldrich, Merck Group KGaA, Darmstadt, Germany), chromium(III) nitrate nonahydrate ($Cr(NO_3)_3$ $9H_2O$, 99%, 400.15 g/mol, CAS 7789-02-8, Sigma-Aldrich, Merck Group KGaA, Darmstadt, Germany), mercury(II) nitrate monohydrate ($Hg(NO_3)_2$ H_2O, ≥99.99%, 342.62 g/mol, CAS 7783-34-8, Sigma-Aldrich, Merck Group KGaA, Darmstadt, Germany), chromium(III) chloride hexahydrate ($CrCl_3$ $6H_2O$, ≥98%, 266.45 g/mol, CAS 10060-12-5, Sigma-Aldrich, Merck Group KGaA, Darmstadt, Germany), and chromium(III) sulfate hydrate ($Cr_2(SO_4)_3$ xH_2O, 99%, 392.17 g/mol, CAS 15244-38-9, Sigma-Aldrich, Merck Group KGaA, Darmstadt, Germany). Chemicals were used as purchased. For the preparation of suspensions and solutions, deionized water (dH_2O) was used.

3.2. Synthesis of MNPs

The synthesis of the maghemite (γ-Fe_2O_3) MNPs was carried out as described in our previous studies [32]. First, 30 mL of NH_4OH was added to a 100 mL glass flask and heated up to 90 °C in an oil bath, under constant stirring at 220 rpm. Afterward, 50 mL of an aqueous solution prepared at a stoichiometric ratio of 1:2 using $FeSO_4$ $7H_2O$ and $Fe_2(SO_4)_3$ xH_2O salts was added to the reaction flask. Synthesis then proceeded in alkaline conditions at pH 10 for 1 h at 90 °C. After the reaction was finished, the suspension was cooled down to room temperature (RT), and the magnetic sediment was settled out for 30 min using an external permanent magnet. After magnetic separation, the supernatant was decanted and

discarded. The colloid was rinsed several times with dH_2O, centrifuged at 3500 rpm for 15 min and, finally, separated and allowed to settle on the external magnet overnight.

3.3. Stabilization of MNPs

The rinsed γ-Fe_2O_3 MNPs were suspended in 100 mL of NH_4OH overnight at RT under constant stirring (330 rpm) for the stabilization process. After 16 h, the stabilized maghemite MNPs were separated into two phases overnight on an external magnet. The upper phase was decanted, and the colloid was prepared for further functionalization.

3.4. Functionalization of MNPs

Amino-functionalization of the γ-Fe_2O_3 MNPs was carried out with tetraethyl orthosilicate (TEOS) and (3-aminopropyl)trimethoxysilane (APTMS) precursors, with a water-to-TEOS molar ratio R = 293 and TEOS-to-APTMS molar ratio P = 1:2. After the stabilization phase, 4 mL of γ-Fe_2O_3 colloidal solution was added to the mixture of 21.6 mol% 2-propanol, 2.2 mol% NH_4OH, 15.1 mol% dH_2O, 0.25 mol% TEOS, and 0.36 mol% APTMS, and then mixed vigorously for 5 min. After 24 h of reaction (at RT under constant stirring at 220 rpm), the colloidal solution was intensively washed with ethanol and dH_2O and centrifuged at 3500 rpm for 5 min to remove agglomerates of non-functionalized γ-Fe_2O_3 MNPs.

3.5. Characterization of Amino-Functionalized γ-Fe_2O_3 MNPs

Characterization of the lab-scale amino-functionalized γ-Fe_2O_3 MNPs (γ-Fe_2O_3@NH_2 NPs) was performed using the appropriate method after each preparation phase (i.e., synthesis, stabilization, functionalization). For characterization purposes, the γ-Fe_2O_3@NH_2 MNPs were dried at 90 °C overnight, and the mass of the obtained dried particles was determined. The prepared γ-Fe_2O_3 and functionalized γ-Fe_2O_3@NH_2 MNPs were characterized by X-ray powder diffractometry (XRD) (Bruker D4 Endeavor, Bruker, Billerica, MA, USA). The thermogravimetric properties were analyzed with a 4000 TGA PerkinElmer analyzer (PerkinElmer, Waltham, MA, USA), FTIR spectra were recorded with a Spectrum Two (PerkinElmer, Waltham, MA, USA), and specific surface area (BET) was measured with a TriStar II 3020 (Micromeritics Instrument Corporation, Norcross, GA, USA). The morphology of the synthesized γ-Fe_2O_3@NH_2 MNPs was investigated using a transmission electron microscope (JEM 2100 JEOL, JEOL Ltd, Musashino Akishima, Tokyo, Japan) equipped with an energy-dispersive X-ray spectroscopy (EDXS) unit and a CCD camera to capture images.

3.6. Adsorption of Heavy Metal Ions in Aqueous Solutions

Batch adsorption tests of Pb^{2+}, CrT, and Hg^{2+} ions were performed. The initial concentration of 200 mg/L of HM ions in the model water solutions was prepared by dissolving Pb $(NO_3)_2$, Cr $(NO_3)_3$ $9H_2O$, and Hg $(NO_3)_2$ H_2O in a 1 L flask. The adsorption efficiency (R %) and adsorption capacity (q_t mg/g) at different pH of the model solution and adsorption at the defined time were calculated using Equations (6) and (7). Additionally, the effect of different adsorbent mass (m_{ads} = 20, 45, 90 mg) was tested, and the impact of various anions (e.g., NO_3^-, Cl^-, and SO_4^{2-}) on the adsorption of CrT ions was investigated. For Pb^{2+} and Hg^{2+} ions, only adsorption at different pH values was tested.

The initial pH values of the solutions were measured and set to pH 4 with 0.1 M and 1 M HNO_3 to simulate an acidic environment, which does not affect the γ-Fe_2O_3@NH_2 NPs, while 1 M NaOH was used to adjust the pH to 7 to simulate actual wastewater conditions. Adsorption was conducted in 50 mL plastic centrifuges into which 20, 45, or 90 mg of the lab-scale γ-Fe_2O_3@NH_2 NPs were weighed. Then, 20 mL of the prepared model salt solution was added to the γ-Fe_2O_3@NH_2 NPs for selected specific adsorption times (1, 5, 10, 15, 30, 60, 240, 480, 720, 1140, and 1800 min). All tests were carried out at RT. To separate the γ-Fe_2O_3@NH_2 NPs from the supernatant after adsorption, a centrifuge (4500 rpm, 15 min) (UNIVERSAL 320, Andreas Hettich GmbH & Co. KG, Tuttlingen, Germany) and

an external magnet were used. The supernatant was decanted into a glass vial; meanwhile, the γ-Fe_2O_3@NH_2 NPs were washed two times with 10 mL of dH_2O.

The concentration of the HM ions in the supernatant was measured via atomic adsorption spectroscopy (AAS PerkinElmer, PerkinElmer, Waltham, MA, USA) and inductively coupled plasma optical emission spectrometry (ICP-OES, SPECTRO CIROS VISION, SPECTRO Analytical Instruments GmbH, Kleve, Germany) for Hg^{2+}. For both analyses, the supernatants were acidified with HNO_3 (0.5 mL of acid to 10 mL of the supernatant sample).

The adsorption efficiency (R %) was calculated using Equation (6) [87]:

$$R = \frac{(C_0 - C_t)}{C_0} \times 100 \quad (6)$$

where R (%) is the adsorption efficiency, C_0 (mg/L) is the initial concentration of HM ions, and C_t (mg/L) is the residual concentration of HM ions.

The adsorption capacity was calculated using Equation (7) [87]:

$$q_t = (C_0 - C_t) \times \frac{V}{m} \quad (7)$$

where q_t (mg/g) is the adsorption capacity, C_0 (mg/L) is the initial concentration of HM ions, C_t (mg/L) is the residual concentration of HM ions, V (mL) is the solution volume, and m (mg) is the adsorption material mass.

3.7. Desorption of HM Ions and Regeneration Experiments

The desorption experiments for Pb^{2+}, Cr^{VI}, and Hg^{2+} ions were conducted to evaluate the recyclability of γ-Fe_2O_3@NH_2 NPs. Desorption tests were performed immediately after specific adsorption times—i.e., 1, 1140, and 1800 min—and after rinsing twice with 10 mL of distilled water. Desorption was performed at RT with 20 mL of 0.1 M HNO_3 added to 45 mg of adsorbent material. Desorption was in contrast to adsorption performed in dynamic mode with an IKA MS3 digital shaker (IKA-Werke GmbH & Co. KG, Staufen, Germany) at minimal rpm. The desorption efficiency was evaluated with AAS for Pb^{2+} and Cr^{VI}, and with ICP-OES for Hg^{2+} ions.

4. Conclusions

In this study, stabilized and amino-functionalized magnetic nanoparticles (γ-Fe_2O_3@NH_2 NPs) with a diameter of 17 ± 1 nm were synthesized, characterized, and used as adsorbents for Pb^{2+}, Cr^{VI}, and Hg^{2+} ions. Adsorbent characterization showed that γ-Fe_2O_3@NH_2 NPs have good thermal stability. The particles were successfully stabilized, and amino-functionalization was confirmed with FTIR spectroscopy.

The adsorption process was carried out in aqueous solutions at pH 4 and 7. The adsorption results showed the highest adsorption efficiency and capacity at pH 7 for all investigated heavy metal (HM) ions, i.e., Pb^{2+}, Cr^{VI}, and Hg^{2+}. The adsorption efficiency was the highest and quickest for Cr^{VI} > Hg^{2+} > Pb^{2+} ions. The maximal adsorption capacity for Hg^{2+} ions was achieved in 30 min, at 85.6 mg/g; for Cr^{VI} and Pb^{2+} ions, the maximal adsorption capacities were achieved after 12 h and were 90.4 mg/g and 83.6 mg/g, respectively. Experiments with different amounts of γ-Fe_2O_3@NH_2 NPs (20/45/90 mg) showed that the optimal mass of adsorbent was 45 mg. Moreover, under optimal adsorption conditions (pH = 7, m_{ads} = 45 mg, c = 200 mg Cr^{VI}/L, and RT), different anions—i.e., NO_3^-, Cl^-, and SO_4^{2-}—showed no effect on the adsorption efficiency of Cr^{VI} ions.

A study of the desorption process with 0.1 M HNO_3 for 1 h showed the possibility of reusing γ-Fe_2O_3@NH_2 NPs. Desorption was effective only for γ-Fe_2O_3@NH_2 NPs after the adsorption process was performed at neutral pH. We observed excellent desorption efficiency for Hg^{2+} (100%), Cr^{VI} (96.7%), and Pb^{2+} (91.3%) ions.

The adsorption–desorption results showed that γ-Fe_2O_3@NH_2 NPs have great ability and potential for specific and selective binding of HM ions and show excellent potential

for real application in the circular economy. For this reason, further investigation of the circular adsorption–desorption process for different HM ions (such as copper, iron, and cadmium) in a single or binary system should be carried out in the near future.

The use of functionalized magnetic nanomaterials as adsorbents in this study showed that they combine the advantages of magnetic properties—which allow the removal of pollutants from water using an external magnetic field—with the properties of other functional materials, improving their adsorption, separation, and regeneration properties. Such adsorption materials are capable of removing the main components of inorganic pollutants, such as heavy metal ions, under different concentrations and pH conditions, due to their chemical and physical stability.

At the same time, this study showed that such functional magnetic nanoparticles, in conjunction with existing treatment technologies, can offer tremendous potential for the effective treatment of water and wastewater. Due to their unique properties related to magnetism and their surface and structural properties, these adsorption materials offer many alternative applications in many other fields. Their use has been growing in recent years, particularly in the recycling of critical materials—including rare-earth elements, which are now used in all high-tech products and are almost impossible to replace because their properties are unique or "rare", which is why they are so highly valued, and their extraction and production pose major problems in terms of environmental pollution. In addition, such functionalized magnetic nanoparticles could also be effectively used to remove organic and biological pollutants such as organic dyes, fluoridated and chlorinated organic compounds, pesticides, bioactive compounds, etc., which are often found in groundwater, drinking water, and wastewater.

Despite the vast potential shown by functionalized magnetic nanomaterials as adsorbents, most of them are still at the laboratory research stage. The lack of legislation and regulation and the issue of toxicity of nanomaterials, which should also not be ignored, represent the major obstacles encountered in the remediation of water and wastewater with nanomaterials, while many other obstacles associated with their use are only temporary, such as high costs and technical handling.

Although many studies have been carried out on the adsorption of heavy metal ions, the mechanism of their interaction with adsorbents is, in many cases, not fully understood. Therefore, more research on the interactions between functionalized magnetic nanomaterials and pollutants is expected in the future, as they are of key importance for the design and improvement of the properties of adsorbents, but the lack of knowledge on their environmental and human impacts has to be taken into account in order to move towards a justification of their use in real environments.

Author Contributions: Conceptualization, A.L. and A.K.; Methodology, M.B. and A.K.; Validation, A.L.; Formal analysis, M.B., A.L. and A.K.; Investigation, A.L. and A.K.; Resources, N.D.; Data curation, M.L. and A.K.; Writing—original draft, M.B.; Writing—review & editing, A.F.P.A.M.R. and A.K.; Supervision, A.L. and A.K.; Project administration, A.L. and A.K.; Funding acquisition, A.L. All authors have read and agreed to the published version of the manuscript.

Funding: The project HMRecycle (E! 113543) has received funding from the Eurostars-2 joint program. We express our gratitude to the national funding organization—the Slovenian Ministry of Economic Development and Technology (MEDT)—for co-financing the project HMRecycle. This work is also supported by an international research project—the Marie Skłodowska-Curie Action "Global Mercury Observation and Training Network in Support to the Minamata Convention", financed under the funding line "excellent science" of the Horizon 2020 research and innovation program of the European Commission under the Marie Skłodowska-Curie grant agreement no. 860497. The results were obtained within the Research program "Design of New Properties of (Nano)materials and Applications", No. P2-0424, and the authors acknowledge the financial support from the Slovenian Research Agency. This research was also funded by the Ministry of Education, Science and Sport, Republic of Slovenia, and by the European Union through the European Regional Development Fund (ERDF), Early Research Careers 2.1 (Contract No. C3330-19-952032).

Institutional Review Board Statement: Not applicable.

Informed Consent Statement: Not applicable.

Conflicts of Interest: The authors declare that they have no conflict of interest.

References

1. Auerbach, R.; Bokelmann, K.; Stauber, R.; Gutfleisch, O.; Schnell, S.; Ratering, S. Critical raw materials—Advanced recycling technologies and processes: Recycling of rare earth metals out of end-of-life magnets by bioleaching with various bacteria as an example of an intelligent recycling strategy. *Miner. Eng.* **2019**, *134*, 104–117. [CrossRef]
2. European Commission; Blengini, G.; Latunussa, C.; Eynard, U.; Matos, C.; Georgitzikis, K.; Pavel, C.; Carrara, S.; Mancini, L.; Unguru, M.; et al. *Study on the EU's List of Critical Raw Materials (2020)*; Factsheets on Critical Raw Materials; Final Report; European Commission: Luxembourg, 2020. [CrossRef]
3. European Commission. *Critical Raw Materials for Strategic Technologies and Sectors in the EU, A Foresight Study*; European Commission: Luxembourg, 2020; ET-04-20-034-EN-N; ISBN 978-92-76-15336-8. [CrossRef]
4. Skirrow, R.G.; Huston, D.L.; Mernagh, T.P.; Thorne, J.P.; Dulfer, H.; Senior, A.B. *Critical Commodities for a High-Tech World: Australia's Potential to Supply Global Demand*; Geoscience Australia: Canberra, Australia, 2013.
5. Huang, H.; Wang, Y.; Zhang, Y.; Niu, Z.; Li, X. Amino-functionalized graphene oxide for Cr (VI), Cu (II), Pb (II) and Cd (II) removal from industrial wastewater. *Open Chem.* **2020**, *18*, 97–107. [CrossRef]
6. Girtan, M.; Wittenberg, A.; Grilli, M.L.; de Oliveira, D.P.S.; Giosuè, C.; Ruello, M.L. The Critical Raw Materials Issue be-tween Scarcity, Supply Risk, and Unique Properties. *Materials* **2021**, *14*, 1826. [CrossRef] [PubMed]
7. Agency for Toxic Substances and Disease Registry (ATSDR). The Priority List of Hazardous Substances. Available online: https://www.atsdr.cdc.gov/spl/index.html#2019spl (accessed on 30 August 2022).
8. Reddy, D.H.K.; Yun, Y.-S. Spinel ferrite magnetic adsorbents: Alternative future materials for water purification. *Coord. Chem. Rev.* **2016**, *315*, 90–111. [CrossRef]
9. Carolin, C.F.; Kumar, P.S.; Saravanan, A.; Joshiba, G.J.; Naushad, M. Efficient techniques for the removal of toxic heavy metals from aquatic environment: A Review. *J. Environ. Chem. Eng.* **2017**, *5*, 2782–2799. [CrossRef]
10. Shrestha, R.; Ban, S.; Devkota, S.; Sharma, S.; Joshi, R.; Tiwari, A.P.; Kim, H.Y.; Joshi, M.K. Technological trends in heavy metals removal from industrial wastewater: A review. *Resour. Conserv. Recycl.* **2020**, *156*, 105688. [CrossRef]
11. Zhang, Y.; Wang, Y.; Zhang, H.; Li, Y.; Zhang, Z.; Zhang, W. Recycling spent lithium-ion battery as adsorbents to remove aqueous heavy metals: Adsorption kinetics, isotherms, and regeneration assessment. *J. Environ. Chem. Eng.* 2021, in press. [CrossRef]
12. Dhiman, V.; Kondal, N. ZnO Nanoadsorbents: A potent material for removal of heavy metal ions from wastewater. *Colloid Interface Sci. Commun.* **2021**, *41*, 100380. [CrossRef]
13. Fu, X.; Feng, X.; Sommar, J.; Wang, S. A review of studies on atmospheric mercury in China. *Sci. Total Environ.* **2012**, *421–422*, 73–81. [CrossRef]
14. Mousavi, A.; Chávez, R.D.; Ali, A.-M.S.; Cabaniss, S.E. Mercury in natural waters: A mini-review. *Environ. Forensics* **2011**, *12*, 14–18. [CrossRef]
15. Wang, J.; Feng, X.; Anderson, C.W.N.; Xing, Y.; Shang, L. Remediation of mercury contaminated sites—A review. *J. Hazard. Mater.* **2012**, *221–222*, 1–18. [CrossRef]
16. Tuzen, M.; Soylak, M. Mercury contamination in mushroom samples from Tokat, Turkey. *Bull. Environ. Contam. Toxicol.* **2005**, *74*, 968–972. [CrossRef] [PubMed]
17. Hu, H.; Lin, H.; Zheng, W.; Tomanicek, S.J.; Johs, A.; Feng, X.; Elias, D.A.; Liang, L.; Gu, B. Oxidation and methylation of dissolved elemental mercury by anaerobic bacteria. *Nat. Geosci.* **2013**, *6*, 751–754. [CrossRef]
18. Unceta, N.; Seby, F.; Malherbe, J.; Donard, O.F.X. Chromium speciation in solid matrices and regulation: A review. *Anal. Bioanal. Chem.* **2010**, *397*, 1097–1111. [CrossRef] [PubMed]
19. Calik, S.; Sözüdogru, O.; Massara, T.M.; Yilmaz, A.E.; Bakirdere, S.; Katsou, E.; Komesli, O.T. Removal of heavy metals by a membrane bioreactor combined with activated carbon. *Anal. Lett.* **2020**, *54*, 1616–1626. [CrossRef]
20. Henze, M.; Comeau, Y. Wastewater characterization. In *Biological Wastewater Treatment: Principles Modelling and Design*; IWA Publishing: London, UK, 2008; pp. 33–52.
21. Crini, G.; Lichtfouse, E. Advantages and disadvantages of techniques used for wastewater treatment. *Environ. Chem. Lett.* **2019**, *17*, 145–155. [CrossRef]
22. Chen, Q.; Yao, Y.; Lia, X.; Lu, J.; Zhou, J.; Huang, Z. Comparison of heavy metal removals from aqueous solutions by chemical precipitation and characteristics of precipitates. *J. Water Process Eng.* **2018**, *26*, 289–300. [CrossRef]
23. Delil, A.D.; Köleli, N.; Dağhan, H.; Bahçeci, G. Recovery of heavy metals from canola (Brassica napus) and soybean (Glycine max) biomasses using electrochemical process. *Environ. Technol. Innov.* **2020**, *17*, 100559. [CrossRef]
24. Dong, L.; Hou, L.; Wang, Z.; Gu, P.; Chen, G.; Jiang, R. A new function of spent activated carbon in BAC process: Removing heavy metals by ion exchange mechanism. *J. Hazard. Mater.* **2018**, *359*, 76–84. [CrossRef]
25. Bauman, M.; Košak, A.; Lobnik, A.; Petrinić, I.; Luxbacher, T. Nanofiltration membranes modified with alkoxysilanes: Sur-face characterization using zeta-potential. *Colloids Surf. A Physicochem. Eng. Asp.* **2013**, *422*, 110–117. [CrossRef]
26. Peydayesh, M.; Mohammadi, T.; Nikouzad, S.K. A positively charged composite loose nanofiltration membrane for water purification from heavy metals. *J. Membr. Sci.* **2020**, *611*, 118205. [CrossRef]

27. Hargreaves, A.J.; Vale, P.; Whelan, J.; Alibardi, L.; Constantino, C.; Dotro, G.; Cartmell, E.; Campo, P. Impacts of coagula-tion-flocculation treatment on the size distribution and bioavailability of trace metals (Cu, Pb, Ni, Zn) in municipal wastewater. *Water Res.* **2018**, *128*, 120–128. [CrossRef] [PubMed]
28. Sun, Y.; Zhou, S.; Pan, S.-Y.; Zhu, S.; Yu, Y.; Zheng, H. Performance evaluation and optimization of flocculation process for removing heavy metal. *Chem. Eng. J.* **2020**, *385*, 123911. [CrossRef]
29. Al-Qahtani, K.M. Water purification using different waste fruit cortexes for the removal of heavy metals. *J. Taibah Univ. Sci.* **2016**, *10*, 700–708. [CrossRef]
30. Singh, N.B.; Nagpal, G.; Agrawal, S. Rachna, Water purification by using Adsorbents: A Review. *Environ. Technol. Innov.* **2018**, *11*, 187–240. [CrossRef]
31. Gul, A.; Khaligh, N.G.; Julkapli, N.M. Surface modification of Carbon-Based Nanoadsorbents for the Advanced Wastewater Treatment. *J. Mol. Struct.* **2021**, *1235*, 130148. [CrossRef]
32. Kegl, T.; Ban, I.; Lobnik, A.; Košak, A. Synthesis and characterization of novel γ-Fe_2O_3,NH_4OH@SiO_2(APTMS) nanoparticles for dysprosium adsorption. *J. Hazard. Mater.* **2019**, *378*, 120764. [CrossRef]
33. Da'na, E.; Awad, A. Regeneration of spent activated carbon obtained from home filtration system and applying it for heavy metals adsorption. *J. Environ. Chem. Eng.* **2017**, *5*, 3091–3099. [CrossRef]
34. Tang, Y.; Liang, S.; Wang, J.; Yu, S.; Wang, Y. Amino-functionalized core-shell magnetic mesoporous composite microspheres for Pb (II) and Cd (II) removal. *J. Environ. Sci.* **2013**, *25*, 830–837. [CrossRef]
35. Ahmadi, A.; Heidarzadeh, S.; Mokhtari, A.R.; Darezereshki, E.; Harouni, H.A. Optimization of heavy metal removal from aqueous solutions by maghemite (γ-Fe_2O_3) nanoparticles using response surface methodology. *J. Geochem. Explor.* **2014**, *147*, 151–158. [CrossRef]
36. Qian, J.; Yang, T.; Zhang, W.; Lei, Y.; Zhang, C.; Ma, J.; Zhang, C. Preparation of NH_2-Functionalized Fe_2O_3 and Its Chitosan Composites for the Removal of Heavy Metal Ions. *Sustainability* **2019**, *11*, 5186. [CrossRef]
37. Duan, C.; Ma, T.; Wang, J.; Zhou, Y. Removal of heavy metals from aqueous solution using carbon-based adsorbents: A review. *J. Water Process Eng.* **2020**, *37*, 101339. [CrossRef]
38. Aguayo-Villarreal, I.A.; Bonilla-Petriciolet, A.; Muñiz-Valencia, R. Preparation of activated carbons from pecan nutshell and their application in the antagonistic adsorption of heavy metal ions. *J. Mol. Liq.* **2017**, *230*, 686–695. [CrossRef]
39. Kołodyńska, D.J.; Krukowska, P. Thomas. Comparison of sorption and desorption studies of heavy metal ions from biochar and commercial active carbon. *Chem. Eng. J.* **2017**, *307*, 353–363, ISSN 1385-8947. [CrossRef]
40. Lo, S.-F.; Wang, S.-Y.; Tsai, M.-J.; Lin, L.-D. Adsorption capacity and removal efficiency of heavy metal ions by Moso and Ma bamboo activated carbons. *Chem. Eng. Res. Des.* **2012**, *90*, 1397–1406. [CrossRef]
41. Sujatha, S.; Sivarethinamohan, R. A critical review of Cr (VI) ion effect on mankind and its amputation through adsorption by activated carbon. *Mater. Today Proc.* **2021**, *37*, 1158–1162. [CrossRef]
42. You, J.; Wang, L.; Zhao, Y.; Bao, W. A review of amino-functionalized magnetic nanoparticles for water treatment: Features and prospects. *J. Clean. Prod.* **2021**, *281*, 124668. [CrossRef]
43. Wang, J.; Zheng, S.; Shao, Y.; Liu, J.; Xu, Z.; Zhu, D. Amino-functionalized Fe_3O_4@SiO_2 core–shell magnetic nanomaterial as a novel adsorbent for aqueous heavy metals removal. *J. Colloid Interface Sci.* **2010**, *349*, 293–299. [CrossRef]
44. Zhao, Y.-G.; Shen, H.-Y.; Pan, S.-D.; Hu, M.-Q.; Xia, Q.-H. Preparation and characterization of ami-no-functionalized nano-Fe_3O_4 magnetic polymer adsorbents for removal of chromium (VI) ions. *J. Mater. Sci.* **2010**, *45*, 5291–5301. [CrossRef]
45. Yavuz, C.T.; Mayo, J.T.; Yu, W.W.; Prakash, A.; Falkner, J.C.; Yean, S.; Colvin, V.L. Low-Field Magnetic Separation of Monodisperse Fe_3O_4 Nanocrystals. *Science* **2006**, *314*, 964–967. [CrossRef]
46. Ritu, D. Ambashta, Mika Sillanpaa. Water purification using magnetic assistance: A review. *J. Hazard. Mater.* **2010**, *180*, 38–49. [CrossRef]
47. Mandel, K.; Hutter, F.; Gellermann, C.; Sextl, G. Modified Superparamagnetic Nanocomposite Microparticles for Highly Selective Hg(II) or Cu(II) Separation and Recovery from Aqueous Solutions. *ACS Appl. Mater. Interfaces* **2012**, *4*, 5633–5642. [CrossRef] [PubMed]
48. Kim, J.S.; Yoon, T.-J.; Yu, K.N.; Kim, B.G.; Park, S.; Kim, H.W.; Lee, K.H.; Park, S.B.; Lee, J.-K.; Cho, M.H. Toxicity and tissue distribution of magnetic nanoparticles in mice. *Toxicol. Sci.* **2006**, *89*, 338–347. [CrossRef] [PubMed]
49. Jane Cypriyana, J.P.J.; Saigeetha, S.; Lavanya Agnes Angalene, J.; Samrot, A.V.; Suresh Kumar, S.; Ponniah, P.; Chakravarthi, S. Overview on toxicity of nanoparticles, its mechanism, models used in toxicity studies and disposal methods. *Biocatal. Agric. Biotechnol.* **2021**, *36*, 102117. [CrossRef]
50. Douglas, L.A.; Baugher Brigitta, M.; Baugher Collen, R.; Schneider Duane, A.; Rahimian, K. Substituent effects on the sol-gel chemistry of organotrialkoxysilanes. *Chem. Mater. Am. Chem. Soc.* **2000**, *12*, 3624–3632. [CrossRef]
51. Brinker, C.J.; Scherer, G.W. *Sol-Gel Science: The Physics and Chemistry of Sol-Gel Processing*; Academic Press: Cambridge, UK, 1990; ISBN 0-12-134970-5.
52. Osterholtz, F.D.; Pohl, E.R. Kinetics of the hydrolysis and condensation of organofunctional alkoxysilanes: A review. *J. Adhes. Sci. Technol.* **1992**, *6*, 127–149. [CrossRef]
53. Colilla, M.; Vallet-Regí, M. Biocompatibility, Surface Engineering, and Delivery of Drugs, Genes and Other Molecules. In *Comprehensive Biomaterials II*; Elsevier: Amsterdam, The Netherlands, 2017. [CrossRef]

54. Zhang, J.; Zhai, S.; Li, S.; Xiao, Z.; Song, Y.; An, Q.; Tian, G. Pb (II) removal of Fe_3O_4@SiO_2–NH_2 core–shell nanomaterials prepared via a controllable sol–gel process. *Chem. Eng. J.* **2013**, *215–216*, 461–471. [CrossRef]
55. Liu, Q.; Liu, Q.; Liu, B.; Hu, T.; Liu, W.; Yao, J. Green synthesis of tannin-hexamethylendiamine based adsorbents for efficient removal of Cr (VI). *J. Hazard. Mater.* **2018**, *352*, 27–35. [CrossRef]
56. Pradhan, D.; Sukla, L.B.; Sawyer, M.; Rahman, P.K.; Rahman, S.M. Recent bioreduction of hexavalent chromium in wastewater treatment: A review. *J. Ind. Eng. Chem.* **2017**, *55*, 1–20. [CrossRef]
57. Takeno, N. Atlas of Eh-pH Diagrams, Intercomparison of Thermodynamic Databases, Geological Survey of Japan Open File Report No. 419, National Institute of Advanced Industrial Science and Technology, Research Center for Deep Geological Environments. May 2005. Available online: https://www.nrc.gov/docs/ML1808/ML18089A638.pdf (accessed on 30 August 2022).
58. De Zoubov, N.; Pourbaix, M. Mercury. In *Atlas of Electrochemical Equilibria in Aqueous Solutions*; Pourbaix, M., Ed.; Section 15.3; Pergamon Press: Oxford, UK, 1966.
59. Baes, C.F.; Mesmer, R.E. *The Hydrolysis of Cations*, 2nd ed.; Kreiger: New York, NY, USA, 1986.
60. Kipton J Powell; Brown, P.L.; Byrne, R.H.; Gajda, T.; Hefter, G.; Sjöberg, S.; Wanner, H.; Hefter, G. Chemical Speciation of Environmentally Significant Heavy Metals with Inorganic Ligands, Part 1: The Hg^{2+}-Cl^-, OH^-, CO_3^{2-}, SO_4^{2-}, and PO_4^{3-} Aqueous Systems. *Pure Appl. Chem.* **2005**, *77*, 739–800. [CrossRef]
61. Sun, M.; Li, P.; Jin, X.; Ju, X.; Yan, W.; Yuan, J.; Xing, C. Heavy metal adsorption onto graphene oxide, amino group on magnetic nanoadsorbents and application for detection of Pb (II) by strip sensor. *Food Agric. Immunol.* **2018**, *29*, 1053–1073. [CrossRef]
62. Li, X.; Wang, S.; Liu, Y.; Jiang, L.; Song, B.; Li, M.; Ding, Y. Adsorption of Cu(II), Pb(II), and Cd(II) ions from acidic aqueous solutions by diethylenetriaminepentaacetic acid-modified magnetic graphene oxide. *J. Chem. Eng. Data* **2017**, *62*, 407–416. [CrossRef]
63. Shahbazi, A.; Younesi, H.; Badiei, A. Functionalized SBA-15 mesoporous silica by Melamine-based dendrimer amines for adsorptive characteristics of Pb(II), Cu(II), and Cd(II) heavy metal ions in batch and fixed bed column. *Chem. Eng. J.* **2011**, *168*, 505–518. [CrossRef]
64. Zhao, G.; Ren, X.; Gao, X.; Tan, X.; Li, J.; Chen, C.; Wang, X. Removal of Pb(II) ions from aqueous solutions on few-layered graphene oxide nanosheets. *Dalton Trans.* **2011**, *40*, 10945–10952. [CrossRef] [PubMed]
65. Nassar, N.N. Rapid removal and recovery of Pb(II) from wastewater by magnetic nano adsorbents. *J. Hazard. Mater.* **2010**, *184*, 538–546. [CrossRef] [PubMed]
66. Jawed, A.; Saxena, V.; Pandey, L.M. Engineered nanomaterials and their surface functionalization for the removal of heavy metals: A review. *J. Water Process Eng.* **2020**, *33*, 101009. [CrossRef]
67. Naseem, T.; Durrani, T. The role of some important metal oxide nanoparticles for wastewater and antibacterial applications: A review. *Environ. Chem. Ecotoxicol.* **2021**, *3*, 59–75. [CrossRef]
68. Samrot, A.V.; Sahithya, C.S.; Selvarani, A.J.; Purayil, S.K.; Ponnaiah, P. A review on synthesis, characterization and potential biological applications of superparamagnetic iron oxide nanoparticles. *Curr. Res. Green Sustain. Chem.* **2021**, *4*, 100042. [CrossRef]
69. Shokrollahi, H. A review of the magnetic properties, synthesis methods and applications of maghemite. *J. Magn. Magn. Mater.* **2017**, *426*, 74–81. [CrossRef]
70. Yang, J.; Hou, B.; Wang, J.; Tian, B.; Bi, J.; Wang, N.; Li, X.; Huang, X. Nanomaterials for the Removal of Heavy Metals from Wastewater. *Nanomaterials* **2019**, *9*, 424. [CrossRef]
71. Yong-Mei, H.; Man, C.; Zhong-Bo, H. Effective removal of Cu (II) ions from aqueous solution by ami-no-functionalized magnetic nanoparticles. *J. Hazard. Mater.* **2010**, *184*, 392–399. [CrossRef]
72. Gallo-Cordova, A.; Morales, M.d.P.; Mazario, E. Effect of the Surface Charge on the Adsorption Capacity of Chromium (VI) of Iron Oxide Magnetic Nanoparticles Prepared by Microwave-Assisted Synthesis. *Water* **2019**, *11*, 2372. [CrossRef]
73. Srikhaow, A.; Butburee, T.; Pon-On, W.; Srikhirin, T.; Uraisin, K.; Suttiponpanit, K.; Chaveanghong, S.; Smith, S.M. Efficient Mercury Removal at Ultralow Metal Concentrations by Cysteine Functionalized Carbon-Coated Magnetite. *Appl. Sci.* **2020**, *10*, 8262. [CrossRef]
74. Mandela, K.; Huttera, F. The magnetic nanoparticle separation problem. *Nano Today* **2012**, *7*, 485–487. [CrossRef]
75. Kegl, T.; Košak, A.; Lobnik, A.; Novak, Z.; Kralj, A.K.; Ban, I. Adsorption of rare earth metals from wastewater by nano-materials: A review. *J. Hazard. Mater.* **2019**, *378*, 120764. [CrossRef]
76. Bhateria, R.; Singh, R. A review on nanotechnological application of magnetic iron oxides for heavy metal removal. *J. Water Process Eng.* **2019**, *31*, 100845. [CrossRef]
77. Jainae, K.; Sukpirom, N.; Fuangswasdi, S.; Unob, F. Adsorption of Hg (II) from aqueous solutions by thiol-functionalized polymer-coated magnetic particles. *J. Ind. Eng. Chem.* **2015**, *23*, 273–278. [CrossRef]
78. Viltužnik, B.; Lobnik, A.; Košak, A. The removal of Hg (II) ions from aqueous solutions by using thi-ol-functionalized cobalt ferrite magnetic nanoparticles. *J. Sol-Gel Sci. Technol.* **2015**, *74*, 199–207. [CrossRef]
79. Chen, Z.; Geng, Z.; Zhang, Z.; Ren, L.; Tao, T.; Yang, R.; Guo, Z. Synthesis of Magnetic Fe_3O_4@C Nanoparticles Modified with–SO_3H and –COOH Groups for Fast Removal of Pb^{2+}, Hg^{2+}, and Cd^{2+} Ions. *Eur. J. Inorg. Chem.* **2014**, *2014*, 3172–3177. [CrossRef]
80. Marimón-Bolívar, W.; Tejeda-Benítez, L.; Herrera, A.P. Removal of mercury (II) from water using magnetic nanoparticles coated with amino organic ligands and yam peel biomass. *Environ. Nanotechnol. Monit. Manag.* **2018**, *10*, 486–493. [CrossRef]

81. Maitlo, H.A.; Kim, K.-H.; Kumar, V.; Kim, S.; Park, J.-W. Nanomaterials-based treatment options for chromium in aqueous environments. *Environ. Int.* **2019**, *130*, 104748. [CrossRef] [PubMed]
82. Nicola, R.; Costisor, O.; Ciopec, M.; Negrea, A.; Lazau, R.; Ianasi, C.; Piciorus, E.-M.; Len, A.; Almásy, L.; Szerb, E.I.; et al. Silica-Coated Magnetic Nanocomposites for Pb^{2+} Removal from Aqueous Solution. *Appl. Sci.* **2020**, *10*, 2726. [CrossRef]
83. Kakavandi, B.; Kalantary, R.R.; Jafari, A.J.; Nasseri, S.; Ameri, A.; Esrafili, A.; Azari, A. Pb (II) adsorption onto a magnetic composite of activated carbon and superparamagnetic Fe_3O_4 nanoparticles:Experimental and modeling study. *CLEAN–Soil Air Water* **2015**, *43*, 1157–1166. [CrossRef]
84. Tao, Y.; Zhang, C.; Lü, T.; Zhao, H. Removal of Pb(II) Ions from Wastewater by Using Polyethyleneimine-Functionalized Fe_3O_4 Magnetic Nanoparticles. *Appl. Sci.* **2020**, *10*, 948. [CrossRef]
85. Gutiérrez-López, D.N.; Flores-Alamo, M.C.; Carreño-de-León, M.C.; Solache-Rios, M.J. Removal of Pb (II) from aqueous solution by using microspheres of Zea mays rachis–sodium alginate by batch and column systems. *Water Supply* **2020**, *20*, 2133–2144. [CrossRef]
86. Luo, Q.; Liu, G.; Wang, L.; Wang, W.; Wang, Y.; Wang, H.; Xu, W. Efficient removal of lead ions from aqueous solution using C-TiO_2 adsorbent. *IOP Conf. Ser. Earth Environ. Sci.* **2021**, *865*, 012040. [CrossRef]
87. Zhang, J.; Lin, S.; Han, M.; Su, Q.; Xia, L.; Hui, Z. Adsorption Properties of Magnetic Magnetite Nanoparticle for Coexistent Cr (VI) and Cu (II) in Mixed Solution. *Water* **2020**, *12*, 446. [CrossRef]
88. Hu, J.; Chen, G.; Lo, I.M.C. Removal and recovery of Cr (VI) from wastewater by maghemite nanoparticles. *Water Res.* **2005**, *39*, 4528–4536. [CrossRef]
89. Baghani, A.N.; Mahvi, A.H.; Gholami, M.; Rastkari, N.; Delikhoon, M. One-Pot synthesis, characterization and adsorption studies of amine-functionalized magnetite nanoparticles for removal of Cr (VI) and Ni (II) ions from aqueous solution: Ki-netic, isotherm and thermodynamic studies. *J. Environ. Health Sci. Eng.* **2016**, *14*, 11. [CrossRef]
90. Trang, V.T.; Tam, L.T.; van Quy, N.; Phan, V.N.; van Tuan, H.; Huy, T.Q.; Dinh, N.X.; Le, A.-T. Enhanced adsorption efficiency of inorganic chromium (VI) ions by using carbonencapsulated hematite nanocubes. *J. Sci. Adv. Mater. Devices* **2020**, *5*, 392–399. [CrossRef]
91. Puszkarewicz, A.; Kaleta, J. Chromium (VI) Adsorption on Modified Activated Carbons. *Appl. Sci.* **2019**, *9*, 3549. [CrossRef]
92. Bafrooee, A.A.T.; Panahi, H.A.; Moniri, E.; Miralinaghi, M.; Hasani, A.H. Removal of Hg^{2+} by carboxyl-terminated hyper-branched poly(amidoamine) dendrimers grafted superparamagnetic nanoparticles as an efficient adsorbent. *Environ. Sci. Pollut. Res.* **2020**, *27*, 9547–9567. [CrossRef] [PubMed]
93. Wang, Z.; Wu, D.; Wu, G.; Yang, N.; Wu, A. Modifying Fe_3O_4 microspheres with rhodamine hydrazide for se-lective detection and removal of Hg^{2+} ion in water. *J. Hazard. Mater.* **2013**, *244–245*, 621–627. [CrossRef] [PubMed]
94. Pan, S.; Shen, H.; Xu, Q.; Luo, J.; Hu, M. Surface mercapto engineered magnetic Fe_3O_4 nanoadsorbent for the removal of mercury from aqueous solutions. *J. Colloid Interface Sci.* **2012**, *365*, 204–212. [CrossRef]
95. Morsi, R.E.; Al-Sabagh, A.M.; Moustafa, Y.M.; ElKholy, S.G.; Sayed, M.S. Polythiophene modified chitosan/magnetite nanocom-posites for heavy metals and selective mercury removal. *Egyption J. Pet.* **2018**, *27*, 1077–1085. [CrossRef]
96. Chen, D.; Awut, T.; Liu, B.; Ma, Y.; Wang, T.; Nurulla, I. Functionalized magnetic Fe_3O_4 nanoparticles for removal of heavy metal ions from aqueous solutions. *E-Polym.* **2016**, *16*, 313–322. [CrossRef]
97. Hao, Y.; Pan, Y.; Du, Q.; Li, X.; Wang, X. Nanoparticle Fe_3O_4 magnetized activated carbon from Armeniaca sibirica shell for the adsorption of Hg(II) ions. *BioResources* **2021**, *16*, 6100–6120. [CrossRef]
98. Zhang, X.; Hao, Y.; Wang, X.; Chen, Z.; Li, C. Competitive Adsorption of Cadmium(II) and Mercury(II) Ions from Aqueous Solutions by Activated Carbon from Xanthoceras sorbifolia Bunge Hull. *J. Chem.* **2016**, 4326351. [CrossRef]
99. Sereshti, H.; Gaikani, H.; Rashidi Nodeh, H. The effective removal of mercury ions (Hg^{2+}) from water using cadmium sulfide nanoparticles doped in polycaprolactam nanofibers: Kinetic and equilibrium studies. *J. Iran. Chem. Soc.* **2018**, *15*, 743–751. [CrossRef]
100. Cullity, B.D.; Stock, S.R. *Elements of X-Ray Diffraction*, 3rd ed.; Prentice-Hall Inc.: Hoboken, NJ, USA, 2001; pp. 96–102. ISBN 0-201-61091-4.
101. Patterson, A. The Scherrer Formula for X-Ray Particle Size Determination. *Phys. Rev.* **1939**, *56*, 978–982. [CrossRef]
102. Pérez-Quintanilla, D.; del Hierro, I.; Fajardo, M.; Sierra, I. Mesoporous silica functionalized with 2-mercaptopyridine: Synthesis, characterization and employment for Hg (II) adsorption. *Microporous Mesoporous Mater.* **2006**, *89*, 58–68. [CrossRef]
103. Pérez-Quintanilla, D.; del Hierro, I.; Fajardo, M.; Sierra, I. 2-Mercaptothiazoline modified mesoporous silica for mercury removal from aqueous media. *J. Hazard. Mater.* **2006**, *134*, 245–256. [CrossRef] [PubMed]
104. Pérez-Quintanilla, D.; del Hierro, I.; Fajardo, M.; Sierra, I. Preparation of 2-mercaptobenzothiazole-derivatized mesoporous silica and removal of Hg (II) from aqueous solution. *J. Environ. Monit.* **2006**, *8*, 214–222. [CrossRef] [PubMed]
105. Liang, R.; Zou, H. Removal of aqueous Hg (II) by thiol-functionalized nonporous silica microspheres prepared by one-step sol–gel method. *RSC Adv.* **2020**, *10*, 18534–18542. [CrossRef] [PubMed]
106. Atul Kumar, M.; Sharma, A.; Maurya, I.K.; Thakur, A.; Kumar, S. Synthesis of ultra-small iron oxide and doped iron oxide nanostructures and their antimicrobial activities. *J. Taibah Univ. Sci.* **2019**, *13*, 280–285. [CrossRef]
107. Smith, B. *Infrared Spectral Interpretation, A Systematic Approach*; CRC Press: Boca Raton, FL, USA, 1999; 288p.

108. Sing, K.S.W.; Everett, D.H.; Haul, R.A.W.; Moscou, L.; Pierotti, R.A.; Rouquerol, J.; Siemieniewska, T. Reporting Physisorption Data for Gas-Solid Systems with Special Reference to the Determination of Surface-Area and Porosity. *Pure Appl. Chem.* **1985**, *57*, 603. [CrossRef]
109. Rouquerol, F.; Rouquerol, J.; Sing, K. *Adsorption by Powders and Porous Solids*; Academic Press: San Diego, CA, USA, 1999; ISBN 0-12-598920-2.
110. Zasonska, B.A.; Liškova, A.; Kuricova, M.; Tulinska, J.; Pop-Georgievski, O.; Čiampor, F.; Vavra, I.; Dušinska, M.; Ilavska, S.; Horvathova, M.; et al. Functionalized porous silica&maghemite core-shell nanoparticles for applications in medicine: Design, synthesis, and immunotoxicity. *Croat. Med. J.* **2016**, *57*, 165–178. [CrossRef]
111. Sun, M.; Cheng, G.; Ge, X.; Chen, M.; Wang, C.; Lou, L.; Xu, X. Aqueous Hg (II) immobilization by chitosan stabilized magnetic iron sulfide nanoparticles. *Sci. Total Environ.* **2018**, *621*, 1074–1083. [CrossRef]
112. Roy, A.; Bhattacharya, J. *Nanotechnology in Industrial Wastewater Treatment*; IWA Publishing: Durham, NC, USA, 2014; Volume 13. [CrossRef]
113. Dinker, M.K.; Kulkarni, P.S. Recent Advances in Silica-Based Materials for the Removal of Hexavalent Chromium: A Review. *J. Chem. Eng. Data* **2015**, *60*, 2521–2540. [CrossRef]
114. Alqadami, A.; Naushad, M.; Abdalla, M.A.; Anhamad, T.; Alothman, Z.A.; Alshehri, S.M. Sythesis and characterization of Fe_3O_4@TSC nanocomposite: Highly efficient removal of toxic metal ions from aqueous medium. *RSC Adv.* **2016**, *6*, 22679–22689. [CrossRef]
115. Gallios, G.P.; Vaclavikova, M. Removal of chromium (VI) from water streams: A thermodynamic study. *Environ. Chem. Lett.* **2008**, *6*, 235–240. [CrossRef]
116. Ghasemi, Z.; Seif, A.; Ahmadi, T.S.; Zargar, B.; Rashidi, F.; Rouzbahani, G.M. Thermodynamic and kinetic studies for the adsorption of Hg (II) by nano-TiO_2 from aqueous solution. *Adv. Powder Technol.* **2012**, *23*, 148–156. [CrossRef]
117. López-Muñoz, M.J.; Arencibia, A.; Cerro, L.; Pascual, R.; Melgar, Á. Adsorption of Hg (II) from aqueous solutions using TiO_2 and titanate nanotube adsorbents. *Appl. Surf. Sci.* **2016**, *367*, 91–100. [CrossRef]

3.3 Publications 3

Summary of Publication 3: As global industrial activities surge, the demand for sustainable solutions to remediate toxic toxic metals and recover valuable rare earth elements (REEs) has become increasingly urgent. Mercury (Hg^{2+}), with its notorious toxicity and bioaccumulative nature, continues to pose grave environmental and public health challenges. Meanwhile, rare earth elements like dysprosium (Dy^{3+}) and terbium (Tb^{3+})—critical for high-tech applications in electronics, magnets, and clean energy technologies—face supply instability, driving the need for efficient recycling techniques. This dual challenge—removing harmful metals while reclaiming valuable resources—has inspired a wave of innovation in material science. This article contributes significantly to that effort, focusing on the design and evaluation of superparamagnetic spinel-ferrite nano-adsorbents for both removal and recovery of Hg^{2+}, Dy^{3+}, and Tb^{3+} ions from aqueous environments.

At the heart of this study is the synthesis of multi-component spinel ferrite nanoparticles, engineered through a sol–gel auto-combustion technique, which allows precise control over chemical composition and crystallinity. These nanomaterials are specifically tailored to possess superparamagnetic properties, enabling easy separation from solution using external magnetic fields—an essential trait for real-world wastewater remediation. Through systematic variation of the cationic content (e.g., Co^{2+}, Mn^{2+}, Zn^{2+}, Ni^{2+}), the study demonstrates how material properties such as surface charge, adsorption affinity, and magnetic responsiveness can be finely tuned.

The article presents a thorough characterization of the nano-adsorbents, employing an array of physicochemical techniques such as X-ray diffraction (XRD), scanning electron microscopy (SEM), transmission electron microscopy (TEM), Brunauer–Emmett–Teller (BET) surface area analysis, and vibrating sample magnetometry (VSM). These tools help to elucidate the crystalline structure, surface morphology, porosity, and magnetic behavior of the materials, all of which play crucial roles in determining their adsorption performance.

A key strength of this work lies in its comparative adsorption analysis for the target ions. The authors conduct batch adsorption experiments to evaluate the efficiency, selectivity, kinetics, and reusability of the nanomaterials. The results are promising: the optimized spinel ferrites exhibit high adsorption capacities for Hg^{2+}, Dy^{3+}, and Tb^{3+}, governed by pseudo-second-order kinetics and Langmuir-type isotherms, indicative of monolayer chemisorption on a homogeneous surface. Importantly, these materials show excellent regeneration potential over multiple adsorption–desorption cycles, making them practical candidates for both remediation and resource recovery.

The article also makes a significant contribution by addressing the biosafety of the nano-adsorbents. Recognizing the potential ecological risks associated with nanoparticle release, the study includes a toxicological assessment using Artemia salina (brine shrimp) bioassays. The findings reveal low toxicity of the synthesized nanoparticles, suggesting that these materials are environmentally benign under realistic exposure conditions.

From an application perspective, the dual functionality of these nano-adsorbents—in detoxifying water systems from mercury while selectively capturing valuable REEs—marks a noteworthy step toward circular economy principles in environmental nanotechnology. The research aligns well with emerging goals in sustainable development, environmental health, and resource recovery.

In conclusion, this article offers a robust, multidisciplinary approach combining materials engineering, environmental chemistry, and ecotoxicology to develop smart, magnetic nano-adsorbents for critical environmental applications. The findings pave the way for scalable implementation in water purification technologies, especially in contexts where toxic metal contamination and REE recovery converge.

International Journal of *Molecular Sciences*

MDPI

Article

Superparamagnetic Spinel-Ferrite Nano-Adsorbents Adapted for Hg^{2+}, Dy^{3+}, Tb^{3+} Removal/Recycling: Synthesis, Characterization, and Assessment of Toxicity

A. F. P. Allwin Mabes Raj [1,2,3], Maja Bauman [3], Nena Dimitrušev [3,4], Lamiaa M. A. Ali [5], Mélanie Onofre [5], Magali Gary-Bobo [5], Jean-Olivier Durand [6], Aleksandra Lobnik [3,4] and Aljoša Košak [4,*]

1 Jožef Stefan International Postgraduate School, Jamova 39, 1000 Ljubljana, Slovenia; allwinamc10@gmail.com
2 Department of Environmental Science, Jožef Stefan Institute, Jamova 39, 1000 Ljubljana, Slovenia
3 Institute for Environmental Protection and Sensors (IOS) Ltd., Beloruska 7, 2000 Maribor, Slovenia
4 Faculty for Mechanical Engineering, University of Maribor, Smetanova 17, 2000 Maribor, Slovenia
5 IBMM, Univ Montpellier, CNRS, ENSCM, 34293 Montpellier, France
6 ICGM, Univ Montpellier, CNRS, ENSCM, 34293 Montpellier, France
* Correspondence: aljosa.kosak@um.si

Abstract: In the present work, superparamagnetic adsorbents based on 3-aminopropyltrimethoxy silane (APTMS)-coated maghemite (γFe_2O_3@SiO_2–NH_2) and cobalt ferrite ($CoFe_2O_4$@SiO_2–NH_2) nanoparticles were prepared and characterized using transmission-electron microscopy (TEM/HRTEM/EDXS), Fourier-transform infrared spectroscopy (FTIR), specific surface-area measurements (BET), zeta potential (ζ) measurements, thermogravimetric analysis (TGA), and magnetometry (VSM). The adsorption of Dy^{3+}, Tb^{3+}, and Hg^{2+} ions onto adsorbent surfaces in model salt solutions was tested. The adsorption was evaluated in terms of adsorption efficiency (%), adsorption capacity (mg/g), and desorption efficiency (%) based on the results of inductively coupled plasma optical emission spectrometry (ICP-OES). Both adsorbents, γFe_2O_3@SiO_2–NH_2 and $CoFe_2O_4$@SiO_2–NH_2, showed high adsorption efficiency toward Dy^{3+}, Tb^{3+}, and Hg^{2+} ions, ranging from 83% to 98%, while the adsorption capacity reached the following values of Dy^{3+}, Tb^{3+}, and Hg^{2+}, in descending order: Tb (4.7 mg/g) > Dy (4.0 mg/g) > Hg (2.1 mg/g) for γFe_2O_3@SiO_2–NH_2; and Tb (6.2 mg/g) > Dy (4.7 mg/g) > Hg (1.2 mg/g) for $CoFe_2O_4$@SiO_2–NH_2. The results of the desorption with 100% of the desorbed Dy^{3+}, Tb^{3+}, and Hg^{2+} ions in an acidic medium indicated the reusability of both adsorbents. A cytotoxicity assessment of the adsorbents on human-skeletal-muscle derived cells (SKMDCs), human fibroblasts, murine macrophage cells (RAW264.7), and human-umbilical-vein endothelial cells (HUVECs) was conducted. The survival, mortality, and hatching percentages of zebrafish embryos were monitored. All the nanoparticles showed no toxicity in the zebrafish embryos until 96 hpf, even at a high concentration of 500 mg/L.

Keywords: nanomaterials; iron oxides; maghemite; cobalt ferrite; adsorption; transition metals; cytotoxicity; terbium; dysprosium; mercury

check for updates

Citation: Allwin Mabes Raj, A.F.P.; Bauman, M.; Dimitrušev, N.; Ali, L.M.A.; Onofre, M.; Gary-Bobo, M.; Durand, J.-O.; Lobnik, A.; Košak, A. Superparamagnetic Spinel-Ferrite Nano-Adsorbents Adapted for Hg^{2+}, Dy^{3+}, Tb^{3+} Removal/Recycling: Synthesis, Characterization, and Assessment of Toxicity. *Int. J. Mol. Sci.* **2023**, *24*, 72. https://doi.org/10.3390/ijms241210072

Academic Editor: Gangho Lee

Received: 4 April 2023
Revised: 22 May 2023
Accepted: 26 May 2023
Published: 13 June 2023

1. Introduction

Transition metals (TM) and internal transition metals (ITM), often referred to as d- and f-block elements, respectively, are key raw materials for the European economy, forming a strong industrial base that produces a wide range of products and applications used in everyday life and modern technologies. Many of these metals are considered to be highly toxic and have negative environmental and human health effects due to anthropogenic factors (e.g., mercury, lead, chromium, etc.). Furthermore, both groups also include strategic metals, such as rare-earth metals (e.g., dysprosium, terbium, samarium, neodymium, etc.), which are in increasing demand and subject to supply risks. Therefore, reliable and unhindered access to these raw materials is a growing concern in the EU and globally [1–5].

Of these metals, mercury (Hg) is particularly noteworthy. It can be found in many common devices, from thermometers, barometers, thermostats, and pressure gauges to fluorescent lamps, etc., and it is considered to be the most toxic heavy metal in the environment, particularly due to its high bioaccumulation and biomagnification capacity [6]. This is because spilled elemental mercury (Hg^0) is converted by microbial processes in the environment, particularly in water, into an organic form called methylmercury (MeHg), which is the most toxic form of mercury. Methylmercury is then transferred to fish and other wildlife and, eventually, it can be ingested, causing adverse health effects [6,7].

The removal of toxic metals, such as mercury, from the environment plays a significant role in minimizing their environmental and human health effects, while the recycling of essential and precious transition metals, such as platinum, palladium, gold, silver, rhodium, iridium, ruthenium, cobalt, niobium, tungsten, etc., and rare-earth metals, such as terbium, dysprosium, neodymium, lanthanum, samarium, cerium, etc., from e-waste and other raw waste materials, is of major importance to increase the availability of secondary resources, as well as improving the knowledge base that provides prerequisites for a circular economy on a larger scale than today [1,6,8–10]. Generally, current processing/removal technologies include, but are not limited to, hydrometallurgy (solvent extraction, ion exchange, precipitation, and crystallization), pyrometallurgy, electrometallurgy (electrorefining, and electrowinning), and aeriometallurgy (supercritical fluid extraction) [11,12].

All these technologies have many disadvantages. Pyrometallurgy is energy-intensive and generates greenhouse gas (GHG) emissions, while hydrometallurgy relies on large volumes of acids and organic solvents, thus generating hazardous wastes [13–15]. The primary disadvantage of aeriometallurgy is that the extraction must be operated at the high pressure (1000–5000 psi) required to maintain the solvent in a supercritical state using supercritical CO_2 [16]. In electrometallurgy, an inert atmosphere is usually required for recycling related to operational and maintenance drawbacks, while the recycling of raw metals can generate a small volume of waste, which is not yet developed, qualified, certified, or accepted. However, the electrometallurgy process also features the drawbacks of huge energy consumption for heating and electrolytic reduction and potential chlorine-gas emission [17,18].

An attractive alternative to these technologies is the solid-phase extraction (SPE) of metal ions from the solution using nanostructured materials as adsorbents, characterized by surface functionality, high surface-to-volume ratio, and/or porosity [19,20]. The use of SPE involves the adsorption of the target-metal ions from the solution onto the adsorbent surface followed by the subsequent recycling of the metals and the regeneration of the adsorbents [21,22]. The advantages of SPE include its low solvent consumption, ease of use, efficient removal of metal ions, even at low concentrations, and automation capabilities.

In the last decade, ferrimagnetic iron-oxide nanoparticles (NPs) have received special attention in the field of adsorbents, as reported in many reviews [23–26]. Magnetite (Fe_3O_4) and maghemite (γFe_2O_3) are the main types of ferrimagnetic NP, and so far, they have received considerable attention due to their nontoxicity and biocompatibility [27–29], as well as their ability to be easily dispersed and collected using an external magnetic field [30–32]. These ferrimagnetic materials, when reduced to particle dimensions smaller than a certain domain, exhibit superparamagnetic behavior, which means that when an external magnetic field is applied, they magnetize to saturation magnetization (σ_s), but when the magnetic field is removed, they no longer exhibit either residual magnetism (M_r) or coercivity (H_c) [33]. Hence, superparamagnetic iron-oxide NPs can be easily guided in the magnetic field [25,27,34,35]. One prominent example is the introduction of cobalt (Co^{2+}) ions into an iron-oxide spinel crystal lattice. Cobalt-doped iron oxides, also known as cobalt ferrites ($CoFe_2O_4$), arouse interest in adsorption applications as their magneto-crystalline anisotropy, which affects the magnetization, coercivity, reversal, and relaxation of nanoparticles, can be tuned by the substitution of cobalt for iron [36–40].

Due to the increasing use of iron-oxide NPs as adsorbents in the recycling of strategic transition metals, there is a high likelihood that these NPs may ultimately enter aquatic

ecosystems through effluent discharge and leaching during or after recycling activities, thereby affecting the environment and human health. Unfortunately, there is a serious lack of accurate and sufficient information on their toxic effects. Therefore, toxicity assessment has become increasingly important to understand the impact of these NPs on human health and the environment [41].

In many studies, it was found that uncoated NPs usually tend to be more toxic than coated particles; therefore, the surface modification of uncoated NPs can significantly reduce their toxicity [41–49]. Other studies revealed significant cytotoxic effects of these NPs, such as inflammation, the formation of apoptotic bodies, impaired mitochondrial function (MTT), the leakage of membrane lactate dehydrogenase (LDH assay), the generation of reactive oxygen species (ROS), increases in the number of micronuclei as indicators of gross chromosomal damage (a measure of genotoxicity), and chromosome condensation [44,48,50–54].

Furthermore, little is known about the toxicity of the metal dopants of iron-oxide NPs such as cobalt (Co^{2+}). The potential toxicity of cobalt-doped iron oxide ($CoFe_2O_4$) is therefore the subject of many debates concerning environmental, health, and safety issues, particularly their use in the environment and their effects on human health [28,44,55–62].

One of the simplest ways to modify the surfaces of NPs is to use alkoxysilanes, which are considered among the preferred coating materials due to their chemical stability, biocompatibility [63–65], and versatility, to achieve the functionality [65,66] required in the end-use applications of NPs.

To ensure the functionality of iron-oxide NPs, various alkoxysilane ligands can be grafted directly to their surfaces in one step, avoiding an intermediate multistage reaction mechanism. The grafting principle of alkoxysilanes is based on the sol-gel hydrolysis of alkoxide groups in the structures of alkoxysilane precursors, producing silanol groups (Si-OH), which undergo condensation reactions to form siloxane bonds (Si–O–Si) on the surface of the iron oxide, resulting in the formation of a protective silica surface layer (SiO_2). Many alkoxysilanes may contain various functional groups in their aliphatic chains, such as hydroxyl (–OH), amine ($–NH_2$), mercapto (–SH), carboxylic (–COOH), sulphonic ($–SO_3H$), phosphonate ($–PO(OH)_2$), phosphate ($–PO_2(OH)_2$), etc., which contain electron-donor atoms (O, N, P, S) and allow the formation of relatively strong complexes with the target transition-metal ions to be recycled [31,41,42,45,67–71].

Although many studies report that alkoxysilanes are non-toxic [18–20,71–73], their toxicity in terms of reactivity, stability, and degradation effects has not yet been thoroughly investigated [74–77].

In the present work, we attempted to fabricate efficient superparamagnetic adsorbents based on two different spinel-type iron oxides, both maghemite (γFe_2O_3) and cobalt ferrite ($CoFe_2O_4$), which were surface-functionalized using a (3-aminopropyl)trimethoxy silane (APTMS) precursor. The functionalized superparamagnetic adsorbents were characterized to test their adsorption efficiency and adsorption capacity towards Dy^{3+}, Tb^{3+}, and Hg^{2+} ions in aqueous solutions and their desorption efficiency when an acidic medium was used. The assessment of the cytotoxicity of both types of NP with and without an aminopropyl ($–(CH_2)_3NH_2$) surface coating was conducted on four different types of healthy cell: human-skeletal-muscle-derived cells, human fibroblasts, murine macrophages cells, and human-umbilical-vein endothelial cells. Further, their toxic effects on zebrafish embryos were also evaluated by recording the survival, mortality, and hatching percentages during embryo development.

2. Results and Discussion

2.1. Synthesis and Characterization of MNPs

The magnetic γFe_2O_3 and $CoFe_2O_4$ NPs prepared by the coprecipitation method were characterized using XRD (Figure 1). All the diffraction peaks of the prepared samples were consistent with the cubic spinel crystal structure (JCPDS Card 39-1346). It can be seen from the XRD pattern that the presence of diffraction lines at 2θ of 30.5°, 35.5°, 43.2°, 53.6°, 57.1°, and 62.9° for both samples corresponded to the cubic crystal planes of (220), (311), (400),

(422), (511), and (440), respectively. The particle sizes of the γFe_2O_3 and $CoFe_2O_4$ were calculated from the broadening of the most intensive diffraction peak corresponding to the (311) crystal plane using the Deby–Scherrer equation [78,79]. The calculated average particle sizes of the γFe_2O_3 and $CoFe_2O_4$ were 10.2 nm and 11.5 nm, respectively, and the crystalline-lattice parameters corresponding to the cubic spinel crystal structure obtained based on Bragg's law were 0.8358 nm and 0.8345 nm, respectively. The presence of broad amorphous diffraction peaks for the functionalized γFe_2O_3@SiO_2–NH_2 and $CoFe_2O_4$@SiO_2–NH_2 NPs, which appeared at a low diffraction angle 2θ of 20°, was due to the presence of the amorphous SiO_2 surface layer, indicating that the crystalline cubic spinel γ-Fe_2O_3 and $CoFe_2O_4$ NPs were successfully surface-functionalized with APTMS [80].

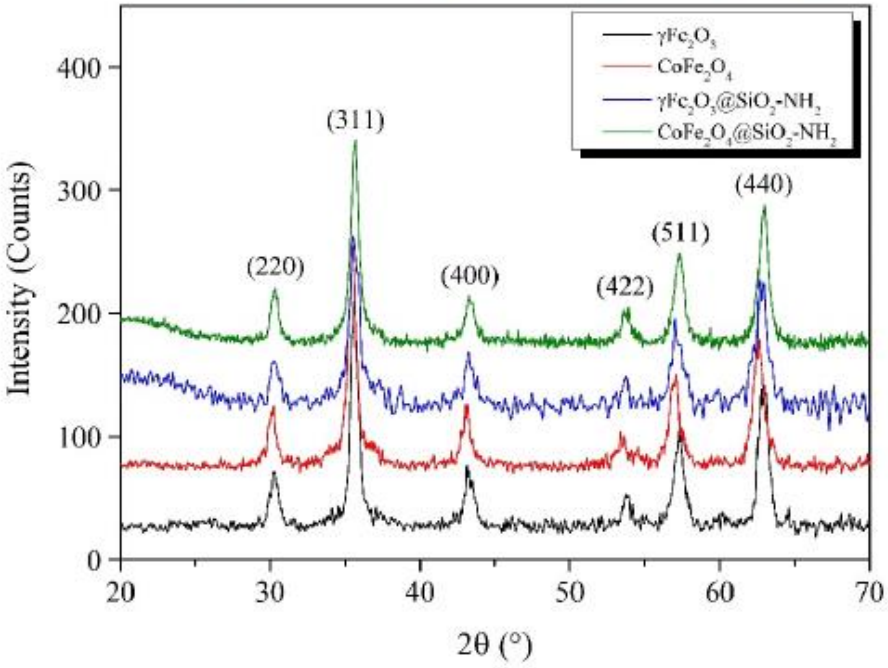

Figure 1. XRD patterns of γFe_2O_3 and $CoFe_2O_4$ NPs.

The positions of the diffraction peaks for the γFe_2O_3@SiO_2–NH_2 and $CoFe_2O_4$@SiO_2-NH_2 NPs were at the same positions 2θ as those of the γFe_2O_3 and $CoFe_2O_4$, indicating that the crystalline cubic spinel structures remained unchanged after their functionalization with APTMS.

The transmission-electron micrographs in Figure 2 represent the morphological properties of the as-prepared γFe_2O_3 and $CoFe_2O_4$ NPs and functionalized Fe_2O_3@SiO_2–NH_2 and $CoFe_2O_4$@SiO_2–NH_2 core@shell nanostructures. It can be seen that the obtained γFe_2O_3 and $CoFe_2O_4$ NPs were relatively spherical in shape, with average particle sizes of (9.9 ± 0.9) nm and (11.5 ± 1.0) nm, respectively, while the particle-size distributions of the functionalized γFe_2O_3@SiO_2–NH_2 and $CoFe_2O_4$@SiO_2–NH_2 NPs were (14.5 ± 1.1) nm and (17.7 ± 1.2) nm, respectively. The electron-diffraction patterns of the γFe_2O_3 and $CoFe_2O_4$ NPs indicated the crystalline nature of the prepared powders, with each of the concentric diffraction rings belonging to the spinel crystal structure.

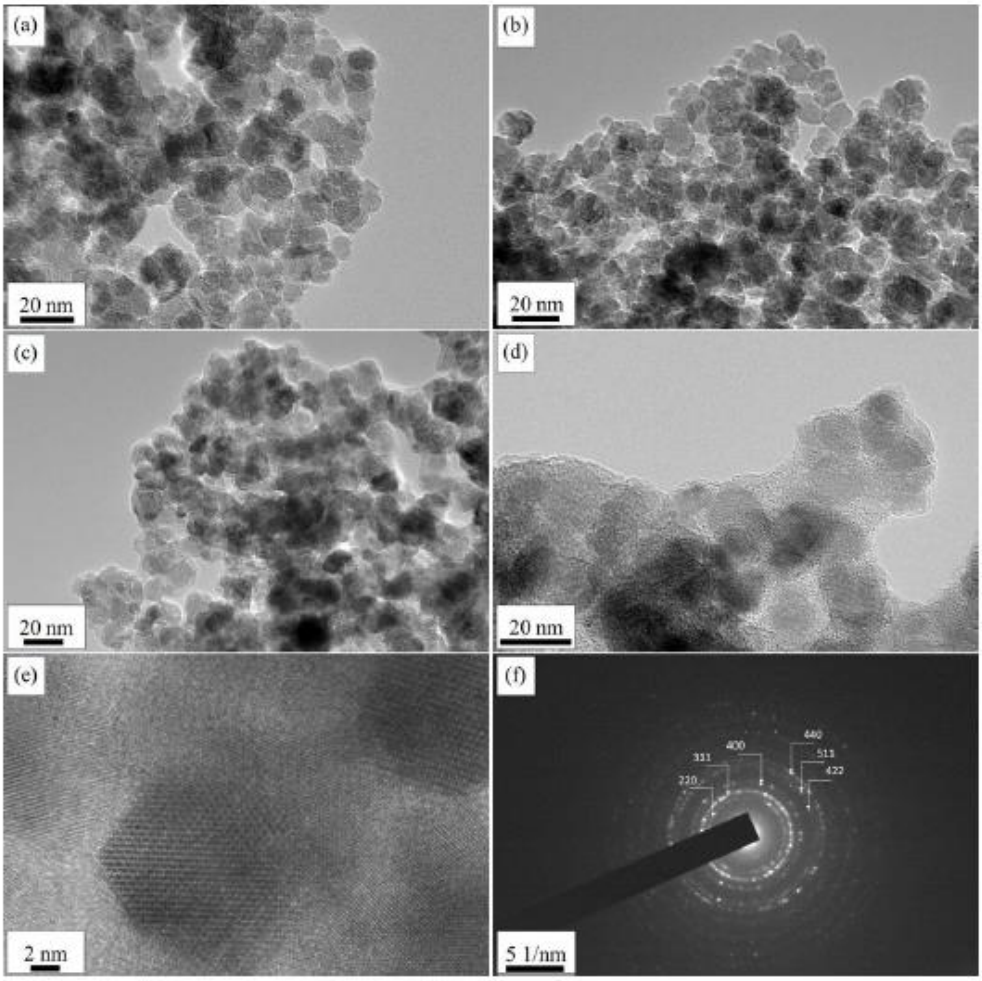

Figure 2. TEM micrographs of (**a**) γFe_2O_3, (**b**) $CoFe_2O_4$, (**c**) γFe_2O_3@SiO_2–NH_2, (**d**) $CoFe_2O_4$@SiO_2–NH_2, (**e**) high-resolution image (HRTEM), and (**f**) electron-diffraction pattern of spinel γFe_2O_3 and $CoFe_2O_4$ NPs.

The EDXS patterns of the γFe_2O_3 and $CoFe_2O_4$ NPs in Figure 3a,b confirm the presence of Co, Fe, and O elements, indicating the formation of γFe_2O_3 and $CoFe_2O_4$ nanostructures, while on the EDXS spectrum of the γFe_2O_3@SiO_2–NH_2 and $CoFe_2O_4$@SiO_2–NH_2 in Figure 3c,d, respectively, the presence of C, O(N), Co, Fe, and Si confirmed the success of the surface functionalization of the γFe_2O_3 and $CoFe_2O_4$ NPs with APTMS and, thus, the formation of the core@shell nanostructures. Small proportions of Cu and C elements belong to the TEM copper-grid supported transparent carbon foil.

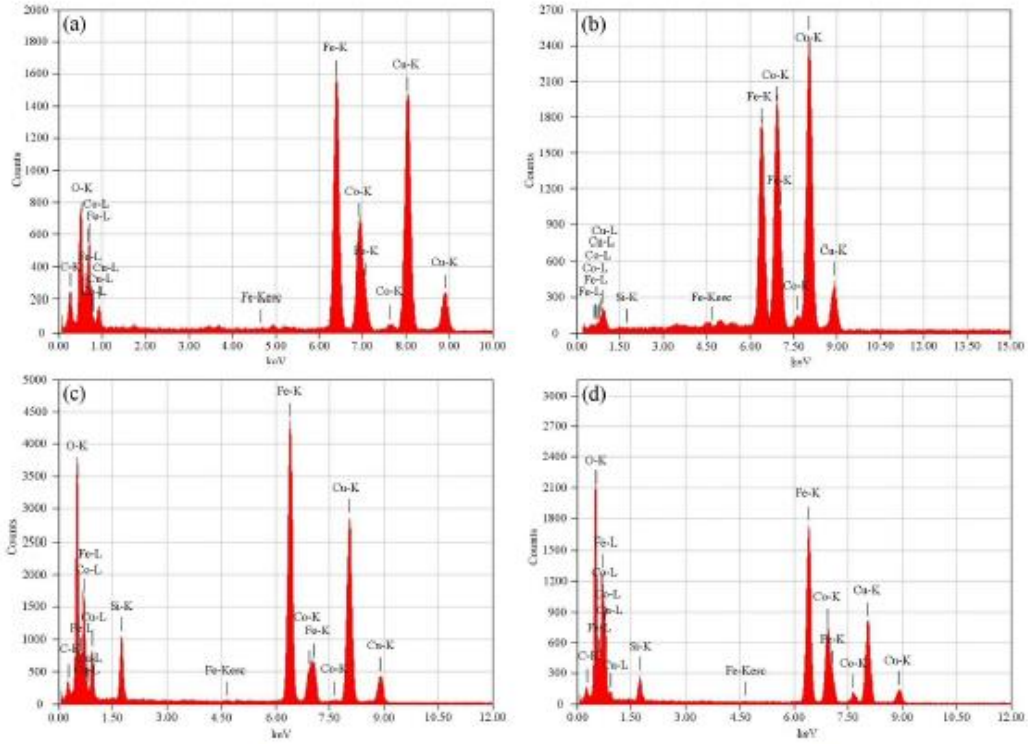

Figure 3. EDXS spectra of (**a**) γFe_2O_3, (**b**) $CoFe_2O_4$, (**c**) γFe_2O_3@SiO_2–NH_2, and (**d**) $CoFe_2O_4$@SiO_2–NH_2 NPs.

The Brunauer–Emmet–Teller (BET) analysis showed specific surface areas of 94.9 m^2/g for the γFe_2O_3 and 62.5 m^2/g for the $CoFe_2O_4$. According to the BET-specific surface area at a relative pressure of 0.3, average particle sizes (d_{bet}) of 15.1 nm and 18.5 nm were calculated for the γFe_2O_3 and $CoFe_2O_4$, respectively, assuming the sphericity of the NPs using the equation $S_{bet} = 6/(d_{bet} \cdot \rho)$, where ρ is a theoretical density of 4.9 g/cm^3 for γFe_2O_3 [81] and 5.2 g/cm^3 for $CoFe_2O_4$ [82]. The average size calculated from the surface area was a little higher than that determined using the XRD, most probably due to the agglomeration of the particles [83]. For the Barrett–Joyner–Halenda (BJH) adsorption, the average pore size was 7.0 nm, with a total pore volume of 0.2335 cm^3/g, for the γFe_2O_3 NPs, and 5.8 nm, with a total pore volume of 0.1275 cm^3/g, for the $CoFe_2O_4$ NPs. Furthermore, for the BJH desorption, the average pore size was 8.4 nm, with a total pore volume of 0.3152 cm^3/g, for the γFe_2O_3, and 6.1 nm, with a total pore volume of 0.1353 cm^3/g, for the $CoFe_2O_4$ NPs.

Due to the surface functionalization of the γFe_2O_3 and $CoFe_2O_4$ NPs with APTMS, the obtained specific surface area decreased to 40.5 m^2/g for the γFe_2O_3@SiO_2–NH_2 and 44.7 m^2/g for the $CoFe_2O_4$@SiO_2–NH_2. It is known that the larger the surface area, the smaller the particle size, and a smaller BET surface area means a larger particle size. According to the specific surface areas, the average particle sizes of the prepared γFe_2O_3@SiO_2–NH_2 and $CoFe_2O_4$@SiO_2–NH_2 samples were calculated as 30.2 nm and 25.8 nm, respectively.

A FTIR analysis (Figure 4) was performed to obtain additional information on the coverage of the NPs with the APTMS.

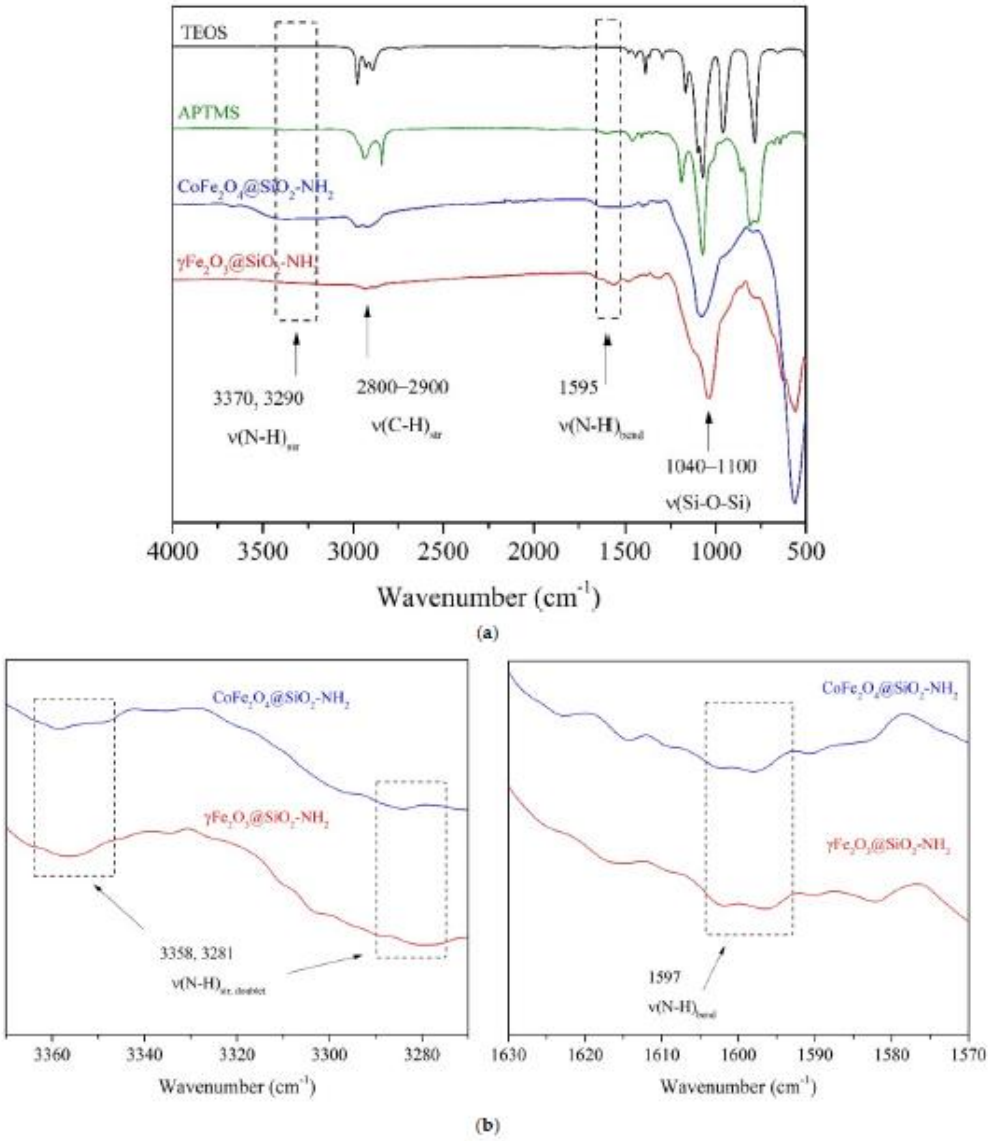

Figure 4. (a) FTIR spectra of as-prepared γFe_2O_3@SiO_2–NH_2 and $CoFe_2O_4$@SiO_2–NH_2 NPs and pure alkoxide precursors TEOS and APTMS, and (b) enlarged area corresponding to vibrations of amino groups.

In the FTIR spectra (Figure 4a), the two peaks near 3400 cm^{-1} and 1630 cm^{-1} were assigned to the hydroxyl group OH for all the synthesized NPs. The functionalization process of the γFe_2O_3 and $CoFe_2O_4$ NPs with alkoxysilanes was verified by the asymmetric stretching vibrations of the Si-O-Si bonds at 1050 cm^{-1} and the bending of the Si-H bonds at 796 cm^{-1} and at 988 cm^{-1}, indicating the formation of silica (SiO_2) shells.

The presence of amino-propyl groups in the γFe_2O_3@SiO_2–NH_2 and $CoFe_2O_4$@SiO_2–NH_2 samples was confirmed by the peaks at 2934 cm^{-1}, 1615 cm^{-1}, 1336 cm^{-1}, and 781 cm^{-1}, which were assigned to the stretching vibrations of the –CH_2–NH_2 bonds, the bending of N–H and NH_2, the wagging and twisting of –CH_2–NH_2, and the wagging and twisting of primary amino groups (–NH_2), respectively. These peaks in the source spectra were not sufficiently visible, but enlarged individual peak areas confirmed their presence (Figure 4b).

A thermogravimetric analysis (Figure S1) was used to determine the thermal stability and the percentage of amino-propyl ligands grafted onto the surface of the magnetic γFe_2O_3 and $CoFe_2O_4$ NPs. According to the literature, the estimation of mass-loss values of 1.1% and 1.3% (not shown in Figure 5) while heating as-prepared magnetic γFe_2O_3 and $CoFe_2O_4$ NPs up to 200 °C usually corresponds to the evaporation of physically and chemically absorbed moisture. Further heating of the γFe_2O_3 and $CoFe_2O_4$ magnetic NPs up to 900 °C, respectively, resulted in additional mass losses of 2.7% and 3.4%, respectively, which were most likely due to phase and surface changes, the reduction in porosity, and the degradation of the remaining surface species.

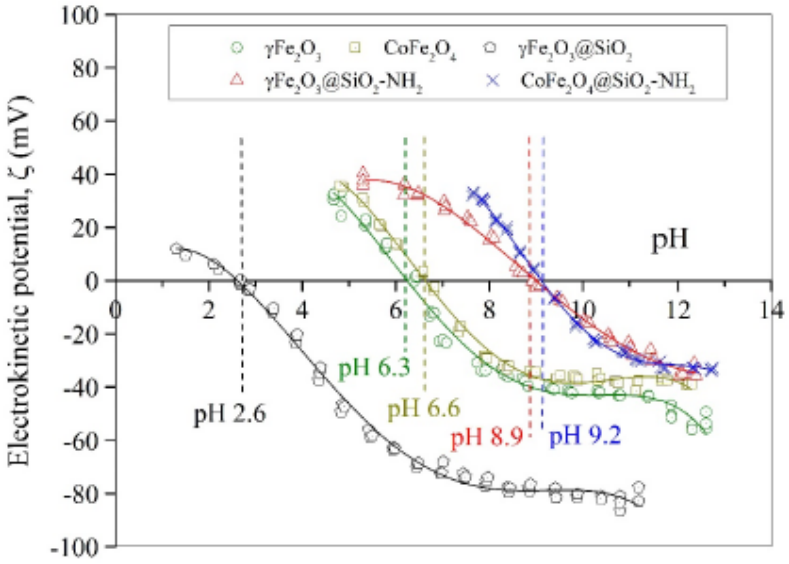

Figure 5. The electrokinetic (ζ) potential of the prepared NPs.

The mass losses of the prepared γFe_2O_3@SiO_2–NH_2 and $CoFe_2O_4$@SiO_2–NH_2 samples of 3.1% and 1.8%, respectively (not shown in Figure S1), began at the initial 30 °C mark and continued evolving up to 150 °C. These changes were related to the evaporation of the absorbed moisture from their structures. Further heating of the γFe_2O_3@SiO_2–NH_2 and $CoFe_2O_4$@SiO_2–NH_2 samples up to 900 °C caused more remarkable mass losses of 21.5% and 20.1%, respectively, which corresponded to the decomposition of the SiO_2 shell and the removal of amino-propyl groups from the NP surfaces, followed by the reduction in the porosity and the cracking of the residual siloxane species, Si–O–Si.

To establish the stability of the prepared γFe_2O_3, $CoFe_2O_4$, γFe_2O_3@SiO_2–NH_2, and $CoFe_2O_4$@SiO_2–NH_2 NPs in an aqueous medium and to determine their surface potential and isoelectric points (IEP), the electrokinetic (ζ) potential as a function of pH media was measured (Figure 5). The pH values of the IEPs for the γFe_2O_3 and $CoFe_2O_4$ NPs were about 6.3 and 6.6, respectively, while the silica-coated NPs showed pH dependencies similar to that of pure silica, i.e., at pH 2–3 [69,84].

The values of the ζ-potential for the γFe_2O_3 and $CoFe_2O_4$ NPs were higher than +30 mV at pH < 5.2 and lower than −30 mV at pH > 7.9, which means that the γFe_2O_3 and $CoFe_2O_4$ NPs were stable in the aqueous media at pH smaller than 5.2 and higher than 7.9. In that pH range, the electrostatic repulsions between the NPs dispersed in an aqueous medium are stronger than the random thermal Brownian motion and, therefore, prevent them from accidental collision and agglomeration and, subsequently, from settling out.

The observed IEP at pH 2.4 for the γFe_2O_3@SiO_2 NPs confirmed that the silica-coating process of the γFe_2O_3 NPs was effective, since the charged surface properties were close to those of pure silica (i.e., at pH 2–3) [84]. The silica shell at the maghemite cores caused an increase in their chemical stability at pH values > 4.1, where the surface potential was lower than −30 mV, thus rendering their performance suitable for environmental applications. Moreover, the silica coating prevented the dissolution of the γFe_2O_3 and $CoFe_2O_4$ NPs and, thus the leaching of potentially toxic Co^{2+} ions from the spinel crystalline structure and the Fe^{2+}/Fe^{3+} oxidation, which otherwise occurs in an acidic medium at values of pH < 3.

It can be seen that an APTMS precursor may be employed to functionalize γFe_2O_3 and $CoFe_2O_4$ NPs to form functional γFe_2O_3@SiO_2–NH_2 and $CoFe_2O_4$@SiO_2–NH_2 core@shell nanostructures. The presence of an amine layer on the surface of the γFe_2O_3@SiO_2–NH_2 and $CoFe_2O_4$@SiO_2–NH_2 NPs makes them positive in a broad range of pH due to the protonation and deprotonation of the amine groups, which depend on the solution's pH values.

The zeta (ζ) potential measurement of the γFe_2O_3@SiO_2–NH_2 and $CoFe_2O_4$@SiO_2–NH_2 NPs in an aqueous solution showed an isoelectric point at about pH 9.0 and stability of the NPs at pH < 6.6 for the γFe_2O_3@SiO_2-NH_2 and at pH < 7.9 for the $CoFe_2O_4$@SiO_2–NH_2, where the ζ–potential was higher than +30 mV, and at pH > 10.6, where the ζ–potential was lower than −30 mV.

We used pH potentiometric titrations for the determination of the total charge of the aqueous colloidal dispersions of the γFe_2O_3@SiO_2–NH_2 and $CoFe_2O_4$@SiO_2–NH_2 NPs.

The results of the potentiometric titration isotherms for the γFe_2O_3@SiO_2–NH_2 and $CoFe_2O_4$@SiO_2–NH_2 NPs are presented in Figure S2. The data exhibited protonation and deprotonation progress for both samples at an alkaline pH of around 10, exhibiting a pKa value of 10.1 for the γFe_2O_3@SiO_2–NH_2 with a maximum charge of 0.0485 mmol/g and a pKa value of 9.9 for the $CoFe_2O_4$@SiO_2–NH_2 with a maximum charge of 0.0155 mmol/g. This can be attributed to the contribution of the total primary amine groups, which is in agreement with data published elsewhere [85,86], and indicates the successful surface functionalization of the MNPs with APTMS.

Figure 6a shows the hydrodynamic size distribution of the aqueous colloidal γFe_2O_3, $CoFe_2O_4$, γFe_2O_3@SiO_2–NH_2, and $CoFe_2O_4$@SiO_2–NH_2 NPs at 21 °C, according to the intensity-distribution pattern, showing a narrow distribution with homogeneous sizes. The γFe_2O_3 and $CoFe_2O_4$ NPs, which were an average diameters of 9.9 nm and 11.5 nm by the TEM, in fact exhibited slightly larger hydrodynamic sizes of approximately 11.7 nm and approximately 14.5 nm, respectively (Figure 6a). On the other hand, after the surface functionalization with the APTMS, the γFe_2O_3@SiO_2–NH_2 and $CoFe_2O_4$@SiO_2–NH_2 NPs showed larger hydrodynamic sizes, of about 16.6 nm and about 19.1 nm, respectively (Figure 6a), compared to the previous primary particle sizes of the same nanoparticles observed by TEM.

It is worth noting that these hydrodynamic sizes were maintained over the applied time range of 1 h (Figure 6a), indicating that both the uncoated γFe_2O_3 and $CoFe_2O_4$ and the surface-functionalized γFe_2O_3@SiO_2–NH_2 and $CoFe_2O_4$@SiO_2–NH_2 NPs retained colloidal stability.

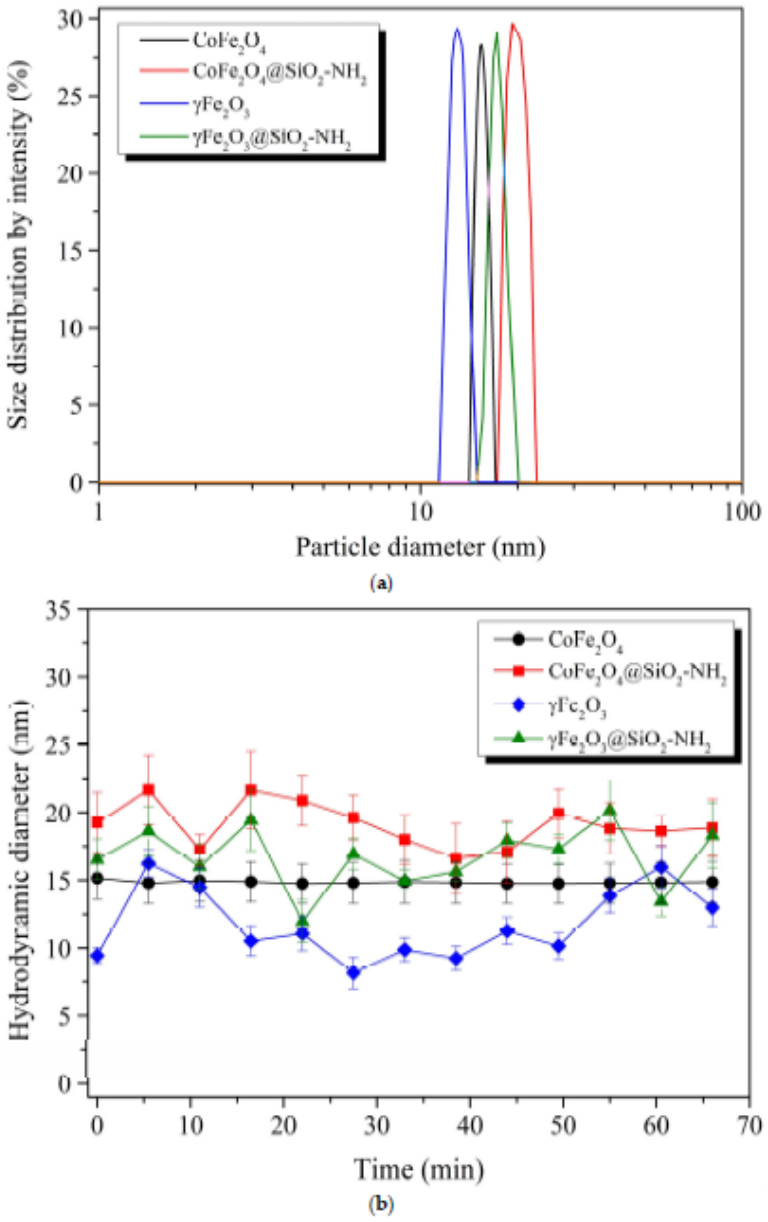

Figure 6. (**a**) Hydrodynamic particle-size distribution for γFe_2O_3, $CoFe_2O_4$, γFe_2O_3@SiO_2–NH_2, and $CoFe_2O_4$@SiO_2–NH_2 NPs, and (**b**) the time-dependent hydrodynamic diameters of uncoated γFe_2O_3 and $CoFe_2O_4$, and coated γFe_2O_3@SiO_2-NH_2 and $CoFe_2O_4$@SiO_2-NH_2 NPs.

The time-dependent hydrodynamic diameters of uncoated γFe_2O_3 and $CoFe_2O_4$, and coated γFe_2O_3@SiO_2–NH_2 and $CoFe_2O_4$@SiO_2–NH_2 NPs, are shown in Figure 6b.

Figure 6b shows the samples showed a trend towards colloidal stability. The hydrodynamic diameter of the colloidal $CoFe_2O_4$ NPs did not change significantly with time. The average hydrodynamic size of the colloidal $CoFe_2O_4$ NPs was maintained at approximately (11.7 ± 1.1) nm over the entire time range. The colloidal γFe_2O_3 NPs also had a similar behavioral pattern in terms of hydrodynamic size, with a slightly larger fluctuation in the values around the average diameter of the NPs of (14.8 ± 1.5) nm. Although the overall maximum average hydrodynamic sizes of the γFe_2O_3 and $CoFe_2O_4$ NPs increased with respect to the particle-size values estimated from the XRD and TEM images, no agglomeration or aggregation of NPs was observed.

After the surface functionalization of the γFe_2O_3 and $CoFe_2O_4$ NPs by the APTMS, a fluctuation and an increase in the hydrodynamic diameters of the γFe_2O_3@SiO_2–NH_2 and $CoFe_2O_4$@SiO_2–NH_2 NPs by about 42% and 30%, respectively, were observed in relation to the uncoated γFe_2O_3 and $CoFe_2O_4$ NPs. The final hydrodynamic sizes of the γFe_2O_3@SiO_2–NH_2 and $CoFe_2O_4$@SiO_2–NH_2 NPs were 16.6 ± 1.5 nm and 19.1 ± 2.0 nm, respectively, compared to the particle-size values estimated from the XRD and TEM images. Despite the fluctuation and increase in the total maximum hydrodynamic sizes of the γFe_2O_3@SiO_2–NH_2 and $CoFe_2O_4$@SiO_2–NH_2 NPs, no agglomeration or aggregation of NPs was observed. The samples showed a trend toward colloidal stability.

It is obvious that the average particle sizes measured by the DLS technique were slightly larger than the average particle sizes estimated on the basis of the XRD and TEM. It is known that the hydrodynamic sizes of particles dispersed in liquids are usually larger than the primary particle sizes, as reported by many other studies [87–90]. The hydrodynamic sizes of particles measured by DLS depend on many factors, particularly the concentration of the dispersion, temperature, pH, etc., due to which dispersed nanoparticles may tend to aggregate; therefore, the measured hydrodynamic diameters in such cases are usually much larger than the actual sizes [88,90].

Figure 7 shows the comparison of the magnetic properties of the uncoated γFe_2O_3 and $CoFe_2O_4$ NPs and the functionalized γFe_2O_3@SiO_2–NH_2 and $CoFe_2O_4$@SiO_2–NH_2 NPs, which were carried out using VSM analysis.

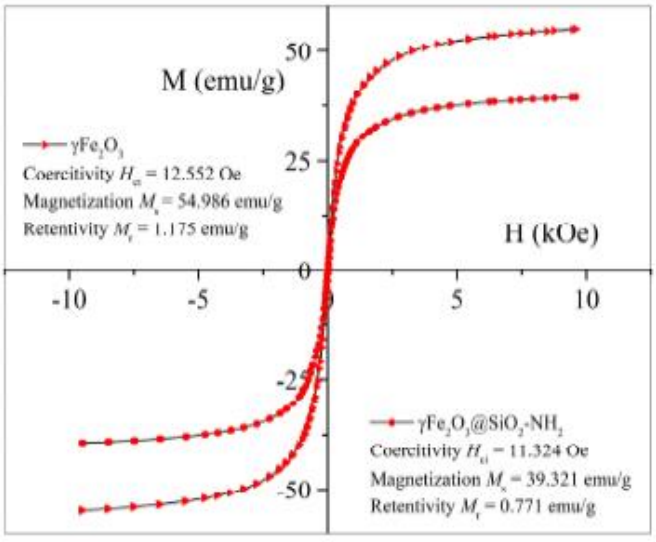

(a)

Figure 7. *Cont.*

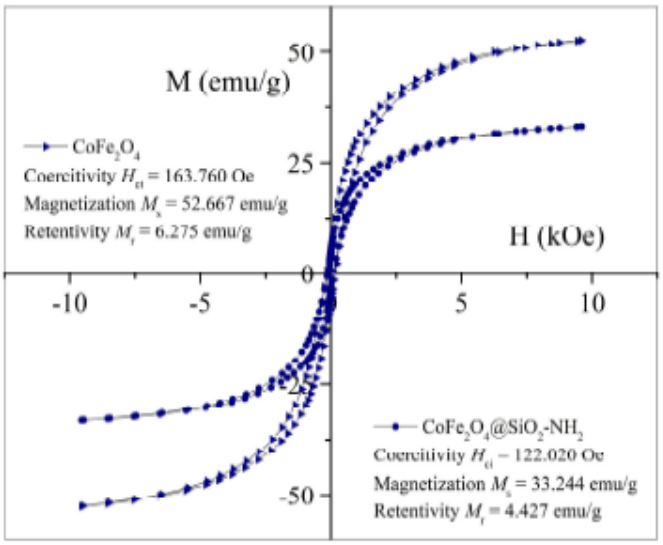

(b)

Figure 7. *M-H* curves of the prepared samples of (**a**) γ-Fe_2O_3 and γ-Fe_2O_3@SiO_2–NH_2 NPs, and (**b**) $CoFe_2O_4$ and $CoFe_2O_4$@SiO_2–NH_2 NPs.

At the maximum magnetic field (*H*) strength in the magnetization phase, the specific mass magnetization (M_s) of the samples γFe_2O_3 and $CoFe_2O_4$ reached values of 54.98 emu/g and 52.67 emu/g, respectively. The remanent magnetization (M_r) and coercivity (H_{ci}) values for the samples γFe_2O_3 and $CoFe_2O_4$ can be determined from the shape of the hysteresis curves in the vicinity of the zero-magnetic-field strength. We determined that the remanent magnetization and coercivity of the γFe_2O_3 sample were 1.17 emu/g and 12.55 Oe, respectively, and that the remanent magnetization and coercivity of the $CoFe_2O_4$ sample were 6.27 emu/g and 163.76 Oe, respectively.

As can be seen, the γFe_2O_3 NPs showed very low coercivity due to the small particle sizes. In this case, the γFe_2O_3 NPs exhibited a superparamagnetic character; in other words, they were monodomain. In contrast, when the iron in the spinel crystal structure of the maghemite (γFe_2O_3) replaced the cobalt ($CoFe_2O_4$), the coercivity was non-zero, and the samples did not show superparamagnetic behavior.

A comparison of the magnetic characteristics of these two samples showed that with the integration of the cobalt into the γFe_2O_3 spinel crystal structure, the coercivity increased by thirteen times, and the remanent magnetization increased by almost five times, while the specific mass magnetization did not change significantly.

The increase in coercivity was the cause of the increase in the magnetocrystalline anisotropy due to the cobalt substitution [39]. Magnetocrystalline anisotropy is a key factor that determines the superparamagnetic behavior of nanocrystalline particles and serves as an energy barrier to block spin relaxation, which changes the magnetic state from ferrimagnetic to superparamagnetic [37,38].

The average particle sizes of samples γFe_2O_3 and $CoFe_2O_4$ were approximately similar (10.2 nm for γFe_2O_3 and 11.5 nm for $CoFe_2O_4$), so the loss of superparamagnetic properties when replacing the iron with the cobalt in the γFe_2O_3 spinel crystal structure may have been due to an increase in the magnetocrystalline anisotropy of the $CoFe_2O_4$ [37].

In the magnetization step, under the maximum magnetic field strength (H_{ci}), the specific mass magnetization (M_s) of the synthesized γFe_2O_3@SiO_2–NH_2 decreased from 54.98 emu/g for the γFe_2O_3 NPs to 39.32 emu/g, and from 52.67 emu/g for the $CoFe_2O_4$

NPs to 33.24 emu/g for the $CoFe_2O_4$@SiO_2–NH_2 NPs. This was due to the presence of a non-magnetic SiO_2-NH_2 coating on the surfaces of the γFe_2O_3 and $CoFe_2O_4$ cores, which, due to its diamagnetic quality, contributed to the reduction in the net-specific magnetization of the γFe_2O_3@SiO_2–NH_2 and $CoFe_2O_4$@SiO_2–NH_2 NPs. After the surface functionalization of the samples γFe_2O_3 and $CoFe_2O_4$, a pronounced decrease in the remanence (M_r) and coercivity (H_{ci}) of the samples was noticed because of the increase in the average particle size at the expense of the SiO_2-NH_2 surface coating. The remanence (M_r) thus decreased from 1.17 emu/g for the sample γFe_2O_3 to 0.77 emu/g for the sample γFe_2O_3@SiO_2–NH_2, and from 6.27 emu/g for the sample $CoFe_2O_4$ to 4.43 emu/g for the sample $CoFe_2O_4$@SiO_2-NH_2, while the coercivity of the sample γFe_2O_3@SiO_2–NH_2 decreased to 11.32 Oe from 12.55 Oe for the γFe_2O_3, and for the sample $CoFe_2O_4$@SiO_2-NH_2 m it decreased to 122.02 Oe from 163.76 Oe for the $CoFe_2O_4$ NPs. The decrease in saturation magnetization (M_s), coercivity (H_{ci}), and remanent magnetization (M_r) in the γFe_2O_3@SiO_2–NH_2 and $CoFe_2O_4$@SiO_2–NH_2 NPs compared to the γFe_2O_3 and $CoFe_2O_4$ NPs was expected due to the larger NP sizes, corresponding to the SiO_2 shell and the functionalization with amino (–NH_2) groups.

2.2. *Adsorption and Desorption Tests*

To evaluate the performances and basic adsorption affinity of the γ-Fe_2O_3@SiO_2–NH_2 and $CoFe_2O_4$@SiO_2–NH_2 adsorbents toward Dy^{3+}, Tb^{3+}, and Hg^{2+} ions in aqueous solutions, batch adsorption experiments at pH 4.5 and with a contact time of 2 h were performed. The graphical representations of the adsorption efficiency and adsorption capacity of the prepared samples are depicted in Figure 8. The numerical results are presented in Table 1.

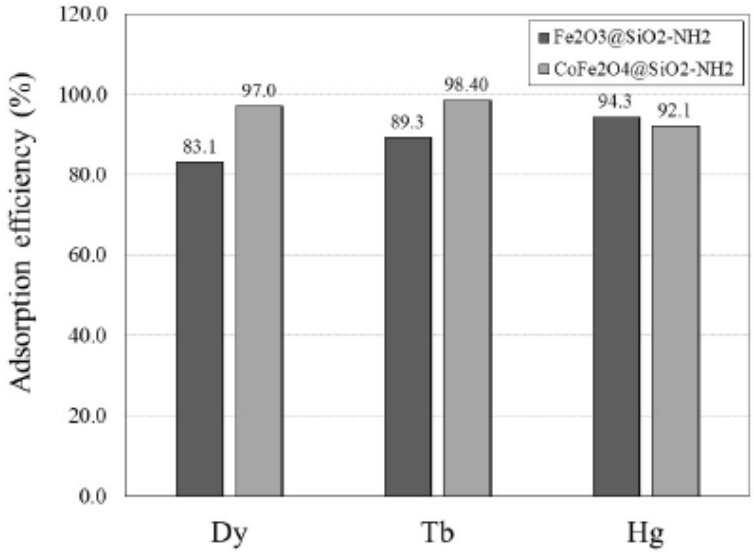

(a)

Figure 8. *Cont.*

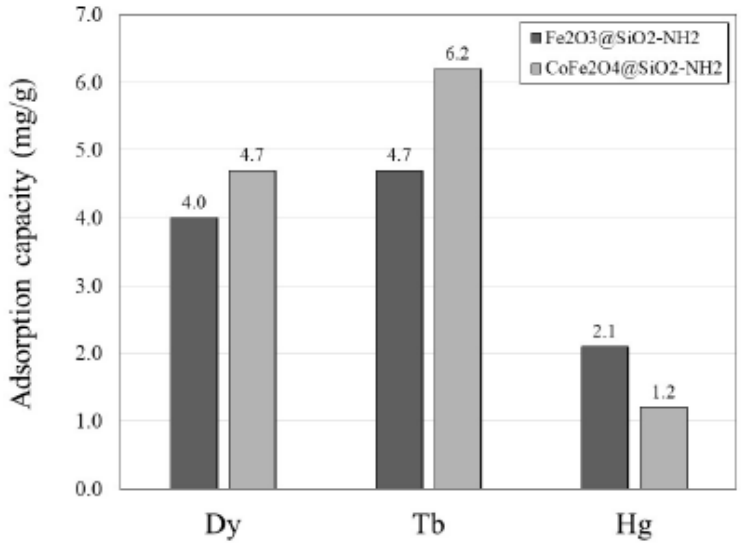

(**b**)

Figure 8. (**a**) Adsorption efficiency (%) and (**b**) adsorption capacity (mg/g) of $\gamma Fe_2O_3@SiO_2–NH_2$ and $CoFe_2O_4@SiO_2–NH_2$ NPs toward Dy^{3+}, Tb^{3+}, and Hg^{2+} ions.

Table 1. Results of the adsorption and desorption tests for Dy^{3+}, Tb^{3+}, and Hg^{2+} ions.

NPs	Adsorption Efficiency $q_{ads,\%}$ (%)			Adsorption Capacity q_{ads} (mg/g)			Desorption Efficiency q_{des} (%)		
	Dy^{3+}	Tb^{3+}	Hg^{2+}	Dy^{3+}	Tb^{3+}	Hg^{2+}	Dy^{3+}	Tb^{3+}	Hg^{2+}
γ-$Fe_2O_3@SiO_2–NH_2$	83.1	89.3	94.3	4.0	4.7	2.1	100	100	100
$CoFe_2O_4@SiO_2–NH_2$	97.9	98.4	92.1	4.7	6.2	1.2	100	100	100

The adsorption results of the Dy^{3+}, Tb^{3+}, and Hg^{2+} ions are presented only for the functionalized NPs, both $\gamma Fe_2O_3@SiO_2–NH_2$ and $CoFe_2O_4@SiO_2–NH_2$, as adsorption by functionalized NPs is usually much more efficient than adsorption by non-functionalized NPs [46].

The adsorption results showed that both the $\gamma Fe_2O_3@SiO_2–NH_2$ and the $CoFe_2O_4@SiO_2–NH_2$ samples had high adsorption affinity towards Dy^{3+} and Tb^{3+} ions, with relatively high adsorption efficiencies of 83.1% and 89.3%, respectively, but low adsorption capacities of 4.0 mg/g and 4.7 mg/g, respectively.

The adsorption affinity of the $\gamma Fe_2O_3@SiO_2–NH_2$ and $CoFe_2O_4@SiO_2–NH_2$ toward the Dy^{3+}, Tb^{3+}, and Hg^{2+} ions in the aqueous medium can be explained by Pearson's hard-and-soft acid-base (HSAB) theory [91]. This concept is based on Lewis' definition of acids as electron acceptors and bases as electron donors, and it states that soft acids prefer to coordinate and form stronger bonds and more stable complexes with soft bases, whereas hard acids prefer to coordinate and form stronger bonds and more stable complexes with hard bases.

According to the HSAB concept, Dy^{3+} and Tb^{3+} ions are classified as hard Lewis acids, and functional amino ($–NH_2$) groups are classified as hard Lewis bases, so Dy^{3+} and Tb^{3+} ions have a high affinity for NH_2 groups. On the other hand, as a soft Lewis acid, Hg^{2+} is a relatively large (1.02 Å) and polarizable atom, which, in practice, prefers to associate with soft bases. Since Hg^{2+} is larger than Tb^{3+} (0.923 Å) and Dy^{3+} (0.912 Å) and, thus, more

polarised, it has a weaker preference for interactions with hard NH_2 groups. This resulted in its significantly lower adsorption capacity of 2.1 mg/g for the γFe_2O_3@SiO_2–NH_2 and 1.2 mg/g for the $CoFe_2O_4$@SiO_2–NH_2 NPs.

The lower adsorption capacity of Hg^{2+} compared to Tb^{3+} and Dy^{3+}, in the context of the HSAB concept, can be explained by the use of the absolute-hardness parameter (η_s). Parr et al. [92] defined the absolute-hardness parameter as $\eta_s = (I_p - A_s)/2$, where I_p (eV) is the ionization potential and A_s (eV) is the electron affinity. Pearson, in a 1988 paper [93], conveniently provided cumulative experimental values for ionization potential and electron affinity, referring to earlier work by Moore [94]. From these values, it is possible to calculate the absolute-hardness parameter (η_s) values, which for Hg^{2+}, Tb^{3+}, and Dy^{3+} are 5.4 eV, 3.1 eV, and 3.1 eV, respectively. Pearson [93] also defined softness (σ_s) as the inverse of hardness, $\sigma_s = 1/\eta_s$, with zero as the maximum softness. The values of the softness parameter for Hg^{2+}, Tb^{3+}, and Dy^{3+} are thus 0.19, 0.32, and 0.32, respectively, indicating the softer nature of Hg^{2+} compared to Tb^{3+} and Dy^{3+}. Therefore, in this case, a higher complexation affinity of the hard NH_2 groups for the hard Tb^{3+} and Dy^{3+} ions and a lower complexation affinity for the softer Hg^{2+} is expected, which also agreed with the results of our work.

A possible explanation for the low adsorption capacity of Hg^{2+} is its unusual chemical properties and its character as a soft Lewis acid. The soft nature of Hg^{2+} is related to its ground-state electronic configuration ($[Xe]4f^{14}5d^{10}6s^2$) with filled electron subshells up to 6s, which, due to its stability, strongly resists electron removal, resulting in the very high ionization potential (I_p 10.434 eV) and moderately high electronegativity (χ_P 2.00 by Pauling) [95,96] of Hg, which is reflected in its low chemical reactivity [97].

Because all the main energy levels of the Hg atom are filled, and because of the unusually stable $6s^2$ electron pair, Hg can form only very weak hard–soft chemical bonds with amino groups, with a covalent character [96]. Therefore, the interactions of soft Hg with the hard electron-donating N-atom in the NH_2 group, which is a small (0.16 Å), low-polarizable atom with high electronegativity (χ_P 3.04 Pauling) and high ionization potential (I_p 14.534 eV), are not favored [95,98].

In contrast, Tb^{3+} and Dy^{3+}, which are hard Lewis acids, according to the HSAB concept, tend to have chemical interactions with the electron-donor N-atoms in the NH_2 groups, which have the character of hard Lewis bases. This is due to differences in the stability of their electron configurations and electron-density distributions. Compared to Hg, which has a stable electron configuration, Tb ($[Xe]6s^24f^9$) and Dy ($[Xe]6s^24f^{10}$) have stabilized 4f electrons that do not contribute to the formation of chemical bonds, and their chemical behavior is dictated by the 6 =s valence electrons [97]. Despite the presence of $6s^2$ electrons in addition to the 4f and [Xe] nuclei in Tb and Dy, their most stable oxidation state in aqueous media is +3, which makes them more reactive than divalent Hg. Their chemical reactivity gradually decreases from terbium towards mercury in the sequence of Tb > Dy > Hg [97], which is also reflected in their higher affinity for the formation of complexes with NH_2 groups of APTMS compared to Hg. This is consistent with our finding, in this study, that the adsorption capacities of Tb^{3+}, Dy^{3+}, and Hg^{2+} decrease in the order of $Tb^{3+} > Dy^{3+} > Hg^{2+}$.

On the other hand, the unexpectedly low adsorption capacity of Tb^{3+} and Dy^{3+} ions, which have the character of hard Lewis acids, is probably also due to the strong hydration of these cations in aqueous solutions and the formation of aqua complexes ($[Ln(OH_2)_9]^{3+}$, Ln = Tb, Dy), which is also reflected in their high hydration-enthalpy values for Tb^{3+} (ΔH_{hydr} −3540 kcal/mol) and Dy^{3+} (ΔH_{hydr} −3570 kcal/mol) [99–101]. Such aqua complexes are easily formed because of excess water, and they are prone to substitution reactions, in which water molecules are successively replaced by amino ligands and vice versa [102].

Bjerrum [103] determined that a metal complex in an aqueous solution is formed by the exchange of a coordinated water molecule directly bound to the central lanthanide ion (Ln^{3+}) with other ligands, provided that the ligand has a sufficiently strong affinity for the lanthanide ion to compete with the affinity of the coordinated water. Such exchanges result

in the formation of strong complexes with inner hydration shells [104]. When the ligand replaces the water molecule of the aqua-complex ion, a new metal complex is formed and equilibrium is established. It is assumed that this formation does not take place in one step, but in several steps, involving the following: (i) the joint diffusion of the hydrated cation and anion, (ii) the partial loss of solvent to form the ion pair, (iii) the loss of water from the first coordination sphere of the cation, and (iv) the formation of the complex species. The rate-determining step is the loss of the water molecule from the coordination sphere of the Ln^{3+} ion and, thus, depends only on the hydration properties of the Ln^{3+} ion [105,106].

In general, a maximum number of water molecules are distributed around Ln^{3+} ions during the hydration process, depending on the size of the Ln^{3+} ion and its electronic properties. It is known that the ionic radii of Ln^{3+} ions in the Ln species decrease as the atomic number increases due to lanthanide contraction, which is a consequence of the incomplete mutual protection of the valence f-orbitals.

According to the ratio of the radii of the Ln^{3+} ions to the radii of the oxygen atoms (1.34 Å) in coordinated water molecules (r_{ion}/r_0), all the hydrated Ln^{3+}-ions in aqueous solutions occupy the configuration of a tricapped trigonal prismatic [107] geometry with six nearly identical water molecules at the vertices of the trigonal prism and the remaining three water molecules capping the prism faces [108].

Hydrates of the lighter Ln^{3+} ions (La^{3+}-Nd^{3+}) have a regular tricapped trigonal prismatic configuration, with slightly longer bond distances from the Ln^{3+} ion to the capping water molecules (Ln-O) than to the water molecules forming the prism. The decrease in the radii of the Ln^{3+}-ions with the increase in the atomic number of the Ln-species starting from Nd^{3+} does not, in principle, affect the structure of the prism, but has a strong effect on the more weakly bound capping positions of the water molecules in the prismatic structure, resulting in a partial loss of the water molecules in the capping positions for the heaviest Ln^{3+}-ions (Ho^{3+}-Lu^{3+}). In fact, studies have shown that the bond strength of the three-capping water molecules is strong at the beginning of the Ln series for nonahydrates (e.g., La^{3+}-Sm^{3+}), while in the Ln series starting from (Sm^{3+}-Lu^{3+}), the Ln–O capping bonds become weaker and shorter at the same time. The Ln–O change in the $[Ln(OH_2)_9]^{3+}$ for Ln^{3+}-ions (e.g., La^{3+}, Sm^{3+}, Tb^{3+}, Dy^{3+}, Ho^{3+}, and Lu^{3+}) occurs in the following sequence: La-O (2.52 Å) > Sm-O (2.46 Å) > Tb-O (2.39 Å) > Dy–O (2.37 Å) > Ho–O (2.36 Å) > Lu–O (2.31 Å) [109]. Consequently, in the lanthanide series starting from Sm^{3+} onward, the three water molecules in the structure are not equally strongly bound and one of the water molecules is at a shorter distance from the Ln-center than the other two. In the series from Ho^{3+} to Lu^{3+}, the water deficit and the differences between the strongly bound water molecules and the more weakly-bound molecules are even greater [108,109].

Therefore, since Ln-O bonds are more easily broken, in the whole Ln series, the lighter lanthanide Ln^{3+} -ions (La^{3+}–Nd^{3+}) form stable nonahydrates, while the heavier Ln^{3+}-ions (Ho^{3+}–Lu^{3+}) form octahydrates. Intermediate Ln^{3+}-ions (Sm^{3+}–Dy^{3+}) favor the formation of complex forms of nona- and octahydrates with non-integer coordination numbers (CN) between 8 and 9. Therefore, the CN of these intermediate lanthanides should be average with respect to the ratio of nona- to octahydrate forms [110,111].

Such Ln-O bond behavior determines the hydration behavior of Ln^{3+} ions and explains their very unusual and complex ligand exchange kinetics throughout the Ln series [110,111]. The peculiarity is that the exchange rate of water molecules between the first hydration shell and the bulk solvent increases in the direction from La^{3+} to Gd^{3+}, reaches its maximum in the central region of the Ln series (Tb^{3+}, Dy^{3+}), and then decreases up to Lu^{3+} [112,113]. The physical reasons for these phenomena are still not well understood and are the subject of many investigations [110,111].

On the other hand, H_2O is also known to be a hard base [114], which, in accordance with the HSAB concept and the above values of absolute hardness, associates with hard ligands rather than soft ligands, because, in this case, hard–hard interactions are more favorable. Since the amino ($–NH_2$) group is a hard Lewis base, the substitution of the amino ligand and H_2O is relatively favorable from this point of view [100,114], which

makes lanthanide-ion complexes of Ln^{3+} (Ln = Tb, Dy) extremely labile [115]. In contrast, for transition metals, the lability of complexes generally varies with their electronic configuration. Some complexes are labile, while others are kinetically very inert, such as d^3 species and low-spin d^6 species, with high stabilities and high activation energies for ligand substitution [115].

The formation of amino complexes is largely related to the availability of active sites on the adsorbent surfaces and the coordination number. The two key factors influencing the coordination number and complex formation, as well as their chemical stability, areas follows: (i) the influence of the donor N-atoms in the immediate vicinity of the metal ion (Tb^{3+}, Dy^{3+}, Hg^{2+}), which, due to interatomic tension, prevent more N-atoms from making contact with the metal ion; and (ii) the steric repulsions between the larger substituent groups in the APTMS, which are bonded to the donor N-atom (i.e., $H_2N(CH_2)_3$-), which determine how much of the ligand can be surrounded by the metal ion [115]. The lack of available active sites thus reduces the ability to form complexes, resulting in a lower adsorption capacity.

The electron-donating N-atoms of the amino groups of APTMS in the surface coating of the adsorbent possess a free-electron pair that can be donated to form a coordination bond with the Tb^{3+}, Dy^{3+}, and Hg^{2+} metal ions in the aqueous medium. Depending on the coordination number, which is 9 for Tb^{3+} and Dy^{3+} [98,116] and 6 for Hg^{2+} [117,118], these metal ions can coordinate linearly with one or two amino groups, with the remaining coordination sites occupied by water molecules. Thus, the coordination mechanism of Tb^{3+}, Dy^{3+}, and Hg^{2+} with the amino groups of APTMS on the surfaces of γFe_2O_3@SiO_2–NH_2 and $CoFe_2O_4$@SiO_2–NH_2 adsorbents can be represented as [101,119,120]:

$$RNH_2 + Ln^{3+} \Leftrightarrow [Ln(RNH_2)(H_2O)_8]^{3+} \text{ (Ln = Tb, Dy)} \quad (1)$$

$$RNH_2 + Hg^{2+} \Leftrightarrow [Hg(RNH_2)(H_2O)_5]^{2+} \quad (2)$$

After the adsorption of Tb^{3+}, Dy^{3+}, and Hg^{2+}, the possibility of recovering both adsorbents, γFe_2O_3@SiO_2–NH_2 and $CoFe_2O_4$@SiO_2–NH_2, for the reuse and recycling of Tb^{3+}, Dy^{3+}, and Hg^{2+} ions were verified by a desorption process. The choice of agent for desorption is based on the type of adsorbate–adsorbent system [121] and depends mainly on the compatibility between adsorbate and adsorbent, the pH and ionic strength of the medium, the complexation ability, the desorption-agent content, and the exposure time, as these variables can modify the desorption behavior or destroy the adsorbent structure [121]. In addition, desorption phenomena are related to a series of surface interactions and diffusion into micropores or the intraparticle spaces of the adsorbents [99].

In our previous research [122,123], we studied some desorption conditions and the use of different acidic desorption agents, such as hydrochloric acid (HCl), nitric acid (HNO_3), and citric acid, and we found that HNO_3 gave better results than the other two desorption agents. Therefore, in the present study, a desorption procedure for Tb^{3+}, Dy^{3+}, and Hg^{2+} was carried out using a 1-M aqueous solution of HNO_3 for 1 h at room temperature and with pH 4.5 [124]. The desorption was carried out in one cycle only due to the loss of material during the desorption process. The results of the desorption efficiency are shown graphically in Figure 9. After 1 h, the Tb^{3+}, Dy^{3+}, and Hg^{2+} ions were completely desorbed from the surfaces of the γFe_2O_3@SiO_2–NH_2 and $CoFe_2O_4$@SiO_2–NH_2 adsorbents, indicating the potential for the stable reusability of the prepared adsorbents and the high potential of these adsorbents for the recycling and removal of heavy metals.

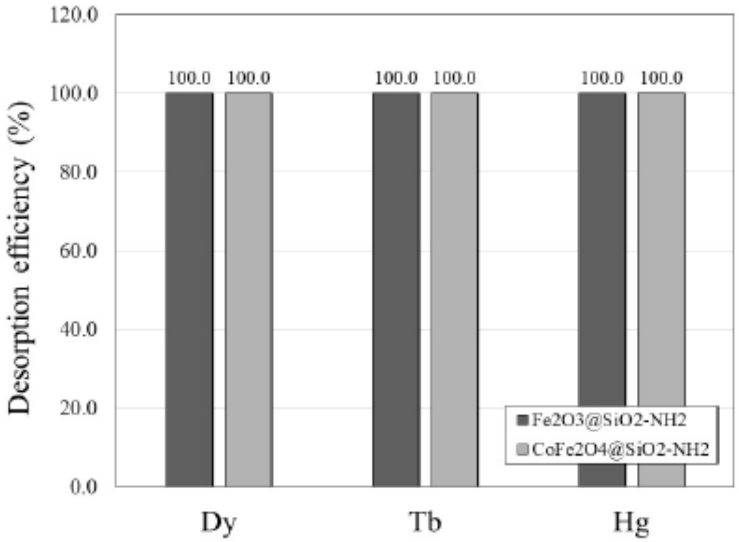

Figure 9. Desorption efficiency of γFe_2O_3@SiO_2–NH_2 and $CoFe_2O_4$@SiO_2–NH_2 NPs.

Table 2 shows the comparison of the adsorption of the Dy^{3+}, Tb^{3+}, and Hg^{2+} ions onto the prepared γFe_2O_3@SiO_2–NH_2 and $CoFe_2O_4$@SiO_2–NH_2 NPs with the adsorption of Dy^{3+}, Tb^{3+}, and Hg^{2+} on different adsorbents. It can be observed that the adsorption conditions, such as the initial adsorbate concentration ($c_{ads,0}$), adsorbent dosage (γ_{ads}), time of adsorption (t_{ads}), adsorption temperature (T_{ads}), and solution pH, were very different, making the comparison of the adsorption performances a difficult and a complex task.

Table 2. The adsorption capacity of Dy^{3+}, Tb^{3+}, and Hg^{2+} with various adsorbent materials.

Adsorbent (NPs)	Adsorbate	Adsorption Conditions					Adsorption/Desorption Characteristics			Ref.
		$c_{ads,0}$ (mg/L)	$\gamma_{ads,NPs}$ (g/L)	t_{ads} (min)	T_{ads} (°C)	pH	q_{ads} (mg/g)	$q_{ads,\%}$ (%)	$q_{des,\%}$ (%)	
	Dysprosium (Dy^{3+})									
Fe_3O_4@SiO_2@polyaniline–graphene oxide	Dy^{3+}	0.01	0.4	2	25	4	16.0	98	95	[125]
Fe_3O_4–C_{18}–chitosan–DETA	Dy^{3+}	50	1.0	720	25	7	28.3	>80	>95	[126]
γ-Fe_2O_3-NH_4OH@SiO_2 (APTMS)	Dy^{3+}	8.125	3.0	120	25	7	23.2	94	N/A	[84]
Synthetic-polymer-based magnetic adsorbent (M-PPTA)	Dy^{3+}	50	3.0	130	25	5.5	24.0	98.4	>84	[127]
Polymeric adsorbents modified with ethylenediamine (EDA) and diglycolamic acid (DGA)	Dy^{3+}	162.5	10.0	4320	25	1	18.4	30	N/A	[128]
Chemically activated carbons from spent-coffee waste	Dy^{3+}	5.0	0.3	120	25	4	31.26	96	N/A	[129]
Physically activated carbons from spent-coffee waste							33.52	99		
Ulva lactuca—Chlorophyta (green)	Dy^{3+}	0.5	3.0	4320	25	N/A (1)	0.570	89	N/A	[130]
Gracilaria sp.—Rhodophyta (red)							0.526	84		
Fe^0–SiO_2–PA/SiO_2–DTPA	Dy^{3+}	1.5	0.5	30	21	3	1.85	N/A	N/A	[131]
γFe_2O_3@SiO_2–NH_2	Dy^{3+}	32	2.5	120	25	4	4.0	83.1	100	This work

Table 2. *Cont.*

Adsorbent (NPs)	Adsorbate	Adsorption Conditions					Adsorption/Desorption Characteristics			Ref.
		$c_{ads,0}$ (mg/L)	$\gamma_{ads,NPs}$ (g/L)	t_{ads} (min)	T_{ads} (°C)	pH	q_{ads} (mg/g)	$q_{ads,\%}$ (%)	$q_{des,\%}$ (%)	
$CoFe_2O_4$@SiO_2–NH_2	Dy^{3+}	32	2.5	120	25	4	4.7	97.9	100	This work
	Terbium (Tb^{3+})									
Fe_3O_4@SiO_2@polyaniline-graphene oxide	Tb^{3+}	0.01	0.4	2	25	4	11.8	98	95	[125]
Fe^0–SiO_2–PA/SiO_2–DTPA	Tb^{3+}	1.5	0.5	30	21	3	1.4	N/A	N/A	[131]
Molecular-sieve zeolite / *B. cereus* biomass-supported zeolite	Tb^{3+}	20	0.5	2880	25	5	2.59 / 5.07	80	>60	[132]
Multi-walled carbon nanotubes with tannic acid (TA-MWCNTs)	Tb^{3+}	40	5	60	20	5	8.55	N/A	>95	[133]
γ-Fe_2O_3–NH_4OH@SiO_2 (APTMS)	Tb^{3+}	0.32	1.5	120	25	7	0.204	93	N/A	[134]
γFe_2O_3@SiO_2–NH_2	Tb^{3+}	32	2.5	120	25	4	4.7	89.3	100	This work
$CoFe_2O_4$@SiO_2–NH_2	Tb^{3+}	32	2.5	120	25	4	6.2	98.4	100	This work
	Mercury (Hg^{2+})									
$CoFe_2O_4$–chitosan–graphene	Hg^{2+}	20	0.12	230	50	7	361.0	90	<5	[135]
Polypyrrole-functionalized magnetic Kaolin (Ppy-Fe_3O_4/kaolin)	Hg^{2+}	50	0.05	420	42	7.2	317.1	N/A	>90	[136]
$CoFe_2O_4$@SiO_2–NH_2	Hg^{2+}	20	0.1	720	25	7	149.3	N/A	75	[137]
$CoFe_2O_4$@SiO_2–EDTA	Hg^{2+}	20	0.1	720	25	7	103.3	>90	>90	[138]
γ-Fe_2O_3@NH_2	Hg^{2+}	200	2.25	30	25	7	85.6	84	100	[122]
Fe_3O_4 / Fe_3O_4–Ag^0	Hg^{2+}	100	2.5	720	23	N/A [2]	28.0 / 71.3	<40 / >80	N/A	[139]
Rice-husk-activated carbon (RHAC)	Hg^{2+}	20	0.2	60	25	5	55.87	N/A	N/A	[140]
Magnetic poly(vinyl alcohol)—procion blue MX-3G / Magnetic poly(vinyl alcohol) (mPVAL)	Hg^{2+}	400	5.0	10	20	6	69.2 / 0.57	>94	95	[141]
Amino-functionalized SiO_2 particles (NH_2@SiO_2)	Hg^{2+}	100	2.25	60	25	4	3.75	88	100	[123]
Activated carbon / Gold-NP-coated silica	Hg^{2+}	0.1–300	2.3	1440	22	7.4	2.5 / 1.4	95 / 96	N/A	[142]
γFe_2O_3@SiO_2–NH_2	Hg^{2+}	40	2.5	120	25	4	2.1	94.3	100	This work
$CoFe_2O_4$@SiO_2–NH_2	Hg^{2+}	40	2.5	120	25	4	1.2	92.1	100	This work

[1] Seawater (salinity 0.175 mol/L–0.525 mol/L); [2] pH not adjusted.

Su et al. [125] studied the adsorption capacity of Dy^{3+} with the adsorbate Fe_3O_4@SiO_2@polyaniline-graphene oxide, and they demonstrated an adsorption capacity of 16.0 mg/g, an adsorption efficiency of 98%, and a desorption efficiency of 95% at pH 4. Liu et al. [126] reported an adsorption capacity of 28.3 mg/g, an adsorption efficiency of >80%, and a desorption efficiency of >95% for Dy^{3+} at pH 7 using Fe_3O_4-C_{18}–chitosan–DETA. With the same pH of 7, using NH_4OH@SiO_2 (APTMS), Kegl et al. [84] reported an adsorption capacity of 23.2 mg/g and an adsorption efficiency of 94% for Dy^{3+}. Javadian et al. [127] reported the adsorption characteristics of synthetic-polymer-based magnetic adsorbent (M-PPTA) toward Dy^{3+} at pH 5.5, and found an adsorption capacity of 24.0 mg/g, an adsorption efficiency of 98.4%, and a desorption efficiency of >84%. Shinozaki et al. [128] noted 18.4 mg/g of adsorption capacity and 30% of adsorption efficiency for Dy^{3+} at pH 1

using an adsorbate of polymeric adsorbents modified with ethylenediamine (EDA) and diglycolamic acid (DGA).

Alcaraz et al. [129] reported the use of chemically and physically activated carbons from spent-coffee waste to adsorbed Dy^{3+} ions. They showed an adsorption capacity of chemically activated carbons toward Dy^{3+} of 31.26 mg/g and an adsorption efficiency of Dy^{3+} of 96% at pH 4. When using physically activated carbons from spent-coffee waste, an adsorption capacity of 33.52 mg/g and an adsorption efficiency of 99% were obtained. Further, Viana et al. [130] reported an adsorption capacity of 0.570 mg/g and an adsorption efficiency of 89% for Dy^{3+} using *ulva lactuca*—Chlorophyta (green), while an adsorption capacity of 0.526 mg/g and an adsorption efficiency of 84% were obtained for Dy^{3+} by using *Gracilaria* sp.—Rhodophyta (red). According to Zhang et al. [131], an adsorption capacity of 1.85 mg/g and an adsorption efficiency of 84% of Dy^{3+} at pH 3 were obtained using an Fe^0–SiO_2–PA /SiO_2–DTPA adsorbent.

Su et al. [125], Zhang et al. [131], Barros et al. [132], Tong et al. [133], and Kegl et al. [134] studied the adsorption capacity of Tb^{3+} using various adsorbent materials under different adsorption conditions. Using graphene oxide at pH 4, Su et al. [125] obtained an adsorption capacity of 11.8 mg/g, an adsorption efficiency of 98%, and a desorption efficiency of 95% for Tb^{3+}. Zhang et al. [131] used an Fe^0–SiO_2–PA/SiO_2–DTPA adsorbate at a pH of 3 and obtained an adsorption capacity of 1.4 mg/g for Tb^{3+}. Barros et al. [132] reported the use of molecular-sieve zeolite for the adsorption of Tb^{3+} ions at a pH of 5, and they noted an adsorption capacity of 2.59 mg/g alongside an adsorption efficiency of 80%, and a desorption efficiency of >60% for Tb^{3+}; furthermore, they obtained an adsorption capacity of 5.07 mg/g for the Tb^{3+} using *B. cereus* biomass-supported zeolite adsorbate. Tong et al. [133] used multi-walled carbon nanotubes with tannic acid (TA-MWCNTs) for the adsorption of Tb^{3+} at pH 5 and obtained an adsorption capacity of 8.55 mg/g, while Kegl et al. [134] used a superparamagnetic γ-Fe_2O_3-NH_4OH@SiO_2 (APTMS) adsorbent and obtained an adsorption capacity of 0.204 mg/g for the adsorption of Tb^{3+} ions from water at a pH of 7.

Adsorption studies on Hg^{2+} ions with $CoFe_2O_4$–chitosan–graphene, polypyrrole-functionalized magnetic kaolin (Ppy-Fe_3O_4/kaolin), and $CoFe_2O_4$@SiO_2–NH_2 adsorbents at a pH of 7 showed adsorption capacities of 361.0 mg/g, 255.2 mg/g, and 149.3 mg/g, respectively. These studies were performed by Zhang et al. [135], Lin et al. [136], and Wang et al. [137], respectively.

In recent works, Xia et al. [138], Allwin Mabes Raj et al. [122], and Inglezakis et al. [139] studied the adsorption of Hg^{2+} using $CoFe_2O_4$@SiO_2–EDTA, γ–Fe_2O_3@NH_2, and Fe_3O_4 as adsorbates, and they noted adsorption capacities of 103.3 mg/g, 85.6 mg/g, and 28.0 mg/g for Hg^{2+}, respectively. Liu et al. [140] studied the adsorption capacity of Hg^{2+} with the adsorbate rice-husk-activated carbon (RHAC) and demonstrated an adsorption capacity of 55.87 mg/g at a pH of 5. Denizli et al. [141] studied the adsorption of Hg^{2+} with magnetic poly (vinyl alcohol)—procion blue MX-3G as the adsorbent and noted an adsorption capacity of 69.2 mg/g, an adsorption efficiency of >94%, and a desorption capacity of 95% for Hg^{2+}. An adsorption study of Hg^{2+} with amino-functionalized SiO_2 particles (NH_2@SiO_2) conducted by Raj et al. [123] and a study with activated carbon performed by Solis et al. [142] showed adsorption capacities of 3.75 mg/g and 2.5 mg/g, respectively.

Nevertheless, it can be observed that the adsorption of Dy^{3+}, Tb^{3+}, and Hg^{2+} ions is tested mostly in acidic or neutral aqueous media, and that the adsorption capacity is higher in surface-functionalized adsorbent nanomaterials. In addition, some adsorbents have significantly higher adsorption properties for Hg^{2+} than for Dy^{3+} and Tb^{3+} ions compared to our prepared adsorbent materials. However, the main advantages of our adsorbents are their relatively fast kinetics of adsorption, which are associated with their nano-size and functionality, their high desorption efficiency, and the convenient and highly efficient sustainable recovery of the used adsorbate material at the end of the adsorption process by magnetic attraction.

2.3. Cytotoxicity Study

The cytotoxicity of the nanoparticles was tested in different healthy cell lines after 3 days of incubation. In the SKMDCs, the γFe_2O_3 nanoparticles showed lower toxicity than the $\gamma Fe_2O_3@SiO_2–NH_2$, as shown in Figure 10a. The cell viability reached 69 ± 0.72% after 3 days of incubation with 5 µg/mL of $\gamma Fe_2O_3@SiO_2–NH_2$, which decreased to 57 ± 0.47% at a concentration of 500 µg/mL. Similarly, the $CoFe_2O_4$ nanoparticles showed lower toxicity than the $CoFe_2O_4@SiO_2–NH_2$. The incubation of the SKMDCs with $CoFe_2O_4@SiO_2–NH_2$ up to a concentration of 125 µg/mL for 3 days showed lower toxicity with a cell viability above 80%; however, the cell viability decreased to 70 ± 3.41% at 500 µg/mL.

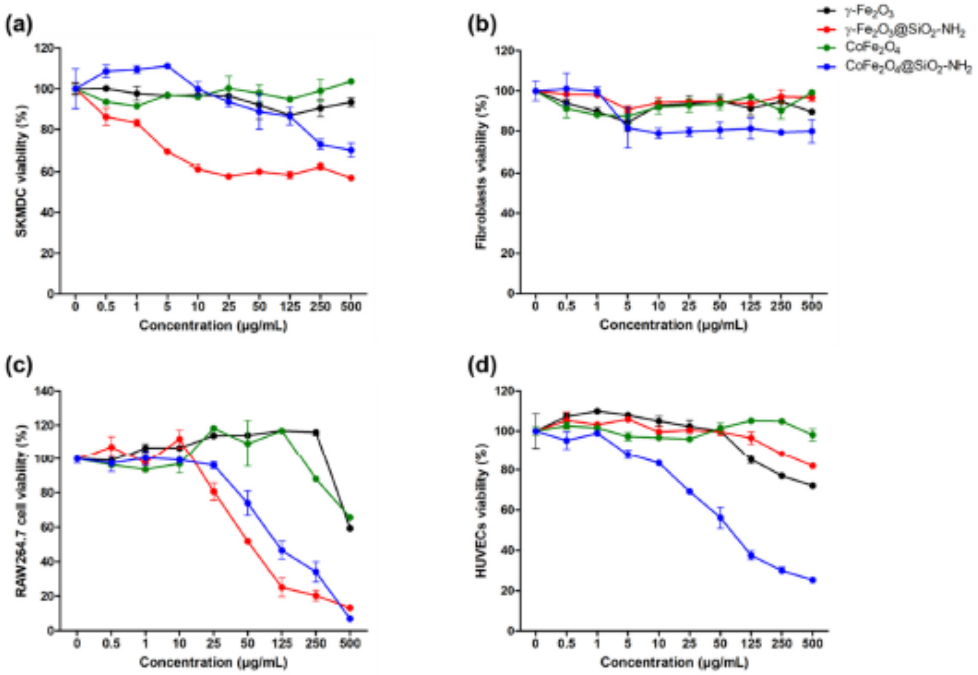

Figure 10. Cell viability (%) of (**a**) SKMDCs, (**b**) fibroblasts, (**c**) RAW264.7, and (**d**) HUVECs treated with different concentrations of nanoparticles for 3 days. Results are presented as mean ± SEM, n = 3.

In the fibroblasts, all the nanoparticles showed lower toxicity when the cell viability was above 80%, with concentrations of up to 500 µg/mL (Figure 10b).

In the macrophage RAW264.7 cell line, both the γFe_2O_3 and the $CoFe_2O_4$ showed lower toxicity than the $\gamma Fe_2O_3@SiO_2–NH_2$ and $CoFe_2O_4@SiO_2–NH_2$ (Figure 10c). At 50 µg/mL, the cell viability reached 52 ± 0.61% and 74 ± 7% for the $\gamma Fe_2O_3@SiO_2–NH_2$ and $CoFe_2O_4@SiO_2–NH_2$, respectively. However, at 500 µg/mL, the cell-viability values were 59 ± 0.10%, 13 ± 0.51%, 66 ± 0.31%, and 7 ± 0.23% for the γFe_2O_3, $\gamma Fe_2O_3@SiO_2–NH_2$, $CoFe_2O_4$, and $CoFe_2O_4@SiO_2–NH_2$, respectively. It is worth mentioning that the macrophage RAW264.7 cells were more sensitive to the $\gamma Fe_2O_3@SiO_2–NH_2$ and $CoFe_2O_4@SiO_2–NH_2$ than the other cell lines.

The toxicity of the nanoparticles was also tested in the HUVECs (Figure 10d). The results showed the low toxicity of the γFe_2O_3, $\gamma Fe_2O_3@SiO_2–NH_2$, and $CoFe_2O_4$ compared with the $CoFe_2O_4@SiO_2–NH_2$, which showed a decrease in cell viability (69 ± 1.26%) at 25 µg/mL, reaching 25 ± 0.86% at 500 µg/mL.

The results presented in Figure 11a show that none of the nanoparticles had hemolytic effects, except the nanoparticles of γFe_2O_3@SiO_2–NH_2, which showed a dose-dependent hemolytic effect. A change in the supernatant color was observed by the naked eye at concentrations of 50 µg/mL and above, indicating the lysis of red blood cells and hemoglobin release (Figure 11b) [5].

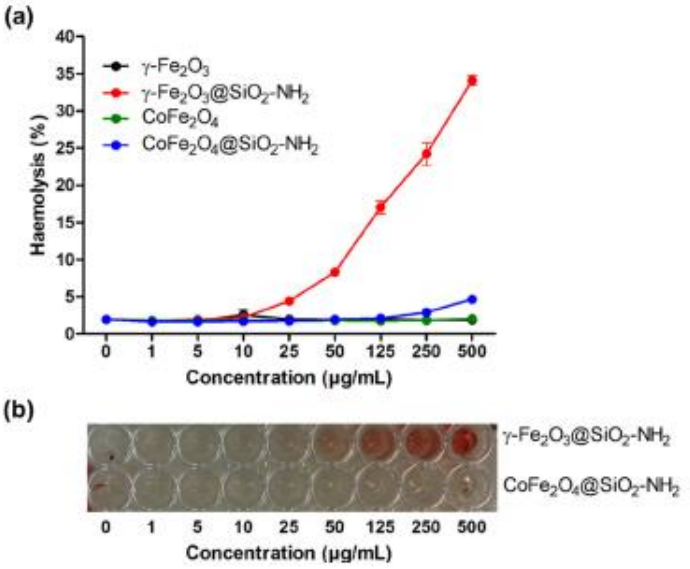

Figure 11. In vitro hemolytic studies. (**a**) Hemolytic effect of different nanoparticles on human blood at different concentrations (**a**), representative image of the hemolytic effect (red-colored supernatant) of nanoparticles (**b**).

A toxicity study on zebrafish embryos exposed to different concentrations of nanoparticles as shown in Figure S3 revealed that none of the nanoparticles had toxic effects on the zebrafish embryos until 96 hpf compared to the control, even at a high concentration of 500 mg/L (Figure 12).

Table S1 depicts the list of various adsorbent materials with their toxicological assessment in different biological systems. Many studies investigating the toxicities of different materials using in vivo and in vitro studies, such as a toxicity study of human kidneys (HEK293) using magnetic, SiO_2-coated nanoparticles with an exposure of up to 1.0 µg/µL for 12 h, which was reported by Shim et al. [143]. In their SiO_2 in vitro study, Pisani et al. [144] used A549 (human) lung cells with 0.1–6-µg/cm^2 dosages and exposed them for 24 h. A toxicity study was reported by Ellinger-Ziegelbauer and Pauluhn [145] on rat-lung cells with MWCNT at a 11-mg/m^3 concentration for a 6-h (aerosol) 90-day post-exposure period. Jovanović et al. [146] studied the TiO_2 (anatase) and hydroxylated fullerene toxicity of 40-µg/mL fullerenes and 170 ng/mL in Danio rerio (embryo). With 2.5 µg/mL and 25 µg/mL of Ag in human colon cells, toxicity was studied by Böhmert et al. [147]. Conde et al. [148] studied toxicity using Au, functionalized with anti-sense cDNAs at dosages of 30 nM in the HCT-116 (human) colon.

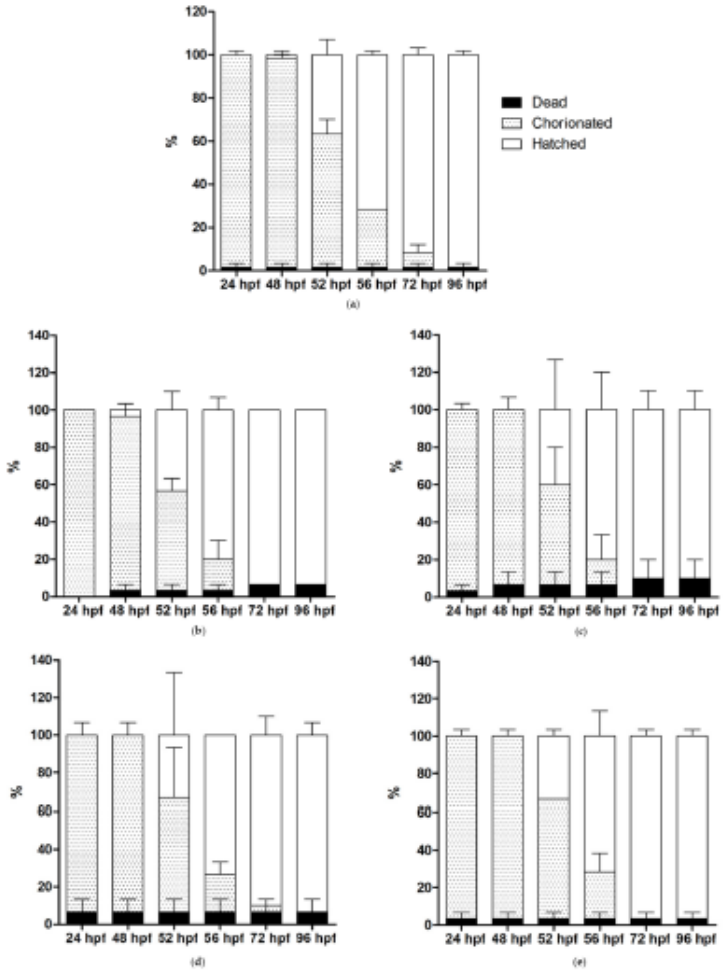

Figure 12. Zebrafish-embryo development expressed as percentages of dead, chorionated, and hatched, in water containing concentration of 500 mg/L of nanoparticles. Control group (**a**) is of growth without the use of any NPs (**b**) γFe_2O_3 (**c**) $\gamma Fe_2O_3@SiO_2–NH_2$ (**d**) $CoFe_2O_4$, and (**e**) $CoFe_2O_4@SiO_2–NH_2$ for 24, 48, 52, 56, 72, and 96 h post-fertilization (hpf). Data are presented as mean ± SEM of two independent experiments.

Our present study investigating the cytotoxicity of iron-oxide NPs generally showed that both these NPs, $\gamma Fe_2O_3@SiO_2–NH_2$ and $CoFe_2O_4@SiO_2–NH_2$, are non-toxic.

3. Materials and Methods

All the chemicals used in this study were generally of reagent grade, obtained from commercial sources without further purification: iron (II) chloride tetrahydrate ($FeCl_2{\cdot}4H_2O$, 98%, 198.81 g/mol, CAS no. 13478-10-9, Sigma-Aldrich, Merck Group KGaA, Darmstadt, Germany), iron (III) chloride hexahydrate ($FeCl_3{\cdot}6H_2O$, ≥98%, 270.3 g/mol, CAS no. 10025-77-1, Sigma-Aldrich, Merck Group KGaA, Darmstadt, Germany), cobalt (II) chloride hexahydrate ($CoCl_2{\cdot}6H_2O$, 98%, 237.93 g/mol, CAS no. 7791-13-1, Sigma-

Aldrich, Merck Group KGaA, Darmstadt, Germany), ammonium hydroxide aqueous solution (NH_4OH, 25%, 35.05 g/mol, 0.91 g/mL, CAS no. 1336-21-6, GramMol, Zagreb, Croatia), sodium hydroxide (NaOH, ≥98% (anhydrous), 40 g/mol, CAS no. 1310-73-2, Sigma-Aldrich, Merck Group KGaA, Darmstadt, Germany), potassium hydroxide (KOH, 1 mol/L (1-N), Titripur®, 56.11 g/mol, 1.05 g/mL, CAS no. 1310-58-3, Sigma-Aldrich, Merck Group KgaA, Darmstadt, Germany), potassium chloride (KCl, ACS reagent, 99.0–100.5%, 74.55 g/mol, CAS no. 7447-40-7, Sigma-Aldrich, Merck Group KgaA, Darmstadt, Germany), hydrochloric acid (HCl, for 1000 mL, 1 mol/L (1-N), Titrisol®, 36.46 g/mol, 1.09 g/ml, CAS no. 7647-01-0, Sigma-Aldrich, Merck Group KgaA, Darmstadt, Germany), nitric acid (HNO_3, ACS reagent, 70%, 63.01 g/mol, 1.413 g/mL, CAS no. 7697-37-2, Sigma-Aldrich, Merck Group KgaA, Darmstadt, Germany), 2-propanol (C_3H_8O, 99.8%, 60.1 g/mol, 0.785 g/mL, CAS no. 67-63-0, GramMol, Zagreb, Croatia), ethanol (C_2H_5OH, 96%, 46.07 g/mol, 0.810 g/mL, CAS no. 64-17-5, GramMol, Zagreb, Croatia), tetraethyl orthosilicate TEOS ($C_6H_{20}O_4Si$, 99%, 208.33 g/mol, 0.94 g/mL, CAS no. 78-10-4, Sigma-Aldrich, Merck Group KGaA, Darmstadt, Germany), 3-aminopropyltrimethoxysilane APTMS ($C_6H_{17}NO_3Si$, 97%, 179.29 g/mol, 1.027 g/mL, CAS no. 13822-56-5, Sigma-Aldrich, Merck Group KGaA, Darmstadt, Germany), terbium (III) chloride hexahydrate ($TbCl_3{\cdot}6H_2O$, 99.9%, 373.38 g/mol, CAS no. 13798-24-8, Sigma-Aldrich, Merck Group KGaA, Darmstadt, Germany), dysprosium (III) nitrate pentahydrate ($Dy(NO_3)_3{\cdot}5H_2O$, 99.9%, 438.59 g/mol, CAS no. 10031-49-9, Sigma-Aldrich, Merck Group KGaA, Darmstadt, Germany), and mercury (II) nitrate monohydrate ($Hg(NO_3)_2{\cdot}H_2O$, ≥98.5%, 342.62 g/mol, CAS no. 7783-34-8, Sigma-Aldrich, Merck Group KGaA, Darmstadt, Germany). For the preparation of all suspensions and solutions, deionized water (dH_2O) was used.

3.1. *Synthesis of Magnetic Nanoparticles (MNPs)*

Spinel-type MNPs of maghemite (γ-Fe_2O_3) and Co-ferrite ($CoFe_2O_4$) were obtained by co-precipitation of M^{2+} (M = Fe, Co) and Fe^{3+} salts at slightly elevated temperature in an alkaline aqueous medium according to Schikorr reaction [149]:

$$M^{2+} + 2Fe^{3+} + 4OH^- + O_2 = MO{\cdot}Fe_2O_{3\,(s)}\downarrow + 2H_2O \quad (3)$$

3.1.1. γ-Fe_2O_3 NPs

For the synthesis of γFe_2O_3 NPs, 50 mL of 25% NH_4OH in a round-bottomed reaction flask was heated up to (87 ± 2) °C by reflux and stirred at 400 rpm. A 0.5-M aqueous solution of Fe^{2+} and Fe^{3+} in a molar ratio of 1:2 was added to the ammonia solution until pH 10 was reached. The reaction was carried out for 1 h at (87 ± 2) °C. Instantly, when the two solutions were mixed, a dark-brown precipitate of magnetic phase was formed. After the reaction, the dark-brown γFe_2O_3 precipitate was separated from the supernatant by settling on the permanent magnet and rinsed with deionized water several times. Finally, the rinsed precipitate was dried in a laboratory oven at 90 °C for 24 h.

3.1.2. $CoFe_2O_4$ NPs

For the synthesis of $CoFe_2O_4$ NPs, stock solutions containing Co^{2+} and Fe^{3+} ions were prepared using $CoCl_2{\cdot}6H_2O$ and $FeCl_3{\cdot}6H_2O$ as source materials. Stoichiometric amounts of the appropriate chlorides were dissolved in deionized water. The concentration of the solution was 0.5 M in all experiments, referred to as chloride concentration. The solution was then hydrolyzed in a 0.5-M aqueous solution of sodium hydroxide preheated to (87 ± 2) °C by reflux and stirred at 400 rpm. The reaction was carried out for 1 h at pH 10. After the reaction was completed, the dark-brown $CoFe_2O_4$ precipitate was separated from the supernatant by settling on the permanent magnet and rinsed with deionized water. The rinsing procedure was repeated several times, and the rinsed precipitate was finally dried in a laboratory oven at 90 °C for 24 h.

3.1.3. γ-Fe_2O_3@SiO_2-NH_2 and $CoFe_2O_4$@SiO_2-NH_2 NPs

For the in situ preparation of γ-Fe_2O_3@SiO_2–NH_2 and $CoFe_2O_4$@SiO_2–NH_2 core@shell NPs, 21.6 mol% of 2-propanol, 15.1 mol% of distilled water, 2.2 mol% of 25% NH_4OH solution, 4 mL of the prepared γ-Fe_2O_3 or $CoFe_2O_4$ colloidal suspension with a mass concentration (γ_i) 1.035 ± 0.005 g/mL, 0.25 mol% of TEOS, and 0.36 mol% of APTMS were mixed under magnetic stirring at 500 rpm in a closed vessel for 24 h at room temperature. After the reaction finished, the sediment was rinsed several times with ethanol (96 wt.%) and distilled water. The obtained core@shell superparamagnetic NPs were separated from the supernatant by using the permanent external magnet and dried overnight in the laboratory oven at 90 °C.

The experimental procedure for this study is schematically presented in Figure 13.

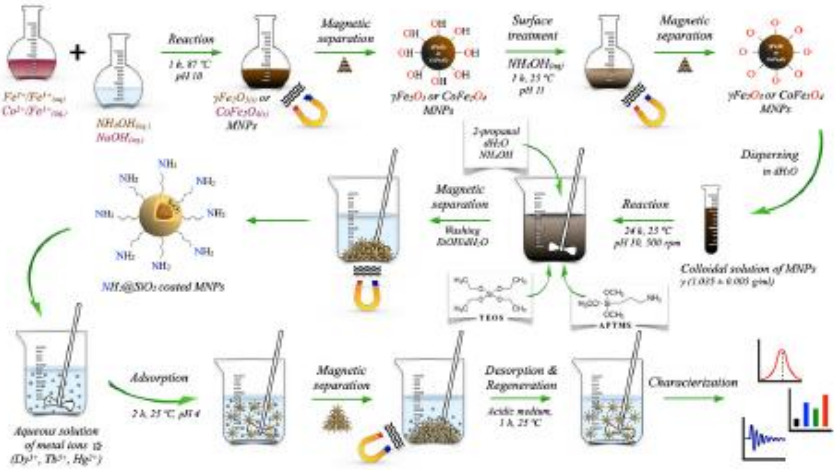

Figure 13. Schematic representation of the experimental procedure.

3.2. *Characterization of MNPs*

Prepared samples were characterized using X-ray diffractometry and transmission-electron microscopy in combination with energy-dispersive X-ray spectroscopy, Brunauer–Emmet–Teller specific-surface-area technique, Fourier-transform infrared spectroscopy, thermogravimetric analysis, electro-kinetic (ξ) potential measurements, inductively coupled plasma atomic emission spectroscopy, and vibrating-sample magnetometry.

3.2.1. X-ray Diffractometry (XRD)

We used X-ray diffractometry (XRD) for structural analysis with a Brucker D4 Endeavor X-ray diffractometer coupled with CuK_α radiation (Bruker D4 Endeavor, Bruker, Billerica, MA, USA). The measurements were performed at room temperature with a time step of 30 s within the range of Bragg's angle 2 θ from 20° to 80°, with an angle step of 0.036°. The XRD utilized a Cu anode with a wavelength of 0.154 nm.

3.2.2. Transmission-Electron Microscopy (TEM) with Energy-Dispersive X-ray Spectroscopy (EDXS)

The TEM images were taken using a JEOL JEM-2100 microscope, operated by drop-casting the nanoparticle suspensions on the thin carbon-coated copper grid (200 mesh, holly carbon) and drying under ambient conditions. The EDXS analyses were performed at 200 kV using a JEOL JEM-2010 microscope (JEM 2100 JEOL, JEOL Ltd., Musashino Akishima, Tokyo, Japan).

3.2.3. Fourier-Transform Infrared Spectroscopy (FT-IR)

The FT-IR data were collected using a Spectrum Two FT-IR Spectrometer (PerkinElmer, Waltham, MA, USA) utilizing a KBr window for data collection over a spectral range of 400 cm^{-1} to 4000 cm^{-1} at a resolution of 0.5 cm^{-1}. The FT-IR spectra were recorded with PerkinElmer's Spectrum 10™ software at room temperature in the transmittance mode.

3.2.4. Brunauer–Emmet–Teller Method (BET)

The BET was used to determine the specific surface areas of NPs by using Micromeritics, Flow Prep 060, with Tristar II 3020 (Micromeritics Instrument Corporation, Norcross, GA, USA). All samples were degassed at 110 °C for 24 h prior to each measurement. The specific surface area was measured in the 0.05–0.3 range of relative pressure in nitrogen gas at a temperature of 77.35 K after 24 h.

3.2.5. Thermogravimetric Analysis (TGA)

To predict the thermal stability and chemical degradation of the functional groups grafted to the surfaces of the NPs, a TGA analysis was performed using a PerkinElmer TGA4000 thermogravimetric analyzer (PerkinElmer, Waltham, MA, USA) calibrated with nickel and iron as Curie-point-reference materials.

For the experiments, prepared powdered sample specimens were placed in a corundum ceramic sample pan, and the weights of these specimens ranged between 2 mg and 50 mg. The experiments were conducted by continuously monitoring the mass of a sample in nitrogen purge gas at a flow rate of 20 mL/min and a heating rate of 10 °C/min over a temperature range of 30 °C to 900 °C, and were controlled by PerkinElmer's thermal software Pyris Software™ version 10.1.

3.2.6. Electro-Kinetic (ξ)-Potential Measurements

Dynamic light scattering was used to determine electro-kinetic phenomena, which involve the interrelation between mechanical and electrical effects at a moving interface. Electro-kinetic results were expressed in terms of ζ-potential, determined from electrophoretic mobility of particles through a field with known strength, and the term of isoelectric point (IEP), referring to the conditions under which the ζ-potential is zero. When pH is equal to or close to the isoelectric point, NPs tend to be unstable, form clusters, and precipitate. The ζ-potential was measured by ZetaSizer Nanoseries Malvern Instruments (Malvern Panalytical Ltd., Spectris Group, London, UK). Aqueous solutions of NaOH and HCl were employed to adjust the pH values of suspensions. All measurements were performed at room temperature.

3.2.7. Potentiometric Titration

The pH potentiometric titrations were used for the determination of the total charge of aqueous colloidal dispersions of MNPs. The titrations were carried out in forward (acidic-to-alkaline) and backward (alkaline-to-acidic) directions at $2.5 < pH < 11.0$ using 0.1-M-HCl and 0.1-M-KOH aqueous solutions as titrants. A two-burette instrument, Mettler T-70 (Mettler Toledo, Columbus, OH, USA), was used. It was equipped with a combined glass-electrode Mettler T DG 117. The burettes were filled with 0.1 M HCl and 0.1 M KOH. All the solutions were prepared with distilled H_2O with a carbonate content $<10^{-6}$ mol/L, which was achieved through boiling and consequent cooling in a nitrogen atmosphere.

Prior to the titration, the ionic strength was adjusted to an approximate value of 0.1 mol/L by the addition of a 3-M-KCl aqueous solution and then maintained constantly within 2% of the initial value upon the addition of HCl and KOH solutions.

The samples were titrated in forward and backward runs between pH 2 and pH 11. After each addition, the volume of the titration reagent was read when the equilibrium condition <0.1 mV/min was reached or the condition of the maximum waiting time of 3 min was satisfied. The blank HCl–KOH titrations were performed under the same conditions as mentioned above [150].

The titrant volume was normalized to the mass of the titrated samples and expressed as a charge per mass Q/m (in mmol/g) vs. pH curve. The amounts of charged NH_2 surface groups in the products were expressed in mmol/g sample. The determination of the amount of charged functional groups is described in detail elsewhere [90,150,151].

3.2.8. Vibrating-Sample Magnetometry (VSM)

For magnetization measurements, a Lake Shore 7400 vibrating-sample magnetometer was used (Lake Shore Cryotronics, Inc, Westerville, OH, USA). The mass magnetization M (emu/g) as a function of the applied magnetic field H (Oe) was measured at room temperature for all the prepared samples.

3.3. Adsorption and Desorption Tests for Dy^{3+}, Tb^{3+} and Hg^{2+} Ions

To evaluate the affinity of Dy^{3+}, Tb^{3+}, and Hg^{2+} ions to the surfaces of the prepared γFe_2O_3@SiO_2–NH_2 and $CoFe_2O_4$@SiO_2–NH_2 adsorbent NPs, 20 mL of 10-mM standard aqueous solutions was prepared from $TbCl_3 \cdot 6H_2O$, $Dy(NO_3)_3 \cdot 5H_2O$, and $Hg(NO_3)_2 \cdot H_2O$ at pH 4 and temperature of 25 °C.

The adsorption study was performed by separate mixing of 50 mg γFe_2O_3@SiO_2-NH_2 and $CoFe_2O_4$@SiO_2–NH_2 adsorbents with the prepared aqueous solutions of Dy^{3+}, Tb^{3+}, and Hg^{2+} ions with a concentration of 10 mM at a temperature of 25 °C, for an adsorption time of 2 h. After the adsorption of Dy^{3+}, Tb^{3+}, and Hg^{2+} ions, the magnetic adsorbents were removed from aqueous solutions with an external permanent magnet. To determine the adsorption efficiency and capacity, the ICP-OES method was used (ICP-OES, SPECTRO CITROS VISION, SPECTRO Analytical Instruments GmbH, Kleve, Germany).

The adsorption capacity q_{ads}, mass (mg) of adsorbed Dy^{3+}, Tb^{3+}, and Hg^{2+} ions per mass (g) of γFe_2O_3@SiO_2–NH_2 or $CoFe_2O_4$@SiO_2–NH_2 adsorbents and adsorption efficiency $q_{ads,\%}$ were calculated by the following equations:

$$q_{ads} = \frac{(c_{ads,0} - c_{ads,e}) \cdot M_{ads} \cdot V}{m_{ads}} \left(\frac{mg}{g}\right) \quad (4)$$

$$q_{ads,\%} = \frac{c_{ads,0} - c_{ads,e}}{c_{ads,0}} (\%) \quad (5)$$

where $c_{ads,0}$ (mol/L) and $c_{ads,e}$ (mol/L) relate to the initial and equilibrium concentrations of Dy^{3+}, Tb^{3+}, and Hg^{2+} ions, respectively, V (L) denotes the solution volume, M_{ads} (g/mol) is the molar mass of adsorbate, and m_{ads} (g) is the mass of adsorbent NPs.

Furthermore, desorption of adsorbed Dy^{3+}, Tb^{3+}, and Hg^{2+} ions from γFe_2O_3@SiO_2–NH_2 and $CoFe_2O_4$@SiO_2–NH_2 adsorbent surfaces was performed by mixing adsorbents with the prepared 1-M aqueous solution of HNO_3 at 25 °C for 1 h. Desorption capacity was determined using the ICP-OES method and calculated by Equation (6):

$$q_{des,\%} = \frac{c_{des}}{c_{ads}} \cdot 100 (\%) \quad (6)$$

where c_{des} (mg/g) is the concentration of adsorbate desorbed and c_{ads} (mg/g) is the concentration of adsorbate adsorbed. Results for adsorption and desorption of Dy^{3+}, Tb^{3+}, and Hg^{2+} ions are shown in Table 1.

3.4. Toxicity Study of MNPs

3.4.1. Cell Cultures

Four different types of healthy cell were used; human-skeletal-muscle-derived cells (SKMDCs), human fibroblasts, murine macrophage cells (RAW264.7), and human-umbilical-vein endothelial cells (HUVECs).

The SKMDCs were maintained in an F-10 nutrient medium supplemented with 25% fetal bovine serum (FBS), 1% penicillin/streptomycin (P/S), 0.1% insulin, 0.01% fibroblast-growth factor (FGF), and 0.01% epidermal growth factor (EGF). Fibroblasts were maintained

in RPMI medium supplemented with 10% FBS and 1% P/S. The RAW264.7 cells were maintained in Dulbecco's Modified Eagle's Medium (DMEM) supplemented with 10% FBS and 1% P/S. The HUVECs were maintained in Endothelial cell Growth Medium 2 supplemented with FBS (2%), EGF (5 ng/mL), basic FGF (10 ng/mL), insulin-like growth factor (ILGF) (20 ng/mL), vascular endothelial growth factor (VEGF) (0.5 ng/mL), ascorbic acid (1 µg/mL), heparin (22.5 µg/mL), and hydrocortisone (0.2 µg/mL), 1% P/S. All cell types were allowed to grow in a humidified atmosphere at 37 °C under 5% CO_2.

3.4.2. Cytotoxicity Study

For cell-viability experiments, cells were seeded in a 96-well plate in 200 µL of their respective culture media; 24 h after cell growth, cells were treated with different concentrations of NPs and incubated for 3 days. Control cells were treated with the vehicle. After the incubation time, cells were incubated for 4 h with 0.5 mg mL^{-1} of 3-(4,5-dimethylthiazol-2-yl)-2,5-diphenyltetrazoliumbromide (MTT). After MTT incubation, MTT/medium was removed, and the precipitated violet crystals were dissolved in ethanol/DMSO (1:1, *v:v*) solution with shaking for 20 min. The absorbance was measured at 540 nm. The percentage (%) of live cells was calculated as $Ab_{test}/Ab_{control}$ 100. The experiment was performed three times.

3.4.3. In Vitro Hemolytic Studies

Human-blood samples were obtained from a local blood bank (Établissement Français du Sang, Occitanie, France). Blood samples were collected in lithium heparin and stored at 4 °C until use. In total, 10 mL of blood were centrifuged at 1500 rpm for 5 min, after which the obtained platelet-poor plasma (PPP) was removed (~5 mL). The blood pellet was washed with 5 mL of phosphate-buffered saline (PBS) and mixed by inversion followed by centrifugation at 1500 rpm for 5 min, a process that was repeated 5 times.

The obtained red blood cells (RBCs) were diluted with PBS (1:10, *v/v*), and then treated with nanoparticles at concentrations ranging from 0 to 500 µg/mL, after which they were incubated at 37 °C for 1 h. The positive controls were RBCs treated with 1% Triton X-100, and the negative control was PBS (diluent). After incubation, samples were centrifuged at 1500 rpm for 5 min and the obtained supernatant was transferred to a polystyrene 96-well plate for reading at 540 nm, corresponding to the free hemoglobin band, using Thermo Scientific™ Multiskan SkyHigh Microplate Spectrophotometer. The hemolysis percentage was calculated as = $(OD_{test} - OD_{PBS}/OD_{positive\ control} - OD_{PBS}) \times 100$, where OD is the optical density.

3.4.4. Toxicity in Zebrafish Embryos

Fertilized wild-type AB zebrafish embryos were obtained from the laboratory facility of molecular mechanisms in neurodegenerative dementia (MMDN), Inserm U1198, Montpellier University, collected and maintained at 28 °C and 14-h-light/10-h-dark cycle.

At 7 h post-fertilization (hpf), embryos were examined under the microscope, and only embryos that developed normally were selected for the study. The 7 hpf embryos (15 per group) were placed in 12-well plates and exposed to 4 mL of water containing 0, 10, 50, 125, and 500 mg/L NPs. The exposure to NPs started at 7 hpf and ended at 96 hpf. The percentages of survival, mortality, and hatching of embryos were recorded using ZEISS Stemi 508 stereo microscope (ZEISS International, Oberkochen, Germany) at 24, 48, 52, 56, 72, and 96 hpf. The experiment was performed twice.

4. Conclusions

Superparamagnetic γFe_2O_3@SiO_2–NH_2 and $CoFe_2O_4$@SiO_2–NH_2 core@shell crystalline NPs were synthesized in a simple manner using two different approaches the classical coprecipitation method and the sol-gel technique, to obtain functionalized nanosized superparamagnetic adsorbents designed for the binding and recycling of Dy^{3+}, Tb^{3+}, and Hg^{2+} ions from aqueous solutions. The synthesized spherical superparamagnetic

γFe_2O_3@SiO_2–NH_2 and $CoFe_2O_4$@SiO_2–NH_2 NPs have excellent characteristics related to their structural, morphological, and surface properties, as well as their thermal stability, functionality, electrokinetic charge, and magnetic responsiveness. These properties were confirmed by TEM/HRTEM/EDXS, FT-IR, XRD, TGA, BET, DLS, and VSM.

Each individual material phase in the prepared γFe_2O_3@SiO_2–NH_2 and $CoFe_2O_4$@SiO_2–NH_2 adsorbent NPs plays a significant role in the adsorption processes. The superparamagnetic γFe_2O_3 and $CoFe_2O_4$ monodomain cores give the adsorbents the necessary magnetic properties and magnetic response in an external magnetic field, while the SiO_2 amorphous shell allows the magnetic cores to be chemically and thermally stable and, due to the high content of hydroxyl groups on its surfaces, allows the high-density grafting of amino functional groups, which is necessary for interactions with metal ions. As Dy^{3+} and Tb^{3+} preferentially react with amino groups, unlike Hg^{2+}, APTMS allows a higher capacity for their adsorption. The maximum adsorption capacities of Dy^{3+}, Tb^{3+}, and Hg^{2+} ions by the γFe_2O_3@SiO_2–NH_2 are 4.0 mg/g, 4.7 mg/g, and 2.1 mg/g, respectively, and 4.7 mg/g, 6.2 mg/g, and 1.2 mg/g by the $CoFe_2O_4$@SiO_2–NH_2. These values were obtained with a mass adsorbate of 50 mg, a contact time of 120 min, an initial concentration of Dy^{3+}, Tb^{3+}, and Hg^{2+} ions of 2×10^{-6} mol/L, and a temperature of 25 °C. The adsorption efficiency toward the Dy^{3+}, Tb^{3+}, and Hg^{2+} ions ranged from 83% to 98% for both the γFe_2O_3@SiO_2–NH_2 and the $CoFe_2O_4$@SiO_2–NH_2. In the post-adsorption treatment of the γFe_2O_3@SiO_2–NH_2 and $CoFe_2O_4$@SiO_2–NH_2 adsorbents in an acidic medium at pH 4.5, the Dy^{3+}, Tb^{3+}, and Hg^{2+} ions were completely desorbed from their surfaces. The desorption efficiency was 100%.

The toxicity assessment of the prepared adsorbents provided information on the relationship between their minimum dose and their responses to adverse effects on SKMDCs, fibroblasts, RAW264.7, and HUVECs, under the expected exposure conditions. The results showed the low toxicity of all the nanoparticles in the fibroblasts; however, higher toxicity was observed in macrophage RAW264.7 cells treated with γFe_2O_3@SiO_2–NH_2 and $CoFe_2O_4$@SiO_2–NH_2. The recording of the survival, mortality, and hatching percentages of zebrafish embryos exposed to different concentrations of the nanoparticles showed no toxicity compared to the control until 96 hpf, even at a high adsorbent concentration of 500 mg/L.

Supplementary Materials: The following supporting information can be downloaded at: https://www.mdpi.com/article/10.3390/ijms24210072/s1.

Author Contributions: Conceptualization, A.L., J.-O.D. and A.K.; methodology: A.F.P.A.M.R., M.B., J.-O.D. and A.K.; formal analysis, A.F.P.A.M.R., L.M.A.A., M.O., M.G.-B. and A.K.; investigation, A.F.P.A.M.R., M.B., L.M.A.A., M.O., M.G.-B., J.-O.D. and A.K.; writing—original draft preparation, A.F.P.A.M.R. and A.K.; writing—review and editing, A.F.P.A.M.R., J.-O.D., L.M.A.A. and A.K.; visualization, A.F.P.A.M.R. and A.K.; supervision, A.K.; project administration, A.L.; funding acquisition, N.D. and A.L. All authors have read and agreed to the published version of the manuscript.

Funding: The project HMRecycle (E! 113543) received funding from the Eurostars-2 joint program. We express our gratitude to the national funding organization, Slovenian Ministry of Economic Development and Technology (MEDT), for co-financing the project HMRecycle. The work was also supported by the international research project, the Marie Skłodowska-Curie Action "Global Mercury Observation and Training Network in Support to the Minamata Convention," financed under the funding line "excellent science" of the Horizon 2020 research-and-innovation program of the European Commission, under the Marie Sklodowska-Curie grant agreement no. 860497. The results were created within the Research program Design of new properties of (nano)materials and applications, no. P2-0424, and the authors acknowledge the financial support from the Slovenian Research Agency. This research was also funded by the Ministry of Education, Science and Sport of the Republic of Slovenia and the European Union, the European, t Regional Development Fund (ERDF), and Early Research Career 2.1 (contract no. C3330-19-952032).

Institutional Review Board Statement: Not applicable.

Informed Consent Statement: Not applicable.

Data Availability Statement: No such data that were created with the scope to share it publically.

Acknowledgments: All authors would like to thank Nicolas Cubedo for providing zebrafish embryos. The author sincerely acknowledges the efforts of Matej Bračič for performing potentiometric titrations, Tjaša Kraševec Glaser B.Sc. for DLS measurements, and Nadir Bettache for the Hemolysis measurement.

Conflicts of Interest: The authors declare that there is no conflict of interest.

References

1. European Commission. COM(2020) 474 COM(2020) 474: Critical Raw Materials Resilience: Charting a Path towards Greater Security and Sustainability. 2020. Available online: https://eur-lex.europa.eu/legal-content/EN/TXT/?uri=CELEX:52020DC0474 (accessed on 31 March 2023).
2. Valko, M.; Morris, H.; Cronin, M.T.D. Metals, Toxicity and Oxidative Stress. *Curr. Med. Chem.* **2005**, *12*, 1161–1208. [CrossRef] [PubMed]
3. Crans, D.C.; Kostenkova, K. Open questions on the biological roles of first-row transition metals. *Commun. Chem.* **2020**, *3*, 1–4. [CrossRef] [PubMed]
4. De Granda-Orive, J.I.; García-Quero, C. E-waste: Rare earth elements, new toxic substances in cigarettes and electronic cigarettes. *Arch. Bronconeumol.* **2020**, *56*, 477–478. [CrossRef] [PubMed]
5. Tchounwou, P.B.; Yedjou, C.G.; Patlolla, A.K.; Sutton, D.J. Heavy Metals Toxicity and the Environment. *EXS* **2012**, *101*, 133–164. [CrossRef] [PubMed]
6. Jaishankar, M.; Tseten, T.; Anbalagan, N.; Mathew, B.B.; Beeregowda, K.N. Toxicity, mechanism and health effects of some heavy metals. *Interdiscip. Toxicol.* **2014**, *7*, 60–72. [CrossRef]
7. Baughman, T.A. Elemental mercury spills. *Environ. Health Perspect.* **2006**, *114*, 147–152. [CrossRef]
8. Blengini, G.A.; Nuss, P.; Dewulf, J.; Nita, V.; Talens Peiró, L.; Vidal-Legaz, B.; Latunussa, C.; Mancini, L.; Blagoeva, D.; Pennington, D.; et al. EU methodology for critical raw materials assessment: Policy needs and proposed solutions for incremental improvements. *Resour. Policy* **2017**, *53*, 12–19. [CrossRef]
9. Gislev, M.; Grohol, M. *European Commission: Report on Critical Raw Materials and the Circular Economy*; Publications Office of the European Union: Luxembourg, 2018. [CrossRef]
10. Azimi, G.; Forsberg, K.; Ouchi, T.; Kim, H.; Alam, S.; Baba, A.A. *Rare Metal Technology 2020*; Springer International Publishing: Cham, Switzerland, 2020. [CrossRef]
11. Cui, J.; Forssberg, E. Mechanical recycling of waste electric and electronic equipment: A review. *J. Hazard. Mater.* **2003**, *99*, 243–263. [CrossRef]
12. Cui, J.; Zhang, L. Metallurgical recovery of metals from electronic waste: A review. *J. Hazard. Mater.* **2008**, *158*, 228–256. [CrossRef]
13. Birloaga, I.; Veglió, F. Simulation and economic analysis of a hydrometallurgical approach developed for the treatment of waste printed circuit boards (WPCB). *Glob. Nest J.* **2018**, *20*, 695–699. [CrossRef]
14. Cui, J.; Roven, H.J. *Electronic Waste*; Elsevier Inc.: Amsterdam, The Netherlands, 2011. [CrossRef]
15. Ebin, B.; Isik, M.I. *Pyrometallurgical Processes for the Recovery of Metals from WEEE*; Elsevier Inc.: Amsterdam, The Netherlands, 2016. [CrossRef]
16. Zhang, J.; Anawati, J.; Yao, Y.; Azimi, G. Aeriometallurgical Extraction of Rare Earth Elements from a NdFeB Magnet Utilizing Supercritical Fluids. *ACS Sustain. Chem. Eng.* **2018**, *6*, 16713–16725. [CrossRef]
17. Gupta, C.K. *Chemical Metallurgy: Principles and Practice*; Wiley-VCH: Weinheim, Germany, 2003.
18. Tan, Q.; Li, J. Rare earth metal recovery from typical e-waste. In *Waste Electrical and Electronic Equipment (WEEE) Handbook*; Elsevier: Amsterdam, The Netherlands, 2019; pp. 393–421. [CrossRef]
19. Jowitt, S.M.; Werner, T.T.; Weng, Z.; Mudd, G.M. Recycling of the rare earth elements. *Curr. Opin. Green Sustain. Chem.* **2018**, *13*, 1–7. [CrossRef]
20. Mezy, A.; Vardanyan, A.; Garcia, A.; Schmitt, C.; Lakić, M.; Krajnc, S.; Daniel, G.; Košak, A.; Lobnik, A.; Seisenbaeva, G.A. Long-chain ligand design in creating magnetic nano adsorbents for separation of REE from LTM. *Sep. Purif. Technol.* **2021**, *276*, 119340. [CrossRef]
21. Eldridge, D.S.; Crawford, R.J.; Harding, I.H. The role of metal ion-ligand interactions during divalent metal ion adsorption. *J. Colloid Interface Sci.* **2015**, *454*, 20–26. [CrossRef] [PubMed]
22. Kampalanonwat, P.; Supaphol, P. The study of competitive adsorption of heavy metal ions from aqueous solution by aminated polyacrylonitrile nanofiber mats. In *Energy Procedia*; Elsevier Ltd.: Amsterdam, The Netherlands, 2014; pp. 142–151. [CrossRef]
23. Das, R.; Vecitis, C.D.; Schulze, A.; Cao, B.; Ismail, A.F.; Lu, X.; Chen, J.; Ramakrishna, S. Recent advances in nanomaterials for water protection and monitoring. *Chem. Soc. Rev.* **2017**, *46*, 6946–7020. [CrossRef]
24. Simeonidis, K.; Mourdikoudis, S.; Kaprara, E.; Mitrakas, M.; Polavarapu, L. Inorganic engineered nanoparticles in drinking water treatment: A critical review. *Environ. Sci. Water Res. Technol.* **2016**, *2*, 43–70. [CrossRef]
25. Leonel, A.G.; Mansur, A.A.P.; Mansur, H.S. Advanced Functional Nanostructures based on Magnetic Iron Oxide Nanomaterials for Water Remediation: A Review. *Water Res.* **2021**, *190*. [CrossRef]

26. Hao, L.; Liu, M.; Wang, N.; Li, G. A critical review on arsenic removal from water using iron-based adsorbents. *RSC Adv.* **2018**, *8*, 39545–39560. [CrossRef]
27. Reddy, L.H.; Arias, J.L.; Nicolas, J.; Couvreur, P. Magnetic nanoparticles: Design and characterization, toxicity and biocompatibility, pharmaceutical and biomedical applications. *Chem. Rev.* **2012**, *112*, 5818–5878. [CrossRef]
28. Laurent, S.; Forge, D.; Port, M.; Roch, A.; Robic, C.; Vander Elst, L.; Muller, R.N. Magnetic iron oxide nanoparticles: Synthesis, stabilization, vectorization, physicochemical characterizations and biological applications. *Chem. Rev.* **2008**, *108*, 2064–2110. [CrossRef]
29. Durán, J.D.G.; Arias, J.L.; Gallardo, V.; Delgado, A.V. Magnetic colloids as drug vehicles. *J. Pharm. Sci.* **2008**, *97*, 2948–2983. [CrossRef]
30. Rehman, A.U.; Nazir, S.; Irshad, R.; Tahir, K.; ur Rehman, K.; Islam, R.U.; Wahab, Z. Toxicity of heavy metals in plants and animals and their uptake by magnetic iron oxide nanoparticles. *J. Mol. Liq.* **2021**, *321*, 114455. [CrossRef]
31. Hadela, A.; Lakič, M.; Potočnik, M.; Košak, A.; Gutmaher, A.; Lobnik, A. Novel reusable functionalized magnetic cobalt ferrite nanoparticles as oil adsorbents. *Adsorpt. Sci. Technol.* **2020**, *38*, 168–190. [CrossRef]
32. Li, F.; Gong, A.; Qiu, L.; Zhang, W.; Li, J.; Liu, Z. Diglycolamide-grafted Fe3O4/polydopamine nanomaterial as a novel magnetic adsorbent for preconcentration of rare earth elements in water samples prior to inductively coupled plasma optical emission spectrometry determination. *Chem. Eng. J.* **2019**, *361*, 1098–1109. [CrossRef]
33. Sumit, W.A. Superparamagnetic iron oxide nanoparticles: Magnetic nanoplatforms as drug carriers. *Int. J. Nanomed.* **2012**, *7*, 3445–3471. [CrossRef]
34. Liu, X.M.; Yang, G.; Fu, S.Y. Mass synthesis of nanocrystalline spinel ferrites by a polymer-pyrolysis route. *Mater. Sci. Eng. C* **2007**, *27*, 750–755. [CrossRef]
35. Koroteev, P.S.; Dobrokhotova, Z.V.; Grechnikov, F.V.; Novotortsev, V.M. Heterometallic Carboxylate Complexes as Precursors for Mixed Oxides: II. d–d Carboxylates. *Russ. J. Gen. Chem.* **2018**, *88*, 1290–1305. [CrossRef]
36. Sajjia, M.; Baroutaji, A.; Olabi, A.G. The Introduction of Cobalt Ferrite Nanoparticles as a Solution for Magnetostrictive Applications. In *Reference Module in Materials Science and Materials Engineering*; Elsevier: Amsterdam, The Netherlands, 2017. [CrossRef]
37. Saddeler, S.; Bendt, G.; Salamon, S.; Haase, F.T.; Landers, J.; Timoshenko, J.; Rettenmaier, C.; Jeon, H.S.; Bergmann, A.; Wende, H.; et al. Influence of the cobalt content in cobalt iron oxides on the electrocatalytic OER activity. *J. Mater. Chem. A* **2021**, *9*, 25381–25390. [CrossRef]
38. Mozaffari, M.; Hadadian, Y.; Aftabi, A.; Oveisy Moakhar, M. The effect of cobalt substitution on magnetic hardening of magnetite. *J. Magn. Magn. Mater.* **2014**, *354*, 119–124. [CrossRef]
39. Slonczewski, J.C. Origin of Magnetic Anisotropy in Cobalt-Substituted Magnetite*. *Phys. Rev.* **1958**, *110*, 1341–1348. [CrossRef]
40. Prado, Y.; Daffé, N.; Michel, A.; Georgelin, T.; Yaacoub, N.; Grenèche, J.M.; Choueikani, F.; Otero, E.; Ohresser, P.; Arrio, M.A.; et al. Enhancing the magnetic anisotropy of maghemite nanoparticles via the surface coordination of molecular complexes. *Nat. Commun.* **2015**, *6*, 10139. [CrossRef] [PubMed]
41. Cypriyana, P.J.J.; Saigeetha, S.; Angalene, J.L.A.; Samrot, A.V.; Kumar, S.S.; Ponniah, P.; Chakravarthi, S. Overview on toxicity of nanoparticles, it's mechanism, models used in toxicity studies and disposal methods—A review. *Biocatal. Agric. Biotechnol.* **2021**, *36*, 102117. [CrossRef]
42. Khanna, R.; Mukherjee, P.S.; Park, M. A critical assessment on resource recovery from electronic waste: Impact of mechanical pre-treatment. *J. Clean. Prod.* **2020**, *268*, 122319. [CrossRef]
43. Devasena, T.; Iffath, B.; Renjith Kumar, R.; Muninathan, N.; Baskaran, K.; Srinivasan, T.; John, S.T. Insights on the Dynamics and Toxicity of Nanoparticles in Environmental Matrices. *Bioinorg. Chem. Appl.* **2022**, *2022*, 1–21. [CrossRef] [PubMed]
44. Singh, N.; Jenkins, G.J.S.; Asadi, R.; Doak, S.H. Potential toxicity of superparamagnetic iron oxide nanoparticles (SPION). *Nano Rev.* **2010**, *1*, 5358. [CrossRef]
45. Zhu, X.; Tian, S.; Cai, Z. Toxicity Assessment of Iron Oxide Nanoparticles in Zebrafish (*Danio rerio*) Early Life Stages. *PLoS ONE* **2012**, *7*, e46286. [CrossRef]
46. Seisenbaeva, G.A.; Ali, L.M.A.; Vardanyan, A.; Gary-Bobo, M.; Budnyak, T.M.; Kessler, V.G.; Durand, J.O. Mesoporous silica adsorbents modified with amino polycarboxylate ligands—Functional characteristics, health and environmental effects. *J. Hazard. Mater.* **2021**, *406*, 124698. [CrossRef]
47. Kim, J.S.; Yoon, T.J.; Yu, K.N.; Kim, B.G.; Park, S.J.; Kim, H.W.; Lee, K.H.; Park, S.B.; Lee, J.K.; Cho, M.H. Toxicity and tissue distribution of magnetic nanoparticles in mice. *Toxicol. Sci.* **2006**, *89*, 338–347. [CrossRef]
48. Hussain, S.M.; Hess, K.L.; Gearhart, J.M.; Geiss, K.T.; Schlager, J.J. In vitro toxicity of nanoparticles in BRL 3A rat liver cells. *Toxicol. In Vitro* **2005**, *19*, 975–983. [CrossRef]
49. Karlsson, H.L.; Gustafsson, J.; Cronholm, P.; Möller, L. Size-dependent toxicity of metal oxide particles-A comparison between nano- and micrometer size. *Toxicol. Lett.* **2009**, *188*, 112–118. [CrossRef]
50. Veranth, J.M.; Kaser, E.G.; Veranth, M.M.; Koch, M.; Yost, G.S. Cytokine responses of human lung cells (BEAS-2B) treated with micron-sized and nanoparticles of metal oxides compared to soil dusts. *Part. Fibre Toxicol.* **2007**, *4*, 2. [CrossRef] [PubMed]
51. Häfeli, U.O.; Riffle, J.S.; Harris-Shekhawat, L.; Carmichael-Baranauskas, A.; Mark, F.; Dailey, J.P.; Bardenstein, D. Cell uptake and in vitro toxicity of magnetic nanoparticles suitable for drug delivery. *Mol. Pharm.* **2009**, *6*, 1417–1428. [CrossRef] [PubMed]

52. Jeng, H.A.; Swanson, J. Toxicity of metal oxide nanoparticles in mammalian cells. *J. Environ. Sci. Health Part A Toxic/Hazardous Subst. Environ. Eng.* **2006**, *41*, 2699–2711. [CrossRef] [PubMed]
53. Stroh, A.; Zimmer, C.; Gutzeit, C.; Jakstadt, M.; Marschinke, E.; Jung, T.; Pilgrimm, H.; Grune, T. Iron oxide particles for molecular magnetic resonance imaging cause transient oxidative stress in rat macrophages. *Free Radic. Biol. Med.* **2004**, *36*, 976–984. [CrossRef] [PubMed]
54. Sadeghiani, N.; Barbosa, L.S.; Silva, L.P.; Azevedo, R.B.; Morais, P.C.; Lacava, Z.G.M. Genotoxicity and inflammatory investigation in mice treated with magnetite nanoparticles surface coated with polyaspartic acid. *J. Magn. Magn. Mater.* **2005**, *289*, 466–468. [CrossRef]
55. Volatron, J.; Kolosnjaj-Tabi, J.; Javed, Y.; Vuong, Q.L.; Gossuin, Y.; Neveu, S.; Luciani, N.; Hémadi, M.; Cam, E.; Alloyeau, D.; et al. Physiological Remediation of Cobalt Ferrite Nanoparticles by Ferritin. *Sci. Rep.* **2017**, *7*, 40075. [CrossRef] [PubMed]
56. Ahmad, F.; Liu, X.; Zhou, Y.; Yao, H. An in vivo evaluation of acute toxicity of cobalt ferrite ($CoFe_2O_4$) nanoparticles in larval-embryo Zebrafish (*Danio rerio*). *Aquat. Toxicol.* **2015**, *166*, 21–28. [CrossRef]
57. Ahmad, F.; Yao, H.; Zhou, Y.; Liu, X. Toxicity of cobalt ferrite ($CoFe_2O_4$) nanobeads in Chlorella vulgaris: Interaction, adaptation and oxidative stress. *Chemosphere* **2015**, *139*, 479–485. [CrossRef]
58. Horev-Azaria, L.; Baldi, G.; Beno, D.; Bonacchi, D.; Golla-Schindler, U.; Kirkpatrick, J.C.; Kolle, S.; Landsiedel, R.; Maimon, O.; Marche, P.N.; et al. Predictive Toxicology of cobalt ferrite nanoparticles: Comparative in-vitro study of different cellular models using methods of knowledge discovery from data. *Part. Fibre Toxicol.* **2013**, *10*, 32. [CrossRef]
59. Romih, T.; Drašler, B.; Jemec, A.; Drobne, D.; Novak, S.; Golobič, M.; Makovec, D.; Susič, R.; Kogej, K. Bioavailability of cobalt and iron from citric-acid-adsorbed CoFe2O4 nanoparticles in the terrestrial isopod Porcellio scaber. *Sci. Total Environ.* **2015**, *508*, 76–84. [CrossRef]
60. López-Moreno, M.L.; Avilés, L.L.; Pérez, N.G.; Irizarry, B.Ä.; Perales, O.; Cedeno-Mattei, Y.; Román, F. Effect of cobalt ferrite ($CoFe_2O_4$) nanoparticles on the growth and development of Lycopersicon lycopersicum (tomato plants). *Sci. Total Environ.* **2016**, *550*, 45–52. [CrossRef] [PubMed]
61. Haneda, K.; Morrish, A.; Morrish, A.H. Magnetite to Maghemite Transformation in Ultrafine Particles. *J. Phys. Colloq.* **1977**, *38*, 321–323. [CrossRef]
62. Li, Z.; Chanéac, C.; Berger, G.; Delaunay, S.; Graff, A.; Lefèvre, G. Mechanism and kinetics of magnetite oxidation under hydrothermal conditions. *RSC Adv.* **2019**, *9*, 33633–33642. [CrossRef]
63. Malvindi, M.A.; Brunetti, V.; Vecchio, G.; Galeone, A.; Cingolani, R.; Pompa, P.P. SiO_2 nanoparticles biocompatibility and their potential for gene delivery and silencing. *Nanoscale* **2012**, *4*, 486–495. [CrossRef] [PubMed]
64. Bardi, G.; Malvindi, M.A.; Gherardini, L.; Costa, M.; Pompa, P.P.; Cingolani, R.; Pizzorusso, T. The biocompatibility of amino functionalized CdSe/ZnS quantum-dot-Doped SiO_2 nanoparticles with primary neural cells and their gene carrying performance. *Biomaterials* **2010**, *31*, 6555–6566. [CrossRef]
65. Malvindi, M.A.; De Matteis, V.; Galeone, A.; Brunetti, V.; Anyfantis, G.C.; Athanassiou, A.; Cingolani, R.; Pompa, P.P. Toxicity assessment of silica coated iron oxide nanoparticles and biocompatibility improvement by surface engineering. *PLoS ONE* **2014**, *9*, e85835. [CrossRef]
66. Juang, J.H.; Wang, J.J.; Shen, C.R.; Kuo, C.H.; Chien, Y.W.; Kuo, H.Y.; Tsai, Z.T.; Yen, T.C. Magnetic resonance imaging of transplanted mouse islets labeled with chitosan-coated superparamagnetic iron oxide nanoparticles. *Transplant. Proc.* **2010**, *42*, 2104–2108. [CrossRef]
67. Kyle, P.B. Toxicology: GCMS. In *Mass Spectrometry for the Clinical Laboratory*; Elsevier Inc.: Amsterdam, The Netherlands, 2017; pp. 131–163. [CrossRef]
68. Dupont, D.; Brullot, W.; Bloemen, M.; Verbiest, T.; Binnemans, K. Selective uptake of rare earths from aqueous solutions by EDTA-functionalized magnetic and nonmagnetic nanoparticles. *ACS Appl. Mater. Interfaces* **2014**, *6*, 4980–4988. [CrossRef]
69. Košak, A.; Bauman, M.; Padežnik-Gomilšek, J.; Lobnik, A. Lead (II) complexation with 3-mercaptopropyl-groups in the surface layer of silica nanoparticles: Sorption, kinetics and EXAFS/XANES study. *J. Mol. Liq.* **2017**, *229*, 371–379. [CrossRef]
70. Topel, S.D.; Legaria, E.P.; Tiseanu, C.; Rocha, J.; Nedelec, J.M.; Kessler, V.G.; Seisenbaeva, G.A. Hybrid silica nanoparticles for sequestration and luminescence detection of trivalent rare-earth ions (Dy^{3+} and Nd^{3+}) in solution. *J. Nanoparticle Res.* **2014**, *16*, 1–17. [CrossRef]
71. Fröhlich, E. The role of surface charge in cellular uptake and cytotoxicity of medical nanoparticles. *Int. J. Nanomed.* **2012**, *7*, 5577–5591. [CrossRef]
72. Zhu, X.M.; Wang, Y.X.J.; Leung, K.C.F.; Lee, S.F.; Zhao, F.; Wang, D.W.; Lai, J.M.Y.; Wan, C.; Cheng, C.H.K.; Ahuja, A.T. Enhanced cellular uptake of aminosilane-coated superparamagnetic iron oxide nanoparticles in mammalian cell lines. *Int. J. Nanomed.* **2012**, *7*, 953–964. [CrossRef]
73. Sun, Z.; Yathindranath, V.; Worden, M.; Thliveris, J.A.; Chu, S.; Parkinson, F.E.; Hegmann, T.; Miller, D.W. Characterization of cellular uptake and toxicity of aminosilane-coated iron oxide nanoparticles with different charges in central nervous system-relevant cell culture models. *Int. J. Nanomed.* **2013**, *8*, 961–970. [CrossRef] [PubMed]
74. Berry, C.C.; Wells, S.; Charles, S.; Curtis, A.S.G. Dextran and albumin derivatised iron oxide nanoparticles: Influence on fibroblasts in vitro. *Biomaterials* **2003**, *24*, 4551–4557. [CrossRef] [PubMed]
75. Berry, C.C.; Wells, S.; Charles, S.; Aitchison, G.; Curtis, A.S.G. Cell response to dextran-derivatised iron oxide nanoparticles post internalisation. *Biomaterials* **2004**, *25*, 5405–5413. [CrossRef] [PubMed]

76. Wu, X.; Tan, Y.; Mao, H.; Zhang, M. Toxic effects of iron oxide nanoparticles on human umbilical vein endothelial cells. *Int. J. Nanomed.* **2010**, *5*, 385–399. [CrossRef]
77. Chen, B.A.; Jin, N.; Wang, J.; Ding, J.; Gao, C.; Cheng, J.; Xia, G.; Gao, F.; Zhou, Y.; Chen, Y.; et al. The effect of magnetic nanoparticles of Fe3O4 on immune function in normal ICR mice. *Int. J. Nanomed.* **2010**, *5*, 593–599. [CrossRef]
78. Patterson, A.L. The scherrer formula for X-ray particle size determination. *Phys. Rev.* **1939**, *56*, 978–982. [CrossRef]
79. Holzwarth, U.; Gibson, N. The Scherrer equation versus the "Debye-Scherrer equation". *Nat. Nanotechnol.* **2011**, *6*, 534. [CrossRef]
80. Viltužnik, B.; Lobnik, A.; Košak, A. The removal of Hg(II) ions from aqueous solutions by using thiol-functionalized cobalt ferrite magnetic nanoparticles. *J. Sol-Gel Sci. Technol.* **2015**, *74*, 199–207. [CrossRef]
81. Spencer, M.P.; Lee, W.; Alsaati, A.; Breznak, C.M.; Braga Nogueira Branco, R.; Dai, J.; Gomez, E.D.; Marconnet, A.; Lockette, P.; Yamamoto, N. Cold sintering to form bulk maghemite for characterization beyond magnetic properties. *Int. J. Ceram. Eng. Sci.* **2019**, *1*, 119–124. [CrossRef]
82. Rajput, A.B.; Hazra, S.; Ghosh, N.N. Synthesis and characterisation of pure single-phase CoFe2O4 nanopowder via a simple aqueous solution-based EDTA-precursor route. *J. Exp. Nanosci.* **2013**, *8*, 629–639. [CrossRef]
83. Košak, A.; Makovec, D.; Drofenik, M. Microemulsion synthesis of MnZn-ferrite nanoparticles. *Mater. Sci. Forum* **2004**, *453–454*, 219–224. [CrossRef]
84. Kegl, T.; Ban, I.; Lobnik, A.; Košak, A. Synthesis and characterization of novel Γ-Fe_2O_3-NH4OH@SiO_2(APTMS) nanoparticles for dysprosium adsorption. *J. Hazard. Mater.* **2019**, *378*, 120764. [CrossRef]
85. Wang, Q.Z.; Chen, X.G.; Liu, N.; Wang, S.X.; Liu, C.S.; Meng, X.H.; Liu, C.G. Protonation constants of chitosan with different molecular weight and degree of deacetylation. *Carbohydr. Polym.* **2006**, *65*, 194–201. [CrossRef]
86. Al-Zebari, N.; Best, S.M.; Cameron, R.E. Effects of reaction pH on self-crosslinked chitosan-carrageenan polyelectrolyte complex gels and sponges. *J. Phys Mater.* **2019**, *2*, 15003. [CrossRef]
87. Jiang, J.; Oberdörster, G.; Biswas, P. Characterization of size, surface charge, and agglomeration state of nanoparticle dispersions for toxicological studies. *J. Nanoparticle Res.* **2009**, *11*, 77–89. [CrossRef]
88. Amornkitbamrung, L.; Mohan, T.; Hribernik, S.; Reichel, V.; Faivre, D.; Gregorova, A.; Engel, P.; Kargl, R.; Ribitsch, V. Polysaccharide stabilized nanoparticles for deacidification and strengthening of paper. *RSC Adv.* **2015**, *5*, 32950–32961. [CrossRef]
89. Elzey, S.; Grassian, V.H. Agglomeration, isolation and dissolution of commercially manufactured silver nanoparticles in aqueous environments. *J. Nanoparticle Res.* **2010**, *12*, 1945–1958. [CrossRef]
90. Bračič, M.; Mohan, T.; Griesser, T.; Stana-Kleinschek, K.; Strnad, S.; Fras-Zemljič, L. One-Step Noncovalent Surface Functionalization of PDMS with Chitosan-Based Bioparticles and Their Protein-Repellent Properties. *Adv. Mater. Interfaces* **2017**, *4*, 1700416. [CrossRef]
91. Pearson, R.G. The HSAB Principle—More quantitative aspects. *Inorg. Chim. Acta* **1995**, *240*, 93–98. [CrossRef]
92. Parr, R.G.; Pearson, R.G. Absolute Hardness: Companion Parameter to Absolute Electronegativity. *J. Am. Chem. Soc.* **1983**, *105*, 7512–7516. [CrossRef]
93. Pearson, R.G. Absolute Electronegativity and Hardness: Application to Inorganic Chemistry. *Inorg. Chem.* **1988**, *27*, 734–740. [CrossRef]
94. Moore, C.E. *Ionization Potentials and Ionization Limits Derived from the Analyses of Optical Spectra*; U.S. Government Printing Office: Washington, DC, USA, 1970. [CrossRef]
95. Allred, A.L.; Rochow, E.G. A Scale of Electronegativity Based on Electrostatic Force. *J. Inorg. Nucl. Chem.* **1958**, *5*, 246–268. [CrossRef]
96. Gaffney, J.; Marley, N. In-depth review of atmospheric mercury: Sources, transformations, and potential sinks. *Energy Emiss. Control Technol.* **2014**, *2*, 1–21. [CrossRef]
97. Huang, C. *Rare Earth Coordination Chemistry: Fundamentals and Applications*; John Wiley & Sons: Singapore, 2010.
98. Li, K.; Xue, D. Estimation of electronegativity values of elements in different valence states. *J. Phys. Chem. A* **2006**, *110*, 11332–11337. [CrossRef]
99. Košak, A.; Lobnik, A.; Bauman, M. Adsorption of mercury(II), lead(II), cadmium(II) and zinc(II) from aqueous solutions using mercapto-modified silica particles. *Int. J. Appl. Ceram. Technol.* **2015**, *12*, 461–472. [CrossRef]
100. Zhao, F.; Repo, E.; Song, Y.; Yin, D.; Hammouda, S.B.; Chen, L.; Kalliola, S.; Tang, J.; Tam, K.C.; Sillanpää, M. Polyethylenimine-cross-linked cellulose nanocrystals for highly efficient recovery of rare earth elements from water and a mechanism study. *Green Chem.* **2017**, *19*, 4816–4828. [CrossRef]
101. Smith, D.W. Ionic Hydration Enthalpies. *J. Chem. Educ.* **1977**, *54*, 540–542. [CrossRef]
102. Sparks, D.L. *Environmental Soil Chemistry*, 2nd ed.; Academic Press Inc.: San Diego, CA, USA, 2003.
103. Bjerrum, J. *Metal Ammine Formation in Aqueous Solution: Theory of the Reversiblestep Reactions*; P. Haase and Son: Copenhagen, Denmark, 1941.
104. Hübener, S. *Actinide Elements, Encyclopedia of Physical Science and Technology*, 3rd ed.; Academic Press: Cambridge, MA, USA, 2003. [CrossRef]
105. Muthaiah, S.; Bhatia, A.; Kannan, M. Stability of Metal Complexes. In *Stability and Applications of Coordination Compounds*; Intechopen: London, UK, 2020; pp. 1–18. [CrossRef]
106. Karraker, D.G. Coordination of Trivalent Lanthanide Ions. *J. Chem. Educ.* **1970**, *47*, 424–430. [CrossRef]

107. Beattie, J.K.; Best, S.P.; Skelton, B.W.; White, A.H. Structural studies on the caesium alums, $CsMIII[SO_4]_2 \cdot 12H_2O$. *J. Chem. Soc. Dalt. Trans.* **1981**, 2105–2111. [CrossRef]
108. Buzko, V.; Sukhno, I.; Buzko, M. Ab initio and DFT study of Lu^{3+} hydration. *J. Mol. Struct. Theocem.* **2009**, *894*, 75–79. [CrossRef]
109. Persson, I. Hydrated metal ions in aqueous solution: How regular are their structures? *Pure Appl. Chem.* **2010**, *82*, 1901–1917. [CrossRef]
110. Rudolph, W.W.; Irmer, G. On the Hydration of the Rare Earth Ions in Aqueous Solution. *J. Solut. Chem.* **2020**, *49*, 316–331. [CrossRef]
111. Zhang, J.; Heinz, N.; Dolg, M. Understanding lanthanoid(III) hydration structure and kinetics by insights from energies and wave functions. *Inorg. Chem.* **2014**, *53*, 7700–7708. [CrossRef]
112. Helm, L.; Merbach, A.E. Inorganic and bioinorganic solvent exchange mechanisms. *Chem. Rev.* **2005**, *105*, 1923–1959. [CrossRef]
113. Dangelo, P.; Zitolo, A.; Migliorati, V.; Chillemi, G.; Duvail, M.; Vitorge, P.; Abadie, S.; Spezia, R. Revised ionic radii of lanthanoid(III) ions in aqueous solution. *Inorg. Chem.* **2011**, *50*, 4572–4579. [CrossRef]
114. Housecroft, C.E.; Sharpe, A.G. *Inorganic Chemistry*, 4th ed.; Pearson Education Limited: London, UK, 2012.
115. Atwood, D.A. *The Rare Earth Elements: Fundamentals and Applications*; John Wiley & Sons Ltd.: Chichester, UK, 2012.
116. Huheey, J.E. *Inorganic Chemistry, Principles of Structure and Reactivity*, 2nd ed.; Harper & Row: New York, NY, USA, 1978.
117. Partana, C.F.; Suwardi; Salim, A. Structure and dynamics of Hg2+ in aqueous solution: An Ab Initio QM/MM molecular dynamics study. *J. Phys. Conf. Ser.* **2019**, *1156*, 12012. [CrossRef]
118. Persson, I. Structures of Hydrated Metal Ions in Solid State and Aqueous Solution. *Liquids* **2022**, *2*, 210–242. [CrossRef]
119. Meyer, G.; Nockemann, P. Affinity of divalent mercury towards nitrogen donor ligands. *Zeitschrift Anorg. Allg. Chem.* **2003**, *629*, 1447–1461. [CrossRef]
120. Chen, H.; Shi, R.; Ow, H. Predicting Stability Constants for Terbium(III) Complexes with Dipicolinic Acid and 4-Substituted Dipicolinic Acid Analogues using Density Functional Theory. *ACS Omega* **2019**, *4*, 20665–20671. [CrossRef] [PubMed]
121. Patel, H. Review on solvent desorption study from exhausted adsorbent. *J. Saudi Chem. Soc.* **2021**, *25*, 101302–101313. [CrossRef]
122. Allwin Mabes Raj, A.F.P.; Bauman, M.; Lakić, M.; Dimitrušev, N.; Lobnik, A.; Košak, A. Removal of Pb^{2}+, CrT, and Hg^{2}+ Ions from Aqueous Solutions Using Amino-Functionalized Magnetic Nanoparticles. *Int. J. Mol. Sci.* **2022**, *23*, 16186. [CrossRef]
123. Raj, A.F.P.A.M.; Krajnc, S.; Bauman, M.; Lakič, M.; Gutmaher, A.; Lobnik, A.; Košak, A. Removal of Pb^{2}+, Cr^{3}+ and Hg^{2}+ ions from aqueous solutions using SiO_2 and amino-functionalized SiO_2 particles. *J. Sol-Gel Sci. Technol.* **2022**, *103*, 290–308. [CrossRef]
124. Liu, C.; Liang, X.; Liu, J.; Yuan, W. Desorption of copper ions from the polyamine-functionalized adsorbents: Behaviors and mechanisms. *Adsorpt. Sci. Technol.* **2016**, *34*, 455–468. [CrossRef]
125. Su, S.; Chen, B.; He, M.; Hu, B.; Xiao, Z. Determination of trace/ultratrace rare earth elements in environmental samples by ICP-MS after magnetic solid phase extraction with Fe_3O_4@SiO_2@polyaniline-graphene oxide composite. *Talanta* **2014**, *119*, 458–466. [CrossRef]
126. Liu, E.; Zheng, X.; Xu, X.; Zhang, F.; Liu, E.; Wang, Y.; Li, C.; Yan, Y. Preparation of diethylenetriamine-modified magnetic chitosan nanoparticles for adsorption of rare-earth metal ions. *New J. Chem.* **2017**, *41*, 7739–7750. [CrossRef]
127. Javadian, H.; Taghavi, M.; Ruiz, M.; Tyagi, I.; Farsadrooh, M.; Sastre, A.M. Adsorption of neodymium, terbium and dysprosium using a synthetic polymer-based magnetic adsorbent. *J. Rare Earths*, 2022; *in press*. [CrossRef]
128. Shinozaki, T.; Ogata, T.; Kakinuma, R.; Narita, H.; Tokoro, C.; Tanaka, M. Preparation of Polymeric Adsorbents Bearing Diglycolamic Acid Ligands for Rare Earth Elements. *Ind. Eng. Chem. Res.* **2018**, *57*, 11424–11430. [CrossRef]
129. Alcaraz, L.; Escudero, M.E.; Alguacil, F.J.; Llorente, I.; Urbieta, A.; Fernández, P.; López, F.A. Dysprosium removal fromwater using active carbons obtained from spent coffee ground. *Nanomaterials* **2019**, *9*, 1372. [CrossRef]
130. Viana, T.; Henriques, B.; Ferreira, N.; Lopes, C.; Tavares, D.; Fabre, E.; Carvalho, L.; Pinheiro-Torres, J.; Pereira, E. Sustainable recovery of neodymium and dysprosium from waters through seaweeds: Influence of operational parameters. *Chemosphere* **2021**, *280*, 130600–130612. [CrossRef] [PubMed]
131. Zhang, H.; Mcdowell, R.G.; Martin, L.R.; Qiang, Y. Selective Extraction of Heavy and Light Lanthanides from Aqueous Solution by Advanced Magnetic Nanosorbents. *ACS Appl. Mater. Interfaces* **2016**, *8*, 9523–9531. [CrossRef] [PubMed]
132. Barros, Ó.; Costa, L.; Costa, F.; Lago, A.; Rocha, V.; Vipotnik, Z.; Silva, B.; Tavares, T. Recovery of rare earth elements from wastewater towards a circular economy. *Molecules* **2019**, *24*, 1005. [CrossRef]
133. Tong, S.; Zhao, S.; Zhou, W.; Li, R.; Jia, Q. Modification of multi-walled carbon nanotubes with tannic acid for the adsorption of La, Tb and Lu ions. *Microchim. Acta* **2011**, *174*, 257–264. [CrossRef]
134. Kegl, T.; Košak, A.; Lobnik, A.; Ban, I. Terbium ion adsorption from aqueous solution by using magnetic-Fe_2O_3-NH4OH@SiO_2 nanoparticles functionalized with amino groups. *Materials* **2019**, *12*, 1294. [CrossRef] [PubMed]
135. Zhang, Y.; Yan, T.; Yan, L.; Guo, X.; Cui, L.; Wei, Q.; Du, B. Preparation of novel cobalt ferrite/chitosan grafted with graphene composite as effective adsorbents for mercury ions. *J. Mol. Liq.* **2014**, *198*, 381–387. [CrossRef]
136. Lin, Z.; Pan, Z.; Zhao, Y.; Qian, L.; Shen, J.; Xia, K.; Guo, Y.; Qu, Z. Removal of Hg2+ with polypyrrole-functionalized Fe3O4/kaolin: Synthesis, performance and optimization with response surface methodology. *Nanomaterials* **2020**, *10*, 1370. [CrossRef]
137. Wang, X.; Zhang, Z.; Zhao, Y.; Xia, K.; Guo, Y.; Qu, Z.; Bai, R. A mild and facile synthesis of amino functionalized $CoFe_2O_4$ @SiO_2 for Hg(II) removal. *Nanomaterials* **2018**, *8*, 673. [CrossRef]
138. Xia, K.; Guo, Y.; Shao, Q.; Zan, Q.; Bai, R. Removal of mercury (II) by EDTA-functionalized magnetic $CoFe_2O_4$@SiO_2 nanomaterial with core-shell structure. *Nanomaterials* **2019**, *9*, 1532. [CrossRef]

139. Inglezakis, V.J.; Kurbanova, A.; Molkenova, A.; Zorpas, A.A.; Atabaev, T.S. Magnetic Fe_3O_4-Ag0 nanocomposites for effective mercury removal from water. *Sustainability* **2020**, *12*, 5489. [CrossRef]
140. Liu, Z.; Sun, Y.; Xu, X.; Qu, J.; Qu, B. Adsorption of Hg(II) in an Aqueous Solution by Activated Carbon Prepared from Rice Husk Using KOH Activation. *ACS Omega* **2020**, *5*, 29231–29242. [CrossRef] [PubMed]
141. Denizli, A.; Dem Arpa, I.V.; Bektas, S.; Genç, Ö. Adsorption of Mercury(II) Ions on Procion Blue MX-3G-attached Magnetic Poly(vinyl alcohol) Gel Beads. *Adsorpt. Sci. Technol.* **2002**, *20*, 91–106. [CrossRef]
142. Solis, K.L.; Nam, G.U.; Hong, Y. Effectiveness of gold nanoparticle-coated silica in the removal of inorganic mercury in aqueous systems: Equilibrium and kinetic studies. *Environ. Eng. Res.* **2016**, *21*, 99–107. [CrossRef]
143. Shim, W.; Paik, M.J.; Nguyen, D.T.; Lee, J.K.; Lee, Y.; Kim, J.H.; Shin, E.H.; Kang, J.S.; Jung, H.S.; Choi, S.; et al. Analysis of changes in gene expression and metabolic profiles induced by silica-coated magnetic nanoparticles. *ACS Nano* **2012**, *6*, 7665–7680. [CrossRef] [PubMed]
144. Pisani, C.; Gaillard, J.C.; Nouvel, V.; Odorico, M.; Armengaud, J.; Prat, O. High-throughput, quantitative assessment of the effects of low-dose silica nanoparticles on lung cells: Grasping complex toxicity with a great depth of field. *BMC Genom.* **2015**, *16*, 315. [CrossRef]
145. Ellinger-Ziegelbauer, H.; Pauluhn, J. Pulmonary toxicity of multi-walled carbon nanotubes (Baytubes®) relative to α-quartz following a single 6 h inhalation exposure of rats and a 3 months post-exposure period. *Toxicology* **2009**, *266*, 16–29. [CrossRef]
146. Jovanović, B.; Ji, T.; Palić, D. Gene expression of zebrafish embryos exposed to titanium dioxide nanoparticles and hydroxylated fullerenes. *Ecotoxicol. Environ. Saf.* **2011**, *74*, 1518–1525. [CrossRef]
147. Böhmert, L.; Niemann, B.; Lichtenstein, D.; Juling, S.; Lampen, A. Molecular mechanism of silver nanoparticles in human intestinal cells. *Nanotoxicology* **2015**, *9*, 852–860. [CrossRef]
148. Conde, J.; Larguinho, M.; Cordeiro, A.; Raposo, L.R.; Costa, P.M.; Santos, S.; Diniz, M.S.; Fernandes, A.R.; Baptista, P.V. Gold-nanobeacons for gene therapy: Evaluation of genotoxicity, cell toxicity and proteome profiling analysis. *Nanotoxicology* **2014**, *8*, 521–532. [CrossRef]
149. Schikorr, V.G. Uber Eisen(II)-hydroxyd und ein Iferromagnetisches Eisen(III)-hydroxyd. *Z. Anorg. Allg. Chem.* **1931**, *35*, 33–39.
150. Čakara, D.; Fras, L.; Bračič, M.; Kleinschek, K.S. Protonation behavior of cotton fabric with irreversibly adsorbed chitosan: A potentiometric titration study. *Carbohydr. Polym.* **2009**, *78*, 36–40. [CrossRef]
151. Dobaj Štiglic, A.; Kargl, R.; Beaumont, M.; Strauss, C.; Makuc, D.; Egger, D.; Plavec, J.; Rojas, O.J.; Stana Kleinschek, K.; Mohan, T. Influence of Charge and Heat on the Mechanical Properties of Scaffolds from Ionic Complexation of Chitosan and Carboxymethyl Cellulose. *ACS Biomater. Sci. Eng.* **2021**, *7*, 3618–3632. [CrossRef] [PubMed]

3.4 Publications 4

Summary of Publication 4: Methylmercury (MeHg) is one of the most insidious environmental pollutants due to its extreme toxicity, persistent bioaccumulation in food chains, and ability to cross biological barriers—including the blood-brain barrier and placenta—causing severe neurological and developmental impairments in humans and wildlife. Its occurrence, largely stemming from microbial methylation of inorganic mercury in aquatic systems, necessitates highly sensitive, selective, and reliable detection tools that can function across varied matrices such as water, sediment, biota, and food. As the urgency of MeHg monitoring grows, analytical science has responded with a suite of powerful and increasingly refined detection methodologies.This review article delves into the intricate and evolving landscape of MeHg detection, providing a structured and comparative analysis of classical and emerging techniques. The authors begin with an in-depth overview of the gold standard instrumental methods, including Gas Chromatography (GC) coupled with Inductively Coupled Plasma Mass Spectrometry (ICP-MS) and High-Performance Liquid Chromatography (HPLC) integrated with Cold Vapor Atomic Fluorescence Spectroscopy (CVAFS). These approaches, while offering exceptional sensitivity and precision, are often constrained by operational complexity, high cost, and the need for sophisticated laboratory infrastructure and trained personnel.

In response to these challenges, the article highlights the rapid development of next-generation detection platforms that are portable, cost-effective, and amenable to on-site and real-time monitoring. Central to this shift is the rise of biosensors and nano-enabled systems, which integrate biological recognition elements—such as aptamers, enzymes, antibodies, and genetically engineered proteins—with transduction mechanisms that translate binding events into measurable signals. The article carefully evaluates electrochemical, optical, piezoelectric, and colorimetric biosensors, comparing their detection limits, selectivity, stability, and field adaptability.

A special focus is placed on the incorporation of nanomaterials—such as gold nanoparticles, graphene derivatives, quantum dots, and metal–organic frameworks (MOFs)—which have revolutionized the sensor performance landscape. These materials not only enhance signal amplification and surface functionalization but also allow for multiplexing and integration into smart sensing platforms.

In addition to technical aspects, the article addresses real-world applications and validation studies, discussing the use of these sensors in complex sample matrices, their ability to discriminate MeHg from other mercury species (e.g., inorganic Hg^{2+}), and their resilience to environmental interferences. Case studies from environmental monitoring projects and food safety assessments underscore the practical utility of these tools.

Another important dimension of the article is its treatment of regulatory and societal implications. The authors note the alignment of technological advancement with global policy frameworks such as the Minamata Convention on Mercury. They also emphasize the need for standardized protocols, inter-laboratory validation, and cross-disciplinary collaboration to translate laboratory innovations into policy-relevant, field-deployable solutions.

In conclusion, this review serves as a comprehensive roadmap for researchers and practitioners navigating the field of MeHg detection.

Trends in Analytical Chemistry 184 (2025) 118157

Contents lists available at ScienceDirect

Trends in Analytical Chemistry

journal homepage: www.elsevier.com/locate/trac

Recent progress and advancement in detecting methylmercury using a battery of biosensors and biomolecular-based techniques: An updated overview

A.F.P. Allwin Mabes Raj [a,b], Raghuraj Singh Chouhan [c], Aljoša Košak [d], Milena Horvat [b,c], Aleksandra Lobnik [a,d], Tomaž Rijavec [c], Aleš Lapanje [c,*]

[a] IOS, Institute of Environmental Protection and Sensors, Ltd., Beloruska 7, SI-2000, Maribor, Slovenia
[b] Jožef Stefan International Postgraduate School, Jamova Cesta 39, Ljubljana, Slovenia
[c] Department of Environmental Science, Jožef Stefan Institute, Jamova 39, 1000, Ljubljana, Slovenia
[d] University of Maribor, Faculty of Mechanical Engineering, Centre of Sensor Technology, Smetanova 17, SI-2000, Maribor, Slovenia

ARTICLE INFO

Keywords:
Methylmercury
Biosensors
Bioaccumulation
Biorecognition
Sensitivity
Selectivity
Nanoparticles

ABSTRACT

Methylmercury (MeHg) represents the most toxic form of mercury, owing to its ability to permeate both the blood-brain and placental barriers, leading to bioaccumulation in organisms. In the marine food web, MeHg concentrations can reach levels millions of times higher than those found in the surrounding environment, posing significant ecological and human health risks. This review provides a comprehensive overviews and critical evaluation of the available biosensor detection platforms for the detection of MeHg, with a focus on their performance based on key parameters such as (i) sensitivity, (ii) selectivity, (iii) response time, and (iv) adaptability to diverse environmental matrices. We examine recent advancements in MeHg biosensing technologies, emphasizing innovative approaches that surpass current methodologies regarding detection limits, reversibility, response time, and operational stability. Furthermore, we present an in-depth discussion on future directions for the development of *in situ* MeHg detection platforms, with potential applications in both biomedical and environmental monitoring. The review concludes by outlining the challenges and opportunities for advancing MeHg sensing technologies to enhance real-time detection in aqueous environments.

1. Introduction

Mercury exists in various chemical forms including Elemental Mercury (Hg^0), Mercuric Ion (Hg^{2+}), Methylmercury (MeHg), Dimethylmercury (CH_3HgCH_3), Mercury Sulfide (HgS) and Ethylmercury ($C_2H_5Hg^+$). Among these, MeHg is the most toxic, posing a significant risk to both the environment and human health, even at concentrations as low as nanomolar (nM) levels. This concentration threshold is remarkably minuscule, diverging by two orders of magnitude from any other mercury species. Despite its minute presence, MeHg has the tendency for biomagnification within the food chain, thereby accumulating in organisms and resulting in neurological disorders, exemplified by Minamata disease [1]. Wild piscivorous fish, mammals, and birds, animals at the highest trophic level, are at risk for elevated dietary methylmercury intake and toxicity due to biomagnification through the food chain. Its neurotoxic effects are especially harmful to developing fetuses and young children, making precise quantification in food samples critical for public health. Monitoring MeHg levels in fish is essential for assessing exposure risks and ensuring food safety standards. Regulatory agencies rely on accurate MeHg detection to guide consumption advisories and protect vulnerable populations. Consequently, the demand for meticulous, sensitive methodologies to detect MeHg with precision has surged, especially in the context of evaluating water pollution dynamics. Biosensors for detecting methylmercury (MeHg) in food samples offer several advantages, including rapid detection and high sensitivity, making them effective at trace-level detection. These devices enable real-time monitoring, providing immediate feedback on MeHg levels, essential for ensuring food safety in vulnerable populations like pregnant women and fetuses. Their cost-effectiveness and potential for on-site application, especially in industries such as aquaculture and agriculture, make them suitable for widespread use. Additionally, integration with smartphone technology allows for automation and ease of

* Corresponding author.
E-mail address: ales.lapanje@ijs.si (A. Lapanje).

https://doi.org/10.1016/j.trac.2025.118157
Received 3 July 2024; Received in revised form 20 January 2025; Accepted 20 January 2025
Available online 21 January 2025

use, improving overall food safety protocols [2–4].

Current conventional methods for MeHg detection employ techniques such as atomic fluorescence spectrometry (AFS) with gold traps and automated systems based on cold vapour atomic fluorescence spectrometry (CVAFS). The CVAFS mechanism involves the conversion of MeHg into volatile ethylmercury through the use of sodium tetraethyl borate. After this conversion, alkyl forms of mercury are purged using nitrogen gas and captured on Tenax columns. After desorption at an elevated temperature, gas chromatography is employed to identify alkyl mercury compounds post-pyrolysis [5–7]. This method currently stands as the most sensitive for MeHg, with an impressively low limit of detection (LOD) at 0.004 ng/L. However, it necessitates the laborious task of sample collection from sites and transport to laboratories, which can be time-consuming and resource-intensive. In addition to sample collection challenges, laboratory-based MeHg measurement entails the extraction of MeHg from complex matrices, including organisms and cells. Specific sample preparation steps are crucial, and tailored to the physicochemical properties of each matrix. Even seemingly simple samples like water require meticulous processing, involving pH adjustment to 4.5 before the addition of sodium tetraethyl borate and overnight derivatization into volatile ethylmercury.

Although the necessary steps to obtain MeHg from biota or naturally occurring complexes cannot be omitted, the specific preparation of samples in laboratories might be simplified, resulting in rapid usage, fewer experts and decreased costs, if sensors can be used instead of using expensive laboratory equipment. Therefore, sensors that can enable measurement of MeHg in the environment are of high priority to increase the amount of data that will precisely map the routes of MeHg for thwarting toxicity reaching the global nutrient cycle and to enable us to determine contaminated food. This will yield biologically relevant information about the biomagnification and bioaccumulation of MeHg under real environmental conditions. Since the processes of methylation and demethylation are continuous, the onsite measurement will give us dense time points, resulting in time and spatially dependant distribution when followed by the precise sampling locations, since laboratory measurements can give results only for a limited number of samples.

Among the several developed platforms, biosensors for detecting methylmercury (MeHg) in food samples offer several advantages, including rapid detection and high sensitivity, making them effective at trace-level detection [8]. These devices enable real-time monitoring, providing immediate feedback on MeHg levels, essential for ensuring food safety in vulnerable populations like pregnant women and fetuses. Their cost-effectiveness and potential for on-site application, especially in industries such as aquaculture and agriculture, make them suitable for widespread use. Additionally, integration with smartphone technology allows for automation and ease of use, improving overall food safety protocols. Microfluidic devices offer high sensitivity and accuracy but may require technical expertise. Lateral flow assays and paper-based assays provide moderate to high sensitivity with ease of use but less accuracy in quantification. Smartphone-based sensors, electrochemical sensors, and optical biosensors achieve high sensitivity and accuracy, with the latter two being highly precise and user-friendly for real-time monitoring.

Although sensors for measuring inorganic mercury (Hg^{2+}) or Total Mercury (THg) have been developed, most MeHg sensors remain at the proof-of-concept stage [1]. To advance the development of MeHg sensors, this review focuses on available detection methods in the literature for MeHg detection, categorising them into six major types: Whole-cell biosensors (WCB), Immunostrip sensors, Small molecule probe-based (SMP) sensors, Metal-Organic Framework (MOF) sensors, Nanoparticle (NPs)-based sensors, and Nanoarchitectonics sensors. This comprehensive overview provides insights and strategies for advancing MeHg sensors by integrating biological, chemical, and nanotechnological approaches. A critical bottleneck in the development of MeHg sensors is the need for a well-integrated system that includes a receptor with high specificity for MeHg, efficient signal transduction, low noise amplifier, and reporters capable of showing realtime high quality data. Addressing these challenges is essential for creating effective and reliable MeHg sensing solutions.

The current state of sensor development underscores the critical role of receptor, transducer, and reporter components in designing highly effective MeHg detection systems. Receptors, which includes proteins, aptamers, and engineered molecules, serve as the primary recognition elements due to their high affinity and selectivity for MeHg binding. Beyond traditional fluorescence, reporters can leverage various detection principles, enhancing versatility across different sensing platforms. The selection of an appropriate transducer is vital, with factors such as sensitivity, matrix compatibility, and detection limits shaping the choice of the sensor architecture.

Electrochemical transducers, for example, enable precise quantification of MeHg concentrations across diverse environmental matrices [9]. In enzymatic sensors, electrochemical transduction is commonly employed, capitalizing on the enzymatic conversion of MeHg into electroactive species [10]. Immunosensors, on the other hand, utilize antibodies or aptamers as receptors and often integrate surface plasmon resonance (SPR) transducers to enable real-time detection [11]. The choice of transducer is pivotal, as it directly impacts the sensor's sensitivity, specificity, and adaptability to different environmental and biological matrices.

This review provides a comprehensive overview of detection platforms for MeHg, with a particular focus on recently developed sensors capable of trace-level detection. The advancements in sensing technologies are highlighted, emphasizing innovative approaches that surpass currently available analytical methods in terms of sensitivity and specificity. Moreover, the review outlines future perspectives to guide further research and development in this field, offering insights into potential improvements and innovations for MeHg detection. A brief conclusion is provided to summarize key findings and suggest pathways for advancing sensor technologies in this direction [9].

Fig. 1 illustrates a range of detection techniques employed in MeHg sensors, including small molecule probes, whole-cell biosensors (WCB), immunostrip assays, metal-organic frameworks (MOFs), and nanoarchitectonics-based sensors. The central diagram highlights the core components of currently known MeHg sensors, emphasizing the interaction between the analyte and the recognition element, followed by signal transduction. These diverse approaches showcase the integration of biological components with advanced materials, significantly enhancing the performance of MeHg detection technologies.

2. Whole cell biosensor platforms

Whole-cell biosensors (WCB) use microbial cell components as the receptors and transducers integrated inside the microbial cell to respond to the presence of chemicals (analyte of interest) and produce detectable output signals. The analytical signals are generally either fluorescence or luminescence. Fluorescence involves the emission of light following excitation by an external light source, commonly utilizing fluorescent proteins or dyes to detect target analytes. Luminescence, on the other hand, is based on light emission resulting from biochemical reactions, such as those catalyzed by luciferase enzymes, which occurs without external excitation. The cells are genetically engineered in a way that genes that are producing sensing components, usually proteins that specifically bind the analyte, are introduced either in the chromosome or kept on plasmids. In many cases, genes encoding reporter proteins or those producing reporter molecules are added to the same operon along with the sensing component, allowing the reporters to indicate the activity of the operon. This combination of sets of genes allows for the detection, recording, and quantification of the target analyte. The advancements in genetic engineering and synthetic biology have substantially enhanced the robustness of WCBs through introduction of genetic constructs into different microbial species that are more relevant for environmental conditions or targeting specific biogeochemical

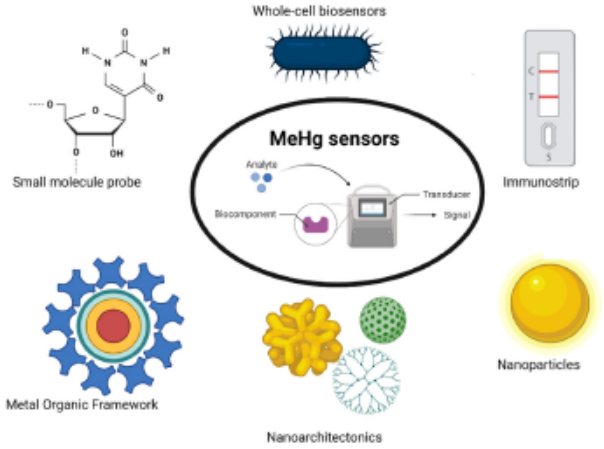

Fig. 1. The schematic illustration presents the various methods for MeHg detection reported in the literature, which include: (1) whole-cell biosensors (WCB), (2) immunostrip sensors, (3) small molecule probe-based (SMP) sensors, (4) metal-organic framework (MOF) sensors, (5) nanoparticle (NP)-based sensors, and (6) nanoarchitectonics sensors. Created with BioRender.com.

processes. Genetically engineering bacterial sensing modules that are introduced into surrogate hosts offers a versatile platform for the development of synthetic receptors with diverse applications (Fig. 2a) [12]. Based on these new approaches it resulted in expanded applicability of WCBs, enabling their use not only for analyzing laboratory-prepared artificial samples but also for measuring analytes directly in real environmental samples such as directly in the river water [11] or in collected contaminated water samples [13]. Based on our comparisons of data obtained from literature the sensitivity of WBC is at least one order of magnitude lower in both the environmental samples as well as in spiked media. However, this lower sensitivity might be due to the lower bioavilability of Hg species since they can get complexed with organic material [14] and as a result it is measured a fraction of relevant information that is representing bioavailable Hg concentrations [14]. Estimates of "bioavailable" mercury, the fraction that can be taken up by microorganisms in the environment, is especially important in oceanic environment since this fraction can play a pivotal role as it represents the bioavailable mercury at the particular niche in the ecosystem and is important for evaluation of potential further biomagnification processes.

Unlike laboratory procedures that often require additional sample preparation, biosensor platforms can achieve maximum sensitivity within 30 min of incubation in most cases. However, for certain samples, such as human urine, increased incubation times of several hours have been reported to enhance sensitivity [15]. Despite these advantages, maintaining stationary cultures of sensing cells for extended periods remains challenging due to factors such as unstable genetic elements, contamination risks, and the high energy demands of reactors. Nonetheless, successful attempts have been made to develop detection devices incorporating whole-cell biosensors (WCBs) in various forms, including fully integrated or non-integrated designs, utilizing microreactors or immobilised cells. These devices are miniaturized, field-deployable, and capable of multiplexed detection [16].

To the best of our knowledge, most whole-cell biosensors (WCBs) for the detection of MeHg exploit genetic constituents of the Hg-resistance operon, which enables microbes to detoxify Hg^{2+} and MeHg. In nature, within bacterial cells, the MeHg detoxification system is comprised of merB gene that is always present together with the merA gene, the gene for Hg^{2+} reductase transforming Hg^{2+} to Hg0, and a gene for the merR sensor protein. Therefore merR-based sensors employing merB genes are detecting Hg^{2+} after MerB protein demethylates MeHg and releases Hg^{2+} of MMHg. In such systems the specificity toward MeHg is problematic and both Hg^{2+} and MMHg are detected. Researchers solved this problem by combining two principles, demethylation with Hg^{2+} sensing, where merB, merR-containing cells and cells having only merR genes were exposed to the same samples separately. The levels of responses on Hg^{2+} are then deducted from signals obtained in cells containing merB together with merR. This was further enhanced by omitting Hg^{2+} transporters or mutating naturally occurring exporting mechanisms that increase specificity and sensitivity to MeHg. Since the genetic sensing elements are responding relatively fast the WCB can be also used in determining dynamics of methylation and demethylation in the culture of Hg methylating strains and conditions enabling their growth giving insights in conditions and ecological interactions that are stimulating or inhibiting MeHg production. Accordingly, Colin et al., 2018 have reported the approach to determine the Hg methylation potential of sulfate-reducing bacteria by using a luminescent biosensor for screening methylmercury production by co-culturing the reporter strain to either methylating or non-methylating *Desulfovibrio* strains [17].

The detection of methylmercury with whole-cell biosensors is influenced by factors such as cell characteristics and their viability including cell type and any additional genetic or phenotypic modifications or characteristics; environmental and experimental conditions like temperature, pH, nutrient availability, and sample matrix; and detection and calibration factors, which encompass MeHg concentration, presence of interferences, and the necessity for proper calibration for each cell type or even batch of culture used in the sensing [18].

The mercury methylation rates generally depend on the activity of the anaerobic Hg methylating microorganisms and the bioavailability of inorganic Hg(II) that can be converted by these bacteria [19]. The uptake of Hg(II) may involve specific Hg(II) complexes or forms of mercury that can bind to a nonspecific transmembrane transport system [19]. We should take into account that dissolved organic matter (DOM) affects mercury methylation due to its influence on bacterial cell physiology (as a potential nutrient) and its influence on Hg(II) speciation in the environment (as a complexing agent), therefore controlling Hg bioavailability [20]. As shown in Table 1, the WCB has proven to be sensitive with a detection limit of 2.5 nM. Further, the effects of chlorides, humic

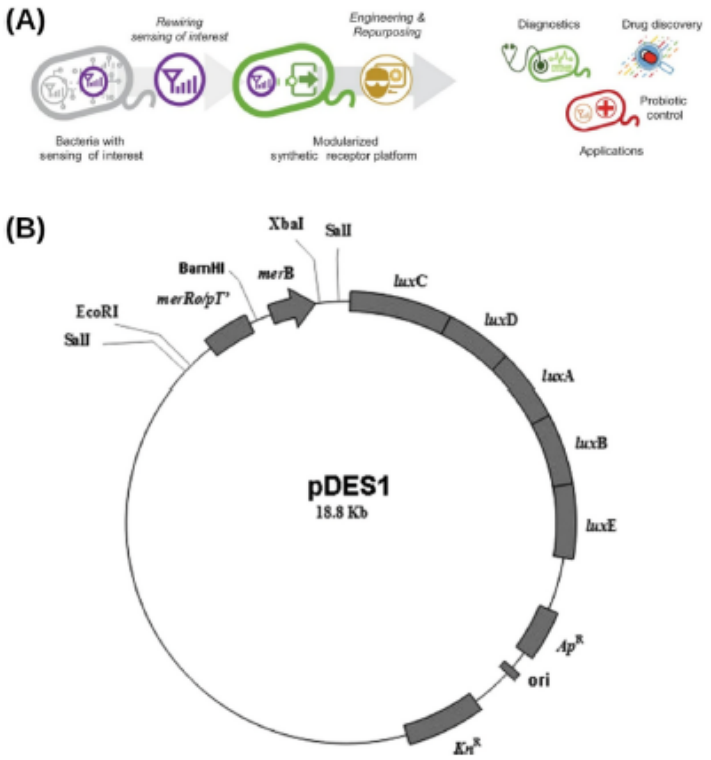

Fig. 2. a) Illustration for genetically engineering bacterial sensing modules into surrogate hosts for the development of a synthetic receptor platform that can be used for multiple application. Reproduced with permission from Ref. [12], Copyright (2021) Springer Nature. b) Diagram of the modification of Prb28 by inserting the merB gene into the *BamHI-XbaI* region under the control of the mer promotor Reproduced with permission from Ref. [21], Copyright (2012) American Society for Microbiology.

acids, and thiols on the bioavailability of MeHg in *E. coli* were also investigated. Here, the concentration of chlorides increased MeHg detection, suggesting that there was passive diffusion of the neutral complex ($MeHgCl_2$) through the cell wall and membrane. In contrast, humic acids reduce the bioavailability of MeHg. Complexation with cysteine resulted in increased bioavailability of MeHg. The bioavailability of MeHg decreased with increasing glutathione concentrations [21]. In this regards, due to the interferences of cellular structures, which are varying among different strains, with the MeHg sensing, researchers should use cell types that are environmentally relevant to ensure accurate and applicable results as it was reported by Rijavec et al. [16]. The performance of different microbial host cells varies based on environmental conditions such as pH, temperature, the analyte of interest, and the specific gene chosen for the operon system [22–24]. The host strain selected must be able to function in different conditions of the regulatory genes [25]. Here, the optimization of the regulatory gene and RBS (Ribosome Binding Site) sequences should be considered. Since in most cases the plasmids are used for DNA cloning, genome editing, recombinant gene expression, and construction of genetic circuits all applicable in sensor construction, therefore, the plasmid copy number (PCN) is the primary consideration for quantitative metabolic flux enhancement as well as quantitative gene expression. The blossoming of synthetic biology not only needs plasmids with fixed PCN to maintain stable and permanent gene expression but also longs for plasmids with dynamically adjusted PCN to cope with changes in the life cycle and cellular metabolism [26]. Dynamic control of PCN will break the limitation of canonical plasmids with fixed PCN. So far, dynamic PCN control has only been achieved for pSC101 and ColE1 plasmids, which are both designed for *Escherichia coli*. We can envision that dynamic PCN control can facilitate the dynamic spatial organization of metabolism by adjusting the number of scaffolds for enzyme binding. With these updates, dynamic PCN control may produce a profound effect on calibration of the WCB since the activity of sensing genetic construct would be less impacted by the number of genetic elements.

Moreover, genetic systems exhibit population based response variety, a consequence of both stochastic processes and the mutability of underlying genetic programs. Improvement in the ability to monitor the behaviour of single cells has provided insight into how stochastic processes generate noises in isogenic population [27]. Fluctuations in the availability of shared resources of the host, such as polymerase and ribosomes, have influence on expression levels. In contrast, the biochemical processes responsible for the expression of individual genes cause further variation. In prokaryotes, the balance between transcription and translation strength strongly influences expression noise, with low transcription and high translation, which generates the most variability [28].

In addition, besides the internal cellular or population effects on the WCB the environmental factors are also making the biased responses. As an example, the WCB that can have growth optima in mild conditions cannot be used in extreme environments. However, if we prepare the

Table 1
Biological-based detection platform for MeHg.

No.	Hg species	(LOD)	Sample matrix	Sensor components			Sensing mechanism	References
				Bioreceptor	Transducer	Reporter		
1.	MeHg	10 pM with 1 ml sample	Contaminated environmental water samples	*MerB* gene	*MerR* of the mer-operon from Pseudomonas K-62 plasmid pMR26, *Vibrio harveyi*	Lux-AB	Luminescence based biosensor	[13]
2.	MeHg	2 nM	Model waters	pmerR	*Desulfovibrio* strains	$pmerR_{BS}BPmerlux$	Bacterial luminescent biosensor	[17]
3.	MeHg	2.5 nM	Model waters	mer-lux operon	*E. coli*	mer-lux WCB	Bacterial bioreceptor	[21]
4.	MeHg	0.238 nM	Natural water samples	pmerR	*E. coli* MC1061	lux	Luminescent bacterial based sensor	[11]
5.	MeHg	0.11 pM	Model waters	$pmerR_{BS}BPmerlux$	19sp (luxCDABE)	lux	Recombinant whole-cell luminescent bacterial sensors	[34]
6.	Hg^{2+} and MeHg	1.6×10^{-7} M and 5.0×10^{-7} M for Hg^{2+} 8.0×10^{-7} M and $1.0 \times 10-6$ M for MeHg	Model water	Anti-MeHg monoclonal antibody (mAb)	Immunostrip	immunochromatographic reporter	Indirect competitive enzyme-linked immunosorbent assay (ic-ELISA) and an immunochromatographic reporter	[35]
7.	MeHg	5.0 nM	Environmental samples	Aptamer (H_{T7})	AuNPs	Colourimetric detection	Chromogenic reaction of 3,3,5,5-tetramethylbenzidine (TMB)-H_2O_2	[36]
8.	MeHg and ethyl-mercury (C_2H_5Hg)	5000 nM, 600 nM	Model water and Fish sample	T-rich aptamers (HT_5 and H_{T7})	DNA-templated alloy Ag–Au nanoparticles	Color change in the solution	The aptamers specifically bind to MeHg and C_2H_5Hg, thus facilitating the formation of alloy Ag–Au NPs, which display a color change in the solution	[37]
9.	Hg^{2+} and MeHg	1000 nM	Environmental samples	Thymine moiety	AuNP	Naked-eye detection	Functionalized AuNPs with thymine moiety that sandwiches single mercuric species between two thymine molecules on the surface of the NPs	[38]
10.	MeHg	0.4 nM	Model water and Fish Samples	aptamer (H_{T7})	DNA functionalized AgNPs	Fluorescence	Metal amalgamation between mercury atoms and certain metal atoms with MeHg-specific scaffolds. They have also utilized the potential of aptamers (H_{T7}) that have a specific affinity towards MeHg than Hg^{2+}	[39]
11.	Hg^{2+} and MeHg	Hg^{2+} and MeHg were 3 pM and 4 nM, respectively	Seawater	Lysozyme type VI	lysozyme type VI-stabilized gold nanoclusters (Lys VI-AuNCs)	Fluorescence quenching mechanism	High affinity between Hg^{2+} and Au^{+} on the Au surface	[40]
12.	Hg^{2+} and MeHg	≥0.1 nm	Model waters	Adenine (A) conjugated small organic semiconductor (BNA) and deoxyribooligothymidine (dT_n)	Thin films containing bioreceptor	Conductivity measurement	Mutually templated co-assembly (BNA_ndT_n) of an organic semiconductor (BNA) and deoxyribo-oligothymidine (dT_n)	[41]

recombinant host adapted to the toxic environment it can be then used in sensing pollutant in extreme conditions. For example, *Acidothiobacillus ferrooxidans* BY-3 was used for the bioleaching of As(III) in extremely acidic conditions (pH < 1.8) [29,30]. It is also important to consider interfering pollutants when applying whole-cell biosensors (WCBs) because such pollutants can disrupt cell-cell interactions, substrate exchange, and signal transduction. However, we should not exclude possible horizontal gene transfer between cells that can in turn increase their tolerance to these interfering pollutants especially if used in longer sensing experiments [20].

During cell-cell interaction of the host in the environment and *in vitro* applications when cells are used in the biosensing application, secreted diffusible siderophores and other shared resources leading to cooperative, exploitative and competitive interactions between individuals that can affect sensor performance. These social interactions, in turn, can spur co-evolutionary arms races between strains and other species in the environmental matrices for WCBs, leading to ecological dependencies between them. The negative ecological interaction such as bacterial predation can decrease the number of WCS and give false low concentrations especially during the long incubation times during the induction. All the above phenomena should be taken into account for further WCB for MeHg detection [31].

Not only sensing components but also the reporting ones of the WCB are important to get proper intensity of the signal. Reporter genes can be

engineered into chromosomal DNA, inserting in the chromosome and disrupting specific gene. It can increase the sensitivity of biosensors but makes cells more vulnerable if the insertion of the sensing genes is in the region that have important cell function. Sometimes, reporter genes under the control of the corresponding promoters are introduced into the chromosome using mobile genetic elements or transposons. On other hand, a transcriptional fusion of reporter genes with an inducible promoter cloned in a plasmid is more frequently used in WCB platforms. In this case the construct is introduced into the appropriate plasmid compatible cells.

According to the type of the produced reporter proteins it is also expected to obtain different noise to signal ratios, sensitivity for physical conditions and time for obtaining appropriate signal. Several reporter genes are used in biosensing applications [16], including β-Galactosidase (lacZ) [32], luciferase (Luc), and various fluorescent proteins such as Green Fluorescent Protein (GFP), Red Fluorescent Protein (RFP), and Yellow Fluorescent Protein (YFP). Each reporter has specific advantages and disadvantages: lacZ offers sensitivity dependent on the substrate and requires no ATP but has low permeability and can be used if cells are lysed. Luciferase is highly sensitive and provides rapid responses but requires substantial oxygen and ATP; in bioreactors, real-time detection can be hindered by simultaneous stirring that is giving additional noise when measured using PMT or photodiode. GFP is stable, moderately sensitive, and substrate-independent with no ATP requirement but can exhibit fluorescence after cell death, the protein needs approximately a few hours to form appropriate secondary structure, and in some cells the autofluorescence background might increase noise. Additional drawback represent also that the induction of recombinant protein expression typically occurs when cells reach a specific optical density, which is dependent on their generation time. Selecting an appropriate host for quicker protein expression can significantly reduce production costs.

Additionally, for monitoring environment and further enhancement either sensing proteins or reporters the directed evolution is a valuable method for biosensor development, involving the creation of a diverse gene library through targeted or random mutagenesis, followed by screening to identify variants with enhanced properties. This approach can lead to the development of robust enzymes for environmental sensing applications. Other strategies include engineering thermostable proteins through ancestral sequence reconstruction or incorporating thermostable protein motifs into other functional genes [33]. These approaches can be used especially in developing WCB for extreme environments such as environments with higher or extremely low temperatures, strict anaerobic conditions, salt water, etc.

Among reporter genes the most suitable represent luminiscence based reporting mechanisms, which might be either indigenous or needed to be added as a luciferin component externally. As reported by Rantala et al. (2011), the luciferin-luciferase system (lux operon) was utilized as a reporter for MeHg detection in their study. This system requires no substrate additions, enabling homogeneous, real-time monitoring of reporter gene expression. They developed a WCB strain, *Escherichia coli* MC1061, containing the recombinant plasmid (pmerRBlux), which responds to total mercury content in samples. The MerR operon, which regulates genes involved in bacterial mercury resistance, controls this system. In the absence of Hg^{2+}, MerR binds to DNA and represses transcription [11]. Upon Hg^{2+} binding, the DNA bound to MerR undergoes untwisting and unbending which facilitates open complex formation. Since the environmental matrix might be toxic due to other substances or inappropriate physiological conditions, researchers were normalizing sensor readings using the non-inducible, constitutively expressing lucifein/luciferase system in a toxicity control setup. Here the *Escherichia coli* MC1061 with the recombinant construct (pmerRBlux), which offers resistance toward MeHg (Fig. 2b) was used as a WCB. The merB mediates the cleavage of the carbon–mercury bond of MeHg to yield Hg^{2+}, which binds to MerR sensing component, induces the reporter genes and produces a self-luminescent organism due to the expression of lux enes. To decrease interferences of available Hg^{2+} present in the environment the ethylenediaminetetraacetic acid (EDTA) has been employed as a chelating agent to bind inorganic mercury (Hg^{2+}) from the sample, using an optimized concentration. *E. coli* MC1061 (pmerRBlux) can detect methylmercury (MeHg) at subnanomolar levels with high sensitivity under optimized assay conditions. The limit of detection (LOD) of 0.238 nM enables the measurement of MeHg even in complex real samples (see Table 1) [11].

In another study, Ivask et al. (2009) developed "lights-on" sensors, which are typically recombinant microbial cells containing a metal-response unit fused to a promoterless reporter gene that encodes a reporting signal with addition of external luciferin substrate. These bioluminescent strains detect metals, with expression levels indicating sub-toxic metal concentrations, allowing for the quantitative determination of bioavailable metals. Among these sensors, one was specifically designed for the detection of methylmercury (MeHg) in aqueous samples, achieving a detection limit of 0.11 pM [34]. Similar approach as reported by Ivask et al. (2009), Ndu et al. (2012) have developed a mer-lux WCB to determine the bioavailability of MeHg in *E. coli*.

There is another report in which Nagata et al. (2010) developed a WCB that carries a luciferin-luciferase gene constructs, luxAB, from *Vibrio harveyi* as a reporter under the control of the mercury-inducible MerR of the mer-operon from Pseudomonas K-62 plasmid pMR26 using similar principles as described above where merB gene that encodes organomercurial lyase cleaves the C–Hg bond of MeHg to give Hg^{2+} and is co-expressed with MerR in the sensor. The mer-promoter is activated when Hg^{2+} released from MeHg binds to the regular MerR protein. Light is emitted when mercurials in this specific form are present in the cytoplasm of the sensor bacteria, which merR did not recognize CH_3Hg^+ as an inducer. The concentration of CH_3Hg^+ can be determined by measuring the intensity of luxAB-specified luminescence. The resulting bacterial sensor responded specifically to MeHg, and the lowest detectable concentration of MeHg was 10 pM (Table 1) with a 1 ml sample in the optimized assay conditions. This detection limit is enough to detect many contaminated and pristine environmental samples [13]. Additionally, Colin et al. (2018) developed a luminescent biosensor for screening MeHg production and validated it by exposing the reporter strain to both methylating and non-methylating *Desulfovibrio* strains. Methylation activity, often associated with sulfate-reducing bacteria under anoxic conditions, was assessed using this biosensor. The sensitivity of the biosensor to MeHg was highly dependent on the growth conditions of sulfate-reducing bacteria. Sulfide concentrations ranging from 1 to 10 mM resulted in a 40–70 % decrease in luminescence as sulfide levels increased. Among inorganic ligands, sulfides are considered the most effective under anoxic conditions, as they significantly influence mercury speciation in ecosystems [17].

Besides WCB, there are reported also other attempts using bio-based approaches to detect MeHg. The use of monoclonal antibodies against conjugated MeHg with immunogenic molecules was reported. Indirect enzyme-linked immunosorbent assay (ic-ELISA) as the potential immobilization platform for biomolecules was developed for the detection of MeHg. As compared to other analytical methods, the further developed ic-ELISA in a immunostrip-based detection of methylmercury (MeHg) showed low sensitivity, with a limit of detection (LOD) of 1.6×10^{-7} M for Hg^{2+} and 8.0×10^{-7} M for MeHg, as shown in Table 1 [35].

Towards the development of rapid visual color change platforms, Chen et al. (2013) reported the use of T-rich aptamers (H_{T5} and H_{T7}) for the detection of MeHg, achieving a LOD 5000 nM. In their approach, DNA-templated alloy Ag–Au nanoparticles functionalized as transducers with color changes in the solution serving as the reporting mechanism.

Employed a nanoarchitectonics-based approach using adenine-rich sequences instead of aptamers, significantly improving sensitivity by more than four orders of magnitude under controlled laboratory conditions. However, this method failed to demonstrate efficacy in environmental samples [37,41].

Additionally, Lin and Tseng (2010) demonstrated an indirect detection mechanism for MeHg in the nanomolar range using lysozyme

type VI (Lys VI) in combination with the formation of gold nanoclusters (Lys VI-AuNCs). This method utilized fluorescence quenching as the transduction and reporting mechanism [40].

Further details on these platforms, including their working principles and detection capabilities, are presented in Chapter 3 (immunostrips) and Chapter 6 (aptamers), with specific examples provided for the measurement of MeHg.

3. Immunostrip based MeHg detection

Immunostrips assays are widely used for their simplicity, affordability, and portability, enabling rapid, on-site detection with high specificity and sensitivity. They consist of a sample pad, conjugate pad (with labeled antibodies), nitrocellulose membrane (test and control lines), and absorbent pad to ensure efficient operation (Fig. 3). These features make them ideal for environmental monitoring, food safety, and diagnostics. Immunostrip assays are based on the reaction between immobilized antibodies or conjugate on the membrane and the binding of the analyte of interest [42]. Advancements in immunostrips have been used in combination with novel nanomaterials, such as gold nanoparticles (GNPs), quantum dots, and upconversion materials. Immunostrips are widely employed in medical diagnostics due to their rapid, simple, and cost-effective nature.

Lateral flow assays (LFIA) offers several advantages, including rapid results, ease to use, and the ability to function in resource poor settings without extensive laboratory infrastructures [43]. LFIA provide quantitative and semiquantitative testing applications such as detection and determination of nucleic acids [44], proteins, whole-cell bacteria [45,46] and also in rapid biosensing technology in point-of-care testing (POCT). Gold nanoparticles as reporters are often used in most of the assays and in recent years much attention has been paid to upconversion nanoparticles (UCNPs), for instance, lanthanide-doped nanocrystals as fluorescence signal nanomaterials [47–49]. This is mainly because of their high anti-Stokes shifts, optical stability, multiple emission bands and long lifetime. However, imunostrips are an ideal tool for the visual and fast estimation of analyte in "yes" and "No" forms, there are numerous challenges that need to be addressed for the future development of Immunostrips, such as selectivity, sensitivity, and response time.

In comparison to other MeHg sensing approaches, only one report has been published in this direction. Zou et al. (2017) described an immunostrip approach for the detection of MeHg utilizing MeHg-specific antibodies [35]. The study developed an indirect competitive enzyme-linked immunosorbent assay (ic-ELISA) and an immunochromatographic strip assay for detecting methylmercury (MeHg) in tap water. The authors have reported high specificity with an IC50 of 16.64 ng/mL and a limit of detection (LOD) of 2.03 ng/mL for ic-ELISA. The strip assay had a cut-off value of 500 ng/mL and a LOD of 11.3 ng/mL, with recovery rates of 98.13 % and 107.87 %, respectively. The most important feature of this study was its high specificity for MeHg without cross-reactivity with other metal ions and the convenience of not requiring sample derivatization. However, drawbacks include the need for optimization of assay conditions and potential variability in monoclonal antibody performance, with the strip assay possibly lacking quantitative accuracy compared to ic-ELISA. The assay can be improved by enhancing sensitivity and specificity, exploring alternative antibody production methods (eg. egg yolk antibodies), and integrating and interfacing these strips with reflectometer with portable detection devices for on-site testing.

4. Small molecule probes (SMP) in MeHg detection

Small molecule probes (SMP) are low molecular weight chemical compounds designed to selectively detect specific biological, chemical, or environmental targets through measurable changes, such as fluorescence, luminescence, or color shifts [50–57]. These probes often consist of a recognition moiety that interacts with the target and a reporter unit that produces a detectable signal upon binding or reaction. SMPs are extensively being used in diverse fields such as biology, physiology, medicine, pharmacology, and environmental sciences for their high specificity, sensitivity and versatility in detecting small molecules, ions, or biomolecules in complex systems. These fluorescent probes exhibit changes in intensities/emission wavelengths through possible sensing mechanisms which include Förster resonance energy transfer (FRET), intramolecular charge transfer (ICT), photoinduced electron transfer (PeT), excited-state intramolecular proton transfer (ESIPT) [57], and aggregation-induced emission (AIE) (Fig. 4a) [58]. The development of SMP has been rapidly increasing due to advancements in its application, such as g-fluorescence imaging modalities.

An ideal system of SMP-based fluorescent sensing platforms would provide a reliable signal read-out response under analytical conditions, which in turn helps us to measure the concentration of the analyte. The SMP that forms a reversible interaction between the analyte and the probe is categorized as a chemosensor measuring the accurate concentration of the analyte over time. If the sensing machinery is irreversible when contacted with the analyte, the probe is categorized as a chemodosimeter, in which the response will indicate only the maximum concentration of the analyte present in a time unit. Taking account of the above properties of SMP various MeHg detection platforms have been reported in recent years.

A simple turn-on fluorescence probe in real samples was developed by Shu et al. (2015) which demonstrated the design and synthesis principle. The group has developed a 4-hydroxynaphthalimide-derived fluorescent probe (1) to detect both organic mercury and Hg^{2+} in the aqueous medium. The mechanism of action for the sensing is with the dimethyl-thio carbamide ester group acting as the recognition unit, and N-butyl-4-hydroxy-1,8-naphthalimide acting as the fluorophore (Fig. 4b). The developed platform can be used as a "naked-eye" indicator for mercury species with the help of hydrogen peroxide (H_2O_2), which acts as a fluorescent enhancement. The study demonstrates that dimethyl-thiocarbamic ester moiety is a new design strategy for the

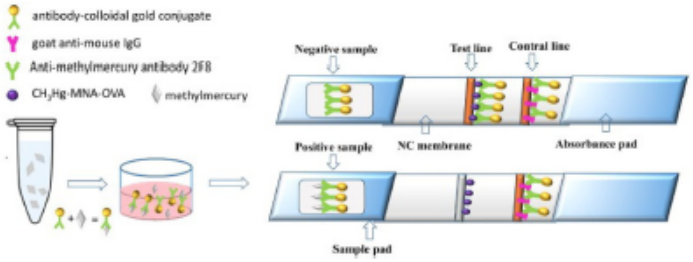

Fig. 3. Principle illustration of the immunochromatographic strip assay for MeHg detection. Reproduced with permission from Ref. [35], Copyright (2017) Taylor & Francis.

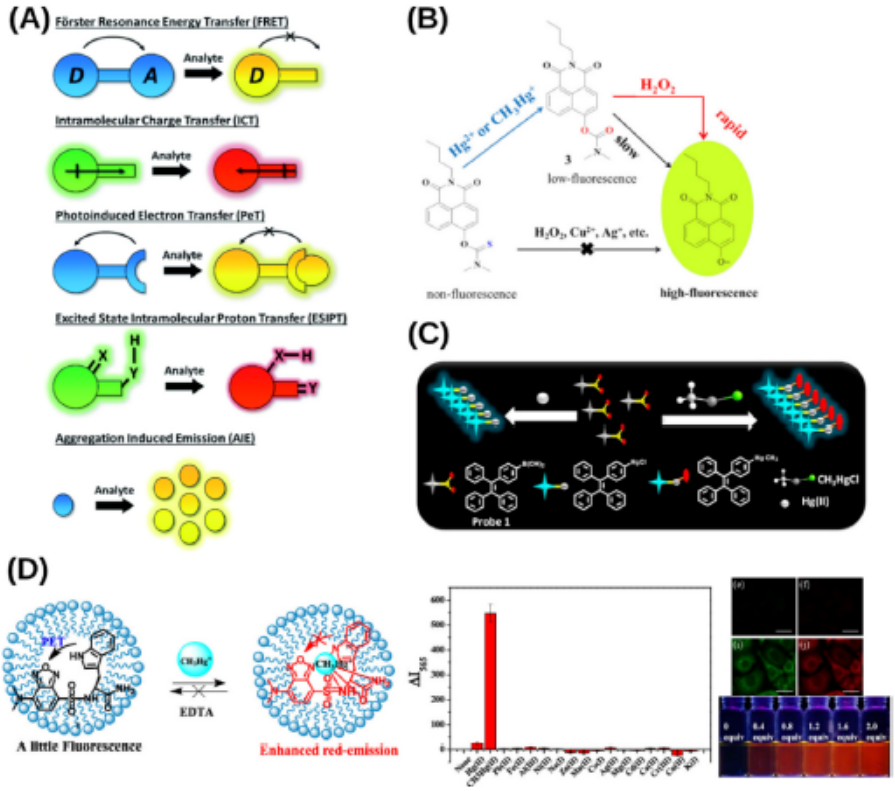

Fig. 4. a) General scheme for recent advances in SMP. Reproduced with permission from Ref. [58]. Copyright (2021) Royal Society of Chemistry. b) Reaction mechanism of probe 1 for mercury species with the help of H_2O_2. Reproduced with permission from Ref. [59]. Copyright (2015) American Chemical Society. c) A schematic representation of the sensing process of probe 1 towards Hg^{2+} and CH_3Hg^+ by turn-on type AIE. Reproduced with permission from Ref. [60]. Copyright (2017) American Chemical Society. d) Fast and sensitive fluorescent detection method of CH_3Hg^+ and Hg^{2+} using a reversible fluorescent molecular probe and SDS micelles. Reproduced with permission from Ref. [62] Copyright (2020) American Chemical Society.

construction of highly selective and sensitive probes for the simultaneous detection of inorganic and organic mercury species with the amplification reagent of H_2O_2. The sensitivity of the developed method was attained with the LOD of 2.4 nM for Hg^{2+} and 5.8 nM for MeHg in an aqueous solution [59].

Similarly, a highly sensitive and selective aggregation-induced emission (AIE)-based turn-on probe for both inorganic mercury ions and organicmercury species was reported by Chatterjee et al. The probe's mechanism is based on the mercury ion-promoted transmetallation reaction of aryl boronic acid. The probe, a tetraphenylethylene (TPE)-monoboronic acid (1), was used for the detection of mercury species (Fig. 4c). Both Hg^{2+} and MeHg ensued a fast transmetallation of TPE-boronic acid, causing a drastic reduction in the solubility of the resulting product (TPE-HgCl/TPE-HgMe) in the working solvent system. At the dispersed phase, the aggregated form of TPE-mercury ions recovers planarity as a result of restricted rotational freedom, promoting aggregation-induced emission [60]. This was the first report on the AIE based fluorescence imaging study on MeHg contaminated live cells and zebrafish. However, based on our knowledge and literature information the TPE stability with prolonged time may be compromised in extreme environmental conditions and cannot be appropriately used in various environments.

As previously seen in the work of Chatterjee et al. using the AIE turn-on probe strategy for dual detection of mercury species, Neupanea et al. (2020) developed a novel fluorescent probe for the detection of Hg^{2+} and MeHg in aqueous solutions using the displacement reaction of aryl boronic acid with mercury species. This probe demonstrated effective sensing properties for both Hg^{2+} and MeHg by forming a covalent adduct. The aryl boronic acid derivatives used in the displacement reaction enabled the development of a sensor with limits of detection (LOD) of 4.02 nM in distilled water, 1.82 nM in aqueous buffered solutions, and 10 nM in drinking water (Table 2). The major advantage of this platform is the detection time of less than 2 min for Hg^{2+} and less than 5 min for MeHg, and runs effectively in aqueous matrices [61].

Most of the SMPs are based on the fluorescence probe and researchers are trying to use different synthetic molecules to enhance the detection capabilities in coming years. In yet another report, Oh et al. (2020) developed a fluorescent detection method for Hg^{2+} ions and MeHg using an amino-acid-based fluorescent probe in combination with Sodium Dodecyl Sulfate (SDS) micelles (Fig. 4d). The fluorescent probe in SDS micelles sensitively and selectively detected Hg^{2+} ions and MeHg by the enhancement of the red emission at 575 nm in a purely aqueous solution, and the detection of MeHg was completed within 1 min which showed comparatively fast responses to the reported results of

Table 2
Chemical-based detection techniques for methylmercury.

No.	Hg species	(LOD)	Sample matrix	Sensor components			Sensing mechanism	References
				Bioreceptor	Transducer	Reporter		
1.	Hg^{2+} and MeHg	2.4 nM - Hg^{2+} 5.8 nM - MeHg	River water samples	Dimethyl-thioc varbamide ester group	4-hydroxynaphthalimide	Fluorescence	Dimethyl-thiocarbamide ester group acts as the recognition unit, and N-butyl-4-hydroxy-1, 8-naphthalimide acts as the fluorophore	[59]
2.	Hg^{2+} and MeHg	598.2 nM	Fish samples	TPE-monoboronic acid	Aggregate induced emission (AIE)	Fluorescence	Dimethyl-thiocarbamide ester group acts as the recognition unit, and N-butyl-4-hydroxy-1, 8-naphthalimide acts as the fluorophore	[60]
3.	Hg^{2+} and MeHg	4.02 nM 1.82 nM 10 nM	Environment samples	Displacement reaction of aryl boronic acid	Fluorescent probe based on displacement reaction of arylboronic acid	Fluorescence	Displacement reaction of aryl boronic acid with mercury species	[61]
4.	Hg^{2+} and MeHg	9.1 nM for Hg^{2+} and 206 nM for MeHg	Model water	Aamino-acid-based (indole, sulfonamide, and amide groups) and Sodium Dodecyl Sulfate (SDS) micelles.	Amino acid – based fluorescent probe (1) and SDS micelles	Fluorescence	Mercury ion-promoted transmetallation reaction of aryl boronic acid	[62]
5.	Hg^{2+} and MeHg	Hg^{2+} is 20 nM MeHg is 50 nM	Cells and living systems	pyridyl group	Coordination-induced emission	Fluorescence	The rotation of 1,8-naphthalimide moieties would be restricted due to the chelation between 1,8-naphthalimide and MeHg, which results in enhanced fluorescent emission	[63]
6.	Hg^{2+} and MeHg	94 nM	Model water	1,1,2,2-tetrakis[4-(3-methyl-1H-benzimidazol-1-yl) phenyl ethylene tetraiodide (Tmbipe)	1,1,2,2-tetrakis[4-(3-methyl-1H-benzimidazol-1-yl) phenyl ethylene tetraiodide (Tmbipe)	Fluorescence	Displacement reaction of aryl boronic acid with mercury species	[64]
7.	Hg^{2+} and MeHg	54 nM 19.08 nM	Model water	zeolitic imidazolate framework-7 (ZIF-7) and zeolitic imidazolate framework-60 (ZIF-60)	Coordinated induced emission	Fluorescence	Strict cavity confinement towards Hg^{2+} and MeHg	[65]
8.	Hg^{2+} and MeHg	1.79 nM	Model water	MIL-53(Fe) with CCl_4	MIL-53(Fe)	Fluorescence	Amino-acid-based fluorescent probe and Sodium Dodecyl Sulfate (SDS) micelles with enhancement of the red emission at 575 nm	[66]
9.	Hg^{2+}, Hg_2^{2+} and MeHg	5.0 pM	Environmental water	Piperazine derivative, HEPPSO, i.e., N-(2-Hydroxyethyl) piperazine-N′-(2-hydroxypro-panesulfonic acid)	catalysis-reduction in an aqueous solution through the cooperative effect of AuNP-catalyzed properties and the formation of gold amalgam	Absorption using UV-Spectrophotometer	Organic reaction catalyzed by AuNP and measured the change in the catalytic product induced by the deposition of Hg atoms on the surface of AuNPs	[67]
10.	Hg^{2+} and MeHg	10 nM for Hg^{2+} and 15 nM for MeHg	Model waters	$CuDDTC_2$ Complex; diethyldithiocarbamate (DDTC)	Au-NPs; AIE	Naked-eye detection	The rotation of 1,8-naphthalimide moieties would be restricted due to the chelation between 1,8-naphthalimide and MeHg, which results in enhanced fluorescent emission	[1]
11.	MeHg	5.9 nM	Environmental samples	PEG	Carbon dots	Fluorescence	Recognition event of the MeHg is dependent on its hydrophobicity and its ultrasound-assisted permeation via PEG	[68]

(continued on next page)

Table 2 (continued)

No.	Hg species	(LOD)	Sample matrix	Sensor components			Sensing mechanism	References
				Bioreceptor	Transducer	Reporter		
12.	MeHg and Hg^{2+}	1.7 nM for DAOC-AgNPs and 7 nM for RhB@DAOC-AgNPs	Contaminated water	amide-modified oxacalix [4] arene derivative viz. Di-acetamido-oxacalix [4] arene (DAOC) (a heteracalixarene host)	Silver nanoparticles (Oxacalix [4]arene templated) - (DAOC-AgNPs)	Fluorescence	The fluorescent dye could rapidly coordinate with Hg2+ species to form a dinuclear Hg^{2+} tetracarbene complex which can then self-aggregate to turn on AIE fluorescence	[69]
13.	MeHg and other toxic cations	~1 aM (atto molar)	Environmental matrices (Lake water)	Stripped layers of Hexathiol and PEG	Au gold film sputter coated on a glass slide	Conductivity measurement	Changes in the tunneling current across films of NPs protected with striped monolayers of organic ligands	[70]

Chatterjee and Neupanea group previously. The interference studies of the probe were selectively tested with 16 other metal ions and found that the probe in SDS micelles with EDTA exhibits highly sensitive and selective turn-on detection for MeHg over Hg^{2+} [62].

The chemodosimeter, a newly developed method in the area of SMPs, paved the way for the detection of MeHg and Hg^{2+} reported by Zou and Tian (2010). The work includes the synthesis of two novel fluorescent chemodosimeters that displayed selectivity involving receptor and sensing mechanisms consisting of 2,1,3-benzothiadiazole and thiourea signalling and recognition moieties, respectively. The chemodosimeter's spectral and optical properties exclusively distinguish between Hg^{2+} and MeHg and open new opportunities for monitoring. The developed method was able to detect Hg^{2+} with LODs (1.6×10^{-7} M and 5.0×10^{-7} M) and MeHg (3.0×10^{-7} M and 1.0×10^{-6} M) as reflected in Table 2 [71]. However, based on the understanding of the sensing reaction based on the above mentioned constituents the detection of mercury species can be only single use type due to their irreversible reaction. This is also the main reason why this approach can be used in dosimeters and are not suitable for real-time monitoring.

More recently, Yuan et al. (2019) developed a new fluorescent dye for the selective detection of Hg^{2+} ions and organic mercury including MeHg and phenylmercury ($PhHg^{+}$). The sensing mechanism involves the rapid coordination of dye with Hg^{2+} species to form a dinuclear Hg^{2+} tetracarbene complex, which self-aggregate to activate turn on AIE fluorescence. The dye 1,1,2,2-tetrakis[4-(3-methyl-1H-benzimidazol-1-yl) phenyl ethylene tetraiodide (Tmbipe) featured four positively charged methylated benzimidazole groups, conferring excellent water solubility. The fluorescence activation occurs within 3 min driven by synergistic rigidification of the tetraphenylethylene-bridged Tmbipe core through chelation ring formation with mercury, further enhanced by probe aggregation. This system achieves an LOD of 94 nM, as summarized in Table 2 [64]. As in the case of chemodosimeter studies, this work restricts the multiple analysis and may face interference in complex matrices which is not sufficient for ultratrace mercury detection in a strict regulatory context.

With AIE based principle and turn-on fluorescence probe as seen from the above studies for the detection of dual mercury species, Yang et al. (2009) developed a dual fluorescent platform which utilizes intramolecular rotational restriction to designed a molecular probe incorporating a pyridyl group as the chelating unit and 1,8-naphthalimide as the fluorescent unit. This probe produces a very weak fluorescence in the absence of an analyte of interest since the free intramolecular rotations of the 1,8-naphthalimide moieties non-radiatively annihilate its excited state. However, in the presence of analytes (Hg^{2+} or MeHg), the rotation of 1,8-naphthalimide moieties would be restricted due to the chelation between 1,8-naphthalimide and MeHg, which results in enhanced fluorescent emission. The limitation of the sensor is actually the response induced by Hg^{2+} since it is much stronger than the response caused by the MeHg. However, in this type of sensor the problem was tackled by using T-rich DNA that masks Hg^{2+} in solution and therefore enable MeHg detection. With this method, the sensitivity in detection of two mercury species was reached with the LODs of 50 nM (MeHg) and 20 nM (Hg^{2+}). The method has an advantage in terms of selectivity and has shown less or no interference with other metal ions [72].

5. Metal-organic framework (MOF) for MeHg detection

Metal-organic frameworks (MOFs) are crystalline porous materials composed of metal ions or clusters coordinated to organic linkers. According to the International Union of Pure and Applied Chemistry (IUPAC) definition, these are like porous coordination polymers showing crystalline structures and potential voids [73]. MOFs are most compatible with organic and aqueous media with additional advantages such as defined porosity due to the larger spaces such as 544 $m^2 g^{-1}$ and cost-effectiveness. Nitrogen adsorption porosimetry, electronic, optic and atomic force microscopies, powder X-ray diffraction, solid-state NMR, UV–vis and IR spectroscopies are some of the defined techniques that can be used for the characterization of the MOFs [74,75]. Development of MOFs is achieved using autoclaves and fabrication using microwave-assisted techniques to accelerate the kinetics of the coordination or mixing of precursors [76]. In recent years, various new polymerization techniques have been used for fabrication to fine-tune the size and morphology based on the electrosynthesis of the conducting material [77]. For preparation of a MOF different metal ions or clusters are mixed with organic linkers using a convenient solvent. Coordination polymerization takes place between the precursors, resulting in a cross-linked network showing potential voids (Fig. 5) [78].

MOFs offer high surface area, tunable porosity, and chemical versatility, enabling applications in gas storage, catalysis, sensing, and drug delivery [52,54,79,80]. MOFs emerged in the 1990s, with pioneering examples including MOF-5, HKUST-1, MIL-101, and ZIF-8., The developed 1D, 2D, and 3D MOFs have paved the way for the advanced MOF-based sensor systems. Although the integration of MOFs into electronics is still in its infancy, promising applications have been demonstrated in devices such as field-effect transistors (FETs) and resistive random-access memories (RRAM) [9]. In MOF-based electronic sensors, sensitivity is defined as the smallest fluctuation in an external stimulus that induces a measurable signal variation.

In sensors, MOFs function as a receptor or recognition element, enabling the design of MOFs with superior selectivity. MOFs can detect analytes, including MeHg, through mechanisms such as size exclusion (based on porosity) and interactions engineered via specific linkers or precursors. Selectivity is achieved by tailoring the MOFs interaction with the target analyte, leveraging forces such as hydrogen bonding, π-π interactions, and electron donor-acceptor coordination [81,82].

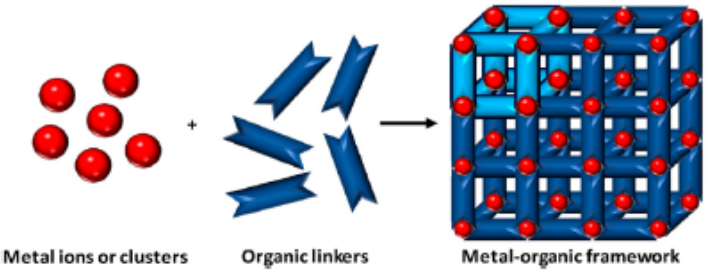

Fig. 5. Scheme for the preparation of a MOF. Different metal ions or clusters are mixed together with organic linkers using a convenient solvent. Over the past few decades, over 100,000 structures have been reported in the "MOF subset" of the Cambridge Structural Database (CSD) Reproduced with permission from Ref. [78] Copyright (2018) MDPI.

Compared to biomolecules MOFs offer advantages as recognition materials, including customizability, cost-effectiveness, high stability, and compatibility with harsh conditions like extreme temperatures and pH levels.

Based on insights we gained through our thorough literature review, metal-organic frameworks (MOFs) can be broadly categorized into four major types: 1) mass-loaded, 2) filtration, 3) electronic function, and 4) optical sensitivity.

Mass-loaded: The porous nature of MOFs can adsorb and preconcentrate the analytes in complex sample matrices, increasing the possibility of host-guest interactions and further improving the sensitivity of the sensors. The selective nature of this MOF type is mainly based on its unique and specific host–guest interaction which is also beside specificity also improves the sensitivity of the sensor. However, the introduction of MOFs into electronic sensors as mass-loaded layer that are sensitive to mass change seems to be more feasible. Integration of MOFs with Quartz crystal microbalance (QCM), surface acoustic wave sensors (SAWS) and microcantilevers have been explored in recent years [9]. MOFs based electronic sensors can only serves as the adsorption layer for different molecules such as gases (CO_2, CO, CH_4) and volatile organic chemicals (VOC) [9].

Filtration: The MOFs filtration properties captures a targeted analyte and serve as the filtration layer to shield other interferences. With this property of MOFs, different platforms were developed to screen, filter and purify mixtures including gases, pollutants and organics [9]. The best example in this direction is ZIF-8 which has high hydrogen permeability due to its pore size (0.34 nm), allowing selective penetration of H_2 molecules (0.289 nm) and excluding their larger gas molecules (diameter >0.34 nm) [9]. In recent years, Koo et al. and Zhou et al. fabricated MOFs designed for H_2 and CH_4 detection by functionalized ZIF-8 as a filtering layer assembled on Pd NWs and ZnO nanorods [83]. The major drawback of the system is that the detection range for analytes is still limited because of mechanisms of filtration adopted for selectivity.

Electronic Function: The long-range order in MOF crystal structures leads to charge transport possibly through the metal ions and the organic linkers. However, MOFs are confronted with the opposite condition where most MOFs suffer from a low degree overlap between the p orbitals in the linker groups and the metal d orbitals since the oxygen atoms of carboxylate ligands coordinate to the metal ions through σ bonds. Therefore, conventional MOFs with low atomic density plus strong electron charge transfer are considered as insulators (conductivity $<10^{-10}$ S cm^{-1}) [84]. Accordingly, most MOFs in the electronic sensors are designed on the on-chip thin film grown directly on electrodes, as a paste or freestanding pellets, and used for sensing gases and other volatiles such as alcohols.

Optical Sensitive: MOFs exhibit superior optical properties deriving from its d–d transition in metal ions and electron transfer in the ligand or metal-to-ligand/ligand-to-metal electron transfer under external stimuli, including light, temperature and pressure. The optical sensing performance of MOF-based sensors stems from the host-guest interaction which converts the recognition interaction into an electronic signal or optical signal [9]. The receptors in MOFs are clustered molecules, such as organic linkers or metal ions, that, in response to analytes like MeHg, induce changes in the structural framework of the MOF [73,85–87]. The reporting system for the MOFs is usually based on the difference in the fluorescence signal detected before the analyte interacts with MOFs and after when the MOF coordination changes. Most of the MOFs reported optical sensors are based on the utilization of monolayer nanofilms and oleylamine (OLA) which provide the water stability of the MOF layer.

To the best of our knowledge, based on a review of the literature, only a few published reports are available on the specific detection of MeHg using MOFs at sensitive and trace levels. Utilizing dual zeolitic imidazolate frameworks (ZIF-7) and (ZIF-60), Xu et al. (2013) have developed a fast, sensitive and facile sensing method on the basis of the fluorescence based mechanism and speciation analysis of inorganic Hg^{2+} and MeHg. The synthesis protocol was simple and based on a microwave-ultrasound-assisted approach. The sensing mechanism is based on the strict cavity confinement of ZIF-7 and ZIF-60 structures, which exhibited excellent selectivity for Hg^{2+} and MeHg even in the presence of various cations or anions. The developed method showed LODs of 54 nM and 19.08 nM for Hg^{2+} and MeHg, respectively (Table 2). The platform was also tested with real samples and the best performance of the sensor was reported at pH 7, with a recovery of 100 % and 96.2 % for Hg^{2+} and MeHg, respectively. respectively [65]. Another pioneering work by Jia et al. (2013) developed a rapid and facile microwave ultrasound-assisted synthesis method for the preparation of MIL-53(Fe) MOF for the direct, rapid, highly selective and ultrasensitive sensing of MeHg. The sensor achieved the detection limit of 1.79 nM, where MIL-53(Fe) suspension, with CCl_4 as the dispersant, served as a fluorescence sensing platform, demonstrating a significant increase in fluorescence intensity upon exposure to MeHg, with minimal interference from other tested Hg species [66].

The complexity of sensor fabrication, which may hinder scalability and reproducibility potentially affects applicability in diverse environments.

6. Nanoparticle (NP) based biosensor

Nanoparticle (NP) based biosensors leverage the high surface area, tunable chemistry, and sensitivity of NPs for precise analyte detection in fields like diagnostics, environmental monitoring, and food safety. Nanomaterials are different in surface effects compared to bulk materials, due to three reasons; (a) large surface area and high particle number per mass unit, (b) the fraction of atoms at the surface is increased, and (c) the atoms situated at the surface have fewer direct

neighbours (Fig. 6a). Among various nanoparticles, gold nanoparticles (AuNPs) and Silver (Ag) are widely used for the detection of methylmercury (MeHg) and mercury (Hg). This is mainly because they are often functionalised with spacers and functional groups to enable selective and specific binding. Their localized surface plasmon resonance (LSPR) enables optical detection with high sensitivity, while their conductivity supports electronic sensing applications. A few examples of functionalized nanoparticles are outlined below.

(i) **AuNPs surface functionalized with diethyldithiocarbamate (DDTC):** AuNPs functionalized with DDTC are highly effective for binding Hg due to the strong affinity of sulfur in DDTC for mercury ions. This binding relies on the soft-soft interaction principle of Hard and Soft Acids and Bases (HSAB) theory. Functionalization enhances the selectivity and sensitivity of AuNPs for Hg detection, with binding causing measurable changes in optical or electronic properties. Based on this principle, Chen et al. (2024) developed a colorimetric nanosensor strategy for various species of Hg in the aqueous phase (Fig. 6b). The proposed method involves $CuDDTC_2$ complex assisted AuNP-Based nanosensors that act as specific ligands to recognize the Hg species. Since Hg has a high affinity for soft donors such as sulfur, in the presence of Hg species, they can immediately displace the Cu^{2+} in the CuDDTC2 complex by promptly forming Hg–DDTC complexes containing two residual thiol groups for Hg^{2+} and one for MeHg. The citrate ions, which keep AuNPs from aggregation on the surfaces, can be easily displaced by thiol groups. Thus, the Hg–DDTC complex can be attached to the surface of AuNPs through Au–S linkages. This interaction destabilizes the system, causing the aggregation of AuNPs and resulting in a colour change in the solution. EDTA was used as a masking agent in the nanosensing mechanism to selectively mask Hg^{2+} from other mercury species. With this method, the dual mercury species were simultaneously determined with the LODs of 10 nM for Hg^{2+} and 15 nM for MeHg. They also tested the selectivity of the sensing mechanisms and found out that the mechanism is very stable toward mercury species against other metal ions [1].

(ii) **Lysozyme type VI-stabilized gold nanoclusters:** This type of functionalization renders the effective binding of Hg via thiol, amine and carboxyl functional groups, which form stable complexes with Hg ions. The use of lysozyme type VI-stabilized gold nanoclusters (Lyz VI-AuNCs) provides significant advantages in maintaining fluorescence stability, enhancing detection capabilities, and ensuring the reliability of the sensing method. A dual-mode detection platform was designed based on the above nanocluster phenomena developed by Lin and Tseng (2010). The method utilizes a one-step approach to prepare Lyz VI-AuNCs for the ultrasensitive detection of Hg^{2+} and MeHg based on a fluorescence quenching mechanism. The study reported the use of 25 mg/mL Lyz VI as a reducing agent, which formed Lyz VI-AuNCs (denoted as Au-631). Au-631 was highly stable in a high concentration of glutathione or high salinity solution such as NaCl. Au-631 was capable of sensing Hg^{2+} and MeHg through the interaction between Hg^{2+}/MeHg and Au^{+} on the Au surface. When EDTA was introduced which acts as the Hg^{2+} masking agent, Au-631 was able to discriminate between Hg^{2+} and MeHg. The LODs obtained in this study were 3 pM and 4 nM for Hg^{2+} and MeHg, respectively. The selectivity of this probe is highly efficient and, in fact, more than 500-fold for Hg^{2+} over any metal ions. The authors have also used bovine serum albumin-stabilized AuNCs, with Au-631, in which Au-631 provided an approximately 330-fold improvement in the detection of Hg^{2+}. Importantly, they have successfully applied this probe for the determination of Hg^{2+} and MeHg in the seawater matrix [40]. In another study, Xie et al. (2018) have developed a simple, rapid and cost-effective colourimetric method for selective and sensitive detection of MeHg. The sensing mechanism is based on the increasing surface deposition of Hg, enhancing the catalytic effect

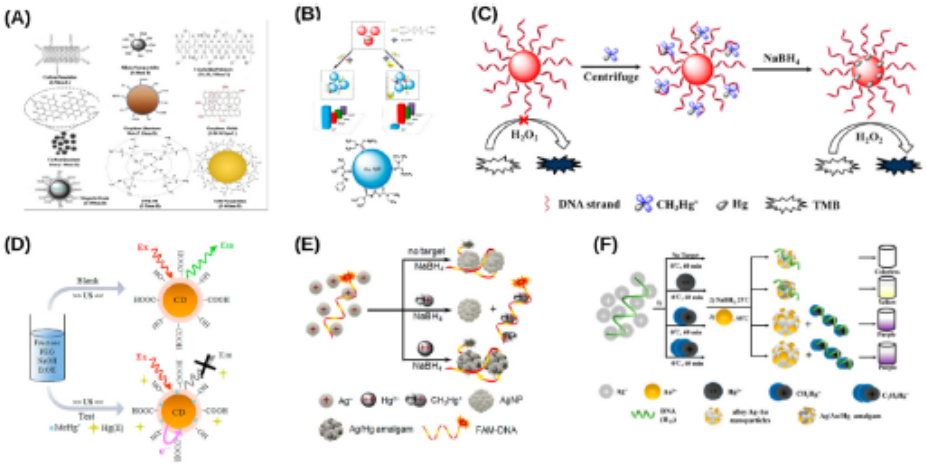

Fig. 6. a) Commonly used nanomaterials in various kinds of sensors fabrication with their sizes. L: length; D: Diameter. Reproduced with permission from Ref. [91] Copyright (2020) MDPI. b) Illustrations of AuNP-Based colorimetric sensing strategy for Hg Species and Hg– DDTC complex attached to the surface of AuNPsc) CH_3Hg^+ sensing mechanism. Reproduced with permission from Ref. [1] Copyright (2014) American Chemical Society. c) CH_3Hg^+ sensing mechanisim. Reproduced with permission from Ref. [89] Copyright (2018) MDPI. d) Schematic representation of the mechanism involved in the fluorescence quenching caused by the presence of MeHg. Reproduced with permission from Ref. [68] Copyright (2014) American Chemical Society. e) Schematic illustration for fluorescent detection of MeHg based upon a dye-labeled T-rich DNA (FAM-DNA). Formation of AgNPs or Ag/Hg amalgams on FAM-DNA template quenches the FAM fluorescence emission; the presence of MeHg suppresses formation of the metal nanostructures, revealing fluorescence enhancement. Reproduced with permission from Ref. [39] Copyright (2015) The Royal Society of Chemistry. f) Schematic illustration of the experimental principle for the colorimetric detection of MeHg and C_2H_5Hg. Reproduced with permission from Ref. [37] Copyright (2018) American Chemical Society.

of AuNPs. The aptamer (H_{77}) was used as a bioreceptor toward MeHg (Fig. 6c) which was used to capture and separate MeHg by using centrifugation. This capturing of MeHg using aptamers functionalized in the AuNPs increased the Hg deposition on Hg onto the surface of AuNPs. This enabled and enhanced the catalytic activity of the AuNPs toward the chromogenic reaction of 3, 3,5,5-tetramethylbenzidine (TMB)-H_2O_2. The LOD of the nanobiosensor was 5.0 nM with a linear range of 10–200 nM [89].

(iii) **AuNPs with thymine moiety:** AuNPs functionalized with thymine are effective for Hg binding due to the high affinity of thymine to Hg ions. Thymine forms stable T-Hg^{2+}-T complexes, where Hg^{2+} bridges two thymine molecules, leading to selective recognition. Based on this, Aulsebrook et al. (2018) developed a tandem colourimetric, temperature-dependent naked eye sensing machine for Hg^{2+} and MeHg. In this study, the authors have functionalized AuNPs with a thymine moiety that sandwiches a single mercuric species between two thymine molecules on the surface of the NPs, and this enables the aggregation of NPs when it is introduced to Hg^{2+} and MeHg species. The interaction/reaction of Hg^{2+} and MeHg caused a significant change in the visible absorbance spectrum, which resulted in a naked eye distinguished colour change from red to blue. Though they were successful in employing the basic chemistry for mercury-induced aggregation in the functionalized AuNPs, the LOD of this approach is much higher than the permissible level of mercury in the environment (1000 nM), which makes it unusable in environmental matrices [38]. The platform was rapid, sensitive and simple it often suffers potential interference with limited detection range due to the stability and complex functionalization process.

(iv) **HEPPSO, N-(2- Hydroxyethyl) piperazine-N′-(2-hydroxypropanesulfonic acid) funetionalized AuNPs:** Functionalization Au surface with HEPPSO showed higher affinity towards Hg ions due to strong chelating properties of the sulfonic acid group ($-SO_3H$) and –OH present in HEPPSO. These functional groups interact specifically with Hg, forming stable complexes. The functionalisation enhances the selectivity and sensitivity of AuNPs for Hg detection. Recently, Li et al. (2017) have developed a dual detection platform for sensing Hg^{2+}, and MeHg using catalysis-reduction in an aqueous solution through the cooperative effect of AuNP-catalysed properties and the formation of gold amalgam. The method utilized an organic reaction catalyzed by AuNP and measured the change in the catalytic product induced by the deposition of atoms of various Hg species on the surface of AuNPs. Piperazine derivative, HEPPSO has been used to functionalize AuNPs to construct a catalysis-reduction assay. HEPPSO specifically reduces Hg species (such as Hg^{2+}, Hg^{2+} and MeHg) into Hg^0. The signal reporter for detecting Hg with an absorption peak at about 340 nm is based on the product of AuNPs that can catalyze HEPPSO. The LOD of the developed sensor was 5.0 pM which was 3 orders of magnitude lower than the U.S. Environmental Protection Agency (EPA) limit value of Hg for drinking water [67]. The method showed promising results with a new functionalisation method with broad applicability, often lacks large scale synthesis and possibly faces practical challenges compared with WCB and MOFs based detection platforms.

(v) **Silver NP funetionalized with amide-modified oxacalix [4] arene derivative viz. Di-acetamido-oxacalix [4] arene (DAOC) (a heteracalixarene host):** This type of surface functionalization are highly effective for Hg detection due to host-guest interaction between Hg ions and the unique structure of DAOC. The amide group in DAOC provide selective binding sites, allowing for the effective complexation with Hg ions. Similarly, Dey et al. (2020) have developed a sensor methodology using amide-modified oxacalix [4] arene derivative viz. Di-acetamido-oxacalix [4] arene. DAOC (a heteracalixarene host) was synthesized for the stabilization of silver nanoparticles (DAOC-AgNPs). The surface of DAOC-AgNPs was functionalized with Rhodamine B (RhB), yielding RhB@DAOC-AgNPs to induce fluorescence activity. DAOC-AgNPs and RhB@DAOC-AgNPs were found to be selective and sensitive sensors with chromogenic mechanisms for the detection of MeHg with an LOD of 1.7 nM and 7 nM respectively. The basic underlying mechanism is postulated as mercury-induced oxidation of DAOC-AgNPs leading to the formation of Ag–Hg nanoalloy, which is the reason for the disappearance of the SPR (Surface plasmon resonance) band. PXRD, SEM, TEM and EDX have been used to characterize the sensors and their sensing mechanism. Cysteine, the amino acid, was also selectively detected with the aid of DAOC-AgNPs and MeHg based on the soft-soft interaction between the thiol group of cysteine and MeHg ions. Utilizing the masking nature of EDTA towards Hg^{2+}, a multilevel INHIBIT-OR logic gate assembly was designed to discriminate MeHg and Hg^{2+} ions. The sensing machinery was employed for onsite detection of MeHg using three different kinds of portable sensors (cellulose fibre strip, hybrid alginate bead and ZIF-8 based nanocomposite); this was accomplished by immobilization of DAOC-AgNPs into cellulose fibre, sodium alginate beads and zeolite imidazole framework (ZIF-8). RhB@DAOC-AgNPs were also additionally employed for *invivo* MeHg detection in brine shrimp (Living system-aquatic crustacean *Artemia salina*) [69]. The developed method has limitations in large scale applications and requires complex functionalization process.

6.1. Carbon dots

Carbon dots (CD) are gaining popularity in biosensing due to their excellent biocompatibility, optical properties, and ease of functionalization. CDs exhibit strong fluorescence, photostability, and minimal cytotoxicity, making them ideal for real-time detection in environmental applications [90]. CDs possess abundant functional groups such as –OH, –COOH, and –NH_2, which enable efficient interactions with Hg^{2+} ions through coordination or electrostatic interactions. These features makes CD an ideal candidate to develop sensor platforms. An in situ fluorescent assay for MeHg detection using CDs as optical nanoprobes for the detection of MeHg was developed by Costas-Mora et al. (2014). The recognition event is based on the hydrophobicity of MeHg and its ultrasound-assisted permeation through the passivation coating made of polyethelyne glycol (PEG). The fluorescent quenching of MeHg is measured using Microvolume fluorospectrometry. The assay uses low amounts of organic precursors (fructose, PEG, and ethanol), and is completed within less than 1 min. The mechanism of fluorescence quenching caused by the presence of MeHg interacted with CD are presented in Fig. 6d. This green synthesis of CDs can substitute various tedious sample preparation methods and the involvement of various analytical instruments. The CDs synthesized in this study has an average size of 2.5 nm used as optical nanoprobes for sensing MeHg with a LOD of 5.9 nM (Table 2). The optical nanoprobe demonstrates high selectivity with detection completed within 1 min with excitation at 470 nm and emission at 517 nm. Fluorescence, AAS, and Fourier transform infrared spectrometry (FTIR) were applied for the determination of sensor machinery and are suggested as the basis of the recognition event. With the help of a portable fluorospectrometer, these nanoprobes can have extended applications in various environmental matrices such as tap water, river water and sea-water [68]. To the best of our knowledge, CDs have demonstrated high sensitivity, eco-friendliness, and cost-effective preparation methods with great versatility. However, despite these advantages, CDs are prone to stability issues in long-term studies.

6.2. Aptamer based detection

Aptamers are short, single stranded DNA or RNA sequences that bind selectively with Hg ions through electrostatic interactions, hydrogen bonding and conformational changes. Upon binding Hg, aptamers undergo structural changes, which can be detected using various analytical methods. This method for detecting Hg is highly effective due to high affinity and specificity of aptamers towards Hg. In another detailed report, Deng et al. (2015) have developed a sensor for MeHg detection and easy discrimination of MeHg from other Hg species based on the interaction of DNA aptamer with Ag ions that can direct formation of three types of nanostructures either (i) Ag-DNA nanoparticles (AgNP) in the absence of MeHg, (ii) Amalgamed AgHg-DNA nanoparticles in the presence of Hg^{2+} ions and just Ag nanoparticles and separated MeHg-DNA complexes. In all of the DNA-NP adducts the fluorescence signal from DNA aptamer is quenched leading to the strong fluorescent signal when MeHg is present in the solution (see Fig. 6e). They have utilized high specificity potential of aptamers (H_{T7}) that have much stronger affinity towards MeHg than Hg^{2+}. With a fluorophore-labeled DNA aptamer, the sensing machinery can detect MeHg down to the picomolar level, which is > 125 times more sensitive than Hg^{2+}. As shown in Table 1, the LODs for the sensing mechanisms are 0.4 nM. The sensor had over 50 times superior selectivity towards MeHg than Hg^{2+} and 106 times than other metal ions. Interestingly they have employed this sensor for testing its capability in monitoring MeHg accumulation in tissues and organs from three kinds of daily consumed fishes; the results show the accumulated order of snakehead > bighead carp > grass carp through the food chain [39].

Recently, Chen et al. (2018) developed a sensor that visually detects MeHg and C_2H_5Hg using DNA-templated alloy Ag–Au NPs. They employed two T-rich aptamers (H_{T5} and H_{T7}) to specifically recognize MeHg, and C_2H_5Hg. When Au^{3+}, Ag^+ and T-rich aptamer, MeHg and C_2H_5Hg all are present in a solution, the aptamers specifically bind to MeHg and C_2H_5Hg, thus facilitating the formation of alloy Ag–Au NPs, which display a color change in the solution (Fig. 6f). The developed platform has a visuable detection range of 5000 nM, and when using UV–visible spectrometry, the LOD can reach as low as 600 nM of MeHg. The developed sensor system was tested with fish muscles showing a recovery rate of 101–109 % [37]. Few examples of recently developed aptamers sequences for MeHg are listed in Table 3.

7. Nanoarchitectonics based detection platforms

Nanoarchitectonics represents an advanced conceptual paradigm for designing and synthesizing of functional materials with nano-sized structural features (Fig. 7a). The term, nanoarchitectonics, was first coined by Masakazu Aono, who proposed this concept in the conference title, 1st International Symposium on Nanoarchitectonics Using Supra-interactions in 2000 [94,95]. The terms "nanoarchitectonics" and "nano + architectonics" have appeared frequently in scientific literature, as evidenced by the publication title by Hecht (2003) [96], and in the names of research centres in Tsukuba (2001) [97] and at the University of California, Los Angeles (2003).

Nanoarchitectonics is a confluence of advanced nanotechnology with scientific disciplines, including supramolecular chemistry and materials processing [98,99]. In the nanoscale regime, accommodating the uncertainties and unexpected disturbances through statistic distributions and thermal fluctuations of functionalized materials and structures that are architecturally designed with atomic/molecular/nanoscopic elements through various processes, including atom/molecular-level manipulations, chemical modification and self-assembly/self-organization, defines the nanoarchitectonics foundations [100,101]. The molecular-level regulations in biology and biomedical fields are still different from the atom/molecular-level controls in nanotechnology, although they both interact on the same scale. The nanoarchitectonics approach seeks to realize precise control over atoms and molecules in manipulations and reactions.

Table 3
List of reported aptamers specific to MeHg.

Type	DNA Seuences	References
H_{T5}	5′-CTTTGTTAAAAATTCTTTG-3′	[37]
H_{T7}	5′-GTTCTTTGTTAAAAATTTGTTC-3′	
H_{T9}	5′-TTGTTCTTTGTTAAAAATTCTTTGTTCTT-3′	
H_{T10}	5′-TTTGTTCTTTGTTAAAAATTCTTTGTTCTTT-3′	
H_{T12}	5′-TTCTTTGTTCTTTGTTAAAAATTCTTTGTTCTTTGTT-3′	
H_8	5′-CTGCTGCTGCAAAAAGCAGCAGCAG-3′	[39]
H_{T7}	5′-GTTCTTTGTTAAAAATTCTTTGTTC-3′	
FAM-H_8	5′-FAM-CTGCTGCTGCAAAAAGCAGCAGCAG-3′	
FAM-H_{T5}	5′-FAM-CTTTGTTAAAAATTCTTTG-3′	
FAM-H_{T7}	5′-FAM-GTTCTTTGTTAAAAATTCTTTGTTC-3′	
FAM-H_{T9}	5′-FAM-TTGTTCTTTGTTAAAAATTCTTTGTTCTT-3′	
dT_6	5′-TTTTTT-3′	[41]
dA_6	5′AAAAAA-3′	
dA_{10}	5′-AAAAAAAAAA-3′	
dT_{10}	5′-TTTTTTTTTT-3′a	
dG_{10}	5′-GGGGGGGGGG-3′	
dC_{10}	5′-CCCCCCCCCC-3′	
dT_{20}	5′-TTTTTTTTTTTTTTTTTT-3′	
dA_{20}	5′-AAAAAAAAAAAAAAAAAAAA-3′	
Apt1	5′CTTTGTTAAAAATTCTTTG-3′	[92]
Apt-com	5′GAAACAATTTTTAAGAAAC-3′	
Apt2	5′CTATGTTAAAAATTCTTTG-3′	
Apt3	5′CTTAGTTAAAAATTCTTTG-3′	
Apt4	5′CTTTCTTAAAAATTCTTTG-3′	
Hp-Fc	5′-SH-GGCGATGTTTTTTCGCC-Fc-3	[93]
S1	5′-CGGATTTTTCTTGC-3′	
S2	5′-SH-GTTCTTTGTTAAAAATTCTTTGTTC-3′	
SA–MB	5′-GAACAAAGAAAAAAAAACAAAGAAC-MB-3′	
ST	5′-GAACAAAGAATTTTTAACAAAGAAC-3′	

AlH_{T5}, H_{T7}, and H_{T9} represent CH_3Hg^+ - Specific DNA with different T bases, H_8 represents random DNA, FAM - 6-carboxyfluorescein.

The nanoarchitectonics concepts have myriad applications in various research fields, such as fabrication of functional materials [102–105], energy and environmental science [106,107], and biological and biomedical applications [103,108,109]. Among these fields, sensing applications represents one of the most crucial areas that can benefit from the nanoarchitectonics approach [94,110]. By tailoring the structure, composition, and surface properties of nanomaterials, such as nanoparticles, nanoclusters, or nanocomposites, researchers can develop highly efficient sensors for Hg detection. Nanoarchitectonics enables the controlled assembly of functional components, such as receptors, ligands, or functional groups, that selectively bind to Hg ions, resulting in measurable changes in optical, electrical, or electrochemical signals.

Since interesting approaches can be built for sensor development using a nanoarchitectonics approach, such as the one that Pandeeswar et al. (2016) have developed, where instead of conventional T and A nucleotides of the DNA are used as a recognition element, they have, using self-assembly, synthesized adenine (A) conjugated small organic semiconductor (BNA) and deoxyribooligothymidine (dT_{18}) as a recognition element for MeHg detection. Nanoarchitectonics also offers possibilities to develop self-assembly based solid-state sensors developed by Cho et al. (2012), which was the only approach that was able to detect MeHg in the real concentration from various environmental matrices such as fish samples and lake water samples [41,70]. Pandeeswar et al. (2016) group have developed a nanoarchitechtonics based ultra-sensitive detection of Hg^{2+} and organometallic mercury, driven by a novel chemical design principle that allows strong mercury thymine interaction. The novel optoelectronic approach based is on nanoarchitectonics of a small molecule templated DNA system that consists of an adenine (A) conjugated small organic semiconductor (BNA) and deoxyribooligothymidine (dT_{18}) (Fig. 7b). The mutually templated co-assembly ($BNA_n dT_{18}$) of an organic semiconductor (BNA) and deoxyribo-oligothymidine (dT_{18}) has tunable chiroptical, morphological and electrical properties tapped in to enable ultrasensitive and selective

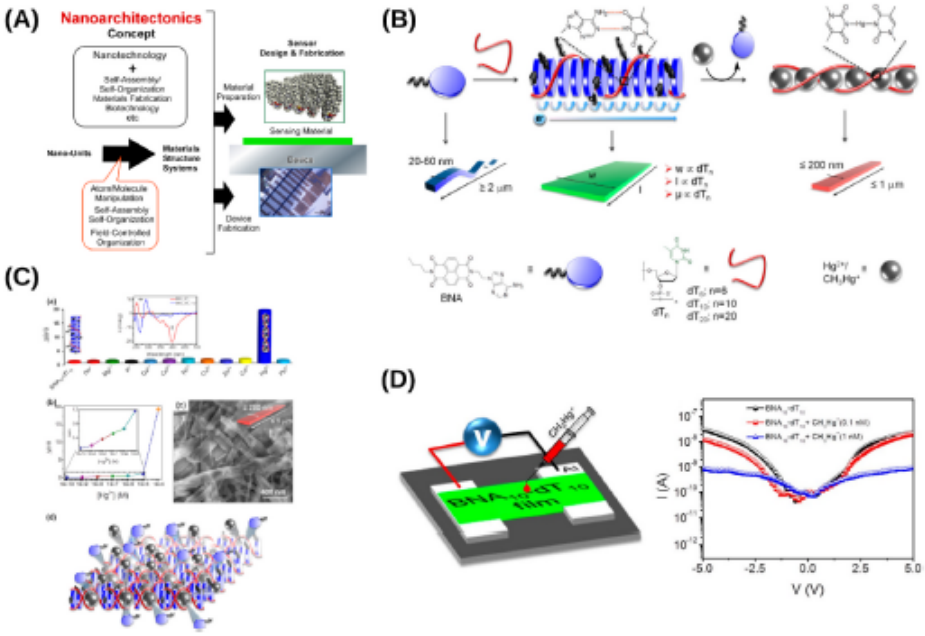

Fig. 7. a) Basic concept of nanoarchitectonics. Reproduced with permission from Ref. [111] Copyright (2019) Beilstein Journal of Nanotechnology. b) Schematic illustration of the nanoarchitectonics of BNA and dT_n coassembly as well as the corresponding molecular structures. Reproduced with permission from Ref. [41] Copyright (2017) American Chemical Society. c) Chiroptical sensing of Hg^{2+}. Schematic representation of Hg^{2+} induced displacement of BNA from the BNA_n-dT_n 2D assembly via formation of a metallo-DNA duplex $[dT\text{-}Hg\text{-}dT]_n$ and self-assembled BNA 1D tapes. Reproduced with permission from Ref. [41] Copyright (2017) American Chemical Society. d) Conductometric sensing of CH_3Hg^+. Schematic representation of CH_3Hg^+ detection device structure. BNA_{10}-dT_{10} device response before and after the addition of different CH_3Hg^+ concentrations (0.1 nM and 0.5 mM). Reproduced with permission from Ref. [41] Copyright (2017) American Chemical Society.

detection of Hg^{2+} and organometallic mercury in water. The rapid conformational change of a BNA_{10}-dT_{10} co-assembly into a metallo-DNA duplex [dT-Hg-dT] n in the presence of Hg^{2+} and organometallic mercury is utilized for a chiro-optical and conductivity (Fig. 7c and d) based rapid and sub-nanomolar sensitivity (≥0.1 nM) to mercury ions in water, as noted in Table 1. The correlation in terms of the dTn sequence length and the stability, integrity and functional properties of the BNAn-dTn co-assembly was obtained from a range of microscopic and spectroscopic measurements. The strategy that they used to advance the nano-approach is redefining the simple interaction of mercury with thymine bases using altered bases i.e. adenine (A) conjugated small organic semiconductor (BNA) and deoxyribooligothymidine (dT_n). Moreover, they have used aptamers which can clearly differentiate MeHg and Hg^{2+}. Rather than using the interaction of the recognition molecule and mercury species in an aqueous phase, they had the novel approach of developing a film that acts as a transducer which selectively hops BNA in the presence of MeHg to influence the conductivity measurement. This design strategy is anticipated to advance the development of novel templated DNA nanoarchitectonics approaches, enabling the creation of bio-optoelectronic devices and sensors for detecting toxic cations such as MeHg [41]. As from our knowledge, and detailed in the publication, this method does not distinguish between inorganic and organic mercury sources, limiting its applicability. Furthermore, the results may be influenced by external factors like pH and ionic strength, affecting reliability and also validation in real-world scenarios is necessary to confirm the robustness of the detection system.

With all the above-based detection platforms, the majority of the platforms are not reproducible, and encounter interference issues. This may be because of the selection of films and lack of integration with appropriate sensing components. Cho et al. (2012) have developed a simple solid-state sensor for the ultrasensitive detection of MeHg in model solutions and environmental matrices. In this study, AuNPs coated with binary mixtures of n-hexanethiol (HT) and glycol (EG) that generates supramolecular structure (HT/EG3) in a solid-state sensor of unmatched sensitivity towards MeHg with a detection limit of −1 aM [88]. This HT/EG3 NPs structure sense CH3Hg + selectively and with a detection limit of −1 aM. The complexity of sensor fabrication, which may hinder scalability and reproducibility potentially affecting applicability in diverse environments.

The mechanism of the sensor is based on the changes in the tunneling current across films of NPs protected with organic ligands-striped monolayers. The sensitivity advancement is enabled by the ligand shell organization of the NPs. When MeHg binds with the metal cation, the electronic structure of the molecular bridges between proximal NPs changes. This will lead to a tunnelling current increase resulting in highly conductive paths, thus resulting in the percolation of the entire film. The nanoscale heterogeneity of the film structure increases the possibilities of the cation-binding constants, which leads to a wide range of sensitivity (remarkably, over 18 orders of magnitude in MeHg concentration) [70]. This study introduced reduced selectivity of the sensors when exposed to mixtures of cations with similar binding characteristics, which can complicate detection in real-world samples. While the sensors demonstrate high sensitivity, their performance may vary based on the specific ligand-shell organization of the nanoparticles, potentially limiting their effectiveness for certain cations. The reliance on specific conditions, which is hard to achieve in environmental samples, may

hinder practical applications in diverse settings.

8. Future perspectives, challenges and conclusions

8.1. Whole-cell biosensors (WCB)

This type of sensor is especially important in determining the ecologically relevant bioavailable fraction of mercury. However, the bioavailable fraction is dependent on the type of the cell and environmental conditions and therefore it is hard to clearly differentiate real bioavailable fraction from the low sensitivity. Based on the current synthetic biology tools the repertoire of the hosts for introducing genetically engineered genes is expanded and should be the concept of bioavailability tackled by combining and comparing (i) chemical laboratory based tools with (ii) the outcome in the environment, e.g. bioaccumulation and (iii) results of using a battery of different WCB environmentally relevant hosts, similar as it was shown by using native marine and freshwater WCB hosts [16], but it should be utilized many different hosts relevant for particular either geochemical cycle or foodchain transformations.

Moreover, the WCB can determine the level of MeHg in the environment in contrast to the standardized approaches therefore minimal disturbance of the environment can be much easier achieved, but still in most cases the samples are tested in laboratory conditions since there are not many attempts to use WCB directly in the field. Therefore, it should be further developed as self sustainable WCB platform bearing alive cells and should be biologically safe not deploying genetically modified strains in the environment. The miniaturization and portable platforms are set to make on-site analysis more desirable but this is facing many challenges such as preserving low fluxes of nutrients and samples such as in microreactors since small designs are prone to clogging, preserving suspended or immobilized cells for monthly operations as well as appropriate calibration. Perhaps advances in cell encapsulation, microfluidics and multi-cell systems are expected to enhance, on one hand the stability and reproducibility and on the other hand the extension of the environmentally relevant information. In this regards the key organisms in the environment must be first identified using state-of-the-art metagenomic approaches, then utilizing advanced culturomics to be able to obtain strains that can be then at the end available for introducing genetic components by using genetic engineering tools and transforming them into WCB.

As described in Chapter 2, the WCB often might have lower genetic stability which hampers the performance over time and calls for either approach to replenish the cells using lyophilized cultures or monitoring sensitivities by appropriate on site calibration.

Although various factors such as complexation with cysteine would increase the uptake of MeHg and the addition of humic acid can reduces the MeHg uptake within the cells, we do not know the precise mechanisms that are aiding in MeHg uptake and WCB can serve us not only as a sensor platform but also to determine key environmentally relevant aspects of MeHg bioavailability. Therefore, further advances need to be carried out in research that clarifies the meaning and applicability of the use of WCB in ecological and human health risk assessment. WCB are best in conditions similar to their natural environment [112] and the temperature, incubation time, medium type, pH, and reagents can all have effects on the performance of the biosensors that can only be understood with further research and testing. Employing advanced cell encapsulation techniques to enhance stability, and optimizing growth conditions to ensure cell functionality will prolong the WCB performance.

Since WCB are also prone to the high background noise that is affecting LOD it would be very important to incorporate the currently developed advanced AI tools or autocorrelative mathematical models to better distinguish signal from the cellular, genetic or environmentally introduced noises resulting in updated sensing platform. By addressing these factors, WCBs can become more reliable, sensitive, and effective for accurate MeHg detection, standing out as the only type of sensor capable of providing environmentally relevant data.

8.2. Immunostrip based MeHg detection

Immunostrips colourimetric detection platforms for MeHg often suffer sensitive limitations, especially for trace levels. They also encounter non-specific bindings or cross-reactivity with other metal ions that can affect the accuracy. The strips can degrade over time, affecting the stability of immobilized biomolecules (antibodies, aptamers, and enzymes). Though the platforms bring advantages such as simplicity, speed and cost-effectiveness, making them suitable for on-field detection platforms, they often encounter lower sensitivity compared with other methods are susceptible to matrix interference and limited ability to distinguish from other mercury species.

Employing MeHg-specific antibodies in conjunction with an improved reporter system could provide enhanced solutions for future MeHg sensors. Integrating antibodies against MeHg with mesoporous materials or AuNPs could significantly improve sensitivity. Additionally, leveraging advanced techniques such as Surface Plasmon Resonance (SPR) or Surface-Enhanced Raman Spectroscopy (SERS) could enable sensors with detection limits several orders of magnitude lowe [35].

As detailed in Chapter 3, the sensitivity of immunostrips can be enhanced by incorporating nanomaterials into the conjugate pads and selecting biomolecules with high affinity for MeHg. A further approach to improve platform sensitivity involves integrating a reflectometer to enhance pixel detection of gold nanoparticle test lines, facilitating more precise intra-sample comparison. Since this platform is useful in semi-quantitative analysis and can be used for rapid onsite "yes" and "No" type detection of MeHg.

8.3. Small molecule probe (SMP) detection platforms

SMP are extensively utilized in various sensing platforms due to their ability to selectively interact with the specific analyte through chemical and physical changes. Most of the SMP utilize fluorescence probes which exhibit lower detection limits compared to more sophisticated platforms like immunoassay or nanoparticle-based systems. The platforms also have limited stability with probes, potential interference from other Hg species and metal ions, and difficulty in achieving real-time detection in complex matrices. Though the SMP is designed for selective analysis, cross-reactivity with structurally similar molecules or ions can occur. The probes often degrade over time, particularly under harsh environmental conditions (eg. UV light, and temperature extremes). SMPs are usually tailored for single analyte detection, making them less suitable for multiplex detection of target analytes. SMPs often require precise environmental control or additional instrumentation for effective detection, such as fluorescence readers or spectrophotometers. Some SMPs may involve the use of organic solvents or chemicals that are less environmentally friendly. A chemodosimeter was developed and demonstrated potential for mercury detection; however, it is limited to single-use applications due to its reliance on an irreversible reaction mechanism.

Among the fluorescent SMP, near-infrared (NIR, 650–900 nm) probes have several advantages over other probes, such as reducing photo-bleaching due to the lower energy of excitation required [113]. As described by Denk et al., 1990 [114], the use of two-photon (TP) excitation has been predominantly used in NIR fluorescent probes [113–115]. Over the last few decades, there have been tremendous improvements in the SMP in the realm of biological sensing and bio-imaging. As described in Chapter 4 and Table 2, most of the SMPs utilize turn-on probe strategy for dual mode detection of mercury species and the major advantage was a shorter detection time (1–5 min), compared with available analytical methods. No SMP can measure MeHg in the seawater matrix and using FRET, ICT, PeT, ESIPT, AIE, and probes combining these modalities can be developed in the future for

MeHg onsite detection in seawater. Combinatorial fluorescence techniques have to be used to overcome the issue of interference and sensitivity for MeHg detection. Several boundaries have to be dismantled to push forward the development of enhanced SMP for MeHg detection in seawater or other environmental matrices beyond the current state-of-the-art.

Future direction in the line of SMPs functionalizing with nanomaterials and integrating into a hybrid platform combined with biological elements (eg aptamers and antibodies) would be an option to increase the sensitivity and stability. Development of SMPs with improved environmental stability and reduced cross-reactivity through advanced chemical synthesis techniques. Enhancing the chemical specificity of the probes and integrating advanced signal processing methods can also improve accuracy and reliability, making SMPs biosensors more effective for MeHg detection in diverse applications.

8.4. Metal organic framework (MOF)

MOFs can suffer from non-specific adsorption, leading to interference from other metal ions and compounds which restricts its limited selectivity. This is because of the porous structure which allows non-target analytes to occupy binding sites, reducing specificity for MeHg detection. Moreover, they encounter challenges including potential instability and degradation under varying environmental conditions, complex and costly synthesis and functionalization processes, and susceptibility to interference from complex sample matrices. The lack of sensitivity is a general barrier when using MOFs for the detection of MeHg as well as other analytes. MOFs often degrade under harsh conditions because of their metal-ligand bonds which are prone to hydrolysis or photodegradation. A complex and time-consuming synthesis process might hinder scalability and widespread use because controlled pore size, structure and functionality is required for selective MeHg sensing.

Most of the MOFs developed in the past are made for gas sensing applications because of their excellent adsorption capacities (chapter 5). Very limited structures of MOFs have been explored to date such as MOF-5,1 HKUST-1,2 MIL-101,3 and classical ZIF-8. As detailed in Chapted 5, MOFs have been used in different layers as selective applications. Although the MOFs offers sensitivity for the detection of MeHg (1 aM), then complicated and sophisticated nanoparticle thin films often limit its scalability and practicality for commercialization. The research should focus on developing more stable MOF materials with improved chemical and mechanical durability, refining synthesis and functionalization protocols to ensure reproducibility and efficiency, and integrating sample pre-treatment techniques to reduce matrix effects. MOFs can be engineered with specific ligands, functional groups, or structural modifications to enhance selectivity for MeHg. Combining MOFs with advanced nanomaterials such as graphene, fullerenes, carbon nitrides, and MXene along with signal amplification strategies, enables the use of different transducers and facilitates optical and electrochemical detection methods, thereby enhancing performance through improved sensitivity and selectivity. MOFs can be engineered with specific ligands, functional groups and should aim at creating portable, cost-effective sensors with improved stability and versatility for diverse environmental and industrial applications, thus expanding their practical use in precise MeHg detection [116–122]. [123].

Functionalized MOFs with specific sensing molecules might be the most suitable to target MeHg and would help reach lower sensitivity for MeHg detection. To the best of our knowledge there are no reports on using analyte-specific aptamers that can be used to link MOFs to build architectures that can specifically coordinate with MeHg. This approach and integration of MOF hybrid aptamer on microfluidic devices allow the high-performance biosensing and the controlled synthesis of MOFs. Develop robust MOFs using hydrophobic linkers, metal clusters, or post-synthetic modifications to withstand harsh environmental conditions. Integrate MOFs with nanomaterials (e.g., gold nanoparticles, carbon dots) or employ advanced detection techniques like SERS or SPR to amplify detection signals. Focus on cost-effective, scalable synthesis methods, such as microwave-assisted or mechanochemical approaches, to promote widespread use. Combine MOFs with other materials, such as polymers or biodegradable membranes, to create hybrid systems that improve selectivity, durability, and detection range in future MeHg based detection platforms.

8.5. Nanoparticles (NPs)

Nanoparticles such as AuNPs, carbon dots, silver nanoparticles, QDs, Magnetic Nanoparticles (MNPs), Carbon Nanotubes (CNTs), graphene, and nanofibres have been put forth for miniaturizing biosensing platforms to the nanoscale to improve the understanding of various properties like optical, electronic, and magnetic characteristics, which would pave the way for their use in bio-sensing systems [124–128]. However, some drawbacks such as cross-reactivity with non-targeted metal ions or compounds, reducing their specificity towards MeHg detection should be the main future focus since these are the main factors limiting their selectivity. These drawbacks are probably the result of unspecific binding to functional groups or surface ligands which interact with a range of analytes leading to false positive results. NPs are being used in various research fields and their potential release into the environment can pose ecological harm and health risks, especially metal-based ones, which are not biodegradable and can accumulate in organisms. NPs possess low stability and often tend to aggregate or degrade in complex matrices like biological fluids or wastewater affecting their performance. This is mainly because of changes in pH, ionic strength or the presence of organic matter. Cost and scalability are the biggest challenges for the synthesis and functionalization of NPs which can be expensive in maintaining the precise size, shape and surface chemistry for effective detection.

NPs integrated with fluorescence, colorimetry, SERS, SPR, and electrochemistry improve the sensitivity of MeHg detection. As discussed in Chapter 6, NPs (AuNPs and AgNP) functionalized with DDTC, Lysozyme, thymine, HEPPSO and DAOC display enhanced selectivity and sensitivity towards MeHg. This is mainly because of the selection of functional groups which interact with MeHg to form a special complex. However, though the methods are promising and can able to detect MeHg at a trace level, they often lack challenges such as large-scale synthesis, complex functionalization process and stability in relevant natural conditions. Attention has been made towards the development of aptamers-based conjugated NPs sensing platforms for the selective detection of MeHg (Section 6, Table 3). This type of approach is time-consuming and laborious in the production of aptamer specific towards MeHg.

To the best of our knowledge, bioconjugated NPs with highly specific biomolecules such as aptamers, antibodies or molecularly imprinted polymers (MIPs) very well minimize cross reactivity, but should be further evaluated in real samples or determining applicability. More research in the direction of the stability of NPs by modifying their surfaces with polymers such as PEG or hydrophobic coating to prevent aggregation and degradation in complex matric are required to be developed in future engineering approaches. Biodegradable NPs with less toxic formulations will mitigate the environmental and health risks. Research directions in the field of QDs [46,129,130], nanofibers [36,67, 131–134], MNPs [135,136][152], and CNTs [137] would remarkably increase the transduction sensitivity and detection capabilities. Cost-effective synthesis based on a greener approach (plant based or biomimetric routes) will reduce the production costs of the NPs for the detection of MeHg. Signal amplification might be better achieved by the integrating NPs with SERS platforms. Combining NPs with MOFs and 2D materials will enhance the performance of the sensors and add multi-functionality and specificity due to the filtration effects of MOFs or higher surface area for attaching sensing part that introduce more higher signal-to-noise ratio.

8.6. Nanoarchitectonics

Nanoarchitectonics involves designing, fabrication and assembling nanoscale structures in a controlled and purposeful manner to achieve special function and properties. Nanoarchitectonic structures enhance the sensitivity and selectivity of biosensors and chemical sensors. For MeHg detection, nanoarchitectonics helps create hybrid structures, such as combining metal nanoparticles with porous frameworks or functionalized surfaces. These tailored architectures enhance sensitivity, selectivity, and stability, providing effective platforms [70]. The complex and intricate design can be time-consuming and expensive, due to nanoscale interactions and self-assembly processes, requiring advanced techniques and resources. As discussed in Chapter 7, very few studies have been reported on the detection of mercury ions with high sensitivity using thymine interactions and ligands-striped monolayers. These sensors failed to distinguish between inorganic and organic mercury which limited its applicability and reduced selectivity of the sensors when exposed to mixtures of cations.

The large-scale production of nanoarchitectonic-based sensors with consistent quality remains challenging. This is mainly because small deviations in synthesis or assembly processes can lead to significant variations in performance. Simplified fabrication methods will scale up the production such as microwave assistant synthesis or templating to streamline the sensor production. One of the main disadvantages of nanoarchitectonics is the structural stability, which can enhanced by modifying using graphene derivatives, MOFs and polymer coating. Plasmonic signals of MOFs can be enhanced by integrating plasmonic nanostructures (e.g., gold or silver) to amplify localized electromagnetic fields, boosting optical detection sensitivity. Their porous structure supports high-density functionalisation with selective agents like aptamers or thiols, minimizing cross-reactivity. MOF pre-concentration of analytes and reduced interference improve signal clarity, while their scaffolding enables multi-step signal amplification for superior detection performance.

9. Conclusion

For efficient MeHg sensors, prioritise the development of advanced materials and biorecognition elements with high specificity for MeHg, such as novel nanomaterials and selective aptamers/antibodies. Optimize signal processing using advanced technologies to improve accuracy and interpret complex data effectively. Implement real-time calibration and adaptive systems to maintain sensor performance under varying environmental conditions. Focus on increasing sensitivity to detect lower concentrations of MeHg and reducing response times for rapid, reliable measurements. Ensure the sensor's usability, cost-effectiveness, and scalability, and validate its performance through extensive field testing and adherence to regulatory standards.

Currently, methods such as Atomic Absorption Spectroscopy (AAS), Atomic Fluorescence Spectroscopy (AFS), Inductively Coupled Plasma Mass Spectrometry (ICP-MS), and X-ray Fluorescence (XRF) Spectroscopy are widely used for mercury (Hg) detection across various matrices. However, these techniques often require extensive sample preparation, have lower sensitivity, perform poorly with liquid samples, are susceptible to matrix interferences, and are costly, requiring highly skilled operators. As a result, sensors for detecting MeHg represent a potential advancement in the field. Unfortunately, current detection methods often lack the necessary sensitivity and specificity, frequently failing to detect concentrations below environmentally relevant thresholds set by regulatory bodies (e.g., 0.1 ng/mL) or based on the effects of biomagnified MeHg, which necessitates lowering regulatory thresholds.

From a biological point of view, MeHg detection is particularly challenging: Even at extremely low concentrations, MeHg can cause biological amplification due to time-dependent or chronic exposure. This makes even current gold-standard laboratory methods not sensitive enough, as MeHg concentrations are often below the limit of detection (LOD). In contrast to the Hg^{2+} where biological responses tend to show concentration-dependent effects in living cells, the biological impact of MeHg is usually only evident in multicellular organisms at higher trophic levels, which is then separating the concentration levels in environmental matrices from the concentrations in organisms, for example ocean waters and fish, respectively, by more than five orders of magnitude.

Based on literature-gained knowledge and on our experiences, we have identified five key steps that should be specifically followed when developing an effective MeHg sensor.

1. Interdisciplinarity: Developing a sensor requires collaboration between analytical chemists, material scientists, physicists, and experts in biology (e.g., biochemists, molecular biologists). A bottom-up approach is needed, beginning with an understanding of interactions of the MeHg with the selected sensing component at the molecular level.
2. Matrix Consideration: The sensor development must begin by selecting the matrix (e.g. fish tissue, ocean water), as this determines the required sample pre-treatment, potential interferences (e.g. co-contaminants, extraction chemicals), expected concentration ranges, and physicochemical conditions such as ionic strength, pH, and temperature.
3. Relevance: Sensor relevance must be evaluated not just by concentration levels but also by the intended application –whether ecological (e.g. bioavailability), health-related, research-orientated, or commercial. The sensor's design should reflect its intended use.
4. Detection Modalities: The sensor should be able to measure concentration (quantitatively or semi-quantitatively), temporal changes, accumulation, or microspatial information (e.g. intracellular accumulation). The specific modality should align with the sensor's intended purpose.
5. Coupling Sensing Element with Transducer: The choice of transducer (electromagnetic, electrical, etc.) must be considered along with noise-to-signal ratio, signal range, and signal linearity. These factors impact signal amplification, filtration, correlation, and other signal-processing steps.

The recent surge in artificial intelligence (AI) has led to substantial advancement across various research domains. To date, most of the currently known MeHg sensing parts are designed based either on the known properties of selected sensing components or materials that preferentially interact with various Hg species, or by trial-and-error experiments. Currently, artificial intelligence tools offer new approaches in material design, discovery, and manufacturing, which can accelerate the development of sensors with improved sensitivity and especially increased selectivity towards MeHg [138]. Furthermore, based on our experiences working on WCBs and detecting very low levels of analytes [16], this process is often prone to a high noise-to-signal ratio. However, adopting machine learning approaches could help refine detection, possibly not for quantitative measurements, but more appropriately for qualitative information. This could be crucial for filtering out contaminated samples, ensuring reliable detection even in complex samples affected by matrix effects.

In conclusion, given the complexities discussed above, creating a universal sensor that functions across all matrices while providing relevant data would be extremely challenging. Therefore, work focused on matrix-specific sensors is necessary to achieve accurate and meaningful MeHg detection.

CRediT authorship contribution statement

A.F.P. Allwin Mabes Raj: Writing – review & editing, Writing – original draft, Methodology, Investigation, Formal analysis, Data curation, Conceptualization. **Raghuraj Singh Chouhan:** Writing – review &

editing, Methodology, Formal analysis, Conceptualization. **Aljoša Košak:** Methodology, Formal analysis. **Milena Horvat:** Writing – review & editing, Validation, Supervision, Resources, Project administration, Investigation, Funding acquisition. **Aleksandra Lobnik:** Writing – review & editing, Supervision, Project administration, Investigation, Funding acquisition. **Tomaž Rijavec:** Writing – review & editing, Visualization, Supervision, Resources, Project administration, Methodology, Investigation, Data curation. **Aleš Lapanje:** Writing – review & editing, Writing – original draft, Supervision, Project administration, Investigation, Funding acquisition, Data curation, Conceptualization.

Declaration of competing interest

We declare No conflict of interest.

Acknowledgements

The authors acknowledge financial support from the Ministry of Education, Science and Sport of Slovenia the ARIS funding through the programmes P1-0143, P2-0150 and ARIS project IsoCont J1-3033.

We also acknowledge European Comission Programmes: EUIA project Applause (UIA02-228), GMOS-Train Program European Union Horizon 2020 research and innovation programme under the Marie Sklodowska-Curie Grant No. 860497, EU-Horizon 2020: GREENER, Grant No.: 826312, European Commission SurfBio project, Grant No.: 952379 and BIOSYSMO Grant No.:101060211.

Data availability

Data will be made available on request.

References

[1] L. Chen, J. Li, L. Chen, Colorimetric detection of mercury species based on functionalized gold nanoparticles, ACS Appl. Mater. Interfaces 6 (2014) 15897–15904, https://doi.org/10.1021/am503531c.

[2] A.M. Scheuhammer, M.W. Meyer, M.B. Sandheinrich, M.W. Murray, Effects of environmental methylmercury on the health of wild birds, mammals, and fish, AMBIO A J. Hum. Environ. 36 (2007) 12–19, https://doi.org/10.1579/0044-7447(2007)36[12:EOEMOT]2.0.CO;2.

[3] L. Anchidin-Norocel, G. Gutt, E. Tătăranu, S. Amariei, Electrochemical sensors and biosensors: effective tools for detecting heavy metals in water and food with possible implications for children's health, Int. J. Electrochem. Sci. 19 (2024) 100643, https://doi.org/10.1016/j.ijoes.2024.100643.

[4] S. Mandal, A. Yadav, F.A. Panme, K.M. Devi, S.M.S. Kumar, Adaption of smart applications in agriculture to enhance production, Smart Agric. Technol. 7 (2024) 100431, https://doi.org/10.1016/j.atech.2024.100431.

[5] S.R. Segade, J.F. Tyson, Determination of methylmercury and inorganic mercury in water samples by slurry sampling cold vapor atomic absorption spectrometry in a flow injection system after preconcentration on silica C18 modified, Talanta 71 (2007) 1696–1702, https://doi.org/10.1016/j.talanta.2006.08.006.

[6] M. Leermakers, W. Baeyens, P. Quevauviller, M. Horvat, Mercury in environmental samples: speciation, artifacts and validation, TrAC, Trends Anal. Chem. 24 (2005) 383–393, https://doi.org/10.1016/j.trac.2004.01.001.

[7] K. Leopold, M. Foulkes, P.J. Worsfold, Preconcentration techniques for the determination of mercury species in natural waters, TrAC, Trends Anal. Chem. 28 (2009) 426–435, https://doi.org/10.1016/j.trac.2009.02.004.

[8] Y. Chen, Y. Guo, Y. Liu, Y. Xiang, G. Liu, Q. Zhang, et al., Advances in bacterial whole-cell biosensors for the detection of bioavailable mercury: a review, Sci. Total Environ. 868 (2023) 161709, https://doi.org/10.1016/j.scitotenv.2023.161709.

[9] L. Zhang, Y. Zhou, S. Han, The role of metal–organic frameworks in electronic sensors, Angew. Chem. 133 (2021) 15320–15340, https://doi.org/10.1002/ange.202006402.

[10] Y. Chen, Enzymatic conversion in MeHg sensing', Biosens. Bioelectron. 32 (1) (2019) n.d..

[11] A. Rantala, M. Utriainen, N. Kaushik, M. Virta, A.-L. Välimaa, M. Karp, Luminescent bacteria-based sensing method for methylmercury specific determination, Anal. Bioanal. Chem. 400 (2011) 1041–1049, https://doi.org/10.1007/s00216-011-4866-x.

[12] H.-J. Chang, A. Zúñiga, I. Conejero, P.L. Voyvodic, J. Gracy, E. Fajardo-Ruiz, et al., Programmable receptors enable bacterial biosensors to detect pathological biomarkers in clinical samples, Nat. Commun. 12 (2021) 5216, https://doi.org/10.1038/s41467-021-25538-y.

[13] T. Nagata, T. Muraoka, M. Kiyonoa, H. Pan-Hou, Development of a luminescence-based biosensor for detection of methylmercury, J. Toxicol. Sci. 35 (2010) 231–234, https://doi.org/10.2131/jts.35.231.

[14] A. Ivask, M. Virta, A. Kahru, Construction and use of specific luminescent recombinant bacterial sensors for the assessment of bioavailable fraction of cadmium, zinc, mercury and chromium in the soil, Soil Biol. Biochem. 34 (2002) 1439–1447, https://doi.org/10.1016/S0038-0717(02)00088-3.

[15] A. Roda, P. Pasini, M. Mirasoli, M. Guardigli, C. Russo, M. Musiani, et al., Sensitive determination of urinary mercury(II) BY a bioluminescent transgenic bacteria-based biosensor, Anal. Lett. 34 (2001) 29–41, https://doi.org/10.1081/AL-100002702.

[16] T. Rijavec, J. Zrimec, F. Oven, M.K. Viršek, M. Somrak, Z. Podlesek, et al., Development of highly sensitive, automatized and portable whole-cell Hg biosensor based on environmentally relevant microorganisms, Geomicrobiol. J. 34 (2017) 596–605, https://doi.org/10.1080/01490451.2016.1257661.

[17] Y. Colin, J. Gury, M. Monperrus, S. Gentes, P. Ayala Borda, M. Goni-Urriza, et al., Biosensor for screening bacterial mercury methylation: example within the Desulfobulbaceae, Res. Microbiol. 169 (2018) 44–51, https://doi.org/10.1016/j.resmic.2017.09.005.

[18] S. Cai, Y. Shen, Y. Zou, P. Sun, W. Wei, J. Zhao, et al., Engineering highly sensitive whole-cell mercury biosensors based on positive feedback loops from quorum-sensing systems, Analyst 143 (2018) 630–634, https://doi.org/10.1039/C7AN00587C.

[19] H. Hsu-Kim, K.H. Kucharzyk, T. Zhang, M.A. Deshusses, Mechanisms regulating mercury bioavailability for methylating microorganisms in the aquatic environment: a critical review, Environ. Sci. Technol. 47 (2013) 2441–2456, https://doi.org/10.1021/es304370g.

[20] A. Sophie Chiasson-Gould, J.M. Blais, A.J. Poulain, Dissolved organic matter kinetically controls mercury bioavailability to bacteria, Environ. Sci. Technol. 48 (2014) 3153–3161, https://doi.org/10.1021/es4038484.

[21] U. Ndu, R.P. Mason, H. Zhang, S. Lin, P.T. Visscher, Effect of inorganic and organic ligands on the bioavailability of methylmercury as determined by using a *mer-lux* bioreporter, Appl. Environ. Microbiol. 78 (2012) 7276–7282, https://doi.org/10.1128/AEM.00362-12.

[22] Hegde K. Saini, S.K. Brar, M. Verma, Advances in whole cell-based biosensors in environmental monitoring. Tools, Techniques and Protocols for Monitoring Environmental Contaminants, Elsevier, 2019, pp. 263–284, https://doi.org/10.1016/B978-0-12-814679-8.00013-3.

[23] Q. Gui, T. Lawson, S. Shan, L. Yan, Y. Liu, The application of whole cell-based biosensors for use in environmental analysis and in medical diagnostics, Sensors 17 (2017) 1623, https://doi.org/10.3390/s17071623.

[24] X. Liu, K.J. Germaine, D. Ryan, D.N. Dowling, Whole-cell fluorescent biosensors for bioavailability and biodegradation of polychlorinated biphenyls, Sensors 10 (2010) 1377–1398, https://doi.org/10.3390/s100201377.

[25] S.V. Bazhenov, U.S. Novoyatlova, E.S. Scheglova, E.V. Prazdnova, M.S. Mazanko, A.G. Kessenikh, et al., Bacterial lux-biosensors: constructing, applications, and prospects, Biosens. Bioelectron. X 13 (2023) 100323, https://doi.org/10.1016/j.biosx.2023.100323.

[26] G. Wang, Q. Wang, Q. Qi, Q. Wang, Dynamic plasmid copy number control for synthetic biology, Trends Biotechnol. (2023) S016777992300238X, https://doi.org/10.1016/j.tibtech.2023.08.004.

[27] A. Raj, A. Van Oudenaarden, Nature, nurture, or chance: stochastic gene expression and its consequences, Cell 135 (2008) 216–226, https://doi.org/10.1016/j.cell.2008.09.050.

[28] A. Raj, C.S. Peskin, D. Tranchina, D.Y. Vargas, S. Tyagi, Stochastic mRNA synthesis in mammalian cells, PLoS Biol. 4 (2006) e309, https://doi.org/10.1371/journal.pbio.0040309.

[29] S.-W. Jeong, Y.J. Choi, Extremophilic microorganisms for the treatment of toxic pollutants in the environment, Molecules 25 (2020) 4916, https://doi.org/10.3390/molecules25214916.

[30] X. You, N. Xu, X. Yang, W. Sun, Pollutants affect algae-bacteria interactions: a critical review, Environ. Pollut. 276 (2021) 116723, https://doi.org/10.1016/j.envpol.2021.116723.

[31] L. Qiu, T. Zhang, J. Jiang, C. Wu, G. Zhu, M. You, et al., Cell membrane-anchored biosensors for real-time monitoring of the cellular microenvironment, J. Am. Chem. Soc. 136 (2014) 13090–13093, https://doi.org/10.1021/ja5047389.

[32] J.C. GutiÃ©rrez, F. Amaro, A. MartÃ-n-GonzÃ¡lez, Heavy metal whole-cell biosensors using eukaryotic microorganisms: an updated critical review, Front. Microbiol. 6 (2015), https://doi.org/10.3389/fmicb.2015.00048.

[33] H. Chang, P.L. Voyvodic, A. Zúñiga, J. Bonnet, Microbially derived biosensors for diagnosis, monitoring and epidemiology, Microb. Biotechnol. 10 (2017) 1031–1035, https://doi.org/10.1111/1751-7915.12791.

[34] A. Ivask, T. Rõlova, A. Kahru, A suite of recombinant luminescent bacterial strains for the quantification of bioavailable heavy metals and toxicity testing, BMC Biotechnol. 9 (2009) 41, https://doi.org/10.1186/1472-6750-9-41.

[35] S. Zou, G. Cui, L. Liu, S. Song, H. Kuang, Development of ic-ELISA and an immunochromatographic strip assay for the detection of methylmercury, Food Agric. Immunol. 28 (2017) 699–710, https://doi.org/10.1080/09540105.2017.1309643.

[36] G. Sun, L. Sun, H. Xie, J. Liu, Electrospinning of nanofibers for energy applications, Nanomaterials 6 (2016) 129, https://doi.org/10.3390/nano6070129.

[37] Z. Chen, X. Wang, X. Cheng, W. Yang, Y. Wu, F. Fu, Specifically and visually detect methyl-mercury and ethyl-mercury in fish sample based on DNA-templated alloy Ag–Au nanoparticles, Anal. Chem. 90 (2018) 5489–5495, https://doi.org/10.1021/acs.analchem.8b01100.

[38] M.L. Aulsebrook, E. Watkins, M.R. Grace, B. Graham, K.L. Tuck, Modified gold nanoparticles for the temperature-dependent colorimetric detection of mercury and methylmercury, ChemistrySelect 3 (2018) 2088–2091, https://doi.org/10.1002/slct.201702572.

[39] L. Deng, Y. Li, X. Yan, J. Xiao, C. Ma, J. Zheng, et al., Ultrasensitive and highly selective detection of bioaccumulation of methyl-mercury in fish samples via Ag ^{0}/Hg ^{0} amalgamation, Anal. Chem. 87 (2015) 2452–2458, https://doi.org/10.1021/ac504538v.

[40] Y.-H. Lin, W.-L. Tseng, Ultrasensitive sensing of Hg(2+) and CH(3)Hg(+) based on the fluorescence quenching of lysozyme type VI-stabilized gold nanoclusters, Anal. Chem. 82 (2010) 9194–9200, https://doi.org/10.1021/ac101427y.

[41] M. Pandeeswar, S.P. Senanayak, T. Govindaraju, Nanoarchitectonics of small molecule and DNA for ultrasensitive detection of mercury, ACS Appl. Mater. Interfaces 8 (2016) 30362–30371, https://doi.org/10.1021/acsami.6b10527.

[42] L. Guo, X. Wu, L. Liu, H. Kuang, C. Xu, Gold nanoparticle-based paper sensor for simultaneous detection of 11 benzimidazoles by one monoclonal antibody, Small 14 (2018) 1701782, https://doi.org/10.1002/smll.201701782.

[43] G.A. Posthuma-Trumpie, J. Korf, A. Van Amerongen, Lateral flow (immuno)assay: its strengths, weaknesses, opportunities and threats. A literature survey, Anal. Bioanal. Chem. 393 (2009) 569–582, https://doi.org/10.1007/s00216-008-2287-2.

[44] H. Liu, F. Zhan, F. Liu, M. Zhu, X. Zhou, D. Xing, Visual and sensitive detection of viable pathogenic bacteria by sensing of RNA markers in gold nanoparticles based paper platform, Biosens. Bioelectron. 62 (2014) 38–46, https://doi.org/10.1016/j.bios.2014.06.020.

[45] X. Cui, Y. Huang, J. Wang, L. Zhang, Y. Rong, W. Lai, et al., A remarkable sensitivity enhancement in a gold nanoparticle-based lateral flow immunoassay for the detection of Escherichia coli O157:H7, RSC Adv. 5 (2015) 45092–45097, https://doi.org/10.1039/C5RA06237C.

[46] L. Zhang, Y. Huang, J. Wang, Y. Rong, W. Lai, J. Zhang, et al., Hierarchical flowerlike gold nanoparticles labeled immunochromatography test strip for highly sensitive detection of *Escherichia coli* O157:H7, Langmuir 31 (2015) 5537–5544, https://doi.org/10.1021/acs.langmuir.5b00592.

[47] C. Ge, L. Yu, Z. Fang, L. Zeng, An enhanced strip biosensor for rapid and sensitive detection of histone methylation, Anal. Chem. 85 (2013) 9343–9349, https://doi.org/10.1021/ac402202x.

[48] M. Haase, H. Schäfer, Upconverting nanoparticles, Angew. Chem. Int. Ed. 50 (2011) 5808–5829, https://doi.org/10.1002/anie.201005159.

[49] F. Auzel, Upconversion and anti-Stokes processes with f and d ions in solids, Chem. Rev. 104 (2004) 139–174, https://doi.org/10.1021/cr020357g.

[50] A.P. De Silva, H.Q.N. Gunaratne, T. Gunnlaugsson, A.J.M. Huxley, C.P. McCoy, J. T. Rademacher, et al., Signaling recognition events with fluorescent sensors and switches, Chem. Rev. 97 (1997) 1515–1566, https://doi.org/10.1021/cr960386p.

[51] J.S. Kim, D.T. Quang, Calixarene-derived fluorescent probes, Chem. Rev. 107 (2007) 3780–3799, https://doi.org/10.1021/cr068046j.

[52] D. Wu, A.C. Sedgwick, T. Gunnlaugsson, E.U. Akkaya, J. Yoon, T.D. James, Fluorescent chemosensors: the past, present and future, Chem. Soc. Rev. 46 (2017) 7105–7123, https://doi.org/10.1039/C7CS00240H.

[53] J. Chan, S.C. Dodani, C.J. Chang, Reaction-based small-molecule fluorescent probes for chemoselective bioimaging, Nat. Chem. 4 (2012) 973–984, https://doi.org/10.1038/nchem.1500.

[54] H.-W. Liu, L. Chen, C. Xu, Z. Li, H. Zhang, X.-B. Zhang, et al., Recent progresses in small-molecule enzymatic fluorescent probes for cancer imaging, Chem. Soc. Rev. 47 (2018) 7140–7180, https://doi.org/10.1039/C7CS00862G.

[55] Y. Fu, N.S. Finney, Small-molecule fluorescent probes and their design, RSC Adv. 8 (2018) 29051–29061, https://doi.org/10.1039/C8RA02297F.

[56] H. Kobayashi, M. Ogawa, R. Alford, P.L. Choyke, Y. Urano, New strategies for fluorescent probe design in medical diagnostic imaging, Chem. Rev. 110 (2010) 2620–2640, https://doi.org/10.1021/cr900263j.

[57] L. Wu, C. Huang, B.P. Emery, A.C. Sedgwick, S.D. Bull, X.-P. He, et al., Förster resonance energy transfer (FRET)-based small-molecule sensors and imaging agents, Chem. Soc. Rev. 49 (2020) 5110–5139, https://doi.org/10.1039/C9CS00318E.

[58] X. Tian, L.C. Murfin, L. Wu, S.E. Lewis, T.D. James, Fluorescent small organic probes for biosensing, Chem. Sci. 12 (2021) 3406–3426, https://doi.org/10.1039/D0SC06928K.

[59] W. Shu, L. Yan, J. Liu, Z. Wang, S. Zhang, C. Tang, et al., Highly selective fluorescent probe for the sensitive detection of inorganic and organic mercury species assisted by H_2O_2, Ind. Eng. Chem. Res. 54 (2015) 8056–8062, https://doi.org/10.1021/acs.iecr.5b02153.

[60] A. Chatterjee, M. Banerjee, D.G. Khandare, R.U. Gawas, S.C. Mascarenhas, A. Ganguly, et al., Aggregation-induced emission-based chemodosimeter approach for selective sensing and imaging of Hg(II) and methylmercury species, Anal. Chem. 89 (2017) 12698–12704, https://doi.org/10.1021/acs.analchem.7b02663.

[61] L.N. Neupane, J. Park, P.K. Mehta, E.-T. Oh, H.J. Park, K.-H. Lee, Fast and sensitive fluorescent detection of inorganic mercury species and methylmercury using a fluorescent probe based on the displacement reaction of arylboronic acid with the mercury species, Chem. Commun. 56 (2020) 2941–2944, https://doi.org/10.1039/C9CC09240D.

[62] S. Oh, J. Jeon, J. Jeong, J. Park, E.-T. Oh, H.J. Park, et al., Fluorescent detection of methyl mercury in aqueous solution and live cells using fluorescent probe and micelle systems, Anal. Chem. 92 (2020) 4917–4925, https://doi.org/10.1021/acs.analchem.9b05025.

[63] Y.-K. Yang, S.-K. Ko, I. Shin, J. Tae, Fluorescent detection of methylmercury by desulfurization reaction of rhodamine hydrazide derivatives, Org. Biomol. Chem. 7 (2009) 4590, https://doi.org/10.1039/b915723a.

[64] B. Yuan, D.-X. Wang, L.-N. Zhu, Y.-L. Lan, M. Cheng, L.-M. Zhang, et al., Dinuclear Hg ^{II} tetracarbene complex-triggered aggregation-induced emission for rapid and selective sensing of Hg $^{2+}$ and organomercury species, Chem. Sci. 10 (2019) 4220–4226, https://doi.org/10.1039/C8SC05714A.

[65] F. Xu, L. Kou, J. Jia, X. Hou, Z. Long, S. Wang, Metal–organic frameworks of zeolitic imidazolate framework-7 and zeolitic imidazolate framework-60 for fast mercury and methylmercury speciation analysis, Anal. Chim. Acta 804 (2013) 240–245, https://doi.org/10.1016/j.aca.2013.09.058.

[66] J. Jia, F. Xu, Z. Long, X. Hou, M.J. Sepaniak, Metal–organic framework MIL-53 (Fe) for highly selective and ultrasensitive direct sensing of MeHg+, Chem. Commun. 49 (2013) 4670, https://doi.org/10.1039/c3cc40821c.

[67] X. Li, Y. Zhang, Y. Chang, B. Xue, X. Kong, W. Chen, Catalysis-reduction strategy for sensing inorganic and organic mercury based on gold nanoparticles, Biosens. Bioelectron. 92 (2017) 328–334, https://doi.org/10.1016/j.bios.2016.10.097.

[68] I. Costas-Mora, V. Romero, I. Lavilla, C. Bendicho, In situ building of a nanoprobe based on fluorescent carbon dots for methylmercury detection, Anal. Chem. 86 (2014) 4536–4543, https://doi.org/10.1021/ac500517h.

[69] S. Dey, A. Kumar, A. Mahto, I.H. Raval, K.M. Modi, S. Haldar, et al., Oxacalix[4] arene templated silver nanoparticles as dual readout sensor: developing portable kit for rapid detection of methylmercury and its speciation, Sensor. Actuator. B Chem. 317 (2020) 128180, https://doi.org/10.1016/j.snb.2020.128180.

[70] E.S. Cho, J. Kim, B. Tejerina, T.M. Hermans, H. Jiang, H. Nakanishi, et al., Ultrasensitive detection of toxic cations through changes in the tunnelling current across films of striped nanoparticles, Nat. Mater. 11 (2012) 978–985, https://doi.org/10.1038/nmat3406.

[71] Q. Zou, H. Tian, Chemodosimeters for mercury(II) and methylmercury(I) based on 2,1,3-benzothiadiazole, Sensor. Actuator. B Chem. 149 (2010) 20–27, https://doi.org/10.1016/j.snb.2010.06.040.

[72] Y. Yang, Z. Yao, W. Li, K. Chen, L. Liu, H.-C. Wu, Selective detection of mercury (II) and methylmercury(II) via coordination-induced emission of a small-molecule probe, Sci. China Chem. 59 (2016) 1651–1657, https://doi.org/10.1007/s11426-016-0137-y.

[73] S.R. Batten, D.R. Turner, S.M. Neville, Coordination Polymers: Design, Analysis and Application, RSC Pub, Cambridge, 2009.

[74] B.E.G. Lucier, S. Chen, Y. Huang, Characterization of metal–organic frameworks: unlocking the potential of solid-state NMR, Acc. Chem. Res. 51 (2018) 319–330, https://doi.org/10.1021/acs.accounts.7b00357.

[75] A.J. Howarth, A.W. Peters, N.A. Vermeulen, T.C. Wang, J.T. Hupp, O.K. Farha, Best practices for the synthesis, activation, and characterization of metal–organic frameworks, Chem. Mater. 29 (2017) 26–39, https://doi.org/10.1021/acs.chemmater.6b02626.

[76] H. Yuan, W. Ji, S. Chu, S. Qian, F. Wang, J.-F. Masson, et al., Fiber-optic surface plasmon resonance glucose sensor enhanced with phenylboronic acid modified Au nanoparticles, Biosens. Bioelectron. 117 (2018) 637–643, https://doi.org/10.1016/j.bios.2018.06.042.

[77] M. Li, M. Dincă, Reductive electrosynthesis of crystalline metal–organic frameworks, J. Am. Chem. Soc. 133 (2011) 12926–12929, https://doi.org/10.1021/ja2041546.

[78] S. Carrasco, Metal-organic frameworks for the development of biosensors: a current overview, Biosensors 8 (2018) 92, https://doi.org/10.3390/bios8040092.

[79] L. Jiao, Y. Wang, H. Jiang, Q. Xu, Metal–organic frameworks as platforms for catalytic applications, Adv. Mater. 30 (2018) 1703663, https://doi.org/10.1002/adma.201703663.

[80] X. Zhao, Y. Wang, D. Li, X. Bu, P. Feng, Metal–organic frameworks for separation, Adv. Mater. 30 (2018) 1705189, https://doi.org/10.1002/adma.201705189.

[81] J.V. Alegre-Requena, E. Marqués-López, R.P. Herrera, D.D. Díaz, Metal–organic frameworks (MOFs) bring new life to hydrogen-bonding organocatalysts in confined spaces, CrystEngComm 18 (2016) 3985–3995, https://doi.org/10.1039/C5CE02526E.

[82] A. Karmakar, P. Samanta, A.V. Desai, S.K. Ghosh, Guest-responsive metal–organic frameworks as scaffolds for separation and sensing applications, Acc. Chem. Res. 50 (2017) 2457–2469, https://doi.org/10.1021/acs.accounts.7b00151.

[83] W.-T. Koo, S. Qiao, A.F. Ogata, G. Jha, J.-S. Jang, V.T. Chen, et al., Accelerating palladium nanowire H_2 sensors using engineered nanofiltration, ACS Nano 11 (2017) 9276–9285, https://doi.org/10.1021/acsnano.7b04529.

[84] I. Stassen, N. Burtch, A. Talin, P. Falcaro, M. Allendorf, R. Ameloot, An updated roadmap for the integration of metal–organic frameworks with electronic devices and chemical sensors, Chem. Soc. Rev. 46 (2017) 3185–3241, https://doi.org/10.1039/C7CS00122C.

[85] K. Uemura, R. Matsuda, S. Kitagawa, Flexible microporous coordination polymers, J. Solid State Chem. 178 (2005) 2420–2429, https://doi.org/10.1016/j.jssc.2005.05.036.

[86] S. Kitagawa, R. Kitaura, S. Noro, Functional porous coordination polymers, Angew. Chem. Int. Ed. 43 (2004) 2334–2375, https://doi.org/10.1002/anie.200300610.

[87] Z. Huang, H.-B. Song, M. Du, S.-T. Chen, X.-H. Bu, J. Ribas, Coordination polymers assembled from angular dipyridyl ligands and Cu ^{II}, Cd ^{II}, Co ^{II} salts: crystal structures and properties, Inorg. Chem. 43 (2004) 931–944, https://doi.org/10.1021/ic034999d.

[88] E.S. Cho, J. Kim, B. Tejerina, T.M. Hermans, H. Jiang, H. Nakanishi, et al., Ultrasensitive detection of toxic cations through changes in the tunnelling current

across films of striped nanoparticles, Nat. Mater. 11 (2012) 978–985, https://doi.org/10.1038/nmat3406.
[89] Z.-J. Xie, X.-Y. Bao, C.-F. Peng, Highly sensitive and selective colorimetric detection of methylmercury based on DNA functionalized gold nanoparticles, Sensors 18 (2018) 2679, https://doi.org/10.3390/s18082679.
[90] J. Liu, R. Li, B. Yang, Carbon dots: a new type of carbon-based nanomaterial with wide applications, ACS Cent. Sci. 6 (2020) 2179–2195, https://doi.org/10.1021/acscentsci.0c01306.
[91] H. Kumar, K. Kuča, S.K. Bhatia, K. Saini, A. Kaushal, R. Verma, et al., Applications of nanotechnology in sensor-based detection of foodborne pathogens, Sensors 20 (2020) 1966, https://doi.org/10.3390/s20071966.
[92] X. Wang, Y. Qiao, J. Zhang, Y. Song, Q. Han, A SYBR Green I-based aptasensor for the label-free, fluorometric, and anti-interference detection of MeHg+, Anal. Bioanal. Chem. 416 (2024) 299–311, https://doi.org/10.1007/s00216-023-05018-6.
[93] Q. Ran, H. Feng, G. Chang, M. Luo, S. Xu, Thymine-mediated electrochemical aptasensor for sensitive and simultaneous detection of Hg2+ and CH3Hg+ in fish samples, Electrochim. Acta 461 (2023) 142406, https://doi.org/10.1016/j.electacta.2023.142406.
[94] K. Ariga, Q. Ji, J.P. Hill, Y. Bando, M. Aono, Forming nanomaterials as layered functional structures toward materials nanoarchitectonics, NPG Asia Mater. 4 (2012) e17, https://doi.org/10.1038/am.2012.30, e17.
[95] K. Ariga, J. Li, J. Fei, Q. Ji, J.P. Hill, Nanoarchitectonics for dynamic functional materials from atomic-/molecular-level manipulation to macroscopic action, Adv. Mater. 28 (2016) 1251–1286, https://doi.org/10.1002/adma.201502545.
[96] S. Hecht, Welding, organizing, and planting organic molecules on substrate surfaces—promising approaches towards nanoarchitectonics from the bottom up, Angew. Chem. Int. Ed. 42 (2003) 24–26, https://doi.org/10.1002/anie.200390045.
[97] A. Masakazu, Nanoarchitectonics-A New Materials Paradigm, 2000.
[98] K. Ariga, M. Li, GaryJ. Richards, Hill JonathanP. Nanoarchitectonics, A conceptual paradigm for design and synthesis of dimension-controlled functional nanomaterials, J. Nanosci. Nanotechnol. 11 (2011) 1–13, https://doi.org/10.1166/jnn.2011.3839.
[99] K. Ariga, Q. Ji, W. Nakanishi, J.P. Hill, M. Aono, Nanoarchitectonics: a new materials horizon for nanotechnology, Mater. Horiz. 2 (2015) 406–413, https://doi.org/10.1039/C5MH00012B.
[100] M. Aono, K. Ariga, The way to nanoarchitectonics and the way of nanoarchitectonics, Adv. Mater. 28 (2016) 989–992, https://doi.org/10.1002/adma.201502868.
[101] K. Ariga, K. Minami, M. Ebara, J. Nakanishi, What are the emerging concepts and challenges in NANO? Nanoarchitectonics, hand-operating nanotechnology and mechanobiology, Polym. J. 48 (2016) 371–389, https://doi.org/10.1038/pj.2016.8.
[102] M. Ramanathan, L.K. Shrestha, T. Mori, Q. Ji, J.P. Hill, K. Ariga, Amphiphile nanoarchitectonics: from basic physical chemistry to advanced applications, Phys. Chem. Chem. Phys. 15 (2013) 10580, https://doi.org/10.1039/c3cp50620g.
[103] K. Ariga, Q. Ji, T. Mori, M. Naito, Y. Yamauchi, H. Abe, et al., Enzyme nanoarchitectonics: organization and device application, Chem. Soc. Rev. 42 (2013) 6322, https://doi.org/10.1039/c2cs35475f.
[104] M. Osada, T. Sasaki, Nanoarchitectonics in dielectric/ferroelectric layered perovskites: from bulk 3D systems to 2D nanosheets, Dalton Trans. 47 (2018) 2841–2851, https://doi.org/10.1039/C7DT03719H.
[105] A. Nayak, S. Unayama, S. Tai, T. Tsuruoka, R. Waser, M. Aono, et al., Nanoarchitectonics for controlling the number of dopant atoms in solid electrolyte nanodots, Adv. Mater. 30 (2018) 1703261, https://doi.org/10.1002/adma.201703261.
[106] H. Abe, J. Liu, K. Ariga, Catalytic nanoarchitectonics for environmentally compatible energy generation, Mater. Today 19 (2016) 12–18, https://doi.org/10.1016/j.mattod.2015.08.021.
[107] Liu K. Zou, M. Abbas, X. Yan, Peptide-modulated self-assembly of chromophores toward biomimetic light-harvesting nanoarchitectonics, Adv. Mater. 28 (2016) 1031–1043, https://doi.org/10.1002/adma.201502454.
[108] W. Nakanishi, K. Minami, L.K. Shrestha, Q. Ji, J.P. Hill, K. Ariga, Bioactive nanocarbon assemblies: nanoarchitectonics and applications, Nano Today 9 (2014) 378–394, https://doi.org/10.1016/j.nantod.2014.05.002.
[109] E. Stulz, Nanoarchitectonics with porphyrin functionalized DNA, Acc. Chem. Res. 50 (2017) 823–831, https://doi.org/10.1021/acs.accounts.6b00583.
[110] S. Ishihara, J. Labuta, W. Van Rossom, D. Ishikawa, K. Minami, J.P. Hill, et al., Porphyrin-based sensor nanoarchitectonics in diverse physical detection modes, Phys. Chem. Chem. Phys. 16 (2014) 9713, https://doi.org/10.1039/c3cp55431g.
[111] K. Ariga, T. Makita, M. Ito, T. Mori, S. Watanabe, J. Takeya, Review of advanced sensor devices employing nanoarchitectonics concepts, Beilstein J. Nanotechnol. 10 (2019) 2014–2030, https://doi.org/10.3762/bjnano.10.198.
[112] T. Petänen, M. Lyytikäinen, J. Lappalainen, M. Romantschuk, J.V.K. Kukkonen, Assessing sediment toxicity and arsenite concentration with bacterial and traditional methods, Environ. Pollut. 122 (2003) 407–415, https://doi.org/10.1016/S0269-7491(02)00307-X.
[113] W.R. Zipfel, R.M. Williams, W.W. Webb, Nonlinear magic: multiphoton microscopy in the biosciences, Nat. Biotechnol. 21 (2003) 1369–1377, https://doi.org/10.1038/nbt899.
[114] W. Denk, J.H. Strickler, W.W. Webb, Two-photon laser scanning fluorescence microscopy, Science 248 (1990) 73–76, https://doi.org/10.1126/science.2321027.
[115] M. Pawlicki, H.A. Collins, R.G. Denning, H.L. Anderson, Two-photon absorption and the design of two-photon dyes, Angew. Chem. Int. Ed. 48 (2009) 3244–3266, https://doi.org/10.1002/anie.200805257.
[116] L.E. Kreno, K. Leong, O.K. Farha, M. Allendorf, R.P. Van Duyne, J.T. Hupp, Metal–organic framework materials as chemical sensors, Chem. Rev. 112 (2012) 1105–1125, https://doi.org/10.1021/cr200324t.
[117] K. Koh, A.G. Wong-Foy, A.J. Matzger, MOF@MOF: microporous core–shell architectures, Chem. Commun. 6162 (2009), https://doi.org/10.1039/b904526k.
[118] Y. Yoo, H.-K. Jeong, Heteroepitaxial growth of isoreticular Metal–Organic frameworks and their hybrid films, Cryst. Growth Des. 10 (2010) 1283–1288, https://doi.org/10.1021/cg9013027.
[119] K.S. Park, Z. Ni, A.P. Côté, J.Y. Choi, R. Huang, F.J. Uribe-Romo, et al., Exceptional chemical and thermal stability of zeolitic imidazolate frameworks, Proc. Natl. Acad. Sci. U.S.A. 103 (2006) 10186–10191, https://doi.org/10.1073/pnas.0602439103.
[120] M.J. Ingleson, J. Perez Barrio, J.-B. Guilbaud, Y.Z. Khimyak, M.J. Rosseinsky, Framework functionalisation triggers metal complex binding, Chem. Commun. 2680 (2008), https://doi.org/10.1039/b718367d.
[121] R.K. Deshpande, J.L. Minnaar, S.G. Telfer, Thermolabile groups in metal–organic frameworks: suppression of network interpenetration, post-synthetic cavity expansion, and protection of reactive functional groups, Angew. Chem. Int. Ed. 49 (2010) 4598–4602, https://doi.org/10.1002/anie.200905960.
[122] W.-J. Li, J. Liu, Z.-H. Sun, T.-F. Liu, J. Lü, S.-Y. Gao, et al., Integration of metal-organic frameworks into an electrochemical dielectric thin film for electronic applications, Nat. Commun. 7 (2016) 11830, https://doi.org/10.1038/ncomms11830.
[123] S. Khan, W.C. Cho, A. Sepahvand, S. Haji Hosseinali, A. Hussain, M.M. Nejadi Babadaei, et al., Electrochemical aptasensor based on the engineered core-shell MOF nanostructures for the detection of tumor antigens, J. Nanobiotechnol. 21 (2023) 136, https://doi.org/10.1186/s12951-023-01884-5.
[124] J. Han, D. Zhang, G. Cheng, L. Guo, J. Ren, Object detection in optical remote sensing images based on weakly supervised learning and high-level feature learning, IEEE Trans. Geosci. Rem. Sens. 53 (2015) 3325–3337, https://doi.org/10.1109/TGRS.2014.2374218.
[125] E. Sapountzi, M. Braiek, J.-F. Chateaux, N. Jaffrezic-Renault, F. Lagarde, Recent advances in electrospun nanofiber interfaces for biosensing devices, Sensors 17 (2017) 1887, https://doi.org/10.3390/s17081887.
[126] S. Vigneshvar, C.C. Sudhakumari, B. Senthilkumaran, H. Prakash, Recent advances in biosensor technology for potential applications – an overview, Front. Bioeng. Biotechnol. 4 (2016), https://doi.org/10.3389/fbioe.2016.00011.
[127] P. Mulvaney, Surface plasmon spectroscopy of nanosized metal particles, Langmuir 12 (1996) 788–800, https://doi.org/10.1021/la9502711.
[128] A. Yu, Z. Liang, J. Cho, F. Caruso, Nanostructured electrochemical sensor based on dense gold nanoparticle films, Nano Lett. 3 (2003) 1203–1207, https://doi.org/10.1021/nl034363j.
[129] Y. Xiao, F. Patolsky, E. Katz, J.F. Hainfeld, I. Willner, "Plugging into enzymes": nanowiring of redox enzymes by a gold nanoparticle, Science 299 (2003) 1877–1881, https://doi.org/10.1126/science.1080664.
[130] R. Freeman, J. Girsh, I. Willner, Nucleic acid/quantum dots (QDs) hybrid systems for optical and photoelectrochemical sensing, ACS Appl. Mater. Interfaces 5 (2013) 2815–2834, https://doi.org/10.1021/am303189h.
[131] A. Luzio, E. Canesi, C. Bertarelli, M. Caironi, Electrospun polymer fibers for electronic applications, Materials 7 (2014) 906–947, https://doi.org/10.3390/ma7020906.
[132] J. Quirós, K. Boltes, R. Rosal, Bioactive applications for electrospun fibers, Polym. Rev. 56 (2016) 631–667, https://doi.org/10.1080/15583724.2015.1136641.
[133] N. Amaly, Y. Si, Y. Chen, A.Y. El-Moghazy, C. Zhao, R. Zhang, et al., Reusable anionic sulfonate functionalized nanofibrous membranes for cellulase enzyme adsorption and separation, Colloids Surf. B Biointerfaces 170 (2018) 588–595, https://doi.org/10.1016/j.colsurfb.2018.06.019.
[134] A.Y. El-Moghazy, E.A. Soliman, H.Z. Ibrahim, J.-L. Marty, G. Istamboulie, T. Noguer, Biosensor based on electrospun blended chitosan-poly (vinyl alcohol) nanofibrous enzymatically sensitized membranes for pirimiphos-methyl detection in olive oil, Talanta 155 (2016) 258–264, https://doi.org/10.1016/j.talanta.2016.04.018.
[135] H. Rahnama, A. Sattarzadeh, F. Kazemi, N. Ahmadi, F. Sanjarian, Z. Zand, Comparative study of three magnetic nano-particles (FeSO4, FeSO4/SiO2, FeSO4/SiO2/TiO2) in plasmid DNA extraction, Anal. Biochem. 513 (2016) 68–76, https://doi.org/10.1016/j.ab.2016.08.029.
[136] K. Li, Y. Lai, W. Zhang, L. Jin, Fe2O3@Au core/shell nanoparticle-based electrochemical DNA biosensor for Escherichia coli detection, Talanta 84 (2011) 607–613, https://doi.org/10.1016/j.talanta.2010.12.042.
[137] A. Le Goff, M. Holzinger, S. Cosnier, Enzymatic biosensors based on SWCNT-conducting polymer electrodes, Analyst 136 (2011) 1279, https://doi.org/10.1039/c0an00904k.
[138] I. Papadimitriou, I. Gialampoukidis, S. Vrochidis, I. Kompatsiaris, AI methods in materials design, discovery and manufacturing: a review, Comput. Mater. Sci. 235 (2024) 112793, https://doi.org/10.1016/j.commatsci.2024.112793.

3.5 Patent Application

3.5.1 Innovative Nanobiosensor for MeHg detection

Introduction Mercury exists in various chemical forms including Elemental Mercury (Hg^0), Mercuric Ion (Hg^{2+}), Methylmercury (MeHg), Dimethylmercury (CH_3HgCH_3), Mercury Sulfide (HgS) and Ethylmercury ($C_2H_5Hg^+$). Among these, MeHg is the most toxic, posing a significant risk to both the environment and human health, even at concentrations as low as nanomolar (nM) levels. This concentration threshold is remarkably minuscule, diverging by two orders of magnitude from any other mercury species. Despite its minute presence, MeHg has the tendency for biomagnification within the food chain, thereby accumulating in organisms and resulting in neurological disorders, exemplified by Minamata disease (L. Chen et al., 2014). Wild piscivorous fish, mammals, and birds, animals at the highest trophic level, are at risk for elevated dietary methylmercury intake and toxicity due to biomagnification through the food chain. Its neurotoxic effects are especially harmful to developing fetuses and young children, making precise quantification in food samples critical for public health. Monitoring MeHg levels in fish is essential for assessing exposure risks and ensuring food safety standards. Regulatory agencies rely on accurate MeHg detection to guide consumption advisories and protect vulnerable populations. Consequently, the demand for meticulous, sensitive methodologies to detect MeHg with precision has surged, especially in the context of evaluating water pollution dynamics. Biosensors for detecting methylmercury (MeHg) in food samples offer several advantages, including rapid detection and high sensitivity, making them effective at trace-level detection. These devices enable real-time monitoring, providing immediate feedback on MeHg levels, essential for ensuring food safety in vulnerable populations like pregnant women and fetuses. Their cost-effectiveness and potential for on-site application, especially in industries such as aquaculture and agriculture, make them suitable for widespread use. Additionally, integration with smartphone technology allows for automation and ease of use, improving overall food safety protocols (Anchidin-Norocel et al., 2024; Mandal et al., 2024; Scheuhammer et al., 2007).

3.5.2 Specific biomolecules for MMHg sensing identified

3.5.2.1 Summary

Mercury-resistant bacterial strains had developed a sophisticated dual-enzyme system, known as the MerB-MerA complex, which enabled them to efficiently convert both ionic and organic forms of mercury, primarily methylmercury (MeHg), into a less hazardous form—volatile elemental mercury (Hg^0). This transformation process, essential for detoxifying mercury, was highly effective and allowed the bacteria to handle mercury contamination in their environment.

The first enzyme in this system, organomercurial lyase MerB, facilitated the protonolysis of the carbon- mercury (C-Hg) bond, a critical reaction in the detoxification pathway. This step resulted in the formation of a reduced carbon compound and the release of inorganic Hg^{2+} ions. The protonolysis catalyzed by MerB broke the bond between mercury and the organic group, making it more accessible for further processing. This process effectively reduced the toxicity of the organic mercury species by converting it into a less harmful inorganic form, Hg^{2+}.

After MerB cleaved the carbon-mercury bond and produced the mercury intermediate, the second enzyme in the system, mercuric ion reductase MerA, took over to reduce Hg^{2+}

into its elemental, volatile form, Hg^0. This reduction process minimized the toxicity of mercury by converting it into a volatile compound that could then be volatilized and removed from the bacterial cell, thus preventing damage to the bacterial machinery.

While MerB exhibited a distinctive structure with no discernible homology to any known genes outside the MerB category—making it unique to mercury resistance pathways.

The active site of MerB contained a catalytic Cys96 residue, which played a crucial role in the enzyme's ability to cleave the carbon-mercury bond. This residue demonstrated versatility by accepting a variety of organomercurial substrates, thus broadening the enzyme's ability to detoxify different types of mercury compounds. By catalyzing the breakdown of organomercurial compounds, MerB functioned as the first step in the bacterial detoxification system, preparing the mercury for reduction by MerA.

Overall, the coordinated action of these two enzymes, MerB and MerA, formed a highly efficient mercury detoxification pathway in these bacteria. This dual-enzyme system enabled the bacteria to thrive in environments contaminated with toxic forms of mercury, thus illustrating the impressive adaptability of microorganisms in response to environmental toxins.

This research investigates the mechanisms employed by bacteria, particularly focusing on their ability to detoxify methylmercury (MeHg) through a specialized dual-enzyme system known as the MerB-MerA complex. This study highlights the enzymatic pathways that enable these microorganisms to thrive in mercury-contaminated environments.

The primary objectives is to: Elucidate the roles of the enzymes MerB in the detoxification of methylmercury.

Assess the specificity and efficiency of these enzymes in transforming toxic mercury compounds into less harmful forms.

Investigate the catalytic mechanisms of MerB

Methods

Enzyme Characterization: The study employed various biochemical assays to analyze the activity of MerB. Key methodologies included:

PCR Amplification: The merA (1600 bp) and merB (607 bp) genes were amplified from plasmids pmerAB and r100 using Polymerase Chain Reaction (PCR).

Cloning and Expression: The pRset expression vector was prepared with a histidine tag for protein purification. The merA and merB genes were subcloned into this vector for expression in bacterial hosts.

Electroporation: Recombinant plasmids were introduced into competent bacterial cells via electroporation, followed by selection of transformants using blue-white colony selection, all above procedures are illustrated in Figure 17, Figure 18 & Figure 19.

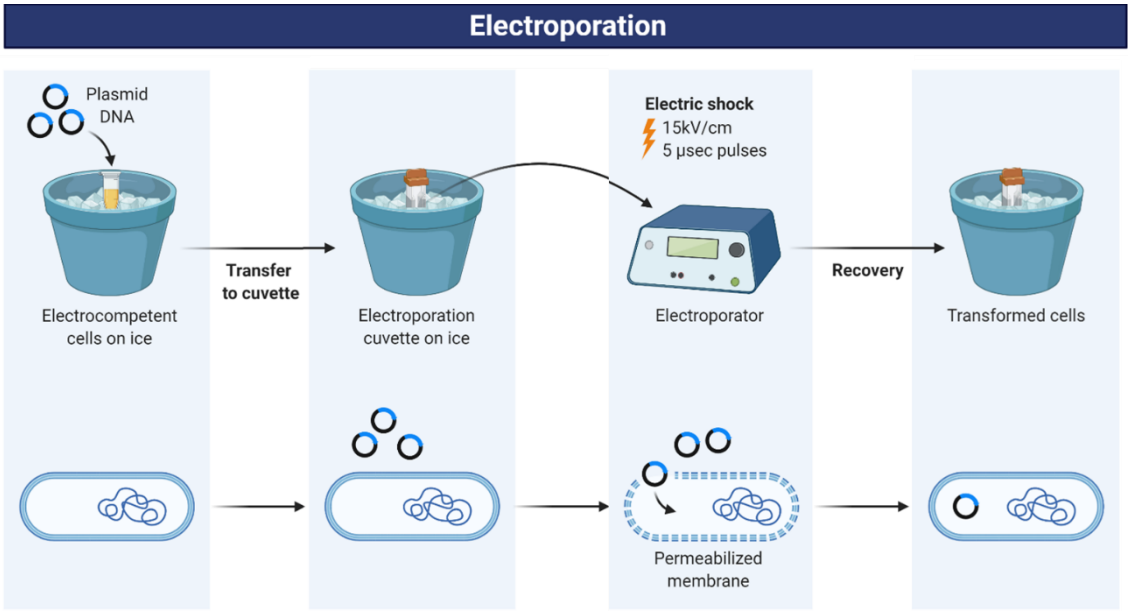

Figure 17: Figure depicts the workflow for electroporation in bacteria.

for transferring the recombinant plasmid into the host. Prepared using BioRender

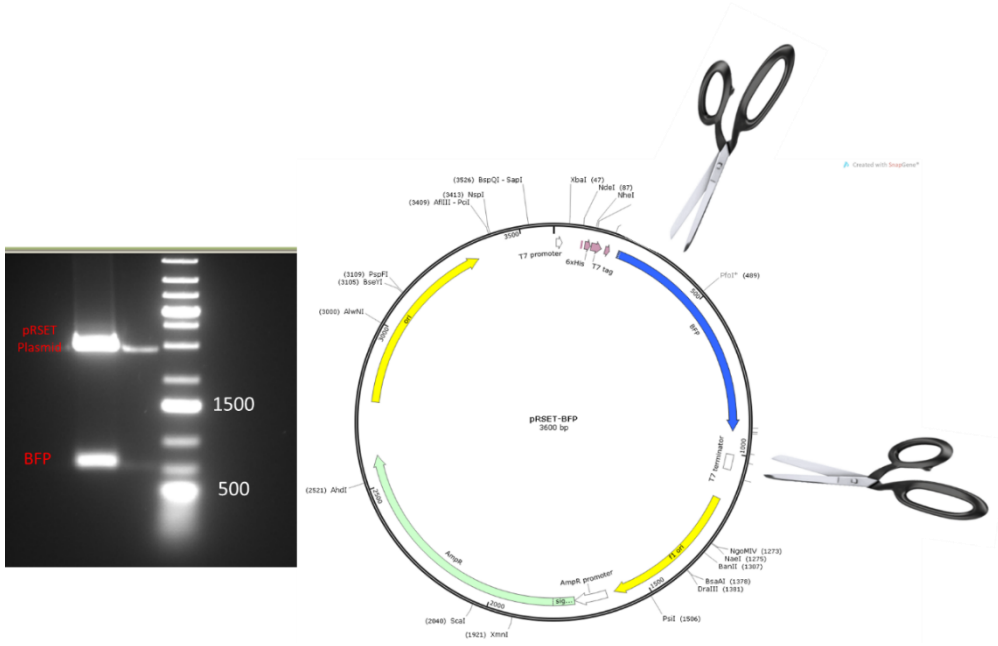

Figure 18: The Figure depicts the workflow of selection of white colonies.

from the classical blue white selection. Plasmid image recreated from SnapGene Viewer. Prepared using BioRender

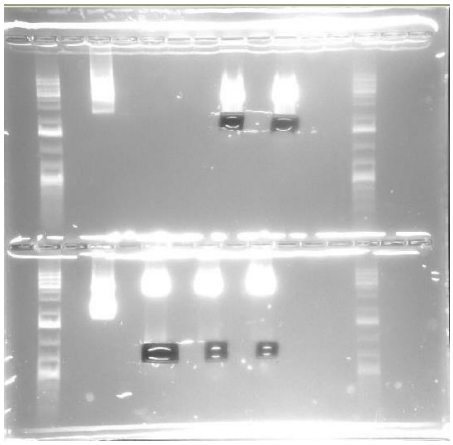

Figure 19: Illustration of gel elusion and purification of merA and merB.

released from TA subcloning vector.

Activity Assays: The activity of MerB was evaluated in whole cells and cell lysates cultivated at different optical densities before induction with 0.5 mM IPTG. Additionally, the specific capturing ability of MerB towards MeHg was assessed, revealing its remarkable selectivity compared to inorganic mercury (Hg^{2+}).

3.5.2.2 Results and Discussion

Enzymatic Functionality: MerB effectively cleaved carbon-mercury bonds, converting MeHg into inorganic Hg^{2+}, demonstrating a high degree of substrate versatility due to the catalytic Cys96 residue in its active site.

Specificity: The experiments confirmed that MerB exhibited exceptional specificity for MeHg, achieving a 33% capture rate at a 1:0.5 molecular weight ratio. In contrast, it showed negligible binding to Hg^{2+}, capturing less than 1%, underscoring its role as a specialized detoxifying agent Figure 20.

The findings illustrate the sophisticated adaptations of Desulfovibrio species in response to mercury contamination. The efficient action of the MerB-MerA complex not only mitigates mercury toxicity but also exemplifies microbial resilience in challenging environments. This research contributes valuable insights into potential bioremediation strategies for mercury pollution by harnessing these natural detoxification pathways.

This study elucidates the critical role of the MerB enzyme system in detoxifying methylmercury in bacteria. By transforming toxic mercury compounds into less harmful forms, these microorganisms showcase remarkable biochemical adaptations that could inform future environmental remediation efforts. We further wanted to develop a transducing material where we immobilize the MerB on to electrode.

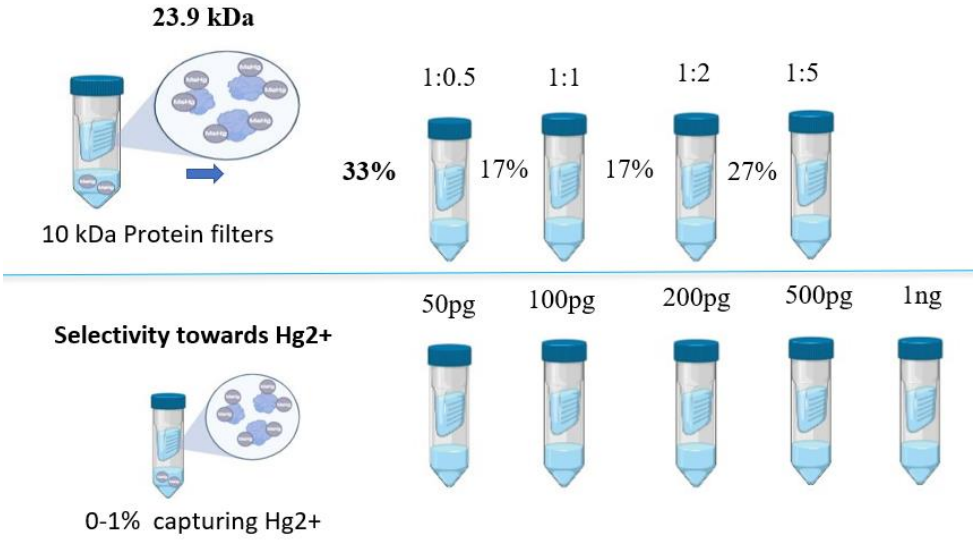

Figure 20: The specific capturing ability of merB towards methyl mercury.

in the first half of the picture when used 1:0.5 Molecular Weight based ratio it showed an excellent 33% capturing. In the below half of the image, even when used varied concentration of inorganic mercury (Hg^{2+}) mer B didn' bind /capture even 1% of Hg^{2+}, proving incredible specific capturing of MeHg. Prepared using BioRender

3.5.3 MMHg selective and coupled biomolecules with nanomaterials.

3.5.3.1 Summary

The development of electrodes functionalized with nanomaterials for protein immobilization is a critical area of research in biosensors and bioelectronics. This study investigates the functionalization of gold nanomaterials and their interaction with histidine-tagged proteins through a linker, allowing for the precise immobilization and detection of proteins on an electrode surface. The functionalization process and the subsequent immobilization of proteins were characterized using several advanced techniques, including scanning electron microscopy (SEM), Fourier-transform infrared spectroscopy (FTIR), and X-ray photoelectron spectroscopy (XPS). Additionally, electrochemical impedance spectroscopy (EIS) was used to confirm protein immobilization.

3.5.3.2 Results and Discussion

3.5.3.2.1 Chemistry for Linker Creation Between Gold Nanomaterials and Histidine-Tagged Protein:

The first step in the immobilization process involves the creation of a linker between goldnanomaterials and the histidine-tagged proteins. The linker is typically formed by functionalizing the gold surface with chemical groups that can interact with both the gold surface and the histidine residues on the protein. Common strategies involve the use of thiol-based linkers such as 3-mercaptopropionic acid (MPA) or NTA (nitrilotriacetic acid), which can chelate metal ions like Nickel (Ni^{2+}) and allow for the selective binding of histidine-tagged proteins to the nanomaterial. The chemistry typically follows the steps:

1. Surface Functionalization of Gold: Gold nanoparticles are functionalized with MPA or NTA to provide a surface that can bind metal ions.

2. Chelation of Nickel: Nickel ions (Ni^{2+}) are introduced, which bind to the NTA/MPA groups.

3. Protein Immobilization: The histidine-tagged protein binds selectively to the nickel ions via the His-tag.

This process ensures a stable and reproducible immobilization of the protein on the electrode surface.

Characterization Techniques and Results:

1. SEM Image of Working Electrode with Gold Nanoparticles A scanning electron microscope (SEM) image was used to observe the morphology of the electrode after functionalization. The SEM image clearly shows the presence of round gold nanoparticles evenly distributed across the surface of the electrode. This uniform distribution of nanoparticles is crucial for ensuring the effective interaction between the electrode and the protein.

2. FTIR Resultsfor Electrode Functionalization Fourier-transform infrared spectroscopy (FTIR) was employed to verify the functionalization of the electrode surface with 3-mercaptopropionic acid (MPA) and nitrilotriacetic acid (NTA). The FTIR spectra showed distinct peaks corresponding to the –SH group of MPA and the – COOH group of NTA, confirming the successful immobilization of these functional groups onto the electrode surface depicted in Figure 21.

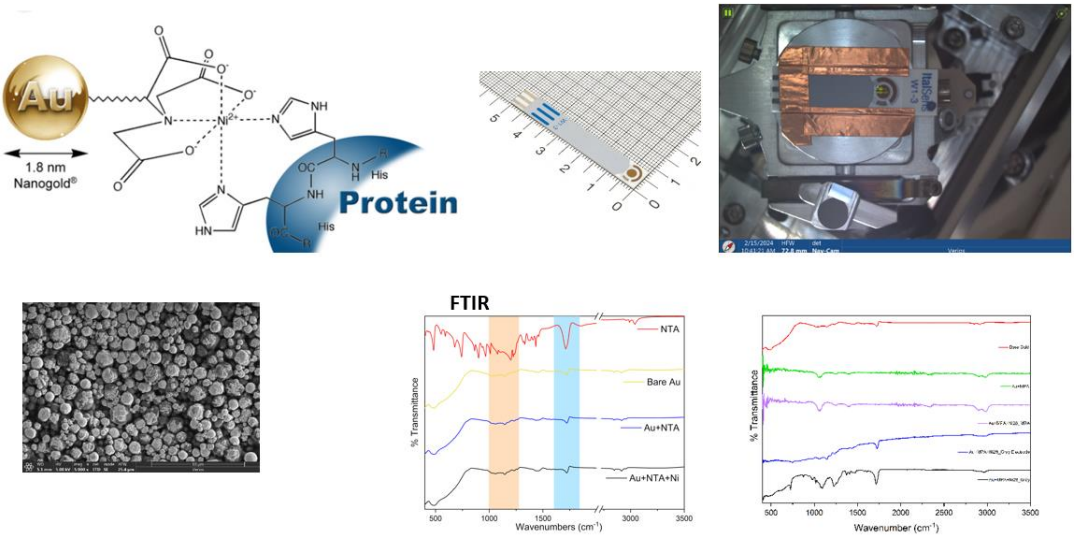

Figure 21: a) Chemistry to achieve linker.

between gold nanomaterial and histidine taged protein, b)image of a electrode used, c) scanning electron microscopic image of the working electrode with round gold nanoparticles, d) FTIR results for the electrode for 3MPA and NTA funcnalization omn to the electrode.

3. XPS Results: Presence of Nickel X-ray photoelectron spectroscopy (XPS) analysis was performed to study the presence of Nickel (Ni) in the electrode after complex formation with MPA/NTA. The XPS spectrum revealed that the nickel content on the electrode was up to 4.1%, confirming the binding of nickel ions to the NTA-functionalized electrode. This presence of nickel ions is crucial for the immobilization of histidine-tagged proteins Figure 22.

4. SEM Image Showing Distribution of Ni^{2+} in Electrode Another SEM image, taken at high resolution, revealed a uniform distribution of Ni^{2+} throughout the electrode surface, indicating that the nickel ions were evenly dispersed after

functionalization. This distribution is essential for ensuring consistent protein immobilization across the entire electrode.

5. Electrochemical Impedance Spectroscopy (EIS) Measurement Electrochemical impedance spectroscopy (EIS) was used to confirm the successful immobilization of the histidine-tagged protein. The impedance measurements showed a clear increase in resistance after washing off unbound proteins, indicating that the protein had been successfully immobilized on the electrode surface. The binding of the protein was further verified by the reduction in current observed after protein immobilization, demonstrating that the protein interaction was stable depicted in Figure 23.

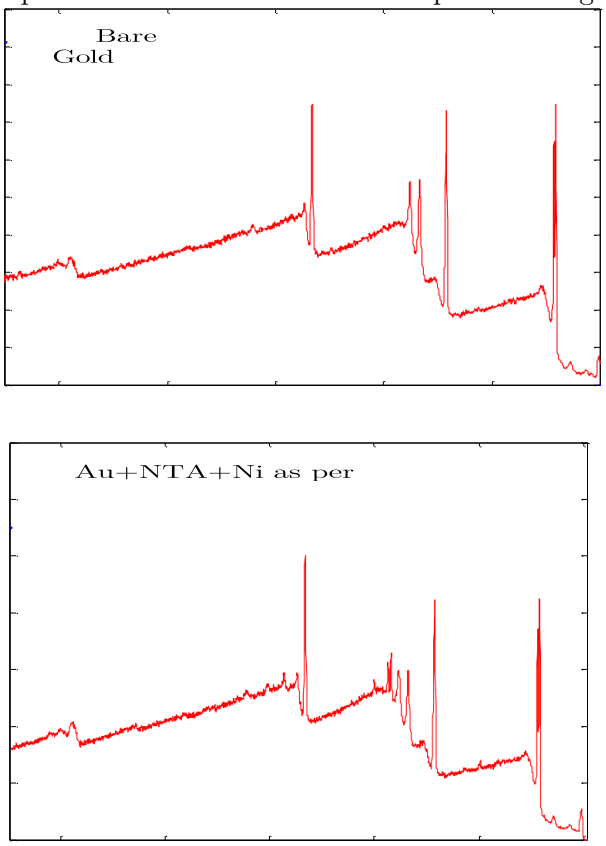

Figure 22: Presence of nitrogen than the control indicating NTA functionalization.

in the electrode in the XPS spectra.

3.5.3.2.2 Validation of protein immobilzation

This study demonstrates a successful approach to functionalizing gold nanomaterials

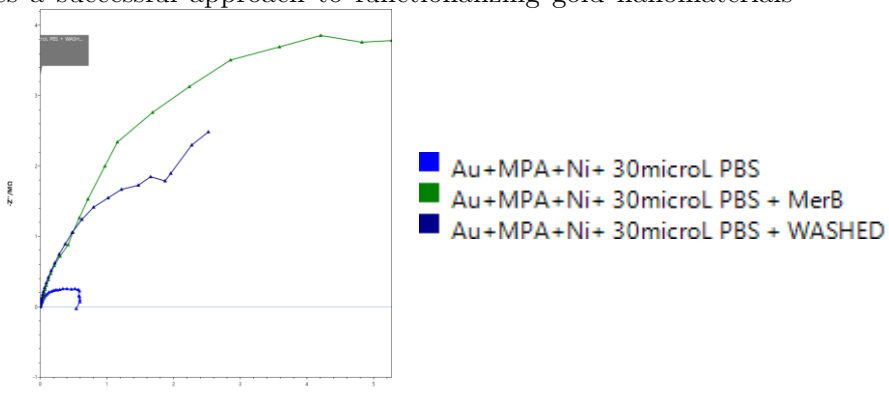

Figure 23: The Electrochemical impedence measurement.

proving the immobilzation of protein after washing the unbound protein

with MPA/NTA linkers to facilitate the immobilization of histidine-tagged proteins on an electrode surface. The comprehensive characterization using SEM, FTIR, XPS, and EIS confirms the successful formation of stable complexes between Ni^{2+} and the functional groups, as well as the effective immobilization of the protein. These findings lay the groundwork for future applications in biosensors and other bioelectronic devices.

3.5.4 Biosensor developed

3.5.4.1.1 Summary

In this study, we developed a novel electrochemical detection system for MeHg, utilizing the MerB system from mercury-resistant bacteria. This dual-enzyme system enabled the detection of MeHg based on its interaction with MerB, and we employed two powerful electrochemical techniques—cyclic voltammetry (CV) and electrochemical impedance spectroscopy (EIS)—to measure the redox signatures and impedance changes that occur during the binding of MeHg to MerB functionalized on gold electrodes.

3.5.4.1.2 Results and Discussion

Cyclic Voltammetric Detection of MeHg: The first detection method we explored was cyclic voltammetry (CV), which measured the redox interactions between MeHg and the MerB enzyme. We hypothesized that the interaction between MeHg and MerB would produce a distinct redox signature, which could be identified by measuring current responses at various potentials. During the CV measurements, different scan rates ranging from 0.01 V/s to 0.1 V/s were applied. The results showed a prominent peak at around 0.3 V on the X-axis, which corresponded to the redox reaction between MeHg and the enzyme, where MeHg was converted into Hg^{2+}. The peak at this potential was consistent across the range of MeHg concentrations tested (4 and 5 ng), confirming the capability of the CV technique to detect MeHg based on the enzymatic reaction. This established CV as a reliable method for detecting MeHg at concentrations as low as nanograms shown in Figure 24.

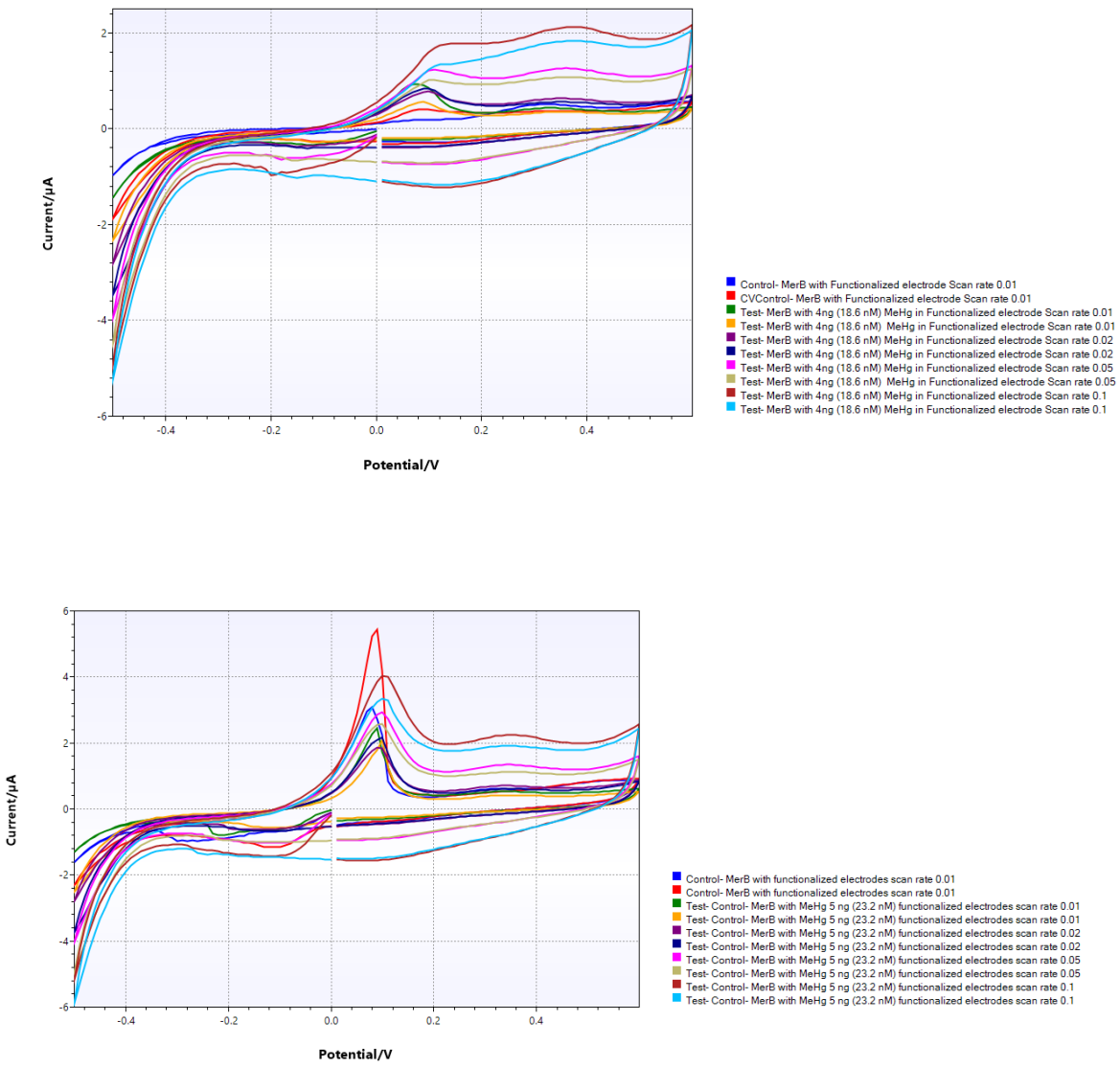

Figure 24: CV measurements (with different scan rates from 0.01 to 0.1).

for 4 and 5 ng of MeHg a signature peak in 0.3V (potential) in the X-axis indicating the redox reactin between MeHg and MerB while converting MeHg into Hg^{2+}.

Electrochemical Impedance Spectroscopy (EIS) Detection of MeHg: In addition to CV, we also investigated the use of electrochemical impedance spectroscopy (EIS) for MeHg detection, which takes advantage of the impedance changes caused by the conformational changes in MerB upon binding with MeHg. The hypothesis was that MeHg binding would lead to measurable alterations in the impedance of the electrochemical system, which could be used as an indicator of the quantity of MeHg present are depicted in Figure 25 &Figure 26.

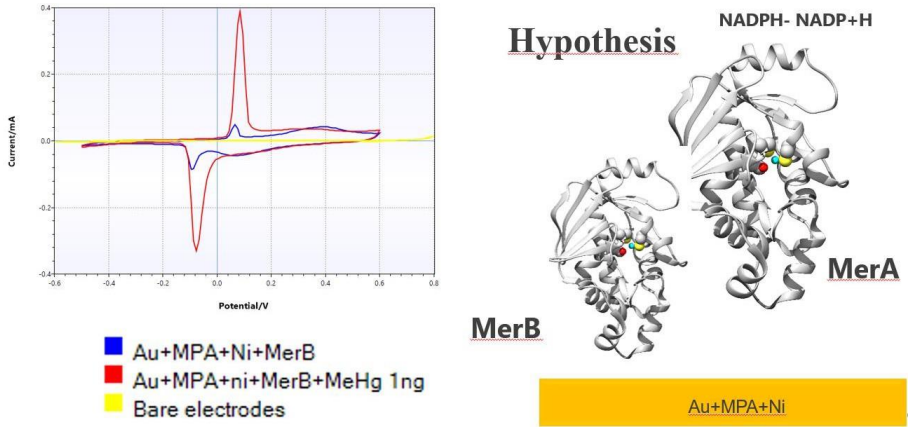

Figure 25: The hypothesis for MeHg detection using cyclic voltametric detection.

which involves finding the redox signature for the interaction between merB and MeHg

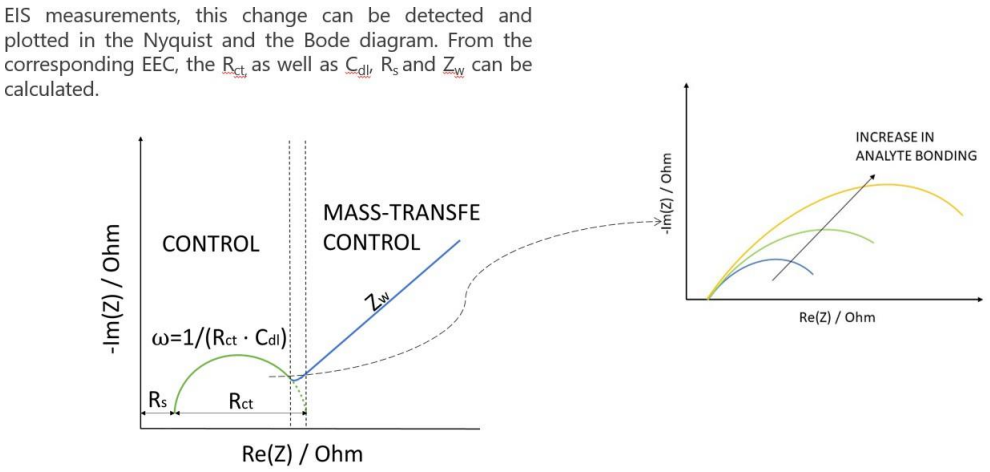

Figure 26: Figure depicting the EIS measurement.

that detect the change and plot in Nyquist and Bode diagram. The increase in Rct is correspond to the quantity of analyte bonded to the biorecognition element.

The EIS measurements detected significant impedance changes upon the interaction of MeHg with the MerB-functionalized electrode, which were consistent with the binding event. The Nyquist and Bode plots from the EIS data showed an increase in charge transfer resistance (Rct), directly correlating with the amount of analyte (MeHg) bound to the biorecognition element. Notably, this increase in Rct was found to be highly sensitive, with detection of MeHg as low as 3 femtograms (fg), a concentration that is unprecedented for electrochemical methods. The remarkable sensitivity of EIS in detecting MeHg at such a low concentration demonstrates its potential for use in environmental monitoring and trace detection of toxic metals are depicted in Figure 27, Figure 28, Figure 29,Figure 30,Figure 31& Figure 32.

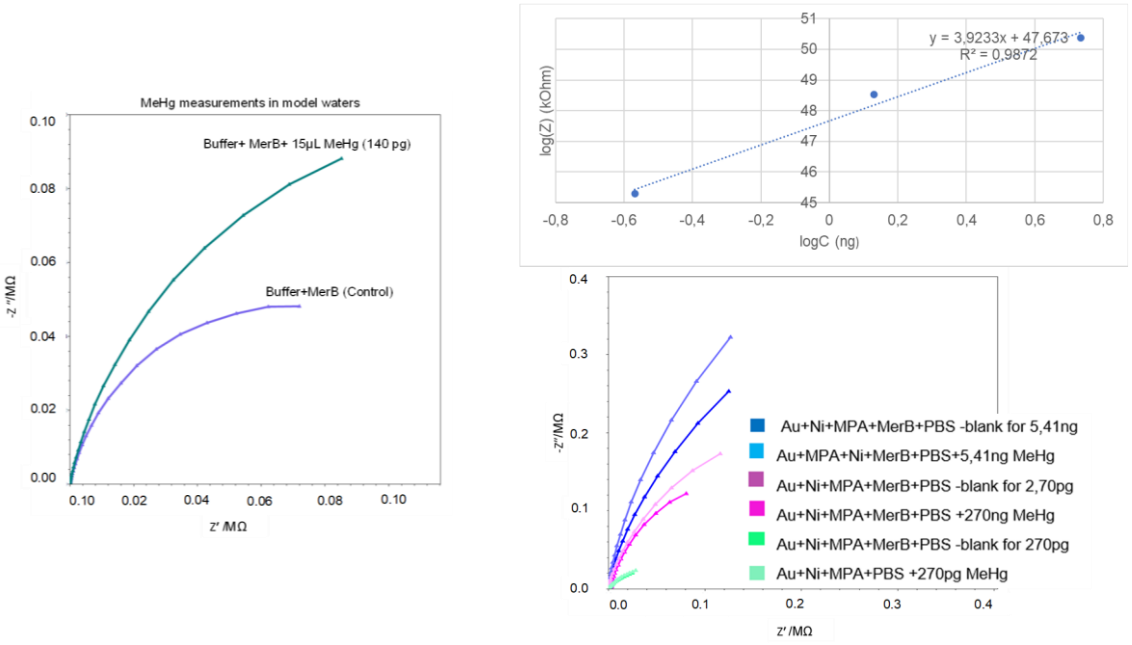

Figure 27 A) The increase in electrochemical impedence in the sensor with 140pg MeHg. than the control merB without MeHg, B) Calibration curve prepared with our MeHg sensor with different concentrations of MeHg, C) Electrochemical impedence for different concentrations.

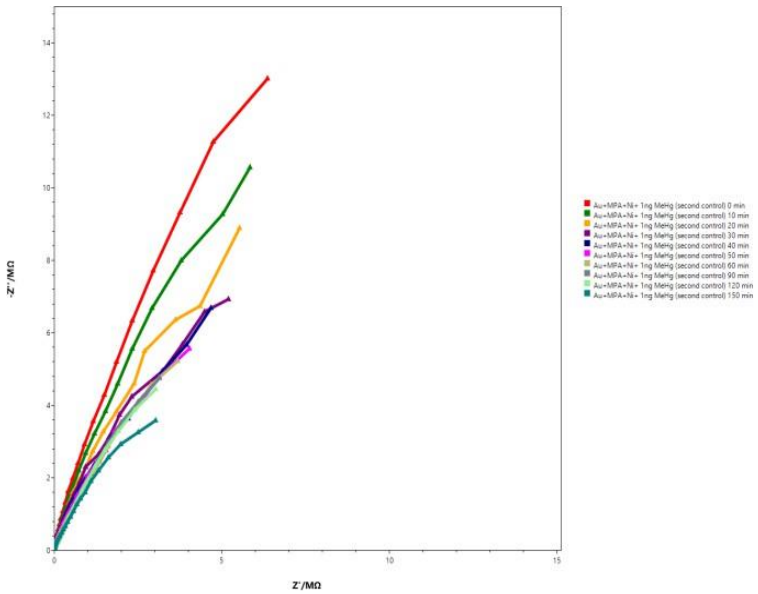

Figure 28: Figure depicting EIS measurement for a control electrode without merB. with methylmercury (1ng) taken in various time points (from 0min to 150min) showing decrease in electrochemical impedence, proving there is no increase in impedence when used without merB.

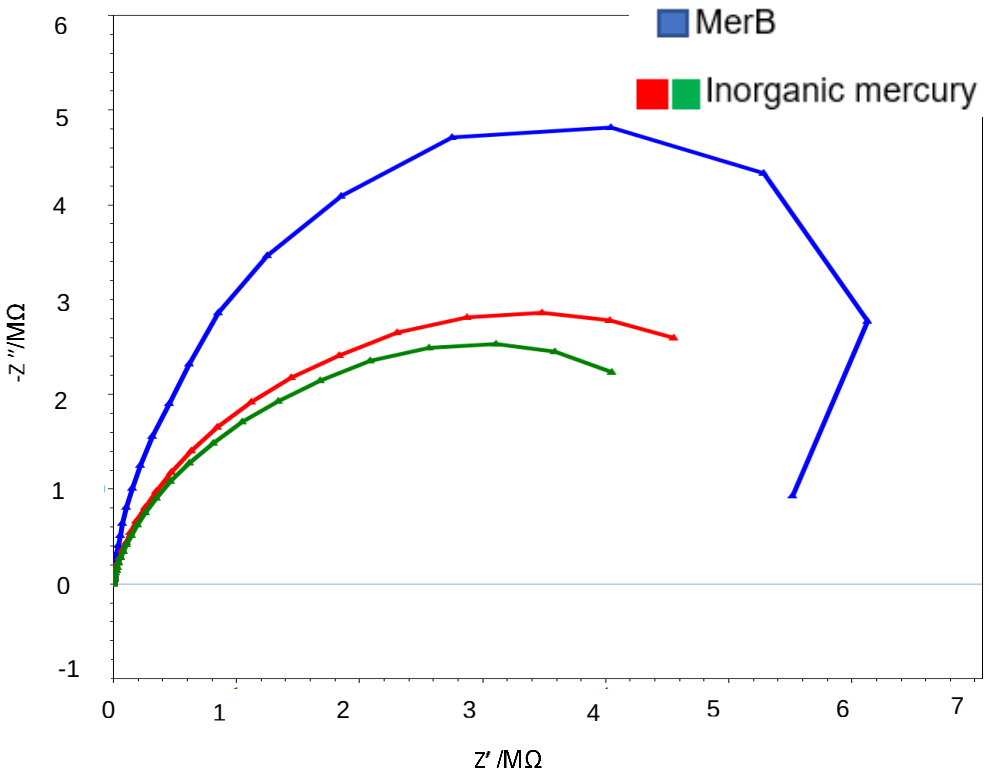

Figure 29 Specificity test for the sensor tend towards Hg^{2+}.

the increase in impedence is 5ng Hg^{2+} from the sensor indicate that the sensor doest not detect Hg.

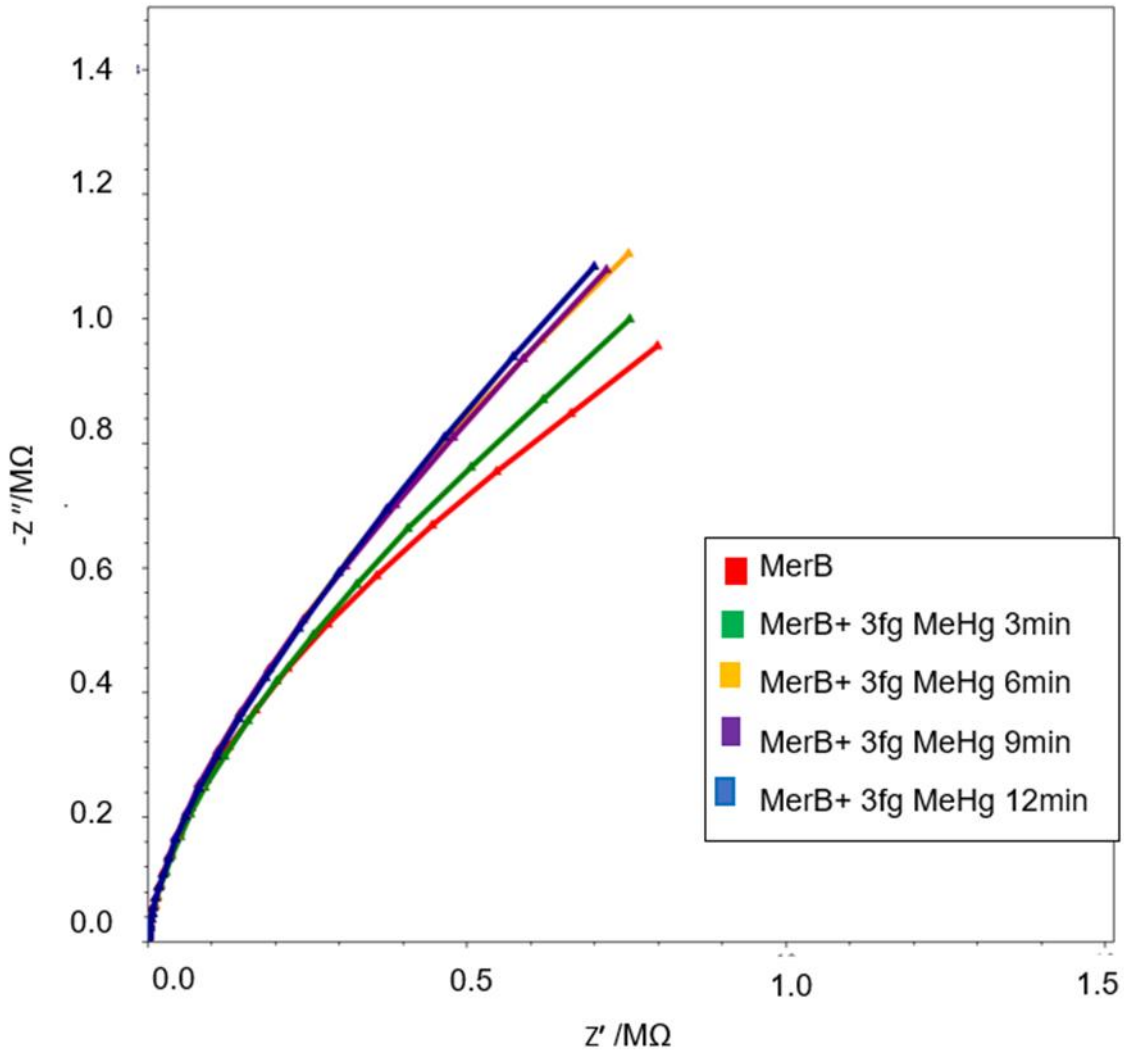

Figure 30 Figure depicting methyl mercury MeHg detection, sensor at 37C.

(The temperatutre which the proteins are initially produced). To detect unprecedented low concentration such as 3fg

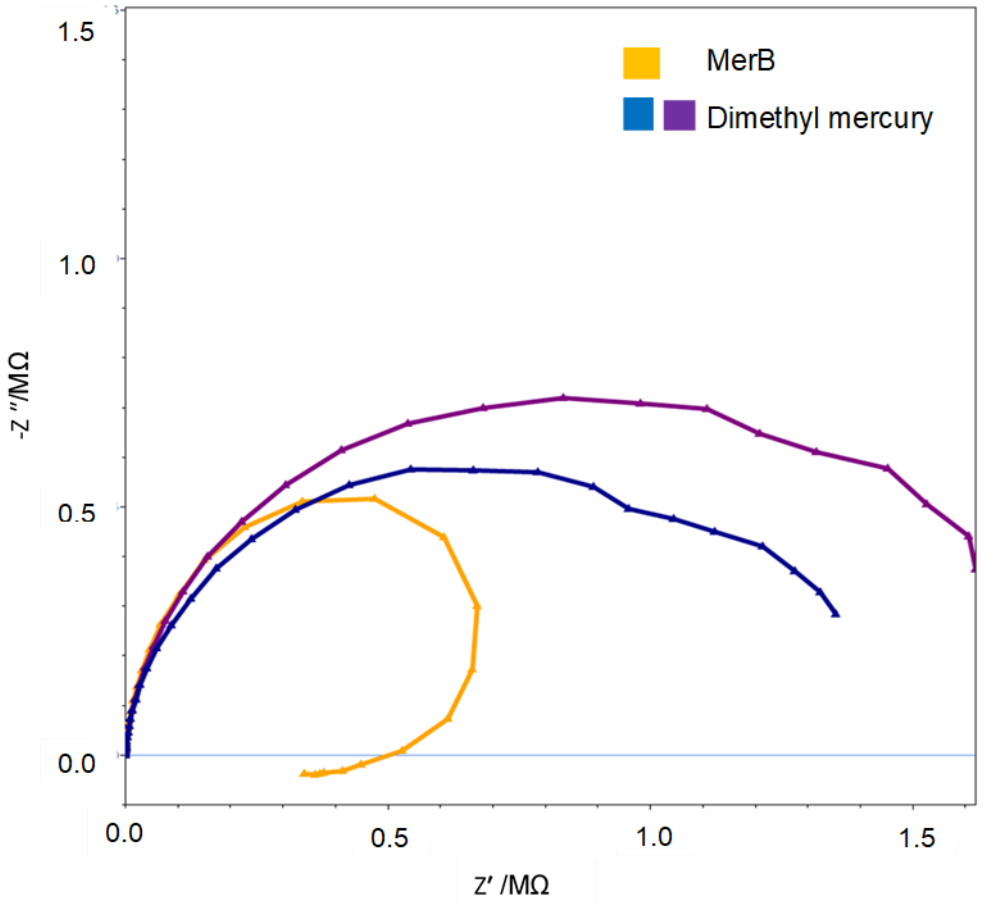

Figure 31 The specificity of sensor towards dmHg.

the increase in impedence than the control merB indicates that 6ng dmHg can also be detected using our sensor.

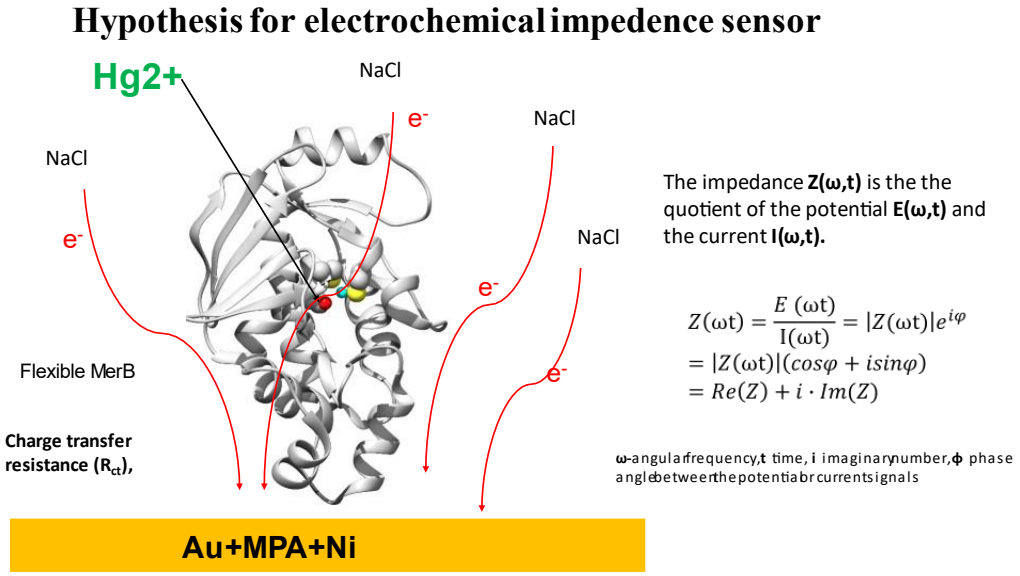

Figure 32 The hypothesis for MeHg detection using Electrochemical impedence.

which involves detecting the impedenc e in the electrochemical system caused by the confirmational changes in merB functionalized in the gold electrode (after intercatimng with MeHg).

Characterization and Validation: Further confirmation of the successful functionalization of the gold electrode with MerB was provided by scanning electron microscopy (SEM), which revealed uniform distribution of the functionalized enzyme on the gold surface, ensuring that the sensor surface was well-prepared for efficient interaction with MeHg. The Fourier-transform infrared spectroscopy (FTIR) analysis confirmed the presence of functional groups (such as amines and carboxyl groups) from the NTA and MPA ligands used to anchor the enzyme to the electrode, further supporting the integrity of the sensor surface.

This study successfully demonstrated the use of MerB-functionalized gold electrodes for the electrochemical detection of MeHg using both cyclic voltammetry and electrochemical impedance spectroscopy. The EIS method, in particular, achieved an unprecedented detection limit of 3 femtograms (fg), illustrating its exceptional sensitivity for trace-level MeHg detection. The ability to detect MeHg at such low concentrations could have significant implications for environmental monitoring, especially in regions where mercury contamination is a growing concern. Further studies are needed to explore the full potential of this detection system in real-world applications and to improve its stability and reproducibility.

3.5.5 Conclusions

For efficient MeHg sensors, prioritise the development of advanced materials and biorecognition elements with high specificity for MeHg, such as novel nanomaterials and selective aptamers/ antibodies. Optimize signal processing using advanced technologies to improve accuracy and interpret complex data effectively. Implement real-time calibration and adaptive systems to maintain sensor performance under varying environmental conditions. Focus on increasing sensitivity to detect lower concentrations of MeHg and reducing response times for rapid, reliable measurements. Ensure the sensor's usability,

cost-effectiveness, and scalability, and validate its performance through extensive field testing and adherence to regulatory standards.

Currently, methods such as Atomic Absorption Spectroscopy (AAS), Atomic Fluorescence Spectroscopy (AFS), Inductively Coupled Plasma Mass Spectrometry (ICP-MS), and X-ray Fluorescence (XRF) Spectroscopy are widely used for mercury (Hg) detection across various matrices. However, these techniques often require extensive sample preparation, have lower sensitivity, perform poorly with liquid samples, are susceptible to matrix interferences, and are costly, requiring highly skilled operators. As a result, sensors for detecting MeHg represent a potential advancement in the field. Unfortunately, current detection methods often lack the necessary sensitivity and specificity, frequently failing to detect concentrations below environmentally relevant thresholds set by regulatory bodies (e.g., 0.1 ng/mL) or based on the effects of biomagnified MeHg, which necessitates lowering regulatory thresholds.

From a biological point of view, MeHg detection is particularly challenging: Even at extremely low concentrations, MeHg can cause biological amplification due to time-dependent or chronic exposure. This makes even current gold-standard laboratory methods not sensitive enough, as MeHg concentrations are often below the limit of detection (LOD). In contrast to the Hg^{2+} where biological responses tend to show concentration-dependent effects in living cells, the biological impact of MeHg is usually only evident in multicellular organisms at higher trophic levels, which is then separating the concentration levels in environmental matrices from the concentrations in organisms, for example ocean waters and fish, respectively, by more than five orders of magnitude.

Based on literature-gained knowledge and on our experiences, we have identified five key steps that should be specifically followed when developing an effective MeHg sensor:

1. Interdisciplinarity: Developing a sensor requires collaboration between analytical chemists, material scientists, physicists, and experts in biology (e.g., biochemists, molecular biologists). A bottom-up approach is needed, beginning with an understanding of interactions of the MeHg with the selected sensing component at the molecular level.

2. Matrix Consideration: The sensor development must begin by selecting the matrix (e.g. fish tissue, ocean water), as this determines the required sample pre-treatment, potential interferences (e.g. co- contaminants, extraction chemicals), expected concentration ranges, and physicochemical conditions such as ionic strength, pH, and temperature.

3. Relevance: Sensor relevance must be evaluated not just by concentration levels but also by the intended application –whether ecological (e.g. bioavailability), health-related, research-orientated, or commercial. The sensor's design should reflect its intended use.

4. Detection Modalities: The sensor should be able to measure concentration (quantitatively or semi- quantitatively), temporal changes, accumulation, or microspatial information (e.g. intracellular accumulation). The specific modality should align with the sensor's intended purpose.

5. Coupling Sensing Element with Transducer: The choice of transducer (electromagnetic, electrical, etc.) must be considered along with noise-to-signal ratio, signal range, and signal linearity. These factors impact signal amplification, filtration, correlation, and other signal-processing steps.

The recent surge in artificial intelligence (AI) has led to substantial advancement across various research domains. To date, most of the currently known MeHg sensing parts are designed based either on the known properties of selected sensing components or materials that preferentially interact with various Hg species, or by trial-and-error experiments. Currently, artificial intelligence tools offer new approaches in material design, discovery, and manufacturing, which can accelerate the development of sensors with improved sensitivity and especially increased selectivity towards MeHg (Papadimitriou et

al., 2024). Furthermore, based on our experiences working on WCBs and detecting very low levels of analytes (Rijavec et al., 2017), this process is often prone to a high noise-to-signal ratio. However, adopting machine learning approaches could help refine detection, possibly not for quantitative measurements, but more appropriately for qualitative information. This could be crucial for filtering out contaminated samples, ensuring reliable detection even in complex samples affected by matrix effects.

In conclusion, given the complexities discussed above, creating a universal sensor that functions across all matrices while providing relevant data would be extremely challenging. Therefore, work focused on matrix-specific sensors is necessary to achieve accurate and meaningful MeHg detection.

The resulting portable biosensor demonstrates the capability to detect MMHg at extremely low concentrations (as low as 3 femtograms), ensuring high specificity against other mercury species, thus making it a promising tool for environmental monitoring and regulatory compliance in contaminated sites.

This biosensor technology represents a significant advancement over conventional methods, offering rapid detection, ease of use, which are crucial for ensuring food safety and protecting vulnerable populations from mercury exposure. Future developments will focus on refining these sensors to improve their integration into real-world monitoring systems, further enhancing public health safety and environmental protection efforts against mercury contamination depicted in Figure 33.

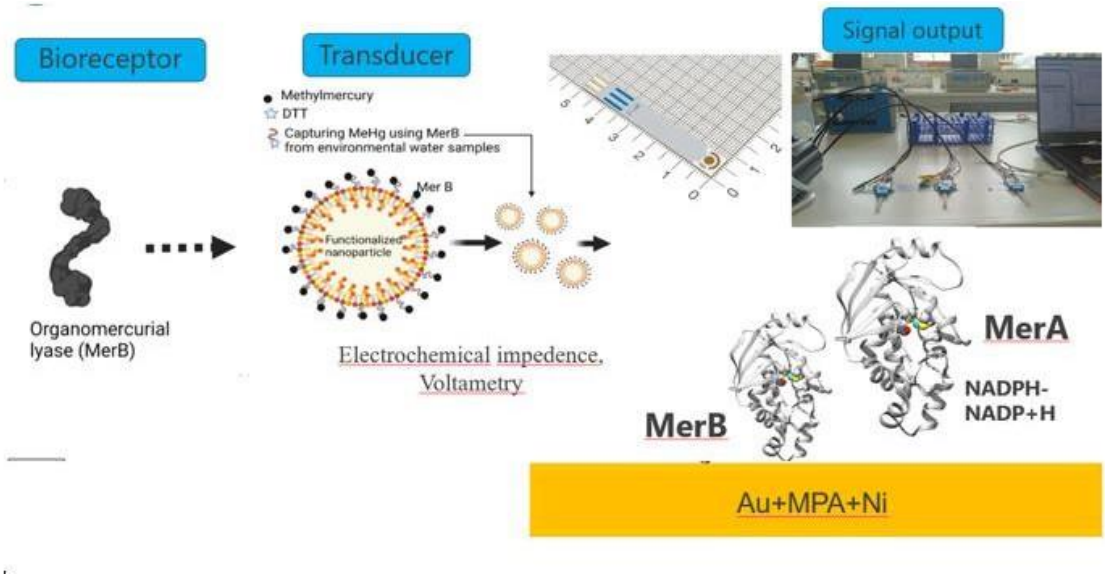

Figure 33 Our MeHg sensor with bioregoniction elements, transducing element and reporting component illustrated. Prepared using BioRender.

Chapter 4

Conclusion

This work advances the development of selective, efficient, and multifunctional nanoengineered platforms for toxic metal remediation and biosensing. Addressing critical environmental contaminants—particularly toxic metals such as Pb^{2+}, Cr^{3+}, Hg^{2+}, and organomercurials like MeHg—the study integrates materials science, surface chemistry, microbiology, and electrochemical techniques into a unified framework for sustainable detection and removal technologies.

The synthesized adsorbents, including amino-functionalized SiO_2 and γ-Fe_2O_3@NH_2 magnetic nanoparticles, demonstrated high surface reactivity and specificity toward priority metals. Their strong affinity under environmentally relevant conditions, excellent regeneration capability, and magnetic retrievability underscore their potential in decentralized water purification applications. Additionally, sol–gel derived spinel ferrite nanoparticles proved effective in co-adsorption of Hg^{2+} and recovery of rare earth elements (REEs), representing a step toward circular economy-compatible remediation technologies.

A major innovation of the study was the development of a biosensor for ultra-trace MeHg detection, leveraging MerB an organomercurial lyase enzyme as the biorecognition element. The sensor design incorporated MerB immobilized on gold nanoparticle-modified screen-printed electrodes via Ni^{2+}-NTA chelation chemistry. The complete workflow: from comparative evaluation of MeHg sensing techniques, hypothesis generation based on microbial mercury sequestration, to cloning, expression, and purification of MerB, and finally to electrochemical integration and sensor validation.

The MerB protein exhibited outstanding specificity for MeHg, showing a 33% capture rate at molecular weight ratios as low as 1:0.5, while exhibiting negligible interaction with inorganic Hg^{2+} even at higher concentrations. Surface functionalization of the electrodes was verified using SEM, FTIR, elemental mapping, and EDX. Electrochemical Impedance Spectroscopy (EIS) confirmed that MerB immobilization caused a measurable increase in charge transfer resistance (Rct), which directly correlated with MeHg concentration. Importantly, control experiments without MerB showed no impedance change, affirming the biorecognition-driven detection mechanism. The sensor achieved detection limits as low as 3 femtograms, with exceptional specificity toward MeHg over other mercury species, including Hg^{2+}.

This study validates the integration of genetically expressed enzymes with nanoscale electrode platforms as a powerful strategy for selective biosensing. The successful immobilization and electrochemical interrogation of MerB lay the groundwork for portable monitoring systems for mercury pollution.

Collectively, this research bridges nanoscale material design and molecular biosensing, delivering a dual-solution framework for environmental mercury management—removal through high-affinity adsorbents and detection via ultra-sensitive enzymatic biosensor.

References

Abd-Elhamid, A. I., El-Aassar, M. R., El Fawal, G. F., & Soliman, H. M. A. (2019). Fabrication of polyacrylonitrile/β-cyclodextrin/graphene oxide nanofibers composite as an efficient adsorbent for cationic dye. *Environmental Nanotechnology, Monitoring & Management*, *11*, 100207.

Abegunde, S. M., Idowu, K. S., Adejuwon, O. M., & Adeyemi-Adejolu, T. (2020). A review on the influence of chemical modification on the performance of adsorbents. *Resources, Environment and Sustainability*, *1*, 100001. https://doi.org/10.1016/j.resenv.2020.100001

Ahsan, M. A., Jabbari, V., Islam, M. T., Turley, R. S., Dominguez, N., Kim, H., Castro, E., Hernandez-Viezcas, J. A., Curry, M. L., Lopez, J., Gardea-Torresdey, J. L., & Noveron, J. C. (2019). Sustainable synthesis and remarkable adsorption capacity of MOF/graphene oxide and MOF/CNT based hybrid nanocomposites for the removal of Bisphenol A from water. *Science of The Total Environment*, *673*, 306–317. https://doi.org/10.1016/j.scitotenv.2019.03.219

Akbarian, M., Khani, A., Eghbalpour, S., & Uversky, V. N. (2022). Bioactive Peptides: Synthesis, Sources, Applications, and Proposed Mechanisms of Action. *International Journal of Molecular Sciences*, *23*(3), 1445. https://doi.org/10.3390/ijms23031445

Alkhaldi, H., Alharthi, S., Alharthi, S., AlGhamdi, H. A., AlZahrani, Y. M., Mahmoud, S. A., Amin, L. G., Al-Shaalan, N. H., Boraie, W. E., Attia, M. S., Al-Gahtany, S. A., Aldaleeli, N., Ghobashy, M. M., Sharshir, A. I., Madani, M., Darwesh, R., & Abaza, S. F. (2024). Sustainable polymeric adsorbents for adsorption-based water remediation and pathogen deactivation: A review. *RSC Advances*, *14*(45), 33143–33190. https://doi.org/10.1039/D4RA05269B

Amaly, N., Si, Y., Chen, Y., El-Moghazy, A. Y., Zhao, C., Zhang, R., & Sun, G. (2018). Reusable anionic sulfonate functionalized nanofibrous membranes for cellulase enzyme adsorption and separation. *Colloids and Surfaces B: Biointerfaces*, *170*, 588–595.

Anchidin-Norocel, L., Gutt, G., Tătăranu, E., & Amariei, S. (2024). Electrochemical sensors and biosensors: Effective tools for detecting heavy metals in water and food with possible implications for children's health. *International Journal of Electrochemical Science*, *19*(8), 100643.

Atta, N. (2015). Graphene—A Platform for Sensor and Biosensor Applications. In *2015*. InTech. http://dx.doi.org/10.5772/60676

Babatunde, K. A., Negash, B. M., Jufar, S. R., Ahmed, T. Y., & Mojid, M. R. (2022). Adsorption of gases on heterogeneous shale surfaces: A review. *Journal of Petroleum Science and Engineering*, *208*, 109466. https://doi.org/10.1016/j.petrol.2021.109466

Byrappa, K., & Adschiri, T. (2007). Hydrothermal technology for nanotechnology. *Progress in Crystal Growth and Characterization of Materials*, *53*(2), 117–166. https://doi.org/10.1016/j.pcrysgrow.2007.04.001

Cao, X., Ma, C., Zhao, J., Guo, H., Dai, Y., Wang, Z., & Xing, B. (2019). Graphene oxide mediated reduction of silver ions to silver nanoparticles under environmentally relevant conditions: Kinetics and mechanisms. *Science of The Total Environment*, *679*, 270–278. https://doi.org/10.1016/j.scitotenv.2019.05.034

Caravanos, J., Clark, E., Fuller, R., & Lambertson, C. (2011). Assessing Worker and Environmental Chemical Exposure Risks at an e-Waste Recycling and Disposal Site in Accra, Ghana. *Journal of Health and Pollution*, *1*(1), 16–25. https://doi.org/10.5696/jhp.v1i1.22

Çetin M.Z., P. C. (2018). An amperometric glucose biosensor based on PEDOT nanofibers, RSC Advences, 8 19724-19731. *DOI:10.1039/C8RA01385C.*

Chen, Y. et al. (2019). Enzymatic Conversion in MeHg Sensing. *Biosensors and Bioelectronics, 32(1), Pp.*

Chen, L., Li, J., & Chen, L. (2014). Colorimetric Detection of Mercury Species Based on Functionalized Gold Nanoparticles. *ACS Applied Materials & Interfaces*, *6*(18), 15897–15904.

Chen, Z., Wang, X., Cheng, X., Yang, W., Wu, Y., & Fu, F. (2018). Specifically and Visually Detect Methyl-Mercury and Ethyl-Mercury in Fish Sample Based on DNA-Templated Alloy Ag–Au Nanoparticles. *Analytical Chemistry*, *90*(8), 5489–5495. https://doi.org/10.1021/acs.analchem.8b01100

Chirinos-Peinado, D., Castro-Bedriñana, J., Rivera-Parco, F., & Ríos-Ríos, E. (2025). Lead, Cadmium, and Arsenic in Edible Tissues of Guinea Pigs Raised in the Central Andes of Peru: Potential Human Health Risk? *Veterinary Sciences*, *12*(4), 292. https://doi.org/10.3390/vetsci12040292

Chugh, M., Kumar, L., Shah, M. P., & Bharadvaja, N. (2022). Algal Bioremediation of heavy metals: An insight into removal mechanisms, recovery of by-products, challenges, and future opportunities. *Energy Nexus*, *7*, 100129. https://doi.org/10.1016/j.nexus.2022.100129

Dabioch, M., Skorek, R., Kita, A., Janoska, P., Pytlakowska, K., Zerzucha, P., & Sitko, R. (2013). A study on adsorption of metals by activated carbon in a large-scale (municipal) process of surface water purification. *Open Chemistry*, *11*(5), 742–753. https://doi.org/10.2478/s11532-013-0209-4

Díez-Pascual, A. M. (2022). Surface Engineering of Nanomaterials with Polymers, Biomolecules, and Small Ligands for Nanomedicine. *Materials*, *15*(9), 3251. https://doi.org/10.3390/ma15093251

Doyo, A. N., Kumar, R., & Barakat, M. A. (2023). Recent advances in cellulose, chitosan, and alginate based biopolymeric composites for adsorption of heavy metals from wastewater. *Journal of the Taiwan Institute of Chemical Engineers*, *151*, 105095. https://doi.org/10.1016/j.jtice.2023.105095

El-Moghazy, A. Y., Soliman, E. A., Ibrahim, H. Z., Marty, J.-L., Istamboulie, G., & Noguer, T. (2016). Biosensor based on electrospun blended chitosan-poly (vinyl alcohol) nanofibrous enzymatically sensitized membranes for pirimiphos-methyl detection in olive oil. *Talanta*, *155*, 258–264.

Fouda-Mbanga, B. G., Onotu, O., & Tywabi-Ngeva, Z. (2024). Advantages of the reuse of spent adsorbents and potential applications in environmental remediation: A review. *Green Analytical Chemistry*, *11*, 100156. https://doi.org/10.1016/j.greeac.2024.100156

Fu, Y., Liu, T., Wang, H., Wang, Z., Hou, L., Jiang, J., & Xu, T. (2024). Applications of nanomaterial technology in biosensing. *Journal of Science: Advanced Materials and Devices*, *9*(2), 100694. https://doi.org/10.1016/j.jsamd.2024.100694

Gilfillan S.C. (1965). *Lead poisoning and the fall of Rome.*

Gkika, D. A., Tolkou, A. K., Katsoyiannis, I. A., & Kyzas, G. Z. (2025). The adsorption-desorption-regeneration pathway to a circular economy: The role of waste-derived adsorbents on chromium removal. *Separation and Purification Technology*, *368*, 132996. https://doi.org/10.1016/j.seppur.2025.132996

González Fernández, L. A., Medellín Castillo, N. A., Sánchez Polo, M., Navarro Frómeta, A. E., & Vilasó Cadre, J. E. (2025). Algal-Based Carbonaceous Materials for Environmental Remediation: Advances in Wastewater Treatment, Carbon Sequestration, and Biofuel Applications. *Processes*, *13*(2), 556. https://doi.org/10.3390/pr13020556

Gu, X., Wang, L., Guan, X., Wang, Y., Cheng, Y., & Wu, Y. (2024). Advances in the design, preparation and application of biomimetic damping materials. *Giant*, *19*, 100321. https://doi.org/10.1016/j.giant.2024.100321

Hamidi, A., Atia, D., Rebiai, A., Reghioua, A., Zobeidi, A., Messaoudi, M., Seghir, B. B., Pohl, P., & Simal-Gandara, J. (2024). Investigation of adsorption kinetics and isothermal thermodynamics for optimizing methylene blue adsorption onto a modified clay with cellulose using the response surface approach. *Biomass Conversion and Biorefinery*, *14*(18), 22573–22587. https://doi.org/10.1007/s13399-023-04397-1

Harada, M. (1995). Minamata Disease: Methylmercury Poisoning in Japan Caused by Environmental Pollution. *Critical Reviews in Toxicology*, *25*(1), 1–24. https://doi.org/10.3109/10408449509089885

Holzinger, M., Le Goff, A., & Cosnier, S. (2014). Nanomaterials for biosensing applications: A review. *Frontiers in Chemistry*, *2*. http://journal.frontiersin.org/article/10.3389/fchem.2014.00063/abstract

Hossini, H., Shafie, B., Niri, A. D., Nazari, M., Esfahlan, A. J., Ahmadpour, M., Nazmara, Z., Ahmadimanesh, M., Makhdoumi, P., Mirzaei, N., & Hoseinzadeh, E. (2022). A comprehensive review on human health effects of chromium: Insights on induced toxicity. *Environmental Science and Pollution Research*, *29*(47), 70686–70705. https://doi.org/10.1007/s11356-022-22705-6

Hou, Y., Zhao, Y., Lu, J., Wei, Q., Zang, L., & Zhao, X. (2023). Environmental contamination and health risk assessment of potentially toxic trace metal elements in soils near gold mines – A global meta-analysis. *Environmental Pollution*, *330*, 121803. https://doi.org/10.1016/j.envpol.2023.121803

Hu, H., Zhang, J., Wang, T., & Wang, P. (2022). Adsorption of toxic metal ion in agricultural wastewater by torrefaction biochar from bamboo shoot shell. *Journal of Cleaner Production*, *338*, 130558. https://doi.org/10.1016/j.jclepro.2022.130558

Huang, D., Li, B., Ou, J., Xue, W., Li, J., Li, Z., Li, T., Chen, S., Deng, R., & Guo, X. (2020). Megamerger of biosorbents and catalytic technologies for the removal of heavy metals from wastewater: Preparation, final disposal, mechanism and influencing factors. *Journal of Environmental Management*, *261*, 109879. https://doi.org/10.1016/j.jenvman.2019.109879

Huang, Y., Guo, X., Wu, Y., Chen, X., Feng, L., Xie, N., & Shen, G. (2024). Nanotechnology's frontier in combatting infectious and inflammatory diseases: Prevention and treatment. *Signal Transduction and Targeted Therapy*, *9*(1), 34. https://doi.org/10.1038/s41392-024-01745-z

Huang, Y., Su, W., Wang, R., & Zhao, T. (2019). Removal of Typical Industrial Gaseous Pollutants: From Carbon, Zeolite, and Metal-organic Frameworks to Molecularly Imprinted Adsorbents. *Aerosol and Air Quality Research*, *19*(9), 2130–2150. https://doi.org/10.4209/aaqr.2019.04.0215

Jang, G. G., Kasturi, A., Stamberga, D., Custelcean, R., Keum, J. K., Yiacoumi, S., & Tsouris, C. (2023). Ultra-fast microwave regeneration of CO2 solid sorbents for energy-efficient direct air capture. *Separation and Purification Technology*, *309*, 123053. https://doi.org/10.1016/j.seppur.2022.123053

Kabata-Pendias, A. (2010). *Trace Elements in Soils and Plants* (0 ed.). CRC Press. https://doi.org/10.1201/b10158

Khan, S., Cho, W. C., Sepahvand, A., Haji Hosseinali, S., Hussain, A., Nejadi Babadaei, M. M., Sharifi, M., Falahati, M., Jaragh-Alhadad, L. A., Ten Hagen, T. L. M., & Li, X. (2023). Electrochemical aptasensor based on the engineered core-shell MOF nanostructures for the detection of tumor antigens. *Journal of Nanobiotechnology*, *21*(1), 136.

L Järup, M Berglund, C G Elinder, G Nordberg, & M Vahter. (1998). *Health effects of cadmium exposure—A review of the literature and a risk estimate.*

Lan, J., Wang, B., Bo, C., Gong, B., & Ou, J. (2023). Progress on fabrication and application of activated carbon sphere in recent decade. *Journal of Industrial and Engineering Chemistry*, *120*, 47–72. https://doi.org/10.1016/j.jiec.2022.12.045

Lanphear, B. P., Hornung, R., Khoury, J., Yolton, K., Baghurst, P., Bellinger, D. C., Canfield, R. L., Dietrich, K. N., Bornschein, R., Greene, T., Rothenberg, S. J., Needleman, H. L., Schnaas, L., Wasserman, G., Graziano, J., & Roberts, R. (2005). Low-Level Environmental Lead Exposure and Children's Intellectual Function: An International Pooled Analysis. *Environmental Health Perspectives*, *113*(7), 894–899. https://doi.org/10.1289/ehp.7688

Le Goff, A., Holzinger, M., & Cosnier, S. (2011). Enzymatic biosensors based on SWCNT-conducting polymer electrodes. *The Analyst*, *136*(7), 1279.

Leermakers, M., Baeyens, W., Quevauviller, P., & Horvat, M. (2005). Mercury in environmental samples: Speciation, artifacts and validation. *TrAC Trends in Analytical Chemistry*, *24*(5), 383–393.

Leermakers, M., M. ;. Baeyens, W. ;. Quevauviller, P. ;. Horvat. (2005). Mercury in Environmental Samples: Speciation, Artifacts, and Validation. *TrAC, Trends Anal.*

Leopold, K., Foulkes, M., & Worsfold, P. J. (2009). Preconcentration techniques for the determination of mercury species in natural waters. *TrAC Trends in Analytical Chemistry*, *28*(4), 426–435.

Liu, X., Pang, H., Liu, X., Li, Q., Zhang, N., Mao, L., Qiu, M., Hu, B., Yang, H., & Wang, X. (2021). Orderly Porous Covalent Organic Frameworks-based Materials: Superior Adsorbents for Pollutants Removal from Aqueous Solutions. *The Innovation*, *2*(1), 100076. https://doi.org/10.1016/j.xinn.2021.100076

Liu, X., Xu, X., Dong, X., & Park, J. (2019). Competitive Adsorption of Heavy Metal Ionsfrom Aqueous Solutions onto Activated Carbonand Agricultural Waste Materials. *Polish Journal of Environmental Studies*, *29*(1), 749–761. https://doi.org/10.15244/pjoes/104455

Luo, Y., Zhang, Y., Xiong, Z., Chen, X., Sha, A., Xiao, W., Peng, L., Zou, L., Han, J., & Li, Q. (2024). Peptides Used for Heavy Metal Remediation: A Promising Approach. *International Journal of Molecular Sciences*, *25*(12), 6717. https://doi.org/10.3390/ijms25126717

Luzio, A., Canesi, E., Bertarelli, C., & Caironi, M. (2014). Electrospun Polymer Fibers for Electronic Applications. *Materials*, *7*(2), 906–947.

Mabes Raj, A. F. P. A., Chouhan, R. S., Košak, A., Horvat, M., Lobnik, A., Rijavec, T., & Lapanje, A. (2025). Recent progress and advancement in detecting methylmercury using a battery of biosensors and biomolecular-based techniques: An updated overview. *TrAC Trends in Analytical Chemistry*, *184*, 118157. https://doi.org/10.1016/j.trac.2025.118157

Manawi, Y. M., Ihsanullah, Samara, A., Al-Ansari, T., & Atieh, M. A. (2018). A Review of Carbon Nanomaterials' Synthesis via the Chemical Vapor Deposition (CVD) Method. *Materials*, *11*(5), 822. https://doi.org/10.3390/ma11050822

Mandal, S., Yadav, A., Panme, F. A., Devi, K. M., & Kumar S. M., S. (2024). Adaption of smart applications in agriculture to enhance production. *Smart Agricultural Technology*, *7*, 100431.

Manesh, K. M., Kim, H. T., Santhosh, P., Gopalan, A. I., & Lee, K.-P. (2008). A novel glucose biosensor based on immobilization of glucose oxidase into multiwall carbon nanotubes–polyelectrolyte-loaded electrospun nanofibrous membrane. *Biosensors and Bioelectronics*, *23*(6), 771–779.

Moghimi Dehkordi, M., Pournuroz Nodeh, Z., Soleimani Dehkordi, K., Salmanvandi, H., Rasouli Khorjestan, R., & Ghaffarzadeh, M. (2024). Soil, air, and water pollution from mining and industrial activities: Sources of pollution, environmental impacts, and prevention and control methods. *Results in Engineering*, *23*, 102729. https://doi.org/10.1016/j.rineng.2024.102729

Mourão, P. A. M., Carrott, P. J. M., Ribeiro Carrott, M. M. L., & Marques, L. (2008). Different Ways to Regenerate an Activated Carbon: Comparison between an Activated Carbon from Cork and a Commercial Carbon. *Materials Science Forum*, *587–588*, 844–848. https://doi.org/10.4028/www.scientific.net/MSF.587-588.844

Mulvaney, P. (1996). Surface Plasmon Spectroscopy of Nanosized Metal Particles. *Langmuir*, *12*(3), 788–800.

Needleman, H. L., Schell, A., Bellinger, D., Leviton, A., & Allred, E. N. (1990). The Long-Term Effects of Exposure to Low Doses of Lead in Childhood: An 11-Year Follow-up Report. *New England Journal of Medicine*, *322*(2), 83–88. https://doi.org/10.1056/NEJM199001113220203

Pellenz, L., De Oliveira, C. R. S., Da Silva Júnior, A. H., Da Silva, L. J. S., Da Silva, L., Ulson De Souza, A. A., De Souza, S. M. D. A. G. U., Borba, F. H., & Da Silva, A. (2023). A comprehensive guide for characterization of adsorbent materials. *Separation and Purification Technology*, *305*, 122435. https://doi.org/10.1016/j.seppur.2022.122435

Peris-Díaz, M. D., Guran, R., Domene, C., De Los Rios, V., Zitka, O., Adam, V., & Krężel, A. (2021). An Integrated Mass Spectrometry and Molecular Dynamics Simulations Approach Reveals the Spatial Organization Impact of Metal-Binding Sites on the Stability of Metal-Depleted Metallothionein-2 Species. *Journal of the American Chemical Society*, *143*(40), 16486–16501. https://doi.org/10.1021/jacs.1c05495

Quansah, R., Armah, F. A., Essumang, D. K., Luginaah, I., Clarke, E., Marfoh, K., Cobbina, S. J., Nketiah-Amponsah, E., Namujju, P. B., Obiri, S., & Dzodzomenyo, M. (2015). Association of Arsenic with Adverse Pregnancy Outcomes/Infant Mortality: A Systematic Review and Meta-Analysis. *Environmental Health Perspectives*, *123*(5), 412–421. https://doi.org/10.1289/ehp.1307894

Quirós, J., Boltes, K., & Rosal, R. (2016). Bioactive Applications for Electrospun Fibers. *Polymer Reviews*, *56*(4), 631–667.

Raji, Z., Karim, A., Karam, A., & Khalloufi, S. (2023). Adsorption of Heavy Metals: Mechanisms, Kinetics, and Applications of Various Adsorbents in Wastewater Remediation—A Review. *Waste*, *1*(3), 775–805. https://doi.org/10.3390/waste1030046

Rantala, A., Utriainen, M., Kaushik, N., Virta, M., Välimaa, A.-L., & Karp, M. (2011). Luminescent bacteria-based sensing method for methylmercury specific determination. *Analytical and Bioanalytical Chemistry*, *400*(4), 1041–1049.

Rijavec, T., Zrimec, J., Oven, F., Viršek, M. K., Somrak, M., Podlesek, Z., Gostinčar, C., Leedjärv, A., Virta, M., Tratnik, J. S., Horvat, M., & Lapanje, A. (2017). Development of Highly Sensitive, Automatized and Portable Whole-Cell Hg

Biosensor Based on Environmentally Relevant Microorganisms. *Geomicrobiology Journal*, *34*(7), 596–605.

Sakka, S. (2013). Sol–Gel Process and Applications. In *Handbook of Advanced Ceramics* (pp. 883–910). Elsevier. https://doi.org/10.1016/B978-0-12-385469-8.00048-4

Santos, D. H. D. S., Xiao, Y., Chaukura, N., Hill, J. M., Selvasembian, R., Zanta, C. L. P. S., & Meili, L. (2022). Regeneration of dye-saturated activated carbon through advanced oxidative processes: A review. *Heliyon*, *8*(8), e10205. https://doi.org/10.1016/j.heliyon.2022.e10205

Sapountzi, E., Braiek, M., Chateaux, J.-F., Jaffrezic-Renault, N., & Lagarde, F. (2017). Recent Advances in Electrospun Nanofiber Interfaces for Biosensing Devices. *Sensors*, *17*(8), 1887.

Scheuhammer, A. M., Meyer, M. W., Sandheinrich, M. B., & Murray, M. W. (2007). Effects of Environmental Methylmercury on the Health of Wild Birds, Mammals, and Fish. *AMBIO: A Journal of the Human Environment*, *36*(1), 12–19.

Segade, S. R., & Tyson, J. F. (2007). Determination of methylmercury and inorganic mercury in water samples by slurry sampling cold vapor atomic absorption spectrometry in a flow injection system after preconcentration on silica C18 modified. *Talanta*, *71*(4), 1696–1702.

Sheoran, K., Kaur, H., Siwal, S. S., Saini, A. K., Vo, D.-V. N., & Thakur, V. K. (2022). Recent advances of carbon-based nanomaterials (CBNMs) for wastewater treatment: Synthesis and application. *Chemosphere*, *299*, 134364. https://doi.org/10.1016/j.chemosphere.2022.134364

Shukla, A. K., Verma, M., & Acharya, A. (2020). Biomolecules Immobilized Nanomaterials and Their Biological Applications. In A. Acharya (Ed.), *Nanomaterial—Based Biomedical Applications in Molecular Imaging, Diagnostics and Therapy* (pp. 79–101). Springer Singapore. https://doi.org/10.1007/978-981-15-4280-0_5

Sinha, P., Datar, A., Jeong, C., Deng, X., Chung, Y. G., & Lin, L.-C. (2019). Surface Area Determination of Porous Materials Using the Brunauer–Emmett–Teller (BET) Method: Limitations and Improvements. *The Journal of Physical Chemistry C*, *123*(33), 20195–20209. https://doi.org/10.1021/acs.jpcc.9b02116

Smith, L. (2017). Historical Perspectives on Water Purification. In *Chemistry and Water* (pp. 421–468). Elsevier. https://doi.org/10.1016/B978-0-12-809330-6.00012-X

Sun, G., Sun, L., Xie, H., & Liu, J. (2016). Electrospinning of Nanofibers for Energy Applications. *Nanomaterials*, *6*(7), 129.

Thekkudan, V. N., Vaidyanathan, V. K., Ponnusamy, S. K., Charles, C., Sundar, S., Vishnu, D., Anbalagan, S., Vaithyanathan, V. K., & Subramanian, S. (2017). Review on nanoadsorbents: A solution for heavy metal removal from wastewater. *IET Nanobiotechnology*, *11*(3), 213–224. https://doi.org/10.1049/iet-nbt.2015.0114

Tian, K., Li, C., Liu, H., & Wang, L. (2025). Functionalization of biochar using SDS/SAP nanomicelles enhanced its immobilization capacity for dyes and heavy metals in water. *Scientific Reports*, *15*(1), 7199. https://doi.org/10.1038/s41598-025-91229-z

Vigneshvar, S., Sudhakumari, C. C., Senthilkumaran, B., & Prakash, H. (2016). Recent Advances in Biosensor Technology for Potential Applications – An Overview. *Frontiers in Bioengineering and Biotechnology*, *4*. http://journal.frontiersin.org/Article/10.3389/fbioe.2016.00011/abstract

Wang, J., & Guo, X. (2022). Rethinking of the intraparticle diffusion adsorption kinetics model: Interpretation, solving methods and applications. *Chemosphere*, *309*, 136732. https://doi.org/10.1016/j.chemosphere.2022.136732

Wang, L., Ok, Y. S., Tsang, D. C. W., Alessi, D. S., Rinklebe, J., Mašek, O., Bolan, N. S., & Hou, D. (2022). Biochar composites: Emerging trends, field successes and

sustainability implications. *Soil Use and Management*, *38*(1), 14–38. https://doi.org/10.1111/sum.12731

Wang, X., Qiao, Y., Zhang, J., Song, Y., & Han, Q. (2024). A SYBR Green I-based aptasensor for the label-free, fluorometric, and anti-interference detection of MeHg+. *Analytical and Bioanalytical Chemistry*, *416*(1), 299–311.

Wieszczycka, K., Staszak, K., Woźniak-Budych, M. J., Litowczenko, J., Maciejewska, B. M., & Jurga, S. (2021). Surface functionalization – The way for advanced applications of smart materials. *Coordination Chemistry Reviews*, *436*, 213846. https://doi.org/10.1016/j.ccr.2021.213846

Xie, R., Jin, Y., Chen, Y., & Jiang, W. (2017). The importance of surface functional groups in the adsorption of copper onto walnut shell derived activated carbon. *Water Science and Technology*, *76*(11), 3022–3034. https://doi.org/10.2166/wst.2017.471

Xu, R., Ouyang, L., Chen, H., Zhang, G., & Zhe, J. (2023). Recent Advances in Biomolecular Detection Based on Aptamers and Nanoparticles. *Biosensors*, *13*(4), 474. https://doi.org/10.3390/bios13040474

Yan, X., Chio, C., Li, H., Zhu, Y., Chen, X., & Qin, W. (2024). Colonization characteristics and surface effects of microplastic biofilms: Implications for environmental behavior of typical pollutants. *Science of The Total Environment*, *937*, 173141. https://doi.org/10.1016/j.scitotenv.2024.173141

Yang, X., Wan, Y., Zheng, Y., He, F., Yu, Z., Huang, J., Wang, H., Ok, Y. S., Jiang, Y., & Gao, B. (2019). Surface functional groups of carbon-based adsorbents and their roles in the removal of heavy metals from aqueous solutions: A critical review. *Chemical Engineering Journal*, *366*, 608–621. https://doi.org/10.1016/j.cej.2019.02.119

Yang, Y.-K., Ko, S.-K., Shin, I., & Tae, J. (2009). Fluorescent detection of methylmercury by desulfurization reaction of rhodamine hydrazide derivatives. *Organic & Biomolecular Chemistry*, *7*(22), 4590.

Yuan, H., Ji, W., Chu, S., Qian, S., Wang, F., Masson, J.-F., Han, X., & Peng, W. (2018). Fiber-optic surface plasmon resonance glucose sensor enhanced with phenylboronic acid modified Au nanoparticles. *Biosensors and Bioelectronics*, *117*, 637–643.

Zeng, S., Yu, X., Law, W.-C., Zhang, Y., Hu, R., Dinh, X.-Q., Ho, H.-P., & Yong, K.-T. (2013). Size dependence of Au NP-enhanced surface plasmon resonance based on differential phase measurement. *Sensors and Actuators B: Chemical*, *176*, 1128–1133.

Zhang, T., T. ,. Zhou, Y. ,. &. Han. (2021). The Role of Metal–Organic Frameworks in Electronic Sensors. *Angewandte Chemie, 133(28), 15320-15340.*

Zhang, X., Zhang, H., Chen, P., Liu, M., Wu, P., Liu, C., & Jiang, W. (2022). One-step dye wastewater treatment by combined adsorption, extraction, and photocatalysis using g-C3N4 pickering emulsion. *Colloids and Surfaces A: Physicochemical and Engineering Aspects*, *644*, 128814. https://doi.org/10.1016/j.colsurfa.2022.128814

Zhao, C., Liu, G., Tan, Q., Gao, M., Chen, G., Huang, X., Xu, X., Li, L., Wang, J., Zhang, Y., & Xu, D. (2023). Polysaccharide-based biopolymer hydrogels for heavy metal detection and adsorption. *Journal of Advanced Research*, *44*, 53–70. https://doi.org/10.1016/j.jare.2022.04.005

Zhao, X., Wang, Y., Li, D.-S., Bu, X., & Feng, P. (2018). Metal–Organic Frameworks for Separation. *Advanced Materials*, *30*(37), 1705189.

Zheng, A., Yin, K., Pan, R., Zhu, M., Xiong, Y., & Sun, L. (2023). Research Progress on Metal–Organic Frameworks by Advanced Transmission Electron Microscopy. *Nanomaterials*, *13*(11), 1742. https://doi.org/10.3390/nano13111742

Zhu, H., Chen, S., & Luo, Y. (2023). Adsorption mechanisms of hydrogels for heavy metal and organic dyes removal: A short review. *Journal of Agriculture and Food Research*, *12*, 100552. https://doi.org/10.1016/j.jafr.2023.100552

Zhu, H., Du, M., Zhang, M., Wang, P., Bao, S., Wang, L., Fu, Y., & Yao, J. (2013). Facile fabrication of AgNPs/(PVA/PEI) nanofibers: High electrochemical efficiency and durability for biosensors. *Biosensors and Bioelectronics*, *49*, 210–215.

Zuo, Z., Zhang, H., Gao, S., Wang, C., Chen, W.-T., & Hu, G. (2024). Recent progress in porous organic frameworks for electrochemical sensing of environmental pollutants. *Journal of Environmental Chemical Engineering*, *12*(5), 113263. https://doi.org/10.1016/j.jece.2024.113263

Bibliograph

Publications Related to the Thesis

Allwin Mabes Raj A.F.P, A.M., Krajnc, S., Bauman, M. et al. Removal of Pb^{2+}, Cr^{3+} and Hg^{2+}ions from aqueous solutions using SiO2 and amino-functionalized SiO2 particles. J Sol-Gel Sci Technol 103, 290–308 (2022). https://doi.org/10.1007/s10971-022-05830-z

Allwin Mabes Raj A.F.P, Bauman M, Lakić M, Dimitrušev N, Lobnik A, Košak A. Removal of Pb^{2+}, CrT, and Hg^{2+} Ions from Aqueous Solutions Using Amino-Functionalized Magnetic Nanoparticles. International Journal of Molecular Sciences. 2022; 23(24):16186. https://doi.org/10.3390/ijms232416186

Allwin Mabes Raj A.F.P, Bauman, M., Dimitrušev, N., Ali, L. M., Onofre, M., Durand, J., Lobnik, A., & Košak, A. (2022). Superparamagnetic Spinel-Ferrite Nano-Adsorbents Adapted for Hg^{2+}, Dy^{3+}, Tb^{3+} Removal/Recycling: Synthesis, Characterization, and Assessment of Toxicity. International Journal of Molecular Sciences, 24(12), 10072. https://doi.org/10.3390/ijms241210072

Allwin Mabes Raj A.F.P, CHOUHAN, Raghuraj S., KOŠAK, Aljoša, HORVAT, Milena, LOBNIK, Aleksandra, RIJAVEC, Tomaž, LAPANJE, Aleš. Recent progress and advancement in detecting Methylmercury using a battery of biosensors and biomolecular-based techniques: An updated overview. TrAC. Trends in analytical chemistry. 2025, vol. 184, art. 118157, str. 1-21. ISSN 0165-9936. https://doi.org/10.1016/j.trac.2025.118157

Patent

Innovative Nanobiosensor for MeHg detection- manuscript under preparation.

Other Publications:

Dimitrušev, N., Nedeljko, P., Allwin Mabes Raj A.F.P, & Lobnik, A. (2023). Comparison of Surface and Spectral Properties of Optical Sensor Layers Prepared by Spin/Spray Coating and Printing Techniques. Chemosensors, 11(2), 136. https://doi.org/10.3390/chemosensors11020136

Allwin Mabes Raj A.F.P, Andreja Gutmaher, Aleksandra Lobnik, Lamiaa M.A. Ali, Mélanie Onofre, Magali Gary-Bobo, Jean-Olivier Durand, Aljoša Košak,. Toxicity Assessment of thiol functionalized magnetic nanoparticles: Facile synthesis, characterization, and transition metal adsorption

Conference publication:

1. Advancing mercury detection [Elektronski vir]: a MerB (organomercurial-lyase)-based solid-state voltammetry sensor for methylmercury detection

Allwin Mabes Raj A.F.P, Rijavec, Tomaž; Sharifi, Tayebeh; Živković, Igor; Klemenčič, Polona; Alilović, Adna; Begu, Ermira; Horvat, Milena; Lobnik, Aleksandra; Košak, Aljoša; Lapanje, Aleš

Tip dela: 1.12 objavljeni povzetek znanstvenega prispevka na konferenci

Leto: 2024

Vir: ICMGP 2024 [Elektronski vir]: abstract & poster book; Cape Town, South Africa, 21 - 26 July. - Str. 168

COBISS.SI-ID 210866947

2. Advancing mercury detection: A merB (organomercurial-lyase)-based solid-state voltammetry sensor for methylmercury detection

Allwin Mabes Raj A.F.P, Rijavec, Tomaž; Sharifi, Tayebeh; Živković, Igor; Klemenčič, Polona; Alilović, Adna; Begu, Ermira; Horvat, Milena; Lobnik, Aleksandra; Košak, Aljoša; Lapanje, Aleš

Tip dela: 1.12 objavljeni povzetek znanstvenega prispevka na konferenci
Leto: 2024
Vir: NANOAPP 2024 [Elektronski vir]: nanomaterials & applications; book of abstracts; 5th International Scientific Conference NANOAPP 2024 - Nanomaterials & Applications; Ptuj, 18-24 June, 2024, Slovenia. - str. [35]
COBISS.SI-ID 203204611

3. Amino-modified iron oxide nanoparticles for efficient adsorption of Cu (II), Fe (III), Co (II), and Cd (II) Ions from water solutions [Elektronski vir]
Bauman, Maja; Košak, Aljoša; Hadela, Ajra; Mabes Raj, Allwin; Lobnik, Aleksandra
Tip dela: 1.12 objavljeni povzetek znanstvenega prispevka na konferenci
Leto: 2024
Vir: NANOAPP 2024 [Elektronski vir]: nanomaterials & applications; book of abstracts; 5th International Scientific Conference NANOAPP 2024 - Nanomaterials & Applications; Ptuj, 18-24 June, 2024, Slovenia. - str. [40-41]
COBISS.SI-ID 203207427

4. GMOS-Train uncertainty course - training young scientists in fundamentals of metrology and determination of measurement uncertainty
Živković, Igor; Koenig, Alkuin Maximilian; Vijayakumaran Nair, Sreekanth; Waqar Ali, Saeed; Andron, Teodor Daniel; Allwin Mabes Raj A.F.P; Horvat, Milena
Tip dela: 1.12 objavljeni povzetek znanstvenega prispevka na konferenci
Leto: 2024
Vir: ICMGP 2024 [Elektronski vir]: abstract & poster book; Cape Town, South Africa, 21 - 26 July. - Str. 165
COBISS.SI-ID 210280195

5. Mer B (organomercurial-lyase) mediated quartz crystal microbalance (qcm) based methylmercury detection
Allwin Mabes Raj A.F.P, Rijavec, Tomaž; Sharifi, Tayebeh; Živković, Igor; Klemenčič, Polona; Alilović, Adna; Begu, Ermira; Horvat, Milena; Lobnik, Aleksandra; Košak, Aljoša; Lapanje, Aleš
Tip dela: 1.12 objavljeni povzetek znanstvenega prispevka na konferenci
Leto: 2024
Vir: From Biotechnology to Human and Planetary Health [Elektronski vir]: XIII Congress of Microbiologists of Serbia - Mikromed regio 5; Mona Plaza Hotel Belgrade, Serbia - 4th-6th of April, 2024; book of abstracts. - Str. 26
COBISS.SI-ID 194036739

6. MerB (organomercurial-lyase) mediated quartz crystal microbalance (QCM) based Methylmercury detection
Allwin Mabes Raj A.F.P, Rijavec, Tomaž; Sharifi, Tayebeh; Živković, Igor; Klemenčič, Polona; Alilović, Adna; Begu, Ermira; Horvat, Milena; Lobnik, Aleksandra; Košak, Aljoša; Lapanje, Aleš
Tip dela: 1.12 objavljeni povzetek znanstvenega prispevka na konferenci
Leto: 2024
Vir: NANOAPP 2024 [Elektronski vir]: nanomaterials & applications; book of abstracts; 5th International Scientific Conference NANOAPP 2024 - Nanomaterials & Applications; Ptuj, 18-24 June, 2024, Slovenia. - str. [50]
COBISS.SI-ID 203312131

7. Methylmercury detection through changes in the electrical conductivity across gold films with MerB (organomercurial-lyase) functionalized nanoparticles [Elektronski vir]
Allwin Mabes Raj A.F.P, Rijavec, Tomaž; Horvat, Milena; Lobnik, Aleksandra; Košak, Aljoša; Lapanje, Aleš
Tip dela: 1.12 objavljeni povzetek znanstvenega prispevka na konferenci
Leto: 2023
Vir: Goldschmidt2023: Lyon, 9-14 July 2023. - 1 spletni vir
COBISS.SI-ID 167070723

8. Organomercurial lyase (MerB) enabled methylmercury detection
Allwin Mabes Raj A.F.P, Rijavec, Tomaž; Horvat, Milena; Lobnik, Aleksandra; Košak, Aljoša ; Lapanje, Aleš
Tip dela: 1.12 objavljeni povzetek znanstvenega prispevka na konferenci
Leto: 2023
Vir: Power of Microbes in Industry and Environment: book of abstracts; May 15 - 18, 2023, Poreč, Croatia. - Str. 62
COBISS.SI-ID 165314819

9. Organomercurial lyase (MerB): the global tweezers that can be used for cutting, capturing and biosensing aqueous Methylmercury
Allwin Mabes Raj A.F.P, Rijavec, Tomaž; Horvat, Milena; Lobnik, Aleksandra; Košak, Aljoša; Lapanje, Aleš
Tip dela: 1.12 objavljeni povzetek znanstvenega prispevka na konferenci
Leto: 2022
Vir: ICMGP, Mercury as a Global Pollutant, 24th - 29th July 2022, virtual event [Elektronski vir].
COBISS.SI-ID 187260931

10. Organomercurial lyase (MerB): the global tweezers that can be used for cutting, capturing and biosensing aqueous Methylmercury
Allwin Mabes Raj A.F.P, Rijavec, Tomaž; Horvat, Milena; Lobnik, Aleksandra; Košak, Aljoša ; Lapanje, Aleš
Tip dela: 1.12 objavljeni povzetek znanstvenega prispevka na konferenci
Leto: 2022
Vir: Goldschmidt 2022: Honolulu, Hawai'i, USA and online,10-15 July 2022.
COBISS.SI-ID 187256579

11. Organomercurial lyase (MerB) enabled methylmercury detection [Elektronski vir]
Allwin Mabes Raj A.F.P, Rijavec, Tomaž; Horvat,Milena; Lobnik, Aleksandra ; Košak, Aljoša ; Lapanje, Aleš
Tip dela: 1.12 objavljeni povzetek znanstvenega prispevka na konferenci
Leto: 2022
Vir: Book of abstracts [Elektronski vir]: Week of Microbial Technologies; Ljubljana, Slovenia, November 7-11, 2022. - Str. 57
COBISS.SI-ID 137953795

12. Organomercurial lyase (MerB) enabled methylmercury detection
Allwin Mabes Raj A.F.P, Rijavec, Tomaž; Horvat, Milena; Lobnik, Aleksandra; Košak, Aljoša; Lapanje, Aleš
Tip dela: 1.12 objavljeni povzetek znanstvenega prispevka na konferenci

Leto: 2022
Vir: 15th International Symposium on the Interactions Between Sediments and Water [Elektronski vir] : Piran, Slovenia, June 12-15, 2022; book of abstracts.
COBISS.SI-ID 187254787

13. Rapid detection of aqueous MeHg using cell-free transcription biosensing system
Allwin Mabes Raj A.F.P, Rijavec, Tomaž ; Horvat, Milena ; Lobnik, Aleksandra ; Košak, Aljoša
Tip dela: 1.12 objavljeni povzetek znanstvenega prispevka na konferenci
Leto: 2022
Vir: 14. študentska konferenca Mednarodne podiplomske šole Jožefa Stefana = 14th Jožef Stefan International Postgraduate School Students' Conference: knjiga povzetkov = book of abstracts; 1. - 3. junij 2022, Kamnik, Slovenia = 1st - 3rd June, 2022, Kamnik, Slovenia. - str. 36
COBISS.SI-ID 115103747

14. Removal of Pb^{2+}, Cr^{3+} and Hg^{2+}Ions from aqueous solutions using SiO2 and amino-functionalized SiO[sub]2 particles
Lobnik, Aleksandra; Dimitrušev, Nena; Allwin Mabes Raj A.F.P,
Tip dela: 1.12 objavljeni povzetek znanstvenega prispevka na konferenci
Leto: 2022
Vir: Goldschmit [Elektronski vir] : Hawai'i 2022; [virtual conferences].
COBISS.SI-ID 13820979

Biography

Professional Experience

Allwin Mabes Raj Antoney Francis Paulraj is a doctoral candidate at the *Jožef Stefan International Postgraduate School*, affiliated with both *IOS d.o.o.* (Maribor) and the *Jožef Stefan Institute* (Ljubljana), Slovenia. His research lies at the intersection of **environmental nanotechnology**, **biosensor development**, and **toxic metal remediation**, supervised by **Prof. Dr. Aleksandra Lobnik** and **Assoc. Prof. Dr. Aleš Lapanje**. His PhD committee is chaired by **Prof. Dr. Milena Horvat**, a leading authority in mercury research and environmental health.

Allwin has participated in **multi-institutional and international research collaborations** across Europe and Asia, contributing to projects on **water purification, environmental monitoring, and biosensing**. He has provided scientific consultation and has mentored interns and junior researchers in areas such as **nanomaterials synthesis, functionalization, and electrochemical sensor fabrication**.

He also gained international experience through an **Erasmus+ research exchange at the University of Hildesheim, Germany**, where he explored environmental applications of biosensors. Additionally, he served as a **research fellow for four years** in the *Department of Genetics, School of Biological Sciences, Madurai Kamaraj University (India)*, where he contributed to an **Indo-UK collaboration titled "RiceFuel"** — a sustainable bioenergy project funded by the Newton-Bhabha initiative, aimed at valorizing rice straw through microbial bioconversion into renewable fuels and chemicals.

Education & International Experience

M.Sc. Zoology (Specialization in Biotechnology)
Madurai Kamaraj University, Tamil Nadu, India

B.Sc. Zoology (Specialization in Biotechnology)
Madurai Kamaraj University, Tamil Nadu, India

Study Abroad Program – University of Hildesheim, Germany
Selected to represent the American college through a competitive exchange program at the **University of Hildesheim**, Lower Saxony, Germany, as part of an academic and cultural immersion initiative under the Erasmus framework.

Research & Projects

GMOS-TRAIN: **European Union's Horizon 2020 research and innovation programme** under the **Marie Skłodowska-Curie grant agreement No. 860497**.

"Electrochemical detection of methylmercury", funded by **ARIS (L7-60161(C))** through slovenian national research funding ARIS.

Awards & Recognition

Marie Skłodowska-Curie Early-Stage Research Fellowship (Horizon 2020, GMOS-Train Consortium)

Department of Biotechnology - Research Fellowship for the Rice fuel project.

Best Poster Award, *MicroTech Week 2024*, Jožef Stefan Institute

Co-author of multiple peer-reviewed publications, including:

TrAC – Trends in Analytical Chemistry (biosensor innovations for methylmercury detection)

International Journal of Molecular Sciences, *Chemosensors*, and others
First position in Instituion for Masters research scoring 84%

Contributor to **whole genome sequencing** and GenBank submissions (e.g., *Bacillus paralicheniformis* MKU3)

Presenter at international scientific conferences: *Goldschmidt*, *ICMGP*, *IPSSC*, and *Power of Microbes*